QUANTITATIVE CHARACTERISATION OF AIRBORNE ELECTROMAGNETIC SYSTEMS

A THESIS SUBMITTED IN FULFILLMENT

OF THE

REQUIREMENTS FOR THE DEGREE OF

DOCTORATE OF PHILOSOPHY

AARON CHARLES DAVIS

BSC, MSC

Applied Physics

Applied Sciences

Science, Engineering and Technology

RMIT University

August 2007

Declaration of the Candidate

I certify that except where due acknowledgement has been made, the work is that of the candidate alone. This body of work has not been submitted previously, in whole or in part, to qualify for any other academic award. The content of this thesis is the result of work which has been carried out since the official commencement date of the approved research program. Any editorial work, paid or unpaid, carried out by a third party is acknowledged.

Aaron Charles Davis

August 2007

Acknowledgements

With any sort of written project that takes time and effort, more people than just the author contribute to the work. It is no different in the present case with my thesis, and I have many people to thank for their contributions.

Firstly, I must express the immense gratitude that I feel toward my supervisor, Professor James Macnae. Jim has helped me understand the physics of electromagnetic induction in an entirely new way, taking me from a knowledge of the Maxwell equations to a daily working familiarity that is to be expected from a master in the field. Jim has patiently guided my thoughts, corrected the wrong ideas that I had formed about EM theory and read and re-read my written works many times over. A good friend and a great leader.

I would like to thank my second supervisor, Dr. Terry Robb, whose mathematical abilities outstrip those of most people I know. Terry was an excellent sound-board for my ideas on the mathematical derivations of mutual inductance that I had to slog through.

For financial assistance, I would like to thank the following sponsors from the Amira project p407b: AngloGold Ashanti, CRC - Landscape Environments and Mineral Exploration (CRC LEME), CVRD, Defence Science & Technology Organisation, Geoscience Australia, Noranda Inc/Falconbridge Ltd, Rio Tinto Exploration Pty Limited, Xstrata Copper and Xstrata Nickel Limited. This project enabled me to conduct my work with an APAI Scholarship through ARC Linkage Grant LP0348409. Thanks also to the SEG Scholarship Foundation for a scholarship in

the years 2005–2007, the G. W. H. Hohmann Memorial Trust for a scholarship in the years 2005–2006, and the ASEG for a travel bursary that subsidised a trip to Denver, Colorado in October 2004.

Thank you to my workmates, who made coming to RMIT University an enjoyable experience. In order of appearance, Yusen Ley-Cooper, Adam Smiarowski, Chris Adams, Nick Ebner and John Chung. Thank you all for the good times, the good discussions, and all the laughs. I have never had such a good work group.

Finally, my most heartfelt thanks go to Libby, my wonderful wife, friend and partner. Your help and love throughout have been my support. Thank you so much, you are so special.

Contents

List of Tables

List of Figures

Summary

There are several needs for quantitative analysis of data from airborne electromagnetic (AEM) surveys which have increased attention to the conductivity structure of the top 5–20 m of the earth's surface. In applying the airborne electromagnetic method for shallow-earth purposes such as environmental monitoring, sea-ice thickness prediction and saltwater bathymetry, problems have been identified that affect the quantitative interpretation of data.

In this thesis, I address the geometrical problem of the pendulum-like swinging of towed transmitters and receivers (birds) when they are employed as part of the AEM platform. By using video recordings and simultaneous position solutions of the GPS antennas on the towed birds and aircraft, I establish a link between bird swing and its effect on survey data for the RESOLVE and DIGHEM systems. The link is explained by a model that compares actual survey data to the calculated mutual inductance coupling of a dipole pair to an infinitely conductive half space, which pair is permitted arbitrary pitch, roll and altitude changes. Different models are provided for aircraft-mounted altimetry and bird-mounted altimetry. Problems such as slant range error and watercourse effects are defined with both altimetry methods. I develop a non-linear filter that removes bird swing effects from survey data which successfully corrects data from three different AEM surveys. A mathematical model based on Lagrangian and Hamiltonian mechanics is derived which approximates to first order the different periods of swing of towed birds.

Calibration of the AeroTEM, HoistEM, VTEM, and SkyTEM time domain AEM systems is attempted using an accurately laid out and surveyed, closed, multi-turn loop of known resistance and self inductance that is placed on—but insulated from—resistive ground. I derive a rigourous mathematical model that predicts the airborne receiver's response to the mutual inductance coupling of the AEM transmitter to the ground loop based on a knowledge of the transmitter current waveform and system geometry. Although the method is proven to be successful over resistive ground, significant problems are identified such as: altimetry errors, spatial averaging of the data during postprocessing, errors in the predicted horizontal positions of the AEM platform, receiver windowing and timing errors and bird swing. I show that, although we can calibrate a time domain AEM system for waveform and geometry over one flyover, it is impossible to calibrate an AEM system for geometry: bird swing has too great an effect. As an intermediate step in the calibration process, I show that by monitoring the current induced in the ground loop we can obtain the waveform of the transmitter current through deconvolution in the Fourier domain: a very useful feature for AEM systems such as HoistEM which, at the publication of this thesis are unable to monitor the transmitter current waveform during the transmitter on-time.

Simple and cost effective methods for the improvement of quantitative AEM data are presented in this thesis. However, until the geometry problem of AEM platforms is solved, full system calibration will not be obtained and filters will need to be applied to the data. I recommend the use of: GPS antennas mounted on all towed birds, able to be post-processed for accurate position recovery, reliable bird-mounted scanning altimeters that do not rely on range-finding technology but instead employ a shortest path algorithm, pitch and roll sensors mounted on the trailed bird and the measurement of airspeed of both the towed bird and the aircraft during surveys.

Chapter 1

Introduction

After the Second World War, the global economy suffered from a lack of strategic metals like lead, iron, copper and nickel. Countries around the world were faced with the difficulty of finding raw mineral and metal resources; countries such as Canada and Australia were faced with an even greater difficulty—that of finding mineral resources in remote and inaccessible areas (Palacky and West, 1991). In order for such large and sparsely populated countries to harvest their mineral resources, a better method of mining exploration needed to be developed that could help discover mineral bodies cheaply and effectively. It was believed that electric and electromagnetic methods as they existed were too costly to use for large-scale exploration operations, so the innovation was made to place a transmitter dipole in the fuselage of an airplane and tow a receiver dipole behind it (Fountain, 1998). This marked the beginning of a new era in exploration geophysics: airborne electromagnetics (AEM). The AEM application is now used successfully and routinely in most areas of the world for the detection of metal ore deposits. Today, countries such as Australia, Canada, Brazil, Argentina, South Africa, and India routinely use AEM as part of their mineral exploration operations (Fountain, 1998).

From the first AEM flights circa 1946 (Palacky and West, 1991) and the first ore body discovery from an AEM survey in New Brunswick, Canada shortly after

(Fountain, 1998), the field of AEM has been expanding and is now a major field of study. From early analog systems that explorers used in the recently glaciated pre-cambrian terrains to detect bumps in an otherwise flat background signal, to fully digital, multi-loop, multi-component surveys that offer simultaneous electromagnetic and magnetic data acquisition, greater emphasis has been placed on system development, increased signal to noise ratios and geophysical and geological interpretation. The field of AEM has expanded a great deal over the last 50 years and offers many different systems to prospective clients based on individual needs (Fountain, 1998). This lead to the development of both more powerful fixed-wing towed bird systems such as GEOTEM (Fugro Airborne Surveys, 2005*a*), and to highly versatile helicopter-borne systems such as DIGHEM (Fraser, 1978) and RESOLVE (Fugro Airborne Surveys, 2005*c*). In turn, the application of AEM has broadened from massive sulfide detection to specific problems such as the detection of small deposits of precious metals (like gold and silver), the discovery of diamonds in kimberlite deposits (Macnae, 1979), and more environmental applications, such as the mapping of sea ice thickness (e.g. Kovacs and Holladay, 1990; Pfaffling et al., 2007), shallow water depths (e.g. Vrbancich, Fullagar and Macnae, 2000), contaminants (Beamish and Klinck, 2006) and near-surface salinity (e.g. Fitterman and Deszcz-Pan, 1998; George et al., 1998; George and Woodgate, 2002). Yet, with new applications more stringent demands are being placed on the systems in use. For example, the maximum rooting depths of cropland plants worldwide is less than 5 m (Canadell et al., 1996), which is close to the maximum conductance resolution of most AEM systems used for salinity mapping (George et al., 1998). Recently, these accuracy issues have been identified in the usage of AEM systems for environmental applications. In their national report concerning the evaluation of AEM for managing water catchments, George et al. (1998) stated that AEM systems are limited in their quantification of electrical conductivity in the near surface; although the existence of conductivity anomalies can be detected in the top 0–10 m of the soil, they

cannot be resolved. Similarly, George and Green (2000) identified problems with AEM system geometry, altimetry and calibration which create a negative impact on the quality of conductivity maps, thereby limiting their usefulness. In the determination of sea ice thickness, Holladay et al. (1997) established a relationship between towed bird swings and errors in ice thickness, while (Deszcz-Pan et al., 1998) added a ground-speed dependent bird altitude adjustment to their inversions for resistivity depth-models.

While efforts have been made to estimate the effect of transmitter and receiver altitude and attitude changes on AEM data (e.g. Green, 1998; Fitterman and Yin, 2004; Yin and Fraser, 2004), monitor bird position using recorded primary field measurements (Smith, 2001) and even to encompass all AEM geometry variations in a 'total' inversion algorithm (Brodie and Sambridge, 2006), bird swing problems still exist. For example, there are at present no models that account for the swinging action of a towed bird on survey nor has the relative motion of the bird to the aircraft been studied. There have been no significant statistical surveys or predictions of mean bird swing periods from currently obtainable AEM survey data. Few attempts have been made at tracking the swinging and pitching motion of towed birds on survey and, despite having models that describe the coupling changes of pitched and rolled birds, no attempts have been made at deriving a method that corrects historical datasets that have no bird pitch or roll information. Furthermore, although altimetry problems have been identified and warnings have been issued about the trustworthiness of laser and radar altimeters in AEM surveys (Brodie and Lane, 2003; Kratzer et al., 2007), no modelling has been done to ascertain the different effects of aircraft-mounted and bird-mounted altimetry. Attitude effects can become important considerations when attempting to find conductivity information in the near surface (e.g. in the top 20 m of soil), as well as when using AEM to determine sea ice thicknesses (Holladay et al., 1997). Whenever highly conductive ground is studied, for example in the regolith of Australian conditions, bird swing and transmitter attitude will be an important issue.

In addition to more stringent requirements on total system geometry, environmental and near-surface applications require AEM systems that have been reliably and accurately calibrated. As an example, Fitterman (1998) showed that various errors can exist and be produced due to poor calibration techniques for frequency domain HEM systems. Ley-Cooper et al. (2006) used the dimensionless altitude-corrected $\phi\beta$ domain to determine calibration and altitude errors in HEM systems flown over sea water. In order to achieve reasonable seawater depth estimates using AEM data obtained with the HoistEM helicopter-borne time domain system (Boyd, 2004), Vrbancich and Fullagar (2004) were forced to use an incorrect seawater conductivity in their inversion calculation. This was further addressed in 2007 (Vrbancich and Fullagar, 2007*a*; Vrbancich and Fullagar, 2007*b*). Calibration of AEM systems can be difficult: for example, the system geometry specified for many fixed-wing systems that tow a receiver during operations is a nominal value. Other systems cannot have receivers with a gain suitable for secondary detection during the transmitter current pulse. Other transmitters need the cooling effect of rushing air to be fully operational and cannot be tested on the ground at full power. Currently, no reliable method exists that can be used to accurately calibrate all AEM systems before during and after survey.

The fundamental aim of this thesis is to improve the quality of AEM survey data. This will be achieved in two parts: 1) the study of the swinging motion of towed birds while on survey, and 2) the development of a simple calibration method that can be applied to any AEM system as a routine part of its survey.

Chapter 2 will cover a review of the theory of electromagnetism as it pertains to the physics and calibration of airborne electromagnetic devices. I will discuss the theory of magnetic inductance and give an assortment of calculations of the mutual and self inductance of circuits and wire loops. Chapter 3 will give evidence of how bird swing can be detected in data collected from airborne electromagnetic surveys. I will also point out that, at present, there exist problems with altimetry

that need to be addressed by the AEM-geophysical community. In Chapter 4, I will develop models of bird swing for the helicopter-borne RESOLVE AEM system that will show how bird swing effects can conveniently be broken down into altitude and coupling components. I design two filters that operate on airborne data to remove the effects of bird swing and show, in a few examples, the efficacy of the filter and the overall improvement in spatial consistency of AEM survey data. A study of the pendulum-like swinging of a scale model will also lend some insight into bird swing, and I use the time evolution of the swinging motions to produce a mathematical model that describes the basic behaviour of a towed bird on survey.

Further advances in the improvement of quantitative airborne data will be made in Chapters 5 and 6, where I develop and test the method of calibration of AEM systems with the use of an accurately laid out and surveyed calibration ground loop of well-known electrical properties. In these chapters, I show how the mathematical models may be used to predict the airborne receiver response of any AEM system as a consequence of fly-over. Several different AEM systems are tested with some intriguing and surprising results. Additionally, in Chapter 6, I show how measurement of the induced current in the ground loop can be used to recover the waveform of the transmitter current of any time domain AEM system.

Chapter 2

EM Background Theory

2.1 Introduction

In order to describe the calibration methods and, to a lesser extent, the electromagnetic induction method of exploration geophysics, it is necessary to understand some basic physics of electrodynamics as it applies to geophysics. In this chapter, I will begin by presenting Maxwell's equations: the fundamental equations of classical electrodynamics. Next, I will discuss a simplified method of calculating magnetic fields by the use of a potential function that relies on the fact that the magnetic field has zero divergence.

The use of the Biot-Savart (Jackson, 1999) law to calculate magnetic fields in wire loops due to constant or time-varying currents is a common approach in geophysics. The procedure is applicable as long as we understand that we are operating under the quasi-static assumption. The quasi-static assumption, or the long wavelength approximation, means that the mathematics becomes simplified; and we can ignore wave physics and only use diffusion physics to calculate physical models. Using the long wavelength approximation, I then present, in Section 2.6, calculations for the magnetic field in space for: a segment of wire, a circular loop of wire, and a magnetic dipole. Each of these models has application in the field of geophysics.

Magnetic mutual inductance is a concept that is very important to the induction method of geophysics. The mutual inductance of two wire loops can be understood from a flux-cutting point of view (e.g. Griffiths, 1989), in that a changing magnetic field produces an electric current in a loop of wire, or from an energy storage point of view (Jackson, 1999), where two loops store magnetic energy between them. The mutual inductance of two skew lines is calculated, as well as the mutual inductance of two dipoles.

Magnetic self inductance is the reaction of a circuit to changes in its own current. If an applied current in a closed circuit changes with time, the self inductance of the circuit opposes the change. Self inductance is in fact a measure of how much magnetic energy can be stored in a circuit by itself; such energy is recoverable. The self inductance of straight segments of wire is presented in Section 2.7.5, and generalised to calculate the total inductance of a loop of wire in Section 2.7.6.

2.2 Maxwell's Equations in General

Classical electromagnetic theory is governed by Maxwell's equations. These are uncoupled linear first order differential equations that describe the relationship between five vectors that can completely determine the electric and magnetic fields within a given region (Griffiths, 1989).

The vector field **E** is the electric field intensity, measured in volts per metre (V/m). The magnetic field or magnetic induction, **B**, is measured in tesla (T). The electric field is related to another field, called the electric displacement, **D** (measured in coulombs per square metre (Q/m^2); while the magnetic field is related to the magnetic field intensity vector field **H** (measured in amperes per metre (A/m)). The final vector field to be named is the electric current density which is measured in ampere per metre squared (A/m^2), and expressed as **J**.

Maxwell's equations are empirical equations that faithfully describe most macroscopic electromagnetic behaviour. The first general law is given the name Faraday's Law in honour of Michael Faraday, and is

$$\boldsymbol{\nabla} \times \mathbf{E} = -\frac{\partial \mathbf{B}}{\partial t}. \tag{2.1}$$

This equation states a time-varying magnetic field generates an electric field that circulates about it.

The next equation, generally known as Ampère's Law, describes the properties of the curl of the magnetic field:

$$\boldsymbol{\nabla} \times \mathbf{B} = \mu_0 \epsilon_0 \frac{\partial \mathbf{E}}{\partial t} + \mu_0 \mathbf{J}, \tag{2.2}$$

where μ_0 is the permeability of free space ($\mu_0 = 4\pi \times 10^{-7}$ N/A^2), and ϵ_0 is the permittivity of free space ($\epsilon_0 = 8.85 \times 10^{-12}$ C/Nm^2). This law states that a magnetic field circulates around a closed path that is proportional in field strength to the total current that the loop encompasses. The total current in this case not only arises from electrical current (the movement of physical charge), but also the displacement current generated from the time rate of change of the electric field.

The next, unnamed equation points to the theoretical exclusion of the presence of magnetic monopoles, namely that

$$\boldsymbol{\nabla} \cdot \mathbf{B} = 0.$$

The final equation is Gauss' Law in differential form, which describes the divergence of the electric field:

$$\boldsymbol{\nabla} \cdot \mathbf{E} = \frac{1}{\epsilon_0} \rho \tag{2.3}$$

This law states that the electric field components diverge from any distribution of charge, where ρ is the charge density, measured in C/m^3.

Maxwell's equations, together with the Lorentz force law,

$$\mathbf{F} = q(\mathbf{E} + \mathbf{v} \times \mathbf{B}),$$

where q is the quantity of electric charge (C), $\mathbf{v}$ is the velocity of the charge, and $\mathbf{F}$ is the resultant force due to the presence of the electric and magnetic fields operating on the charge, completely determine classical electrodynamics (Griffiths, 1989). By applying the divergence operator to equation (2.2), even the continuity equation, or conservation of charge equation can be derived. First we apply the divergence to each side of equation (2.2) to obtain

$$\boldsymbol{\nabla} \cdot \boldsymbol{\nabla} \times \mathbf{B} = \boldsymbol{\nabla} \cdot \left(\mu_0 \epsilon_0 \frac{\partial \mathbf{E}}{\partial t} + \mu_0 \mathbf{J} \right)$$

and since the divergence of the curl of any vector field is zero,

$$\boldsymbol{\nabla} \cdot \mathbf{J} = -\epsilon_0 \boldsymbol{\nabla} \cdot \frac{\partial \mathbf{E}}{\partial t}.$$

Assuming that the electric field is continuous and possesses continuous first and second derivatives, we can change the order of the partial and spatial derivatives, i.e.

$$\boldsymbol{\nabla} \cdot \frac{\partial \mathbf{E}}{\partial t} = \frac{\partial (\boldsymbol{\nabla} \cdot \mathbf{E})}{\partial t}.$$

Using equation (2.3), this yields

$$\boldsymbol{\nabla} \cdot \mathbf{J} = -\frac{\partial \rho}{\partial t},$$

which is the statement that charge is conserved.

When we are trying to determine the electrodynamic and physical properties of the earth, we need to develop these equations into an alternative form. In particular, when dealing with bulk matter and interfaces, it is important to be able to distinguish materials that are subject to electric and magnetic polarisation. Guided by experiment, we can make certain assumptions about the physical properties of the materials that we are considering. This leads into a less generalised set of Maxwell's equations.

2.3 Maxwell's Equations in Matter

Once polarisation becomes an important consideration, we need to define relationships between the fields **D** and **E**, and **H** and **B**. These are known as the constitutive relations (Ward and Hohmann, 1988).

We can define the displacement vector to be

$$\mathbf{D} \equiv \epsilon_0 \mathbf{E} + \mathbf{P}, \tag{2.4}$$

where the polarisation vector **P** arises in polarised materials due to local charge imbalances at an atomic level manifesting at a macroscopic level. Polarisation of a material is often caused by subjecting the material to an electric field, so that

$$\mathbf{P} = \tilde{\boldsymbol{\epsilon}}(\omega, \mathbf{E}, \mathbf{r}, t, T, P, \ldots) \cdot \mathbf{E}.$$

The tensor $\tilde{\boldsymbol{\epsilon}}$ is a complex function that describes the way in which the material being considered changes its polarisation based on such variables as angular frequency, electric field strength, position $\mathbf{r}$, time t, temperature T, pressure P, or other physical variables.

Furthermore, we can define magnetic field intensity in terms of magnetic induction and a vector field **M**, which describes the magnetisation of a material, in the

following manner:

$$\mathbf{H} \equiv \frac{1}{\mu_0}\mathbf{B} - \mathbf{M}. \tag{2.5}$$

The magnetisation vector is caused from microscopic local current circulations that can be seen at a macroscopic level. $\mathbf{M}$ can be determined in much the same way as the polarisation vector, using a tensor quantity $\tilde{\boldsymbol{\mu}}$ that could be a function of angular frequency, magnetic field intensity, position, time, etc.

$$\mathbf{M} = \tilde{\boldsymbol{\mu}}(\omega, \mathbf{H}, \mathbf{r}, t, T, P, \ldots) \cdot \mathbf{H}.$$

For most geophysical electromagnetic considerations, it is reasonable to make the following assumptions about the physical properties of earth material (Ward and Hohmann, 1988):

1. Earth materials are each linear, isotropic, and homogeneous.
2. Electric properties are independent of time, temperature and pressure.
3. The magnetic permeability is assumed to be equal to μ_0, the permeability of free space.

With these assumptions, we can further clarify the relation of $\mathbf{P}$ to $\mathbf{E}$, and $\mathbf{M}$ to $\mathbf{H}$ by imposing linear relations between them. The linear relation between $\mathbf{P}$ and $\mathbf{E}$ can be defined as

$$\mathbf{P} = \epsilon_0 \chi_e \mathbf{E},$$

so that

$$\mathbf{D} = \epsilon_0(1 + \chi_e)\mathbf{E} = \epsilon\mathbf{E},$$

which means that the polarisation of a material is proportional to the electric sus-

ceptibility, χ_e, and further implies that the electric displacement is proportional to the electric field. The value ϵ is the electric permittivity of the material being considered. For linear materials, the magnetisation field can be described in a similar way by using the magnetic susceptibility, χ_m, to define a relation between $\mathbf{M}$ and magnetic intensity, $\mathbf{H}$:

$$\mathbf{M} = \chi_m \mathbf{H},$$

which implies

$$\mathbf{B} = \mu_0(1 + \chi_m)\mathbf{H} = \mu\mathbf{H}. \tag{2.6}$$

Another consequence of the assumptions made above is that there is a direct linear relation between free current density $\mathbf{J_f}$ and electric field $\mathbf{E}$. This relation is known as Ohm's law and can be stated as

$$\mathbf{J_f} = \sigma\mathbf{E},$$

where σ is the electrical conductivity of the material. In general, we allow the electric permittivity and the electrical conductivity to be complex in nature, and to also be functions of angular frequency (Ward and Hohmann, 1988):

$$\mathbf{D} = \epsilon(\omega)\mathbf{E} = \epsilon\mathbf{E}, \tag{2.7a}$$

and

$$\mathbf{J_f} = \sigma(\omega)\mathbf{E} = \sigma\mathbf{E} \tag{2.7b}$$

Once we make the distinction between electric fields, displacement fields, and polarisation fields—and between magnetic intensity, magnetisation and magnetic induction—it is necessary to make distinctions between free and bound charges as well as free and bound currents. Looking back to equation (2.3), we should remember that ρ is the total charge density, and can be divided into free charge, ρ_f, and bound charge, ρ_b. Bound charge, or charge that accumulates due to the polarisation of a material can be found from the divergence of $\mathbf{P}$:

$$\rho = \rho_f + \rho_b,$$

and

$$\rho_b = -\boldsymbol{\nabla} \cdot \mathbf{P}.$$

With this result, we can use equation (2.4), and rearrange equation (2.3) to get a condition for the displacement field:

$$\boldsymbol{\nabla} \cdot \mathbf{E} = \frac{1}{\epsilon_0}(\rho_f + \rho_b),$$

or

$$\boldsymbol{\nabla} \cdot \mathbf{E} = \frac{1}{\epsilon_0}(\rho_f - \boldsymbol{\nabla} \cdot \mathbf{P}),$$

which leads to

$$\boldsymbol{\nabla} \cdot \mathbf{D} = \rho_f.$$

Thus, the divergence of the displacement field is equal to the free electric charge density.

We also need to consider the charge density field, $\mathbf{J}$. When used in equation (2.2), $\mathbf{J}$ should be interpreted as the total current in the entire system under consideration. It is now appropriate to consider the current density as being made up of free current, $\mathbf{J_f}$, bound current resulting from any magnetisation, $\mathbf{J_b}$, and 'polarisation current', $\mathbf{J_p}$, that arises due to time rates of change in the polarisation vector. This is stated mathematically below in equations (2.8)

$$\mathbf{J} = \mathbf{J_f} + \mathbf{J_b} + \mathbf{J_p}, \tag{2.8a}$$

where

$$\mathbf{J_b} = \boldsymbol{\nabla} \times \mathbf{M} \tag{2.8b}$$

and

$$\mathbf{J_p} = \frac{\partial \mathbf{P}}{\partial t}. \tag{2.8c}$$

We then use the definition of magnetic intensity given in equation (2.5) and rearrange the general expression of Ampère's Law equation (2.2) to get

$$\boldsymbol{\nabla} \times \mathbf{B} = \mu_0 \epsilon_0 \frac{\partial \mathbf{E}}{\partial t} + \mu_0 \mathbf{J},$$

which can be expressed as

$$\boldsymbol{\nabla} \times \frac{\mathbf{B}}{\mu_0} = \epsilon_0 \frac{\partial \mathbf{E}}{\partial t} + \mathbf{J_f} + \mathbf{J_b} + \mathbf{J_p},$$

and using equations (2.8),

$$\boldsymbol{\nabla} \times \frac{\mathbf{B}}{\mu_0} = \epsilon_0 \frac{\partial \mathbf{E}}{\partial t} + \mathbf{J_f} + \boldsymbol{\nabla} \times \mathbf{M} + \frac{\partial \mathbf{P}}{\partial t},$$

which implies

$$\boldsymbol{\nabla} \times \mathbf{H} = \mathbf{J_f} + \frac{\partial \mathbf{D}}{\partial t}. \tag{2.9}$$

Gathering all results yields the set of Maxwell's equations in terms of all five vector fields:

$$\left\{ \begin{array}{ll} \boldsymbol{\nabla} \cdot \mathbf{D} = \rho_f & \boldsymbol{\nabla} \cdot \mathbf{H} = 0 \\ \boldsymbol{\nabla} \times \mathbf{E} = -\dfrac{\partial \mathbf{B}}{\partial t} & \boldsymbol{\nabla} \times \mathbf{H} = \mathbf{J_f} + \dfrac{\partial \mathbf{D}}{\partial t} \end{array} \right\}. \tag{2.10}$$

These equations, with the relations stated in (2.6) and (2.7), give Maxwell's equations the following form:

$$\left\{ \begin{array}{ll} \boldsymbol{\nabla} \cdot \mathbf{E} = \rho_f & \boldsymbol{\nabla} \cdot \mathbf{H} = 0 \\ \boldsymbol{\nabla} \times \mathbf{E} = -\mu \dfrac{\partial \mathbf{H}}{\partial t} & \boldsymbol{\nabla} \times \mathbf{H} = \sigma \mathbf{E} + \epsilon \dfrac{\partial \mathbf{E}}{\partial t} \end{array} \right\},$$

which define Maxwell's equations in terms of the electric field and the magnetic field intensity. Either form is correct, with the application being considered governing the choice of the system of equations.

2.4 Magnetic Vector Potential

The magnetic vector potential is a vector field that can be used to determine the magnetic induction, $\mathbf{B}$. It's origin is from the fact that since there have been no physically detected magnetic monopoles (reflected in the equation $\boldsymbol{\nabla} \cdot \mathbf{B} = 0$), there

exists a vector field $\mathbf{A}$ such that

$$\mathbf{B} = \boldsymbol{\nabla} \times \mathbf{A}, \tag{2.11}$$

where $\mathbf{A}$ is called the *vector potential*. Furthermore, we can apply one more condition to the vector potential (Jackson, 1999), which is

$$\boldsymbol{\nabla} \cdot \mathbf{A} = 0. \tag{2.12}$$

We have constrained the vector potential to have no divergence. This condition is referred to as a gauge condition, and equation (2.12) is commonly referred to as the Coulomb gauge (Jackson, 1999). It is particularly useful when dealing with magnetostatics.

The vector potential definition comes to the fore when we use it with Ampère's law (equation (2.2)) under the long wavelength approximation (Section 2.5). The equation for the vector potential is given below.

$$\boldsymbol{\nabla} \times \mathbf{B} = \mu_0 \mathbf{J},$$

and using equation (2.11)

$$\boldsymbol{\nabla} \times (\boldsymbol{\nabla} \times \mathbf{A}) = \boldsymbol{\nabla}(\boldsymbol{\nabla} \cdot \mathbf{A}) - \boldsymbol{\nabla}^2 \mathbf{A} = \mu_0 \mathbf{J}. \tag{2.13}$$

Using equation (2.12) for the divergence of $\mathbf{A}$ in the above equation yields a Poisson equation in three dimensions. The vector potential under the Coulomb gauge becomes

$$\boldsymbol{\nabla}^2 \mathbf{A} = -\mu_0 \mathbf{J},$$

which implies that

$$\mathbf{A} = \frac{\mu_0}{4\pi} \int \frac{\mathbf{J}}{r}\, d\tau, \tag{2.14}$$

provided the current density goes to zero at infinity.

2.5 The Long Wavelength Approximation

One simplification that we often make in the field of geophysics is the assumption of the long wavelength approximation. This approximation has several interpretations, but what it amounts to is that we do not worry about retardation effects when we are calculating electromagnetic fields. This means that we neglect the fact that the speed of light is finite, and we assume that fields transmit information instantaneously through a distance. For example, if a wire loop transmitter has an alternating current forced through it that produces a time-varying magnetic field, we assume that the magnetic field we see at a distance x is exactly in phase with the current in the transmitter. The condition under which this assumption is valid is that x must be less than the wavelength λ of the magnetic field. For a dipole system oscillating at 100 kHz, the wavelength of the magnetic field produced is approximately 3,000 m in air. This is much greater than the length scales of most airborne electromagnetic systems (AEM), which typically operate on the scale of tens of metres.

Mathematically, the long wavelength approximation has two consequences. The first is that we can neglect displacement currents when we calculate the curl of the magnetic intensity. This means that Ampère's law (the fourth equation in (2.10)) simplifies from

$$\boldsymbol{\nabla} \times \mathbf{H} = \mathbf{J_f} + \frac{\partial \mathbf{D}}{\partial t}$$

to

$$\boldsymbol{\nabla} \times \mathbf{H} = \mathbf{J_f}.$$

The second consequence is that we can use the Biot-Savart law, discussed in Section 2.6, to calculate the magnetic field of oscillating systems, even though the calculation is based on magnetostatic theory.

It is important to note that the long wavelength approximation is made to simplify mathematical equations, and it may not accurately reflect what is really occurring in a material body if the excitation frequency is high enough, or if the time scale that we are using is short enough, compared to the rate of transfer of electric and magnetic fields through the medium of interest (Jackson, 1999).

2.5.1 Skin Depth in a Conducting Body

One of the most useful applications of the long wavelength approximation is in the determination of the so-called skin depth of a linear homogeneous medium. Consider an infinite uniform medium in which a uniform magnetic field is set up having a time-varying but spatially constant component in one direction. The steady-state solution for this depends on Maxwell's equations for this configuration.

The significant equations for this situation, using the long wavelength approximation, are given below:

$$\boldsymbol{\nabla} \times \mathbf{H} = \mathbf{J}, \tag{2.15a}$$

$$\boldsymbol{\nabla} \cdot \mathbf{H} = 0, \tag{2.15b}$$

$$\boldsymbol{\nabla} \times \mathbf{E} = -\mu \frac{\partial \mathbf{H}}{\partial t}, \tag{2.15c}$$

and

$$\mathbf{J} = \sigma \mathbf{E}. \tag{2.15d}$$

We proceed by taking the curl of each of (2.15a) and (2.15c) and use the following relation for the curl of a curl of a vector field

$$\boldsymbol{\nabla} \times \boldsymbol{\nabla} \times \mathbf{A} = \boldsymbol{\nabla}(\boldsymbol{\nabla} \cdot \mathbf{A}) - \boldsymbol{\nabla}^2 \mathbf{A}. \tag{2.16}$$

Next, we can take advantage of the fact that $\boldsymbol{\nabla} \cdot \mathbf{B} = 0$ in general and $\boldsymbol{\nabla} \cdot \mathbf{E} = 0$ in conducting bodies to obtain the following relation for both $\mathbf{H}$ and $\mathbf{E}$

$$\left(\boldsymbol{\nabla}^2 - \sigma\mu\frac{\partial}{\partial t}\right)\begin{matrix}\mathbf{E}\\ \mathbf{H}\end{matrix} = 0. \tag{2.17}$$

It is customary, when solving the diffusion equation, to suggest a separation of variables as a solution. Let us consider only the magnetic field intensity, since the mathematics for the electric field are exactly the same. Since we stated that the fields are time-varying, a possible solution is

$$\mathbf{H} = \mathbf{h}(z)\theta(t), \tag{2.18a}$$

or

$$\mathbf{H} = \mathbf{h}(z)e^{iwt}. \tag{2.18b}$$

With this separation, the spatial portion of the magnetic field intensity must satisfy

$$(\boldsymbol{\nabla}^2 - i\omega\sigma\mu)\mathbf{h}(z) = 0. \tag{2.19}$$

Equation (2.19) is a Poisson equation that has a very simple trial solution. The double spatial derivative and the constant term suggest a solution of the form

$$\mathbf{h}(z) = \mathbf{h_0} e^{ikz},$$

with k such that

$$k^2 = i\omega\sigma\mu,$$

or

$$k = \pm\frac{1+i}{\delta},$$

where

$$\delta = \sqrt{\frac{2}{\sigma\mu\omega}}. \tag{2.20}$$

The value δ has special significance. It has units of length that are a characteristic of the medium and whose value depends on the conductivity and permeability of the medium, as well as the frequency of the imposing field. This value is often called the *skin depth* of the material (Jackson, 1999). It is the depth at which the magnetic field intensity (or the electric field) is reduced to $1/e$ of its initial value.

Taking the real part of the solutions as the physical result, the magnetic field inside the conductor is

$$H_x(z,t) = H_0 e^{-z/\delta}\cos\Big(\frac{z}{\delta} - \omega t\Big). \tag{2.21}$$

We can find the electric field by using Ohm's Law and the first term in equa-

tion (2.15):

$$\mathbf{E} = \frac{1}{\sigma}\boldsymbol{\nabla} \times \mathbf{H},$$

which yields only a component in the y-direction

$$E_y = -\frac{1}{\sigma}\frac{dH_x}{dz} = \frac{1-i}{\sigma\delta}H_0 e^{-z/\delta}e^{i(z/\delta-\omega t)}. \tag{2.22}$$

Using equation (2.20), the y-component of the electric field becomes

$$E_y = \frac{\mu\omega\delta}{\sqrt{2}}\left(\frac{1-i}{\sqrt{2}}\right)H_0 e^{-z/\delta}e^{i(z/\delta-\omega t)},$$

or

$$E_y = \frac{\mu\omega\delta}{\sqrt{2}}H_0 e^{-z/\delta}e^{i(z/\delta-\omega t)}e^{-i\pi/4}, \tag{2.23}$$

and we take the real part of (2.23) to finally obtain

$$E_y = \frac{\mu\omega\delta}{\sqrt{2}}H_0 e^{-z/\delta}\cos(z/\delta - \omega t - \pi/4). \tag{2.24}$$

This implies that the electric field is out of phase with the magnetic field intensity by $\pi/4$ radians, and its magnitude is different from the magnitude of the magnetic field intensity by a factor of $\mu\omega\delta/\sqrt{2}$.

The electric field circulating in the material is caused by a local current density that circulates in the same direction as the electric field. Mathematically,

$$J_y = \sigma E_y = \frac{\sqrt{2}}{\delta}H_0 e^{-z/\delta}\cos(z/\delta - \omega t - \pi/4), \tag{2.25}$$

and if we integrate this over the entire depth of the conductor, we see that the

current density can be represented as an effective surface current

$$J_S(t) = \int_0^\infty J_y(z,t)\, dz = H_0 \cos(\omega t). \tag{2.26}$$

For high frequencies, or very conductive materials, the current density becomes a surface current within a region δ of the surface of the conductor that effectively cancels the magnetic field at any depth of $z \gg \delta$ (Jackson, 1999).

2.6 Magnetic Field of Wire Loops

The basic law for calculating the magnetic induction resulting from an arbitrary current density $\mathbf{J}(\mathbf{r})$ is given by the Biot-Savart law (Griffiths, 1989):

$$\mathbf{B}(\mathbf{r}) = \frac{\mu_0}{4\pi} \int \mathbf{J}(\mathbf{r}) \times \frac{\hat{\mathbf{R}}}{|\mathbf{R}|^2}\, d\mathbf{r}', \tag{2.27}$$

where $\mathbf{R} = \mathbf{r} - \mathbf{r}'$. The Biot-Savart law is useful for calculating the magnetic fields of loops of current, either circular or piecewise linear. This is a magnetostatic construct that can be applied to this case with no loss of generality because we assume that the long wavelength approximation is valid.

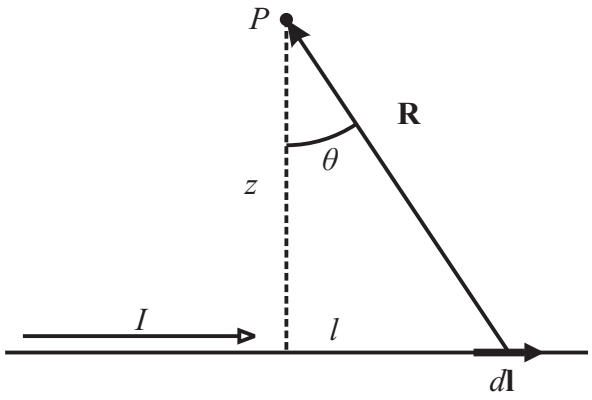

Figure 2.1: *Diagram for calculating magnetic field at point P due to constant current I flowing in a segment of wire.*

2.6.1 Segment of Wire

The first application of the Biot-Savart law will be for the calculation of the magnetic field of a line segment carrying a constant current I. Although this model is physically unrealisable—the current cannot just appear at one point and disappear at another—the segment could represent one portion of a closed loop. We seek the magnetic induction at a point, P. This is shown schematically in Figure 2.1.

In this case, the Biot-Savart equation simplifies greatly. The current density in the integral becomes $I\mathrm{d}\mathbf{l}$, and the current drops out of the integral. The cross product, which yields information about the direction of the magnetic field means that at point P the magnetic field is pointing out of the page. From the geometry of the figure, we can see that the magnitude of the cross product becomes

$$dl\cos\theta,$$

and that

$$l = z\tan\theta, \quad \text{so} \quad dl = \frac{z}{\cos^2\theta}\,d\theta.$$

The denominator becomes

$$\frac{1}{R^2} = \frac{\cos^2\theta}{z^2},$$

so the integral then becomes

$$B = \frac{\mu_0}{4\pi} I \int_{\theta_1}^{\theta_2} \left(\frac{\cos^2\theta}{z^2}\right)\left(\frac{z}{\cos^2\theta}\right)\cos\theta\,d\theta,$$

which simplifies to

$$B = \frac{\mu_0}{4\pi}\frac{I}{z}\int_{\theta_1}^{\theta_2} \cos\theta \, d\theta,$$

and evaluates to

$$B = \frac{\mu_0}{4\pi} I(\sin\theta_2 - \sin\theta_1). \tag{2.28}$$

Equation (2.28) is useful if we remember the direction of **B** implied in the discussion and provided we know the starting and ending angles of the integration. A more useful calculation using vector algebra can be found a vector diagram to describe the wire segment.

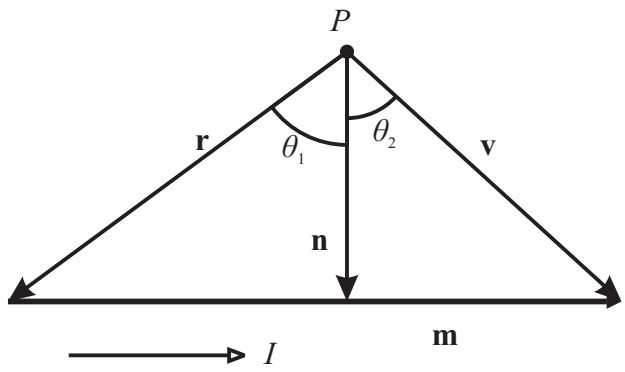

Figure 2.2: *Vector* **m** *defined by vectors* **r** *and* **v**, *such that current flows along* **m** *(***m** = **v** − **r**).

Figure A.1 represents the same geometry as before except that the line segment is now defined in terms of vectors. In this case, the direction of the magnetic field is in the direction given by the cross product of **r** and **v**:

$$\mathbf{B} = B\frac{\mathbf{r}\times\mathbf{v}}{|\mathbf{r}\times\mathbf{v}|}. \tag{2.29}$$

With some algebraic manipulation, we can describe the vector **B** solely in terms of **r**, **v** and **m**. The derivation is presented in Appendix A.1, and the result is given

below in equation (2.30):

$$\mathbf{B} = \frac{\mu_0}{4\pi} I \left[\frac{\mathbf{m} \cdot \mathbf{v}}{|\mathbf{v}|} - \frac{\mathbf{m} \cdot \mathbf{r}}{|\mathbf{r}|} \right] \frac{\mathbf{r} \times \mathbf{v}}{|\mathbf{r} \times \mathbf{v}|^2}. \tag{2.30}$$

2.6.2 Circular Loop of Wire

We will now calculate the magnetic induction field for a circular loop of wire of radius a, Figure 2.3. One condition of the calculation is that a is much larger than the cross-sectional diameter of the current-carrying wire. For this calculation, the use of the vector potential assists the derivation.

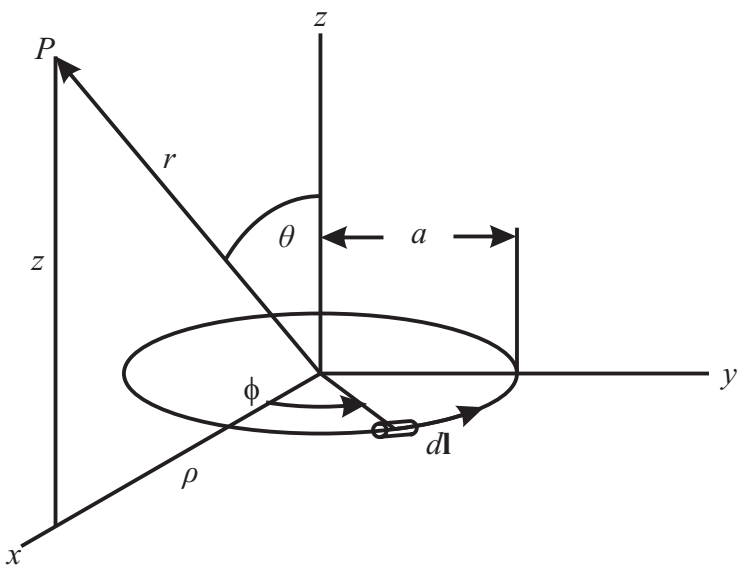

Figure 2.3: *Schematic for calculation of magnetic induction of a circular loop of wire carrying constant current I.*

The point of observation is chosen to be above the x-axis. Since the circuit has cylindrical symmetry, there is no loss of generality. Note that the vector potential is parallel to the current density; so at point P, the current is flowing only in the positive y-direction. The vector potential points in the y-direction as well. Using cylindrical symmetry, we see that the vector potential has only a ϕ component.

An elegant expression for the current density is that given by Jackson (1999):

$$J_\phi = I \sin\theta' \, \delta(\cos\theta') \frac{\delta(r' - a)}{a}$$

and the total current density can be expressed as

$$\mathbf{J} = -J_\phi \sin\phi' \; \hat{\mathbf{i}} + J_\phi \cos\phi' \; \hat{\mathbf{j}},$$

which, when we place into the integral equation (2.14) gives

$$A_\phi(r, \theta) = \frac{\mu_0 I}{4\pi a} \int \frac{\cos\phi' \sin\theta' \, \delta(\cos\theta') \, \delta(r' - a)}{R} \, d\tau. \tag{2.31}$$

I have evaluated the equation above in Appendix A.2, so as to not be waylaid by too much mathematics. The result, in terms of elliptic integrals K and E is given below:

$$A_\phi(z, \rho) = \frac{\mu_0 I}{4\pi} \frac{\sqrt{(a+\rho)^2 + z^2}}{\rho} \big((2 - k^2) K(k) - 2E(k) \big),$$

where

$$k^2 = \frac{4a\rho}{(a+\rho)^2 + z^2}. \tag{2.32}$$

The elliptic integrals that I have used are the ones defined by (Spiegel, 1995), and I have converted the dependence of A_ϕ from spherical to cylindrical coordinates. The magnetic induction equations are now obtained by applying the curl operator to the vector potential equation, ensuring that proper notice is taken of the coordinates. The derivation is presented in Appendix A.2, and the results are given here in terms

of cylindrical coordinates ρ and z:

$$\begin{cases} B_\rho = \dfrac{\mu_0 I z}{2\pi\rho\sqrt{(a+\rho)^2+z^2}}\left(\dfrac{(a^2+\rho^2+z^2)}{(a-\rho)^2+z^2}E(k) - K(k)\right) \\ B_z = \dfrac{\mu_0 I z}{2\pi\rho\sqrt{(a+\rho)^2+z^2}}\left(\dfrac{(a^2-\rho^2-z^2)}{(a-\rho)^2+z^2}E(k) - K(k)\right) \end{cases}$$

where

$$k = \sqrt{\frac{4a\rho}{(a+\rho)^2+z^2}}.$$

2.6.3 Magnetic Dipole

When the point P of observation becomes far enough away from the circular loop of radius a (see Figure 2.3), certain approximations may be made. The condition may be stated mathematically as $r \gg a$. When this occurs, the current loop begins to look like a magnetic dipole of dipole moment

$$\mathbf{m} = \pi a^2 I\, \hat{\mathbf{n}}, \tag{2.33}$$

where $\hat{\mathbf{n}}$ is the unit vector that points in the direction of the area of the circular loop. This direction is found by curling the right hand around the loop in the direction of current flow. For the loop in Figure 2.3, the vector $\hat{\mathbf{n}}$ points in the positive z-direction.

In order to find the magnetic induction of a magnetic dipole, we use the same mathematical construction as was found in equation (2.31). The integral simplifies when the delta functions are integrated. This is done in Appendix A.2. Using the result from equation (A.10), repeated here,

$$A_\phi(r,\theta) = \frac{\mu_0 I a}{4\pi}\int_0^{2\pi} \frac{\cos\phi'\, d\phi'}{\sqrt{r^2+a^2-2ra\sin\theta\cos\phi'}}, \tag{2.34}$$

we make use of the dipole approximation $r \gg a$. To exploit this relationship, we

will factor the value of $r^2 + a^2$ out from the radical in the denominator. This leaves

$$A_\phi(r,\theta) = \frac{\mu_0 I a}{4\pi} \frac{1}{\sqrt{r^2+a^2}} \int_0^{2\pi} \frac{\cos\phi'\, d\phi'}{\sqrt{1 - \dfrac{2ra\sin\theta\cos\phi'}{r^2+a^2}}},$$

which simplifies to

$$A_\phi(r,\theta) = \frac{\mu_0 I a}{4\pi} \frac{1}{\sqrt{r^2+a^2}} \int_0^{2\pi} \frac{1}{\sqrt{1+x}} \cos\phi'\, d\phi' \tag{2.35}$$

when

$$x = \frac{-2ra\sin\theta\cos\phi'}{r^2+a^2},$$

and provides us the expression $\sqrt{1+x^2}$ in the denominator of the integral. Because $r \gg a$, x is a small value; we can make use of a Taylor expansion such as described in (Spiegel, 1995). To first order, then, we have the following evaluation of A_ϕ

$$A_\phi = \frac{\mu_0 I a}{4\pi} \frac{1}{\sqrt{r^2+a^2}} \frac{1}{\sqrt{r^2+a^2}} \int_0^{2\pi} 1 - \frac{1}{2}x + \mathrm{O}\left(x^2\right) \cos\phi' d\phi',$$

which, when we take only terms of first order becomes

$$A_\phi \approx \frac{\mu_0 I a}{4\pi} \frac{1}{\sqrt{r^2+a^2}} \frac{1}{\sqrt{r^2+a^2}} \left(\int_0^{2\pi} \cos\phi' d\phi' + \frac{ra\sin\theta}{r^2+a^2} \int_0^{2\pi} \cos^2\phi' d\phi' \right).$$

The integral evaluates to

$$A_\phi = \frac{\mu_0 I a}{4\pi} \frac{1}{\sqrt{r^2+a^2}} \frac{1}{\sqrt{r^2+a^2}} \left(0 + \frac{ra\sin\theta}{r^2+a^2}\pi \right),$$

which becomes

$$A_\phi = \frac{\mu_0}{4\pi}\frac{\pi a^2 I r \sin\theta}{(r^2+a^2)^{3/2}},$$

and can be expressed in terms of the dipole moment (equation (2.33)) as

$$A_\phi = \frac{\mu_0}{4\pi}\frac{mr\sin\theta}{(r^2+a^2)^{3/2}}. \tag{2.36}$$

We can easily find the magnetic induction components by applying the curl operator to the vector potential. This has been done in Appendix A.3, and the results are presented here for spherical,cylindrical and coordinate-independent components.

Spherical coordinates:

See Appendix A.3.1.

$$\mathbf{B} = \frac{\mu_0}{4\pi}(\pi a^2 I)\left(\frac{\cos\theta}{r^3}\,\hat{\mathbf{r}} + \frac{\sin\theta}{r^3}\,\hat{\boldsymbol{\theta}}\right). \tag{2.37}$$

Cylindrical coordinates:

See Appendix A.3.2.

$$\mathbf{B} = \frac{\mu_0}{4\pi}(\pi a^2 I)\left(\frac{3\rho z}{(\rho^2+z^2)^{5/2}}\,\hat{\boldsymbol{\rho}} + \frac{2z^2-\rho^2}{(\rho^2+z^2)^{5/2}}\,\hat{\mathbf{z}}\right). \tag{2.38}$$

Coordinate-independent:

For an arbitrary magnetic dipole, with dipole moment $\mathbf{m}$, it is possible to write the more general, coordinate-independent result for the magnetic induction as follows (see Appendix A.3.3 for derivation):

$$\mathbf{B} = \frac{\mu_0}{4\pi}\frac{1}{r^3}\big(3(\mathbf{m}\cdot\hat{\mathbf{r}})\,\hat{\mathbf{r}} - \mathbf{m}\big). \tag{2.39}$$

2.7 Magnetic Inductance

Consider two loops of wire placed near one another, Figure 2.4. If Loop 1 has a steady current I_1 run around it, a magnetic induction field $\mathbf{B_1}$ is produced. Some field lines from $\mathbf{B_1}$ will pass through loop 2. We measure the amount of field that threads through loop 2 per unit area, calling the result the magnetic flux Φ_2 of loop 2 due to the field produced by loop 1.

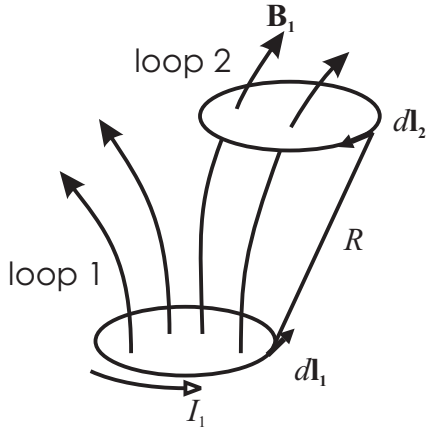

Figure 2.4: *Schematic for calculation of mutual inductance between two wire loops.*

We can use the Biot-Savart equation to calculate the magnetic field produced by loop 1. We see that

$$\mathbf{B_1} = \frac{\mu_0}{4\pi} I_1 \oint d\mathbf{l} \times \frac{\hat{\mathbf{R}}}{|\mathbf{R}|^2} \tag{2.40}$$

is the field due to loop 1; and the magnetic flux through loop 2 is

$$\Phi_2 = \int \mathbf{B_1} \cdot d\mathbf{a_2}, \tag{2.41}$$

which can also be expressed as

$$\Phi_2 = M_{21} I_1. \tag{2.42}$$

The flux through loop 2 is proportional to the current around loop 1. The constant of proportionality M_{12} is called the *mutual inductance* between loop 1 and loop 2.

To calculate the mutual inductance we can make use of the vector potential of the magnetic field as shown in equation (2.14) of section 2.4. For wire loop 1 of current I_1, equation (2.14) simplifies to the closed loop integral

$$\mathbf{A_1} = \frac{\mu_0}{4\pi} I_1 \oint \frac{d\mathbf{l_1}}{R}, \tag{2.43}$$

where R is the distance between the point of observation and the current element. The flux equation (2.41), using equation (2.11) for the equation of magnetic vector potential, can be expressed as

$$\Phi_2 = \int (\boldsymbol{\nabla} \times \mathbf{A_1}) \cdot d\mathbf{a_2},$$

which by using Stokes' Theorem (Griffiths, 1989) becomes

$$\Phi_2 = \oint \mathbf{A_1} \cdot d\mathbf{l_2}.$$

Using equation (2.43) for the vector potential, the flux is

$$\Phi_2 = \frac{\mu_0}{4\pi} I_1 \oint \oint \frac{d\mathbf{l_1} \cdot d\mathbf{l_2}}{R},$$

and we use this result together with the definition of mutual inductance, equation (2.42), to arrive at an integral calculation for the mutual inductance between two loops:

$$M_{21} = \frac{\mu_0}{4\pi} \oint \oint \frac{d\mathbf{l_1} \cdot d\mathbf{l_2}}{R}. \tag{2.44}$$

This definition, based on the flux-cutting concept, is known as Neumann's formula. It appears to be a simple integral, but actually has some thorny issues when R tends to zero. We immediately see that M_{21} is purely geometrical. Mutual inductance simply depends on where loop 1 is relative to loop 2, what sizes they have, and

their shapes. Furthermore, since the order of the dot product in the integral may be switched, $M_{21} = M_{12} = M$. That is, the mutual inductance of loop 2 due to loop 1 is the same as the mutual inductance of loop 1 due to loop 2. This means that the flux through loop 2 due to current I run around loop 1 is the exact same as the flux through loop 1 due to the *same current* I run around loop 2! This is known as reciprocity.

We now must turn to Faraday's law to find relevance in the above discussion, since the principle of mutual inductance is the basis of the whole electromagnetic approach to geophysics. In differential form, Faraday's law is equation (2.1), repeated here:

$$\boldsymbol{\nabla} \times \mathbf{E} = -\frac{\partial \mathbf{B}}{\partial t}.$$

We can examine this in integral form by creating a surface around the magnetic induction field being discussed and applying a surface integral. The presence of the curl operator in equation (2.1) indicates that we should apply Stokes' Theorem (Griffiths, 1989) to transform the surface integral into a contour integral around the boundary of the surface. In the case of one of the loops above, the surface is simply the area defined by the wire loop; the boundary being the wire loop itself.

$$\int (\boldsymbol{\nabla} \times \mathbf{E}) \cdot d\mathbf{a} = \int -\frac{\partial \mathbf{B}}{\partial t} \cdot d\mathbf{a},$$

which, by use of Stokes' Theorem becomes

$$\oint \mathbf{E} \cdot d\mathbf{l} = -\frac{\partial}{\partial t} \int \mathbf{B} \cdot d\mathbf{a},$$

and may be re-written as

$$\mathcal{E} = -\frac{\partial \Phi}{\partial t}. \tag{2.45}$$

The quantity $\mathcal{E}$ is called the electromotive force or emf, even though it is not a force at all: it is the integral over distance of a force per unit charge. The emf can be described in the same way as the potential or voltage of an electric circuit and is responsible for the movement of charge in a closed circuit.

If we look to the example above and allow the current in loop 1 to change the flux through loop 2 will also change. From (2.45), the changing flux generates an emf in loop 2.

Something very important to keep in mind is that we are assuming that the current in loop 1 changes slowly enough for the Biot-Savart law to hold true. In other words, we are assuming that the circuits are operating under the long-wavelength assumption.

2.7.1 Mutual Inductance and its Application to Geophysics

Consider now two current loops mounted in such a way that they are kept in rigid fixed positions relative to another. A time-varying current is driven through one of the loops, say loop 1 in Figure 2.5. This generates an emf $\mathcal{E}$ in loop 2 through the mutual inductance M_{12}. In free space, this should be the only source of emf in loop 2. If we bring the system near the earth, which contains conducting and permeable zones, there will be mutual inductance between loop 1 and the earth and between loop 2 and the earth. Thus, the emf present in loop 2 will be different from that in free space. We will call the emf of loop 2 due to the proximity of the two loops to the earth $\Delta\mathcal{E}$. It arises from the relations of the mutual inductance of loop 1 with the earth, M_{1e}, and from loop 2 with the earth,M_{2e}, which I will replace with a single mutual inductance, M^*. The ratio of $\Delta\mathcal{E}$ to $\mathcal{E}$ is called the *electromagnetic anomaly* (Grant and West, 1965) or the response of the system. Since $\Delta\mathcal{E}$ is typically much smaller than $\mathcal{E}$, the response is often expressed in parts per million (ppm).

$$\frac{\Delta\mathcal{E}}{\mathcal{E}} = \frac{M^*}{M_{12}}. \tag{2.46}$$

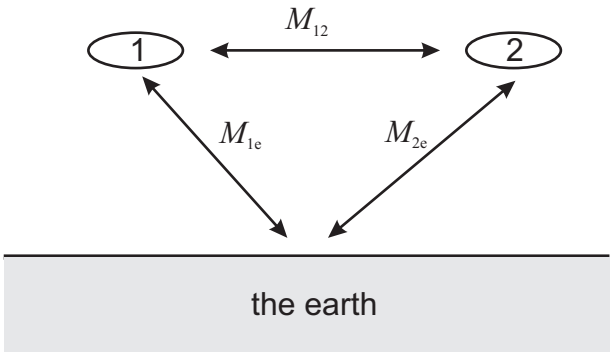

Figure 2.5: *Schematic for the electromagnetic method.*

This is the essence of the electromagnetic method of geophysical prospecting. Electromagnetic anomalies are responsible for changing the coefficient of mutual inductance between the transmitting loop (the loop which has current driven through it) and the receiving loop (the one where we measure the emf induced). The mutual inductance changes due to the proximity of the transmitter-receiver pair to conductive bodies. The detection of conductive bodies relies on our ability to interpret the differences in the emf of the receiving loop.

2.7.2 Mutual Inductance of Two Dipoles

The calculation of the mutual inductance of two dipoles does not need to be done with the full machinery of the Neumann formula. It is most easily done with the coordinate-independent expression of the magnetic field given in equation (2.39). We make the assumption that the magnetic field of dipole 1 will be constant across the surface area of dipole 2. This is reasonable because the dipoles are assumed to have very small cross-sectional area compared to their distance of separation. In that case, the area integral of equation (2.41),

$$\Phi_2 = \int \mathbf{B_1} \cdot d\mathbf{a_2},$$

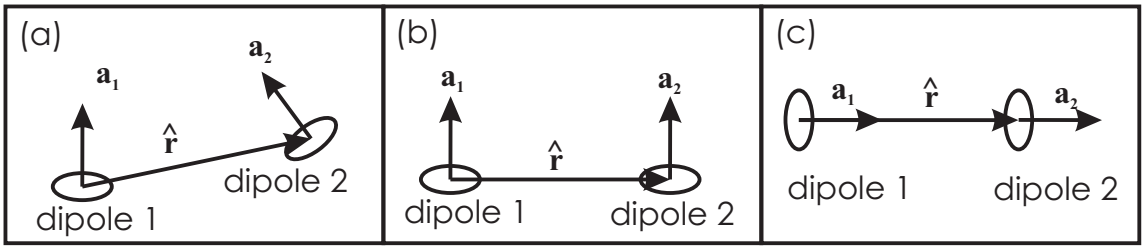

Figure 2.6: *Different orientations between two dipoles. (a) Dipoles are in any arbitrary position. (b) Dipoles are in horizontal coplanar alignment (HCP). (c) Dipoles are coaxial (VCA).*

simplifies to

$$\Phi_2 = \mathbf{B_1} \cdot \mathbf{a_2}.$$

Here, $\mathbf{B_1}$ is the magnetic field from dipole 1 and $\mathbf{a_2}$ is the area vector of dipole 2. Using equation (2.39), we get

$$\Phi_2 = \frac{\mu_0}{4\pi}\frac{1}{r^3}\big(3(\mathbf{m}\cdot\hat{\mathbf{r}})\,\hat{\mathbf{r}} - \mathbf{m}\big)\cdot\mathbf{a_2}.$$

Using equation (2.33), the definition of magnetic dipole moment, the flux can be expressed as

$$\Phi_2 = \frac{\mu_0}{4\pi}\frac{1}{r^3} I_1\big(3(\mathbf{a_1}\cdot\hat{\mathbf{r}})\,\hat{\mathbf{r}} - \mathbf{a_1}\big)\cdot\mathbf{a_2}, \tag{2.47}$$

where $\mathbf{a_1}$ has magnitude πa_1^2, and $\mathbf{a_2}$ has magnitude πa_2^2. The vector $\hat{\mathbf{r}}$ is the unit vector pointing from dipole 1 to dipole 2, Figure 2.6a. In general, the mutual inductance between two dipoles is

$$M = \frac{\mu_0}{4\pi}\frac{1}{r^3}\big(3(\mathbf{a_1}\cdot\hat{\mathbf{r}})\,\hat{\mathbf{r}} - \mathbf{a_1}\big)\cdot\mathbf{a_2}, \tag{2.48}$$

which is similar in form to equation (2.39).

Two dipole arrangements are of importance in this thesis. The first is when vertical dipoles are aligned with area vectors parallel, placed side by side. This is often called *horizontal coplanar* (HCP) due to the current loops being horizontal to the earth and sharing the same plane, Figure 2.6b. The HCP mutual inductance is

$$M_{HCP} = -\frac{\mu_0}{4\pi}\frac{a_1^2 a_2^2}{r^3}. \tag{2.49}$$

The second arrangement, Figure 2.6c, is referred to as *vertical coaxial*. The area (dipole) vectors are horizontal to the earth and they are aligned on a common axis, like hoops on a barrel. In this orientation, the $\mathbf{a_1}$ and $\mathbf{a_2}$ are parallel to the vector $\hat{\mathbf{r}}$ that joins their centres, and the mutual inductance becomes

$$M_{VCA} = \frac{\mu_0}{2\pi}\frac{a_1^2\, a_2^2}{r^3}.$$

The two dipole orientations have significance because they are commonly used in the RESOLVE frequency domain system. This is studied further in Chapter 3.

2.7.3 Mutual Inductance of Two Skew Lines

I will present the mutual inductance of two skew lines. The mutual inductance of two lines of arbitrary orientation relative to one another was first studied by Martens (1909) and later by Campbell (1915). Their results, along with many other mutual and self inductance calculations, were compiled by Grover (1946). The general calculation is both long and laborious. The derivation is included in Appendix B.1; the result is presented below.

To determine the orientation of two skew wires, we require four independent vectors. The first wire is determined by $\mathbf{l_1}$, and the second wire is described by $\mathbf{l_2}$.

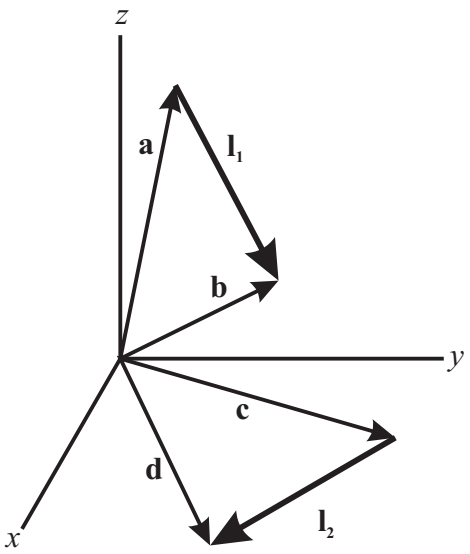

Figure 2.7: *Diagram for the calculation of mutual inductance between two skew lines.*

The 'beginning' of wire 1 lies at the endpoint of $\mathbf{a}$, a vector starting from the origin. The end is determined by $\mathbf{b}$, such that $\mathbf{l_1} = \mathbf{b} - \mathbf{a}$. Similarly, wire 2 is defined by $\mathbf{l_2} = \mathbf{d} - \mathbf{c}$, where both $\mathbf{d}$ and $\mathbf{c}$ start from the origin. All vectors are shown in Figure 2.7.

The vectors $\mathbf{a}$, $\mathbf{b}$, $\mathbf{c}$, $\mathbf{d}$, $\mathbf{l_1}$ and $\mathbf{l_2}$ are used in the calculation of mutual inductance. The equation is:

$$M = \frac{\mu_0}{2\pi}\frac{\mathbf{l_1}\cdot\mathbf{l_2}}{|\mathbf{l_1}||\mathbf{l_2}|}\Bigg((\upsilon + |\mathbf{l_2}|)\tanh^{-1}\Big(\frac{|\mathbf{l_1}|}{|\mathbf{d}-\mathbf{b}|+|\mathbf{d}-\mathbf{a}|}\Big) - 2\upsilon\tanh^{-1}\Big(\frac{|\mathbf{l_1}|}{|\mathbf{c}-\mathbf{a}|+|\mathbf{c}-\mathbf{b}|}\Big) + (\xi + |\mathbf{l_1}|)\tanh^{-1}\Big(\frac{|\mathbf{l_2}|}{|\mathbf{d}-\mathbf{b}|+|\mathbf{c}-\mathbf{b}|}\Big) - 2\xi\tanh^{-1}\Big(\frac{|\mathbf{l_2}|}{|\mathbf{d}-\mathbf{a}|+|\mathbf{c}-\mathbf{a}|}\Big) - \frac{\lambda|\mathbf{l_1}||\mathbf{l_2}|}{|\mathbf{l_1}\times\mathbf{l_2}|}\Omega\Bigg), \quad (2.50)$$

where

$$\xi = \frac{|\mathbf{l_1}||\big((\mathbf{c}-\mathbf{a})\times\mathbf{l_2}\big)\cdot(\mathbf{l_2}\times\mathbf{l_1})|}{|\mathbf{l_1}\times\mathbf{l_2}|^2},$$
$$\upsilon = \frac{|\mathbf{l_2}||\big((\mathbf{c}-\mathbf{a})\times\mathbf{l_1}\big)\cdot(\mathbf{l_2}\times\mathbf{l_1})|}{|\mathbf{l_1}\times\mathbf{l_2}|^2}$$

and

$$\lambda = \frac{|(\mathbf{c}-\mathbf{a})\cdot(\mathbf{l_1}\times\mathbf{l_2})|}{|\mathbf{l_1}\times\mathbf{l_2}|}. \tag{2.51}$$

The last term Ω is described by a collection of arctangent functions (see Appendix B.1 for the derivation):

$$\begin{aligned}\Omega = \tan^{-1}&\left(\frac{\lambda^2\cos\epsilon + (\xi+|\mathbf{l_1}|)(\upsilon+|\mathbf{l_2}|)\sin^2\epsilon}{\lambda|\mathbf{d}-\mathbf{b}|\sin\epsilon}\right)\\ &- \tan^{-1}\left(\frac{\lambda^2\cos\epsilon + (\xi+|\mathbf{l_1}|)\upsilon\sin^2\epsilon}{\lambda|\mathbf{c}-\mathbf{b}|\sin\epsilon}\right) - \tan^{-1}\left(\frac{\lambda^2\cos\epsilon + \xi(\upsilon+|\mathbf{l_2}|)\sin^2\epsilon}{\lambda|\mathbf{d}-\mathbf{a}|\sin\epsilon}\right)\\ &+ \tan^{-1}\left(\frac{\lambda^2\cos\epsilon + \xi\upsilon\sin^2\epsilon}{\lambda|\mathbf{c}-\mathbf{a}|\sin\epsilon}\right)\end{aligned} \tag{2.52}$$

where

$$\sin\epsilon = \frac{|\mathbf{l_1}\times\mathbf{l_2}|}{|\mathbf{l_1}||\mathbf{l_2}|}, \quad \text{and} \quad \cos\epsilon = \frac{\mathbf{l_1}\cdot\mathbf{l_2}}{|\mathbf{l_1}||\mathbf{l_2}|}.$$

This is, to my knowledge, the first time the mutual inductance of two skew lines has ever been published in vector format. Although complex, the first factor contains some useful information. The dot product $\mathbf{l_1}\cdot\mathbf{l_2}$, determines the sign of the mutual inductance. When the skew lines are perpendicular to one another, the dot product and mutual inductance are zero. Parallel lines have maximum mutual inductance.

Equations (2.50)–(2.52) are useful for determining the mutual inductance between two closed loops comprised of line segments. When two loops are close enough that they can no longer be described as dipoles, the mutual inductance between them can be calculated using the above equations. Furthermore, the calculation may be used to find the mutual induction between any two sides of a loop when calculating its *total inductance* (see Section 2.7.6). These calculations will become extremely important in Chapter 5, when I use a ground loop to calibrate the response of airborne electromagnetic systems.

Some readers may be concerned with my interpretation of the mutual inductance of two skew lines because they do not involve a return circuit. It is important to realise that these calculations are incomplete without a returning circuit: they represent portions of mutual inductance between segments in complete circuits. For example, if we have two loops of four sides each, the sum of 16 mutual inductance calculations determines the total mutual inductance of the two loops.

2.7.4 Mutual Inductance of a Dipole and a Line Segment

Another calculation of mutual inductance that is of importance in this thesis is the mutual inductance between a dipole and a segment of current-carrying wire that is part of a closed loop. If a small current loop (such as a receiver) is far enough away from a large current loop, the small loop can be approximated as a dipole. We then assume that the magnetic field across the surface of the dipole as a result of the current in the line segment is constant. The flux through the dipole from the magnetic field of the wire segment is calculated using equation (2.41)

$$\Phi_2 = \int \mathbf{B} \cdot d\mathbf{a},$$

which simplifies to

$$\Phi_2 = \mathbf{B} \cdot \mathbf{a},$$

where $\mathbf{B}$ is the magnetic inductance field from the wire segment, and $\mathbf{a}$ is the area vector of the dipole. If we place the dipole at the point P in Figure A.1, we can use equation (2.30) to calculate the magnetic field due to the wire segment. The flux through the dipole then becomes

$$\Phi_2 = \frac{\mu_0}{4\pi} \frac{I}{|\mathbf{r} \times \mathbf{v}|^2} \left[\frac{\mathbf{m} \cdot \mathbf{v}}{|\mathbf{v}|} - \frac{\mathbf{m} \cdot \mathbf{r}}{|\mathbf{r}|} \right] (\mathbf{r} \times \mathbf{v}) \cdot \mathbf{a}.$$

Since mutual inductance is defined as the ratio of flux and current (equation (2.42)), the mutual inductance of a dipole and a wire segment is

$$M = \frac{\mu_0}{4\pi} \frac{1}{|\mathbf{r} \times \mathbf{v}|^2} \left[\frac{\mathbf{m} \cdot \mathbf{v}}{|\mathbf{v}|} - \frac{\mathbf{m} \cdot \mathbf{r}}{|\mathbf{r}|} \right] (\mathbf{r} \times \mathbf{v}) \cdot \mathbf{a}.$$

2.7.5 Self Inductance

When the current in a closed loop changes, the magnetic field and hence the flux through the loop will also change. This generates a *back* emf that opposes the change in flux. This is known as Lenz's Law, and the relationship is

$$\mathcal{E} = -L \frac{dI}{dt}, \tag{2.53}$$

where I is the current in the loop, $\mathcal{E}$ is the emf generated, and L is the self inductance of the loop.

Self Inductance of a Straight Cylindrical Wire Segment

As an example, I will calculate the self inductance of a segment of wire. Self inductance of a segment is only sensible when it forms part of the total self inductance of a closed loop.

A segment of length l is composed of a conductive material of cross-sectional radius ρ, Figure 2.8. The current flowing in the wire is uniformly distributed; it is safe to say that the field produced outside of the wire acts as if the current is concentrated in the middle. The Biot and Savart law determines the magnetic field. From equation (2.27), the differential element of magnetic field outside of the surface of the wire is

$$d\mathbf{B_{out}} = \frac{\mu_0 I}{4\pi} \frac{d\mathbf{y} \times \hat{\mathbf{R}}}{|\mathbf{R}|^2},$$

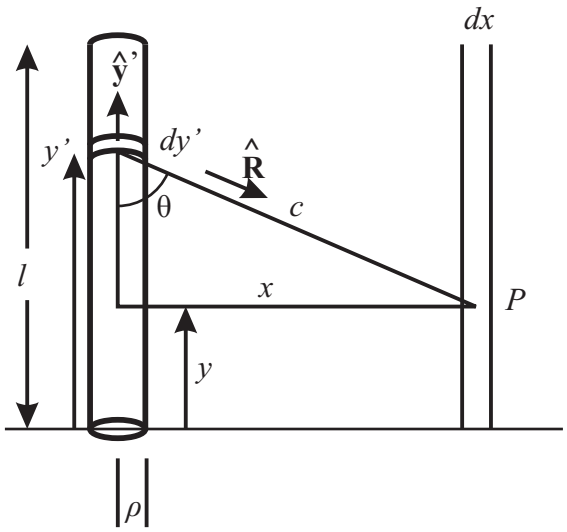

Figure 2.8: *Diagram for the calculation of self inductance of a cylindrical wire.*

which in magnitude is expressed as

$$dB_{out} = \frac{\mu_0 I}{4\pi} \frac{dy' \sin\theta}{c^2},$$

which becomes

$$dB_{out} = \frac{\mu_0 I}{4\pi} \frac{x}{c^3}\, dy', \tag{2.54}$$

where

$$c = \sqrt{(y' - y)^2 + x^2};$$

and the direction of the magnetic field at point P is into the page. The magnitude of the total magnetic induction outside of the wire is equal to the integral of dB_{out} over the length l:

$$B_{out} = \int_0^l dB_{out},$$

using equation (2.54)

$$B_{out} = \frac{\mu_0}{4\pi} Ix \int_0^l \frac{dy'}{\left((y'-y)^2 + x^2\right)^{3/2}},$$

which evaluates to

$$B_{out} = \frac{\mu_0}{4\pi} Ix \left(\frac{y'-y}{x^2\sqrt{(y'-y)^2 + x^2}} \right|_0^l,$$

yielding

$$B_{out} = \frac{\mu_0}{4\pi} \frac{I}{x} \left(\frac{l-y}{\sqrt{(1-y)^2 + x^2}} + \frac{y}{\sqrt{y^2 + x^2}} \right). \tag{2.55}$$

The total magnetic flux outside of the wire is found by integrating the magnitude of the magnetic induction from 0 to l in the y-direction, and from ρ to ∞ in the x-direction. The calculation is shown below:

$$\Phi_{out} = \int_\rho^\infty \int_0^l B_{out}\, dy\, dx$$

which, with equation (2.55) becomes

$$\Phi_{out} = \frac{\mu_0}{4\pi} I \int_\rho^\infty \int_0^l \frac{1}{x} \left(\frac{l-y}{\sqrt{(l-y)^2 + x^2}} + \frac{y}{\sqrt{y^2 + x^2}} \right) dy\, dx,$$

and can be expressed as

$$\Phi_{out} = \frac{\mu_0}{4\pi} I \left(- \int_\rho^\infty \int_l^0 \frac{1}{x} \left(\frac{z}{\sqrt{z^2 + x^2}} \right) dz\, dx + \int_\rho^\infty \int_0^l \frac{1}{x} \left(\frac{y}{\sqrt{y^2 + x^2}} \right) dy\, dx \right). \tag{2.56}$$

In the equations above, I made a substitution in the integral over y to temporarily

remove l from the equation ($z = y - l$). The integrals over x are fairly straightforward, and can readily be found in any table of integrals. We will look at the integral form of

$$F = \int_{\rho}^{\infty} \frac{a}{x\sqrt{x^2 + a^2}} dx,$$

which has the indefinite integral of (Spiegel, 1995)

$$F = \left(-\tanh^{-1}\left(\frac{a}{\sqrt{x^2 + a^2}} \right) \right|_{\rho}^{\infty}$$

and evaluates to

$$F = \tanh^{-1}\left(\frac{a}{\sqrt{\rho^2 + a^2}} \right),$$

which can be expressed as

$$F = \sinh^{-1}\left(\frac{a}{\rho}\right); \tag{2.57}$$

and is valid when ρ is greater than zero. Evaluating the x integration on each of the two terms of equation (2.56) yields

$$\Phi_{out} = \frac{\mu_0}{4\pi} I \left(-\int_{l}^{0} \sinh^{-1}\left(\frac{z}{\rho}\right) dz + \int_{0}^{l} \sinh^{-1}\left(\frac{y}{\rho}\right) dy \right). \tag{2.58}$$

Now we must evaluate the integral of an inverse hyperbolic sine. There are two of these in equation (2.58) which have the same form:

$$F = \int \sinh^{-1}\left(\frac{x}{\rho}\right) dx,$$

which integrates to (Spiegel, 1995)

$$F = x \sinh^{-1}\left(\frac{x}{\rho}\right) - \sqrt{x^2 + \rho^2}. \tag{2.59}$$

The remaining equations, though by no means difficult, are tedious and require care in calculation. Using the indefinite integral of equation (2.59), equation (2.58) becomes:

$$\Phi_{out} = \frac{\mu_0}{4\pi} I \left(\left(-z \sinh^{-1}\left(\frac{z}{\rho}\right) + \sqrt{z^2 + \rho^2} \right|_l^0 + \left(y \sinh^{-1}\left(\frac{y}{\rho}\right) - \sqrt{y^2 + \rho^2} \right|_0^l \right),$$

which evaluates to

$$\Phi_{out} = \frac{\mu_0}{4\pi} I \left(\left(\rho + l \sinh^{-1}\left(\frac{l}{\rho}\right) - \sqrt{l^2 + \rho^2} \right) + \left(l \sinh^{-1}\left(\frac{l}{\rho}\right) - \sqrt{l^2 + \rho^2} + \rho \right) \right). \tag{2.60}$$

Collecting all terms yields the total flux outside of the wire segment

$$\Phi_{out} = \frac{\mu_0}{2\pi} I \left(l \sinh^{-1}\left(\frac{l}{\rho}\right) - \sqrt{l^2 + \rho^2} + \rho \right). \tag{2.61}$$

Since flux is proportional to current (equation (2.42)) the portion of self inductance of the wire that results from its interaction with its own field outside of the wire is

$$L_{out} = \frac{\mu_0}{2\pi} \left(l \sinh^{-1}\left(\frac{l}{\rho}\right) - \sqrt{l^2 + \rho^2} + \rho \right). \tag{2.62}$$

We are not finished yet. The total flux inside the wire due to the current in the wire also needs to be calculated. Inside the wire, the field produced at point x depends on how much current is enclosed in a loop of radius x. The magnetic induction still curls around the uniform current travelling up the wire; its value at

a distance x from the centre of the wire is given by

$$B_{in} = \frac{\mu_0}{4\pi\rho^2} Ix. \tag{2.63}$$

The self inductance is calculated by integrating over the length of the wire and outwards using cylindrical shells:

$$\Phi_{in} = \int B_{in}\, da,$$

which is

$$\Phi_{in} = \frac{\mu_0}{2\pi\rho^2} I \int_0^l \int_0^\rho \frac{x^3}{\rho^2}\, dx\, dy.$$

This evaluates to

$$\Phi_{in} = \frac{\mu_0}{8\pi} Il. \tag{2.64}$$

Since the flux is equal to inductance times current, the self-inductance of the interior of the wire is

$$L_{in} = \frac{\mu_0}{8\pi} l. \tag{2.65}$$

Adding the self-inductance from both inside and outside of the wire, we calculate the total:

$$L_{self} = L_{in} + L_{out},$$

which, from equations (2.62) and (2.65), becomes

$$L_{self} = \frac{\mu_0}{8\pi} l + \frac{\mu_0}{2\pi}\left(l \sinh^{-1}\left(\frac{l}{\rho}\right) - \sqrt{l^2+\rho^2} + \rho \right),$$

and simplifies to

$$L_{self} = \frac{\mu_0}{2\pi}\left(l \sinh^{-1}\left(\frac{l}{\rho}\right) - \sqrt{l^2+\rho^2} + \rho + \frac{1}{4}\right). \tag{2.66}$$

2.7.6 Total Inductance of a Loop

The total inductance of a loop is defined as the sum of the self-inductance and the mutual inductance of each side of the loop interacting with every other side. For example, consider a square loop made of wire that has a circular cross section. The total inductance of the loop is four times the self-inductance of one side (equation (2.66)) minus four times the mutual inductance of two opposite sides (equation (2.50)),

$$L_{tot} = 4L - 4M. \tag{2.67}$$

As an example, consider a square loop of length 100 m to a side. If the loop is made of copper wire that has a diameter of 0.2 mm, the total self induction of the loop is $\sim$1 mH.

2.7.7 Total Energy Paradigm of Magnetic Inductance

So far, we have looked at the concept of magnetic inductance from a flux-cutting point of view. A current loop affects another loop by the amount of magnetic field per unit area that the second loop intercepts from the first one. Another way to consider magnetic inductance is through the concept of the total energy of a system, as proposed by Jackson (1999).

Consider a system of distinct current-carrying circuits. If there are N such circuits in the system, the total magnetic energy is the sum of magnetic energy for each circuit. The total magnetic energy can be expressed as

$$W = \frac{1}{2}\int \mathbf{J}\cdot\mathbf{A}\, d\tau, \tag{2.68}$$

where the volume integral is over all space. Using equation (2.14) as the vector potential, the total energy of the entire collection of circuits becomes

$$W = \frac{1}{2}\frac{\mu_0}{4\pi}\sum_{i=1}^{N}\int d\tau \sum_{j=1}^{N}\int \frac{\mathbf{J_i}\cdot\mathbf{J_j}}{r}\, d\tau. \tag{2.69}$$

In the sums of equation (2.69), there are N terms with $i = j$, and $N(N-1)$ terms with $i \neq j$. We can write these sums in the form of

$$W = \frac{1}{2}\sum_{i=1}^{N} L_i I_i^2 + \sum_{i=1}^{N}\sum_{j>i}^{N} M_{ij} I_i I_j. \tag{2.70}$$

The first term defines L_i, the self-inductance of each individual circuit, while M_{ij} is the mutual inductance between each circuit with every other circuit (except itself). From the above considerations, we can immediately write out the coefficient for self and mutual inductance:

$$L_i = \frac{\mu_0}{4\pi I_i^2}\int d\tau_i \int \frac{\mathbf{J_i}\cdot\mathbf{J_i}}{r}\, d\tau_i, \tag{2.71}$$

and

$$M_{ij} = \frac{\mu_0}{4\pi I_i I_j}\int d\tau_i \int \frac{\mathbf{J_i}\cdot\mathbf{J_j}}{r}\, d\tau_j. \tag{2.72}$$

The consequence of this is that self and mutual inductance are the coefficients of magnetic energy storage. The collection of circuits actually stores some magnetic energy (typically in the form of back emf) that can be recoverable. The amount stored by each circuit is determined by the inductance value for that component. This derivation does not include any reference to the flux-linkage or flux cutting development that I have mentioned before, and thus is perhaps the more aesthetic. It is particularly useful when dealing with the concept of self-inductance, and should actually be considered as the fundamental definitions of mutual and self inductance.

2.8 A Conducting Loop

I will now apply the principles of Section 2.7 to a model of two dipoles in close proximity to a conducting loop. In the simplest sense, this represents what actually takes place in any geophysical electromagnetic survey. Although it has no real application to actual survey conditions (the earth is decidedly *not* a simple wire loop), it is a useful model nonetheless. The arrangement is shown in Figure 2.9. It has direct relevance to my discussion on calibration of time domain systems using a ground loop.

We force an alternating current through loop 0, the transmitter. The alternating current generates a time-varying magnetic field that interacts with both the receiving loop and the main conductor. Let's say that the current in loop 0 is given by

$$I_0(t) = I_0 e^{i\omega t}, \tag{2.73}$$

where the real part of the exponential has physical relevance. There is an emf generated in both the ground loop (loop 1) and the receiving loop (loop 2) according

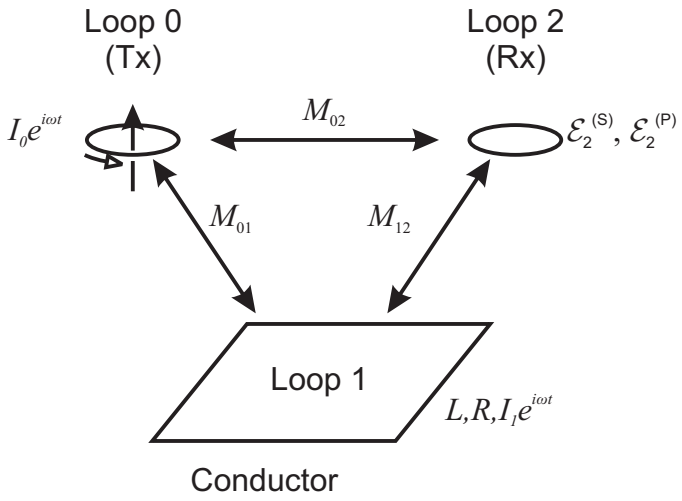

Figure 2.9: *Mutual inductance of three loops. This is the simplest model of the electromagnetic induction method applied to geophysical prospecting.*

to Faraday's law using the concept of mutual induction:

$$\mathcal{E}_j = -M_{ij}\frac{\partial}{\partial t}I_i. \tag{2.74}$$

This means that the emf generated in loop j is equal and opposite to the mutual inductance between the i^{th} and j^{th} loop multiplied by the time rate of change of the current in the i^{th} loop.

Consider first the conductor, loop 1. The emf generates current around loop 1. We immediately write the emf

$$\mathcal{E}_1 = -M_{01}\frac{\partial}{\partial t}I_0,$$

which, with equation (2.73) becomes

$$\mathcal{E}_1 = -i\omega M_{01}I_0e^{i\omega t}. \tag{2.75}$$

Loop 1 generates a back emf due to its self inductance. There will also be a potential drop across the loop due to its electrical resistance. Both potential changes sum to $\mathcal{E}_1^\dagger$ and are expressed as

$$\mathcal{E}_1^\dagger = -RI_1e^{i\omega t} - L\frac{\partial}{\partial t}(I_1e^{i\omega t}),$$

rearranged to

$$\mathcal{E}_1^\dagger = -(R + i\omega L)I_1e^{i\omega t}, \tag{2.76}$$

where R is the resistance of the loop and L is its self inductance (calculated as in

Section 2.7.5). Around any closed loop, the potential must vanish, so we have

$$\mathcal{E}_1 + \mathcal{E}_1^{\dagger} = 0.$$

Using equations (2.75) and (2.76) in the above expression, and solving for I_1 yields

$$I_1 = -\frac{i\omega M_{01}}{R + i\omega L} I_0,$$

which can be rewritten as

$$I_1 = -\frac{M_{01}}{L}\left(\frac{i\omega L(R - i\omega L)}{R^2 + \omega^2 L^2}\right) I_0. \tag{2.77}$$

This is the solution for the eddy current induced in loop 1 due to the magnetic field from loop 0. Current I_1 generates a secondary magnetic field which interacts with the receiving loop in the same manner that loop 0 interacted with loop 1.

There is an emf generated in loop 2 due to the current in loop 0. In geophysics, this is known as the primary response of the loop, $\mathcal{E}_2^{(P)}$. In mathematical terms it is

$$\mathcal{E}_2^{(P)} = -i\omega M_{02} I_0 e^{1\omega t}. \tag{2.78}$$

The response in the receiver due to the ground loop is called the secondary response. It is typically much smaller and more complicated than the primary response. The secondary response is written as

$$\mathcal{E}_2^{(S)} = -i\omega M_{12} I_1 e^{1\omega t}, \tag{2.79}$$

where M_{12} is the mutual inductance between loops 2 and 1.

Commonly, the receiving loop measures the anomalous voltage by comparing it to the primary field in the absence of the ground circuit. The receiving apparatus

measures

$$\frac{\mathcal{E}_2^{(S)}}{\mathcal{E}_2^{(P)}},$$

known as the *response* or the *electromagnetic anomaly* of the system (see Section 2.7.1). The response of the ground loop is

$$\frac{\mathcal{E}_2^{(S)}}{\mathcal{E}_2^{(P)}} = \frac{i\omega M_{12} I_1 e^{i\omega t}}{i\omega M_{02} I_0 e^{i\omega t}},$$

and by substituting equation (2.77) becomes

$$\frac{\mathcal{E}_2^{(S)}}{\mathcal{E}_2^{(P)}} = -i\omega \frac{M_{12} M_{01}}{M_{02}} \frac{(R - i\omega L)}{R^2 + \omega^2 L^2}.$$

Grant and West (1965) define the ratio of the frequency times the self inductance of the ground loop divided by its resistance, as the *response parameter* α.

$$\alpha = \frac{\omega L}{R}, \tag{2.80}$$

so dividing the system response expression through by R^2 yields

$$\frac{\mathcal{E}_2^{(S)}}{\mathcal{E}_2^{(P)}} = -\frac{i}{L}\frac{\omega L}{R}\frac{M_{12} M_{01}}{M_{02}} \frac{\left(1 - i\dfrac{\omega L}{R}\right)}{1 + \left(\dfrac{\omega L}{R}\right)^2};$$

and by using equation (2.80), the system response is

$$\frac{\mathcal{E}_2^{(S)}}{\mathcal{E}_2^{(P)}} = -\frac{M_{12} M_{01}}{L M_{02}} \frac{(\alpha^2 + i\alpha)}{1 + \alpha^2}. \tag{2.81}$$

The first term in equation (2.81) is called the *coupling coefficient*, and its expression is

$$A_0 = -\frac{M_{12} M_{01}}{L M_{02}}. \tag{2.82}$$

The coupling coefficient is a measure of the amount of flux that couples the receiver to the transmitter through the underground circuit in divided by the amount of flux that is coupled between the receiver and transmitter directly (Grant and West, 1965). In the sense of Section 2.7.7, it relates to how much energy can be transferred to the receiver from the transmitter via the ground loop. This coefficient changes with the geometry of the system, i.e. the separation of the system and the ground loop, but is not affected by the frequency of the transmitter current (provided the frequency is low enough that the long wavelength approximation is valid).

The second expression is the *response function*, dependent on the response parameter. The response function is

$$\frac{\alpha^2 + i\alpha}{1 + \alpha^2}. \tag{2.83}$$

The response function is dependent on the electrical properties of the underground loop (R and L) and the frequency ω of the oscillating circuit. It is a complex function whose magnitude is limited between 0 and 1, as shown in Figure 2.10.

The real part of the response function goes from 0 to 1 with changes in the response parameter. The imaginary part goes from zero at low α to 0.5 at $\alpha = 1$, and returns to zero for large values of α. Both the real and the imaginary part are 0.5 when $\alpha = 1$ as can be seen from equation (2.83). The secondary emf goes from 90° out of phase with the primary at low α to 45° out of phase at $\alpha = 1$. At high α, the response is almost completely in-phase.

We divide the response function into two limits. The resistive limit is the response of the system when α is very small and means that either the transmitter current is oscillating at low frequency or that the loop is highly resistive. The current induced in the ground loop is very small and limits the secondary response. There is a 90° phase shift between loop 0 and loop 2, and also two 90° phase shifts between loop 0–1 and 1–2: the secondary response will be out of phase with the primary by 90°.

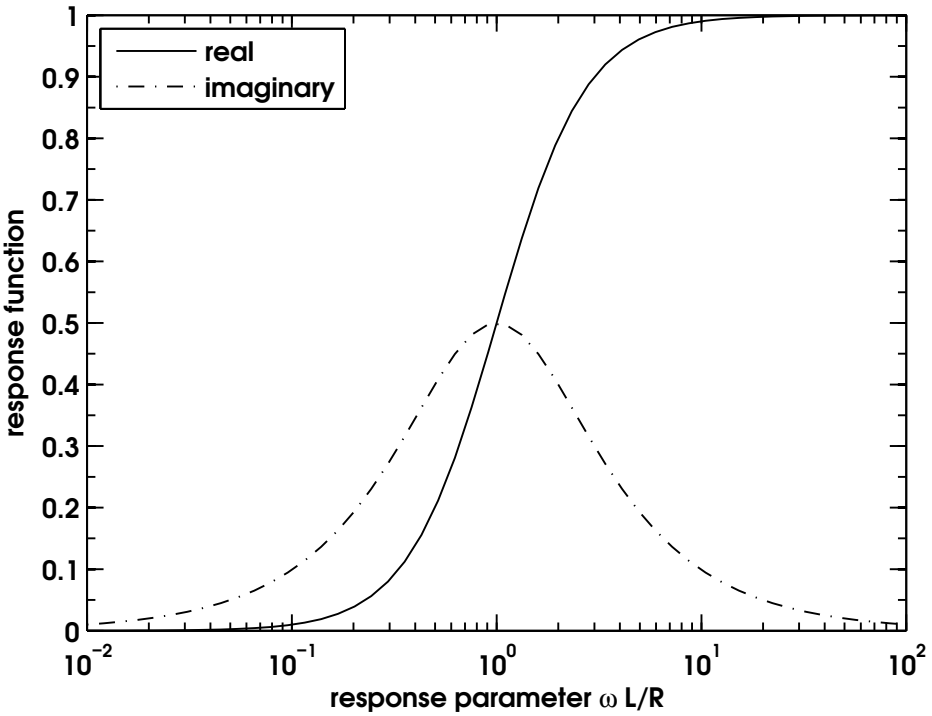

Figure 2.10: *Response function value versus response parameter.*

The second limit is known as the inductive limit. As α increases, so does the secondary magnetic field in the ground loop. The eddy current in the ground loop changes its phase so that the back emf and the potential drop caused by the impedance of the loop add to zero. The magnetic field produced by the ground loop also changes in phase. At the inductive limit, the induced magnetic field and the magnetic field from the transmitter are almost the exact same in magnitude but opposite in direction. The total flux in the ground loop is approximately zero, even though the total magnetic field is not.

In a distributed body, the inductive limit means that eddy currents produced by the primary field are sufficient to generate a secondary magnetic field that completely cancels the primary field everywhere in the body. At the inductive limit, the magnitude of the secondary response will be entirely determined by the coupling coefficient.

2.9 Summary

In this chapter, I have outlined the basic theory of electrodynamics. In particular, I have developed the idea of the magnetic induction field and its relation to the electric and displacement fields through Faraday's law of induction. I have explained how the long wavelength approximation simplifies calculation of the magnetic field by allowing us to use magnetostatic principles to calculate them in complicated structures.

The long wavelength approximation allows us to use the law of Biot and Savart to calculate magnetic induction for structures such as circular loops of wire, segments of straight wire and dipoles—all of which are important to the field of geophysics—and to apply those magnetic fields to dynamic problems such as moving loops. Provided the time scales of observation are long enough, the long wavelength approximation is valid.

The concept of magnetic induction has been introduced, and its relevance to both flux-cutting and energy storage has been discussed. Either interpretation is valid; each may be exploited when calculating inductance. The general case of the mutual inductance of skew lines has been presented and the derivation can be found in Appendix B.1. The mutual inductance of a few other configurations that are important to this thesis have also been presented.

Self inductance is a concept that is most easily understood in terms of the self energy of a circuit. It is a simplified method that avoids the confusion of self-flux linkage. Self inductance is simply a measure of how a circuit reacts to its own changing current (and hence, magnetic field). The self inductance of a segment of wire has been calculated, an example that will become more meaningful in Chapter 5.

In principle, the electromagnetic induction method involves a transmitter and a receiver in proximity to the earth. The transmitter and receiver are coupled directly to each other through inductance. This is called the primary response.

The transmitter also couples to the earth. Mutual inductance of the earth with the transmitter generates eddy currents in the ground which produce secondary magnetic fields. These fields interact with the receiver and produce the secondary response. The electromagnetic response is the ratio of the secondary to the primary response. Electromagnetic geophysics, then, is the exploration of the earth's ability to store electromagnetic energy. This is closely related to conductivity, a physical property that we are most interested in.

Chapter 3

Evidence of Bird Swing in AEM Systems

3.1 Introduction

In the last chapter I gave a brief survey of electrodynamics as it applies to calibration methods and, to a lesser extent, geophysics. A transmitter produces a time-varying magnetic field that penetrates the earth. Currents induced in the earth generate their own time-varying magnetic field which propagates outwards. A receiver measures a secondary field component and compares it to the primary field component from the transmitter. The measure of the secondary response is often given as parts per million of the primary, with a phase difference that accounts for how much of the secondary signal is in-phase and how much is in quadrature or 'out-of-phase' with the primary. The measure of phase, as well as the relative strength of the secondary signal, gives us some idea of what is buried in the earth.

We can determine the structure of buried objects by comparing the phase and strength values to type curves of known or analytic models for a specific system geometry. For example, the RESOLVE system, which I will discuss in this chapter, is often modelled as two dipoles above a layered earth. A layered earth is a model

which separates the earth into layers of differing conductivity values. Other models used are: thin sheets (often used to model conductive overburden), half spaces (for example, sea ice or seawater), or conductive spheres in resistive half spaces (a useful model when exploring for sulphide ores in resistive bedrock). Of course, the earth is none of these, but very good results are achieved with such analytic models (Grant and West, 1965). More modern approaches to determine the conductivity structure of buried objects are also widely practiced (Oldenburg and Li, 2005), including complicated 3D modelling programs. The difficulty underlying such methods are that they are highly computational and sometimes require days to come up with a solution (Hohmann and Raiche, 1988).

As we saw in the last chapter, the simplest model to consider is the three loops of Section 2.8. Another simple model is an extended surface conductor, such as a half space or a thin sheet. At high enough frequency, a conductive half space resembles a thin conductive sheet. Imagine a dipole located height h above a thin sheet of infinite conductivity. The total field at any other point in space above the sheet is the superposition of the field from the source dipole over the field from an image dipole that appears as a mirror image of the source at distance h below the surface of the sheet. This is shown schematically in Figure 3.1. This is known as the method of images (Griffiths, 1989), and it is this concept which I will be using in this chapter when I deal with pendulum motion of the towed bird of the RESOLVE and DIGHEM helicopter electromagnetic (HEM) systems.

3.1.1 Pendulum Motion of AEM Systems

Geophysical electromagnetic systems are classified into two main modes of operation: time domain and frequency domain. AEM systems have the further distinction of being classed according to what type of aircraft is used to support the EM platform: fixed-wing or helicopter borne. AEM systems are popular and useful due to the fact that they are a relatively cheap means to survey a large amount of land in a

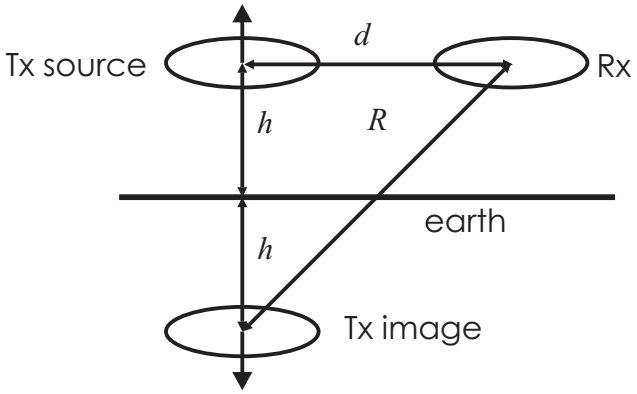

Figure 3.1: *Diagram for the method of images used to estimate the coupling coefficient at the inductive limit for a dipole pair above a conductive half space or thin sheet.*

short period of time. They are particularly useful when the survey area is remote and/or the ground cover is rugged enough that it is difficult to mobilise ground crews. Helicopter borne surveys are particularly useful in remote areas due to their vertical take-off and landing capability, thereby eliminating the need for nearby landing strips or lakes. Despite their popularity, AEM systems are not without their problems. Every towed object behaves like a pendulum when it is towed beneath an aircraft. An AEM bird will be subjected to oscillatory motions that depend on its drag coefficient and airspeed, wind gusts and the ability of the pilot to damp the swinging. In addition to pendulum-like swinging, the towed bird can also undergo rotations of pitch, roll and yaw. Each of these motions alters either the system altitude or the geometry or both. In this chapter, I will examine the effect these motions have on data obtained with the frequency domain HEM systems RESOLVE and DIGHEM^{VRES} flown on survey in Australia. A brief description of both of these systems, together with some pertinent photographs of their geometry, is given in Appendix C.

Bird swing has two major consequences. The swinging of the towed system affects the coupling of the transmitter and receiver system to the earth, thereby affecting both the in-phase and quadrature values of the measured response. This has been noticed by researchers in the past. For example, Holladay et al. (1997) recognised

the problem in measuring sea ice thickness in northern Canada. Deszcz-Pan et al. (1998) cited bird swing as a cause of error when they inverted EM data to measure salt intrusion in the Florida Everglades National Park. Deszcz-Pan also mentioned that there were much greater oscillations in apparent resistivity when inversions were made using bird altitude than when the data were inverted for apparent depth (Deszcz-Pan et al., 1998). Fitterman (1998) attributed some errors in the Florida Everglades HEM data to improper calibration of the towed bird. Calibration error, such as baseline shift and drift cause systematic errors in the data that can change from flight to flight and generally persist for the entire survey. Bird swing error will be more periodic and change from line to line, flight to flight. As a first attempt at correcting attitude error in the RESOLVE system, Yin and Fraser (2004) developed the superposed dipole model over an isotropic layered earth. Their correction procedure relied on simple trigonometric functions applied to the in-phase and quadrature data based on measured pitch and roll angles, and amounts to a geometrical correction of the EM data. Soon after, Fitterman and Yin (2004) developed a much more complicated analytic model based on separated dipoles over a layered earth. They defined bird swing as rotations in three major directions: pitch, roll and yaw. Each rotation affects the measured in-phase and quadrature response of the EM system. Fitterman and Yin (2004) derived corrections to the measured response due to the pitch, roll and yaw of the bird, but in neither paper do the authors account for the second major consequence of bird swing: changes in measured altitude and actual altitude. Both of the consequences of bird swing combine to produce an easily recognisable effect in the measured data. The periodic motion of the swing introduces a systematic error that changes the response at the frequency of the bird's swing. Pitch and roll introduce higher frequency oscillations in the measured response. This will be shown in Section 3.3 when I examine DIGHEM data over seawater in Sydney Harbour.

Bird swing effects are most easily seen when the EM data is transformed to the $\phi\beta$ domain. The $\phi\beta$ domain is a domain that normalises the entire set of in-phase and quadrature data to phase or ϕ values ranging from 0° to 90°, and amplitude or β values from 0 to about 1. It is a comparison of the measured data to what the data would be for the system at the inductive limit, and is thus a means of directly investigating the geometric coupling of the system with the earth. It was first described by Ley-Cooper et al. (2006), and is a convenient way to explore the entire set of survey data for calibration and altitude errors. The next section, which describes the $\phi\beta$ domain, will follow the derivation of Ley-Cooper et al. (2006).

3.2 The $\phi\beta$ Domain

Looking back to section 2.8, we determined the system response for a separated dipole system in proximity to a wire loop. As was mentioned, the receiver records data in parts per million (ppm) of both the in-phase (R) and quadrature (Q) components of the total field. The total field itself, or its magnitude (T), is calculated as

$$T = \sqrt{R^2 + Q^2}.$$

The real part of the response is

$$R = A_0 \frac{\alpha^2}{1 + \alpha^2};$$

and the imaginary part is

$$Q = A_0 \frac{\alpha}{1 + \alpha^2},$$

where α is the response parameter (defined in equation (2.80) and A_0 is the coupling coefficient (given for the wire loop in equation (2.82)). Ley-Cooper et al. (2006) derived a prediction for the wire loop coupling coefficient at the inductive limit (when $\alpha \to \infty$). The coupling coefficient at any time due to the response is A,

defined as:

$$A = \frac{T^2}{R} = \frac{R^2 + Q^2}{R}, \tag{3.1}$$

which is valid when $R \neq 0$ (Ley-Cooper et al., 2006).

The ratio of the in-phase to the quadrature response is just the arctangent of the phase of the secondary response. This becomes obvious when we consider the real response and the imaginary response as the complex quantities of the total response of the system. By calculating the ratio R/Q, we can also get a measure of the response parameter α, which represents the arctangent of the phase, i.e.

$$\alpha = \frac{R}{Q}, \tag{3.2}$$

and so the phase (ϕ) of the response is

$$\phi = \tan^{-1}\left(\frac{R}{Q}\right) = \tan^{-1}(\alpha). \tag{3.3}$$

The phase at any point in the survey is closely related to the response parameter of the system if the ground underneath the system was a wire loop at the inductive limit.

Ley-Cooper et al. (2006) derived another dimensionless parameter, β, which is the ratio of the predicted coupling coefficient A to A_0, the coupling coefficient of a model such as the wire loop. This calculation is given below:

$$\beta = \frac{A_{lim}}{A_0} = \frac{T^2}{RA_0}. \tag{3.4}$$

Let us go back to the definition of the response parameter for a wire loop. It was defined in equation (2.80) as

$$\alpha = \frac{\omega L}{R}.$$

West and Macnae (1988) call the ratio of L/R the time constant of the wire loop,

which indeed it is (it has units of time), and use the symbol τ. Using this notation, we can express the time constant of the wire loop as

$$\tau = \frac{R}{Q\omega},$$

by using equations (3.2) and (2.80).

If we were to plot β versus τ for wire loop data, all data collected would plot on the single point (1, 1) (Ley-Cooper et al., 2006). Likewise, if we were to take all data collected in a flat and level flight over a wire loop and plot it on a β versus ω plot, it would all fall on a horizontal straight line at $\beta = 1$.

For a specific system of rigidly mounted coils that can be approximated by dipoles, Ley-Cooper et al. (2006) claim the coupling coefficient, and hence the inductive limit response, is the same as the image problem discussed earlier in Section 3.1. This is the setup shown in Figure 3.1 and discussed by Grant and West (1965).

Figure 3.1 is a representation of a horizontal coplanar alignment of two dipoles (compare to Figure 2.6b). When the coils are arranged in this configuration the method of images predicts that, for a transmitter dipole at height h, the image will be present at a depth of h below the surface. The dipoles are separated horizontally by a distance x. Ley-Cooper et al. (2006) use this convention to calculate β above a perfectly conductive sheet. The value for β is then the ratio of the predicted coupling coefficient, equation (3.1) to the coupling coefficient using the inductive limit solution for a dipole pair above an extended horizontal conductor. The coupling coefficient of the dipoles is the ratio of the mutual inductance between the receiver and the image (M_{IR}) to the mutual inductance between the transmitter and the receiver (M_{HCP}). Ley-Cooper et al. (2006) call this ratio G. The value M_{IR} is calculated using equation 2.48; this is done in Appendix B.2.

At high enough frequency, the limiting response is a function of altitude only, and the inductive limit coupling coefficient (G) is

$$G = \frac{10^6 d^3 (8h^2 - d^2)}{\sqrt{(4h^2 + d^2)^5}}, \tag{3.5}$$

where d is the separation between the transmitter and receiver in m and h is the altitude of the transmitter off the ground. We then define β as the ratio of the predicted coupling coefficient response of the wire loop to the inductive limit response of a double dipole system above a sheet conductor:

$$\beta = \frac{T^2}{RG}. \tag{3.6}$$

The dimensionless parameter β and the phase angle ϕ are useful in determining altitude variations in airborne electromagnetic data for the RESOLVE and DIGHEM systems. For example, a thin sheet should go from $\beta = 0.5$ at $\phi = 0°$ to $\beta = 1$ at $\phi = 90°$. A half space should go from $\beta = 0$ to $\beta = 1$. This is shown in Figure 3.2, which is a blank $\phi\beta$ graph, reproduced from Ley-Cooper et al. (2006).

Figure 3.2 shows the variation of β with ϕ for thin sheets and half spaces at various depths below a nominal 30 m air layer, beginning at 0 m. The plot is important because electromagnetic data taken from a flight 30 m over a thin sheet should always transform to the first dashed line terminating at 0 m, while a half space at 30 m should always plot along the first solid line in the figure, regardless of altitude or conductivity.

As an example of this concept consider the derivation for the skin depth in a conductive half space described in Section 2.5.1. Sea water has a conductivity σ of $\sim$4.5 S/m; and its magnetic permeability is that of free space. For a RESOLVE system that operates between 400 Hz to 100 000 Hz, the skin depth using the plane wave approximation is from 13 m (at low frequency) to as little as 1 m at high frequency. This means that sea water can be modelled as a conductive half space,

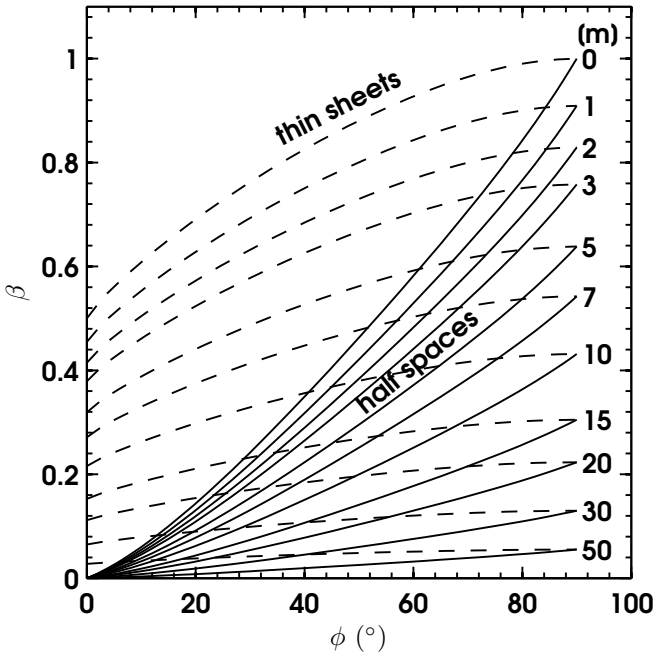

Figure 3.2: *Blank $\phi\beta$ grid based on equation (3.6). Half spaces at different depth below the surface plot as solid lines; thin sheets are plotted as broken lines. When the half space is at surface, β goes from 0 to 1; a thin sheet at surface ranges from 0.5 to 1.*

although local sources can penetrate more deeply under optimum conditions (Reid and Macnae, 1999). So, if we were to fly an HEM system such as RESOLVE or DIGHEM over sea water, all data from the flight should fall on the conductive half space at surface line in Figure 3.2. If the data didn't plot on the half space at surface line, we would suspect that there are internal calibration errors or there is an error in the measured altitude (Ley-Cooper et al., 2006). It turns out that this is exactly what we see.

3.3 Sydney Harbour: DIGHEM^{VRES}

The first set of data that I will discuss is from a survey conducted over Port Jackson in the Sydney Harbour, NSW. This survey was carried out using a DIGHEM^{VRES} HEM system in April 2001 (see Appendix C.2). The survey consisted of 20 lines flown in a northeast and southwest direction, with line spacing of 50 m, covering

an area of roughly 6 km^2. The survey was completed as a follow-up from an earlier test conducted for the Maritime Operations Division of the Defence Science and Technology Organisation of Australia to determine the effectiveness of frequency domain AEM for shallow seawater bathymetry (Vrbancich, Hallett and Hodges, 2000). The flight lines of the survey are shown in Figure 3.3.

The survey area was primarily over water that was greater than 15 m in depth. At this depth, seawater of conductivity 4.5 S/m is practically a conductive half space for the higher frequencies of the DIGHEM^{VRES} system. The plane wave skin depth and the DIGHEM^{VRES} frequencies used in this survey are listed in Table 3.1, below.

Table 3.1: *DIGHEM^{VRES} operation frequency, coil alignment and skin depth over 4.5 S/m seawater.*

Dipole configuration	Frequency (Hz)	Half space skin depth (m)
HCP	387	12.0
	1 601	5.9
	6 259	3.0
	25 800	1.5
	102 700	0.74

The altitude for this survey was measured by a radar altimeter mounted beneath the helicopter. It measured the altitude of the helicopter above the surface of the seawater, which was approximately 60 m for this survey. The altitude of the bird was then calculated from the radar altimeter by subtracting a constant amount of 30 m, the length of the tow cable. My calculation of β was based on this value.

Data from this survey, when plotted in the $\phi\beta$ domain, should plot as a conductive half space for the three highest frequencies (Ley-Cooper et al., 2006). However, as Ley-Cooper et al. (2006) showed in Figure 8 of their paper, the $\phi\beta$ data for each frequency was distributed over the graph, with spreading in both ϕ and β. Their figure, with some modification, is repeated here as Figure 3.4.

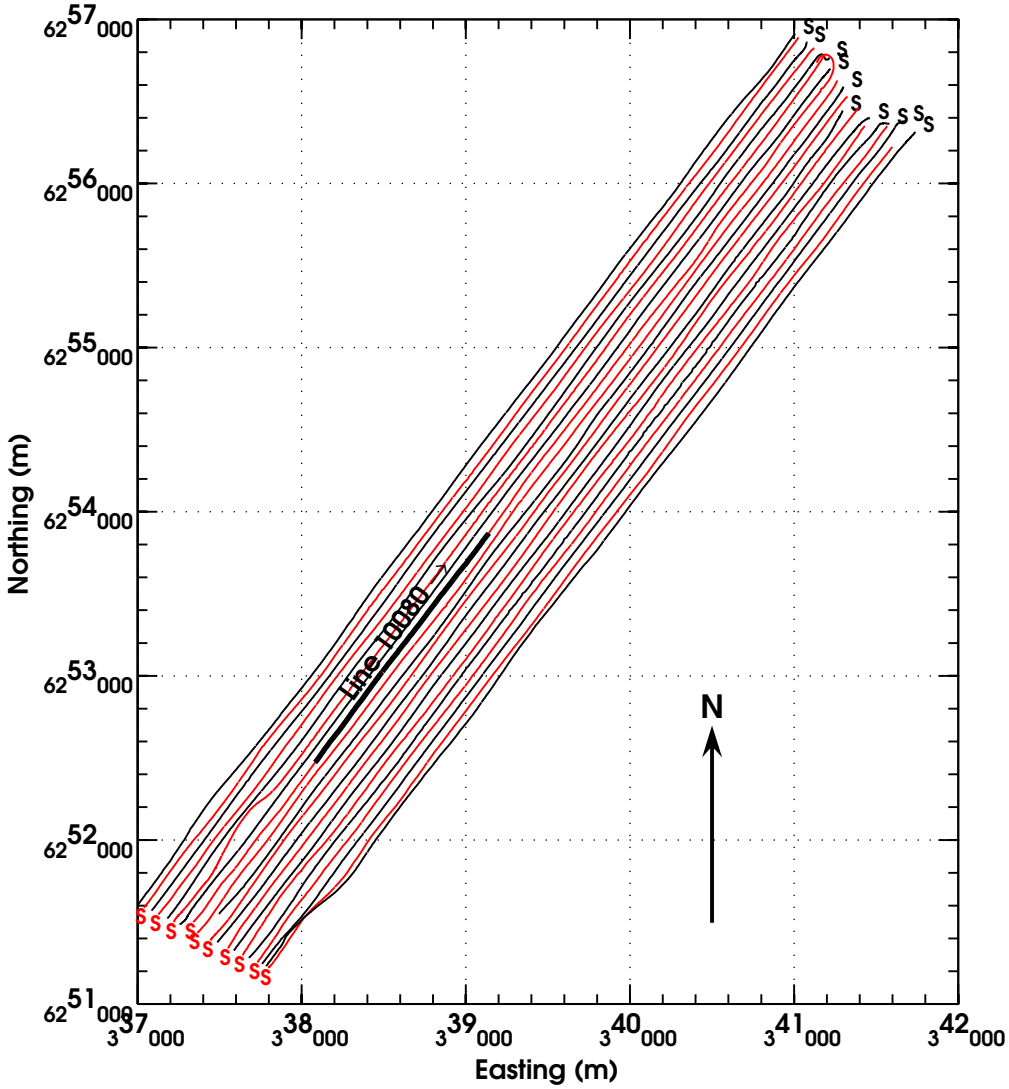

Figure 3.3: *Lines flown for DIGHEM^{VRES} survey over Port Jackson, Sydney Harbour in July 2001. Lines flown to the NE are marked in red. Lines flown to the SW are marked in black. Each line has its starting point marked with the letter 'S'.*

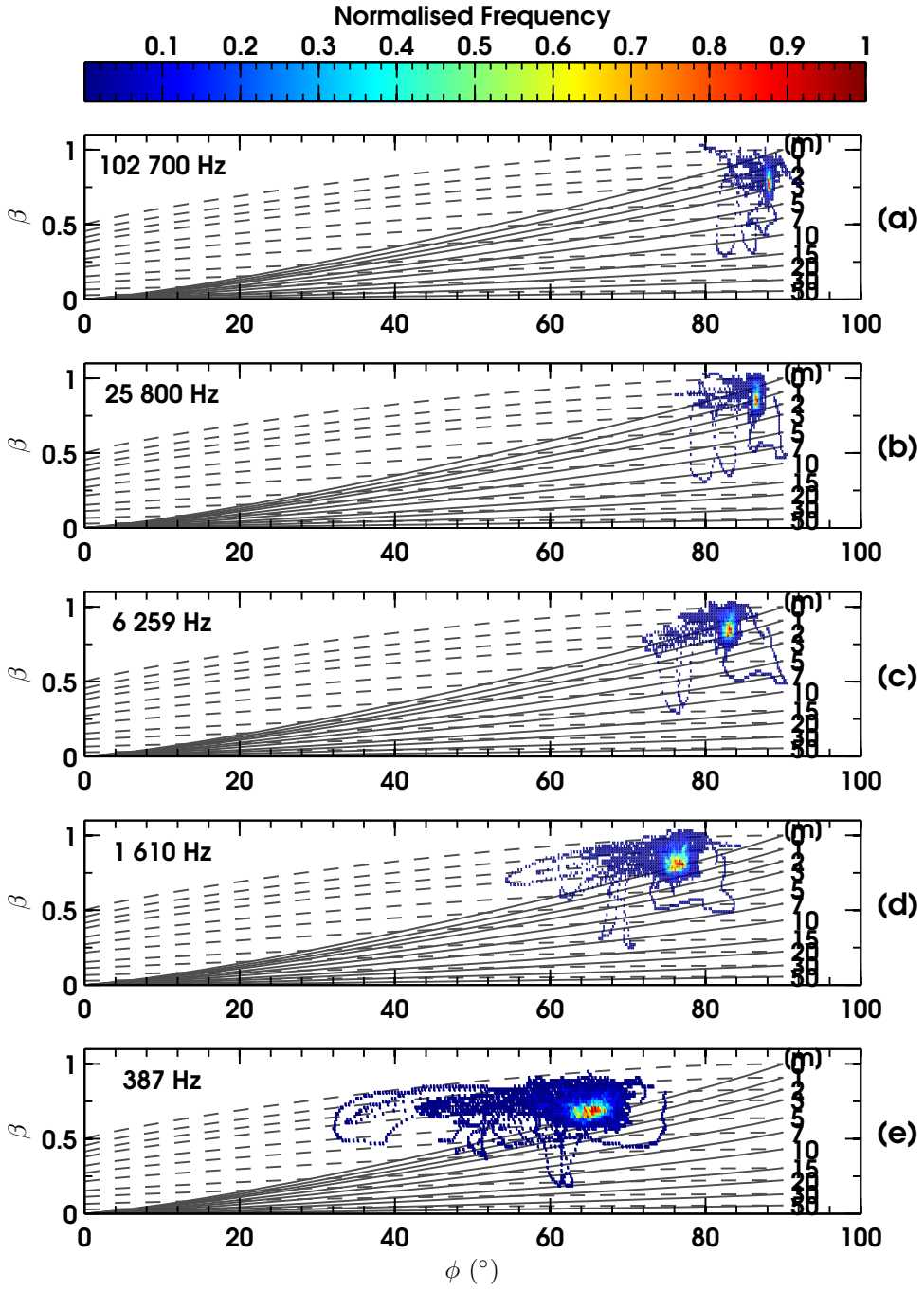

Figure 3.4: *$\phi\beta$ plots of each frequency for the entire 2001 DIGHEM^{VRES} survey of the Sydney Harbour.*

Figure 3.4 is composed of five panels, one for each frequency of the DIGHEM system. Each panel is a reconstruction of the blank $\phi\beta$ graph of Figure 3.2, with the β and ϕ data for that frequency for the entire survey plotted on top. Each plot is a distribution of ϕ and β normalised to 1. Areas of high concentration of ϕ and β are drawn in red, while areas of only 1 occurrence of ϕ and β are drawn in blue. All other areas are blank. Panel (a) shows the data for the 102 700 Hz frequency. The β values indicate that most of the time, the data fit a conductive half plane at about 2.5 m below the surface of the sea. The reason that the panel predicts the surface of the seawater to be 32.5 m below the towed bird can be attributed to calibration or altitude error (Ley-Cooper et al., 2006). The spread in β for the 102 700 Hz data indicates that the data predicts that a conductive half space can be located anywhere from 0 m to 5 m greater than the survey altitude of 30 m. This vertical spread in the β-distribution is consistent for most of the other frequencies as well. I assert that this spread is caused by the altitude error generated by the swinging motion of the towed bird, and will give evidence for this in this chapter.

To illustrate that any swinging motion of the bird will change its altitude and geometric coupling to the water, I will show the calculation of β for all five frequencies over a section of line 10080. The section of line 10080 is labelled and marked in thick black in Figure 3.3; it was chosen because, according to Figure 1 of (Vrbancich, Hallett and Hodges, 2000), it is over an area of fairly deep water (i.e. depth greater than 15 m). Deep seawater very closely approximates a half space for the higher frequencies over this section of line. Figure 3.5 shows the periodic changes of β in all five frequencies. The major oscillations in the mean value of β have a period of 9–10 s. I claim these are caused by bird swing. Calibration error and drift cannot be the cause, because they are normally errors that occur over whole lines or even flights.

Before I give evidence to support my claim that the main periodic changes in β are a result of bird swing, I will point out a further feature in the variation of β with

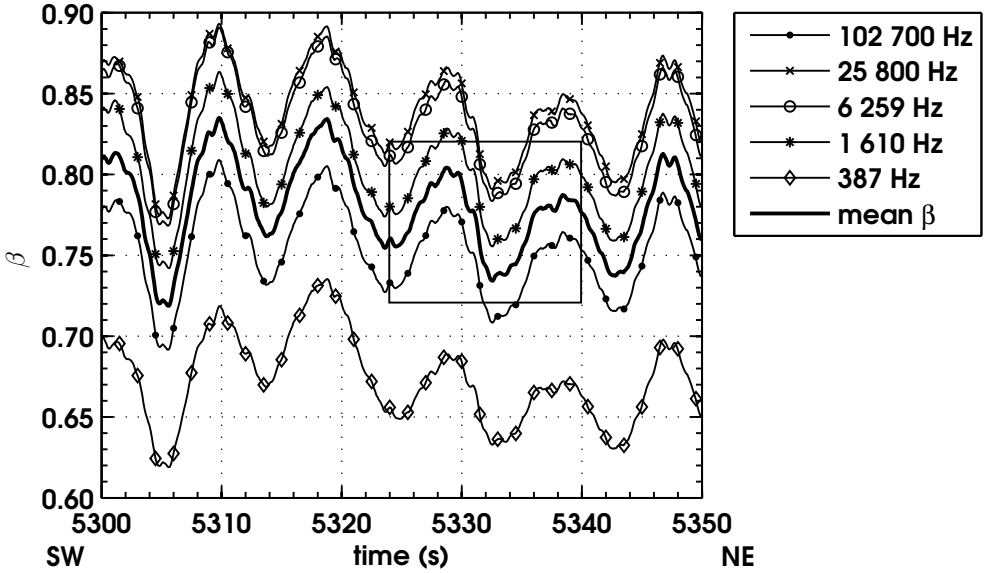

Figure 3.5: *Plot of β versus time for a small section of line 10080, marked in thick black in Figure 3.3. Thick solid black line is the mean of β for all frequencies. Oscillations in the mean of β are plainly seen to have a period of 9–10 s.*

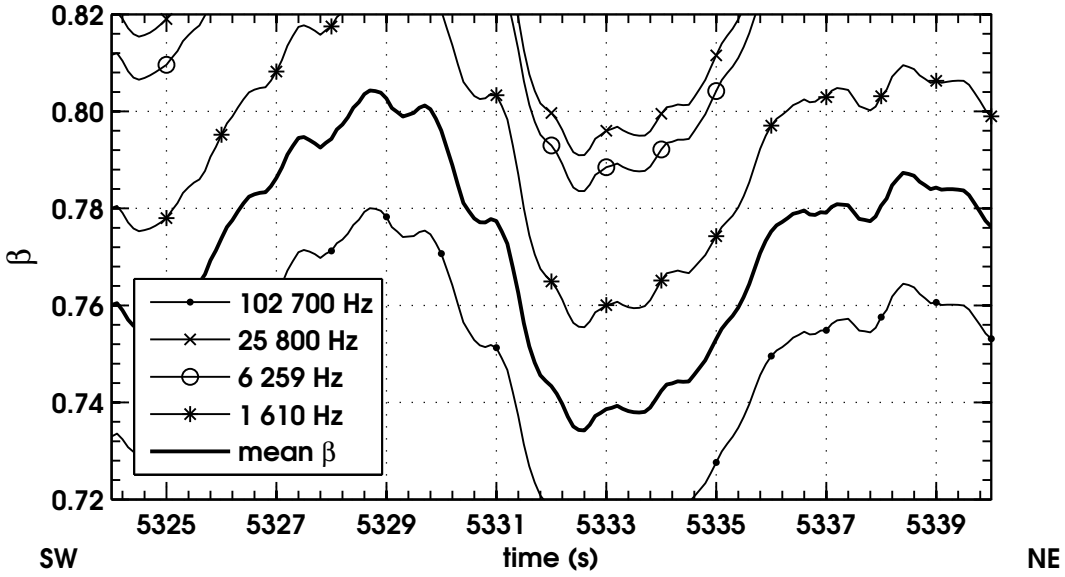

Figure 3.6: *Detail drawn from the rectangular box in Figure 3.5. Smaller oscillations, on the order of 1 s, are easily seen superimposed over the main 9–10 s oscillations of the bird swing.*

time. Figure 3.6 shows the detail of the rectangular box marked in Figure 3.5. Here, the mean value of β from all frequencies is shown in thick black. Superimposed on the main 9–10 s oscillation of β are smaller, higher frequency oscillations that have a period of approximately 1 s. These oscillations are persistent through the entirety of the main oscillation and are clearly seen on every frequency in Figure 3.6. I attribute these to pitching in the bird as a result of rotation about the hitching point. Evidence for this pitching will be given in Section 4.6, when I explore data from the Sunraysia survey outside Mildura, Victoria. But first, I will give conclusive evidence of bird swing with data from a Chowilla Floodplain survey conducted with a RESOLVE HEM system in July 2005, near Renmark, South Australia.

3.4 Chowilla Floodplain: RESOLVE

The Chowilla Floodplain survey was a helicopter electromagnetic study conducted by Fugro Airborne Surveys on behalf of CSIRO Exploration and Mining. The survey was carried out using a RESOLVE HEM system, and consisted of approximately 1 700 line-km flown over 132 lines. Line separation for this survey was 200 m for the main lines and 2 000 m for the tie lines. The lines flown in this survey are shown in Figure 3.7.

While this survey was being conducted, I obtained video recordings of the helicopter and RESOLVE system as it was being flown on four different lines. I then analysed the video data at a frame rate of 2 Hz from the line segments. For reference, the line segments are also shown in thick black in Figure 3.7, while the camera positions are marked with a small dot and a number designating day. In each frame, the nose and tail of the helicopter and the towed bird were manually picked and the positions of each were recorded. GPS antenna locations on the helicopter and bird were then calculated for each line. The relative separation of helicopter GPS antenna to bird GPS antenna for each segment of line (from video data) is shown as

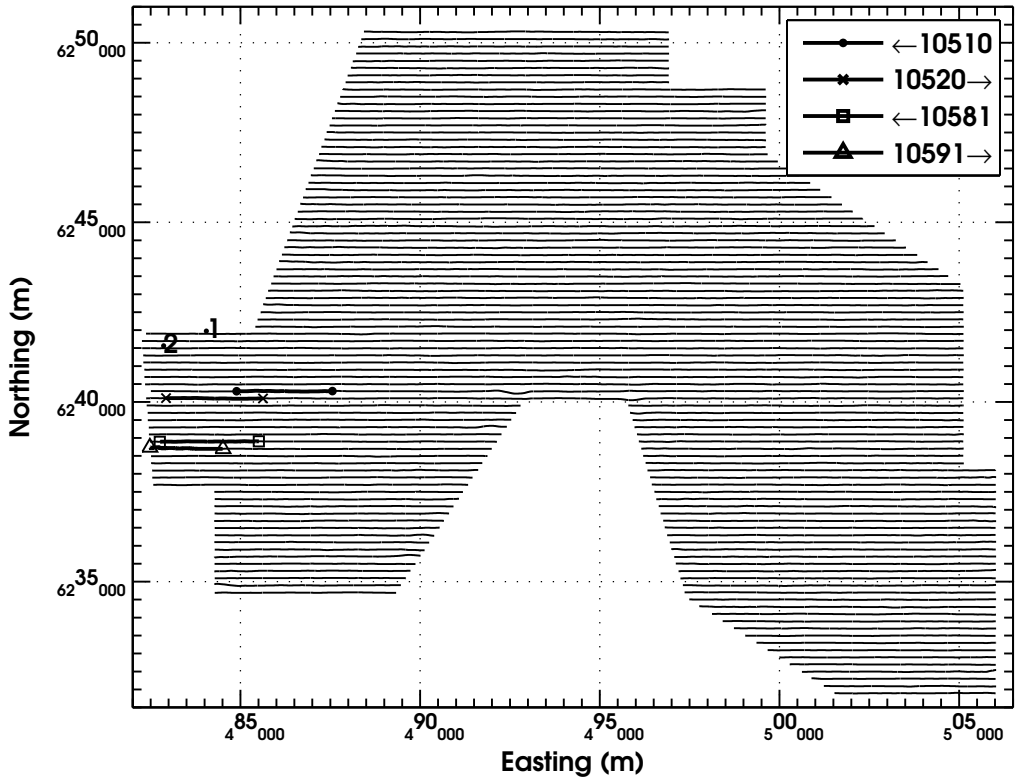

Figure 3.7: *Lines flown for the RESOLVE apparent resistivity survey conducted over the Chowilla Floodplain outside Renmark, South Australia. Position of video camera on each day marked with a dot and a number beside it.*

solid lines in Figure 3.8. Additionally, the actual helicopter and bird GPS antenna separations have been calculated for the line segments, and are shown with dots in each panel of the figure. Fugro Airborne Surveys claim that GPS antenna accuracy is less than 1 m, so the correlation found by trial and error between video and survey data oscillations is remarkable. There is a definite periodic motion of the bird relative to the helicopter along the profile. Similar periodic motions are observed for each line that was recorded; the frequency of oscillation is typically 8-10 s, as can be clearly seen in each panel.

Figure 3.8 is divided into four panels. The videos represented in panels (a) and (b) were recorded on the first day of video recording, and the videos in (c) and (d) were recorded on the next day of the field trip, from a different location. The

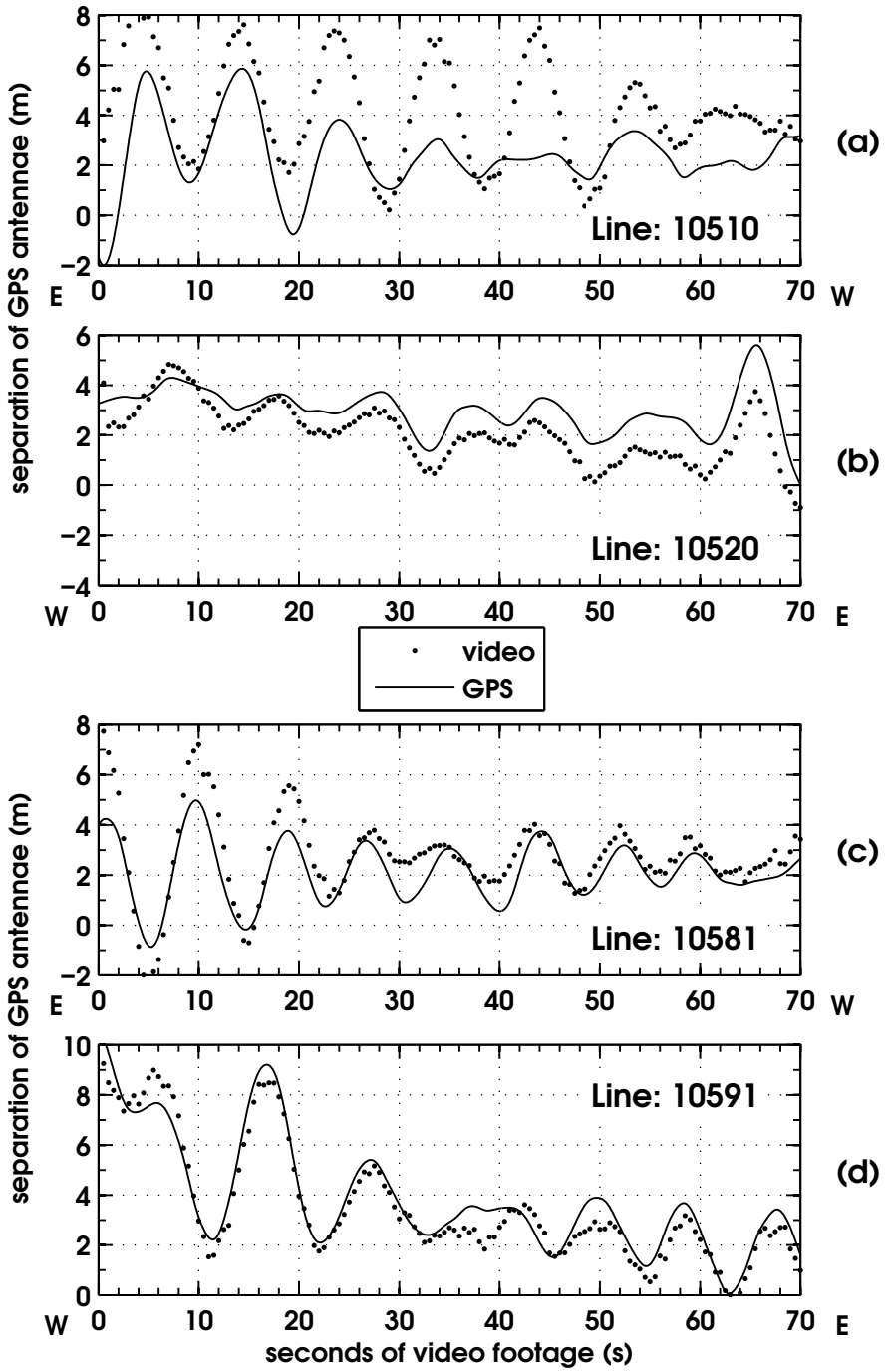

Figure 3.8: *In-line separation of GPS antenna mounted on helicopter tail to the GPS antenna mounted on the fore of the towed bird from video recorded and survey data (4 line sections). The solid black line is from survey data, the dots calculated from video. Panels (a) and (b) show a systematic offset of ∼2 m, due to parallax error in the video data, and error in calculating the position of the GPS antenna due to poor image resolution.*

match between the data calculated from video and survey data is poor in panels (a) and (b) of Figure 3.8; I attribute this to poor resolution in the images of the video data and parallax error due to poor positioning of the camera whilst recording. On the second day, the camera operator attached a zoom lens to the camera and thereby increased the resolution of the recorded image. Figure 3.7 also shows that the parallax error during Day 2 was lower due to the reduced camera viewing angle. Panel (d) of Figure 3.8 has the closest match, and clearly shows that the calculated separation of GPS antennas from video evidence reflects the in-line separation of the GPS antennas given in the survey data. The video recordings for each line are included in Appendix D.1.

From video evidence, the cable that attaches the bird to the helicopter acts like an inextensible cord. For most of the in-line oscillations, bird swing results in pitch of the bird. However, there are also times when the pitch of the bird is out of phase with the swing of the cable. For example, a forward swing of the cable sometimes results in a slight downward pitch of the bird, contrary to a rigid model. This uncoupled motion cannot be detected by analysis of the helicopter and bird GPS. Consideration of this type of motion is the subject of Section 4.7.

Several problems exist with recording video data of towed bird EM systems. It is extremely difficult to obtain continuous video of the system being flown while it is on survey. This is mainly due to line-of-sight considerations and the approximate 30–40 m/s ground speed of the helicopter. Analysis for tracking of the towed system becomes problematic due to a significant amount of parallax error involved in determining the relative positions of the helicopter and bird, even when the camera is positioned far away from the survey line. Furthermore, it is quite labour-intensive to manually select the pixel positions of the helicopter and the bird in each frame. These considerations led me to examine the relative GPS positions of the helicopter and bird.

Sampling frequency for the bird GPS was 1 Hz, while the helicopter sampling rate was 2 Hz; both are interpolated to 10 Hz. Bird GPS accuracy is stated to operate to

better than 1 m in all 3 directions in differential mode, while the navigation GPS on the helicopter states a better than 5 m accuracy for real-time differential operation. The sampling rate and distance flown for the entire survey amounted to a database of approximately 300 000 points. This amounts to ∼80 hours of data: enough for a meaningful statistical analysis. Lines for this survey were flown east-west with 200 m line spacing. With an estimated bird swing period of 10 s and a ground speed of 40 m/s, we expect to find about 12 oscillations for a 5 km segment of line. Figure 3.9(a) shows a plan view of a segment of a typical line. The flight path of both the helicopter and the bird are shown in the first panel. Helicopter accelerations and wind gusts generate horizontal displacements of the bird beneath the helicopter; this in turn triggers pendulum motions. The motion is divided into two orthogonal directions; one in the direction of the flight line, and the other perpendicular to the direction of the flight line. The reason for this separation is that in-line motions mainly cause pitch of the bird, while cross-line motions mostly cause roll.

Simultaneous decomposition of the bird motion into the orthogonal coordinates is shown in panels (b) and (c) of Figure 3.9. Clearly, there exists a relation between what I have termed the in-line and cross-line motions of the towed bird. However, the motions have two different periods of oscillation. The in-line motion exhibits fewer oscillations in 60 s than the cross-line motion. The cause of this is drag, which we can assume is proportional to the square of air-speed, and affects the in-line pendulum motions more than the cross-line motions. Imprinted on the observed motions are, of course, the driving effect of helicopter accelerations.

When viewed over the entire survey, the swinging motion of the bird becomes more apparent. Figure 3.10 shows a section view of the in-line and vertical separation of the helicopter and bird GPS antennas for the entire database of points. It is clear from this figure that the GPS antenna of the towed bird has a mean position of approximately 2 m ahead of and 31 m below the GPS antenna of the helicopter. However, the range of the in-line swings is from 5 m behind the mean position, to

8 m in advance of the mean position. If the distribution is modelled as a normal distribution, the GPS antenna has a mean in-line position of (2.18 ± 0.01) m with a distribution of (2.18 ± 1.11) m. There is some spread in the vertical separation of the GPS antennas as well. The mean vertical separation of the GPS antennas is distributed as (31.1 ± 0.5) m. The anomalous distribution in the figure that is labelled 'flight-to-flight variation' is due to the last four flights of the survey. When an in-line versus vertical separation distribution is made for these flights, the vertical separation and the error in the separation increases. The cause for this is not

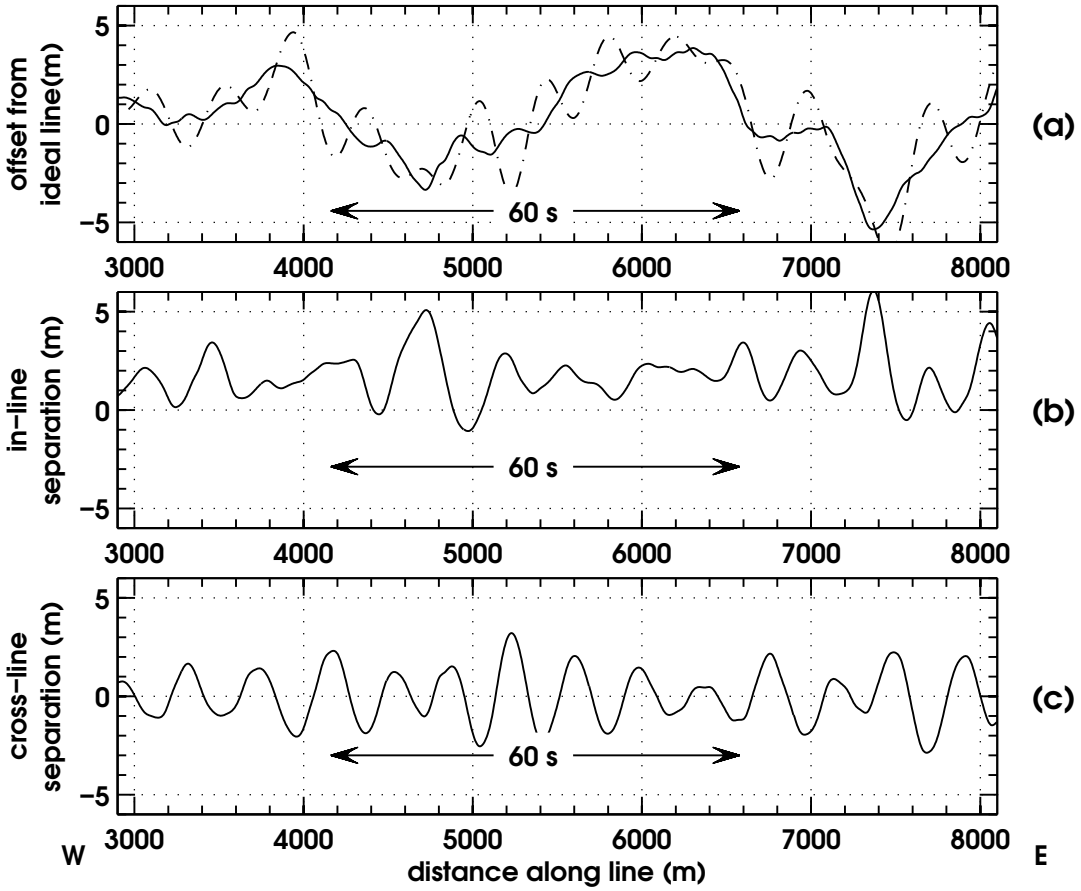

Figure 3.9: *Plan view of flight path of helicopter and towed bird GPS antennas along a segment of line 10591. (a) Offset of helicopter (solid) and towed bird (dashed) from ideal east-west line. Also marked is a 60 s interval. Motion of the towed bird relative to the helicopter hitching point can be most conveniently divided into two motions, oscillations that occur in the direction of flight (in-line) as shown in panel (b); and oscillations across the flight direction (cross-line) shown in (c). The motions are coupled; but they are not predictable from each other.*

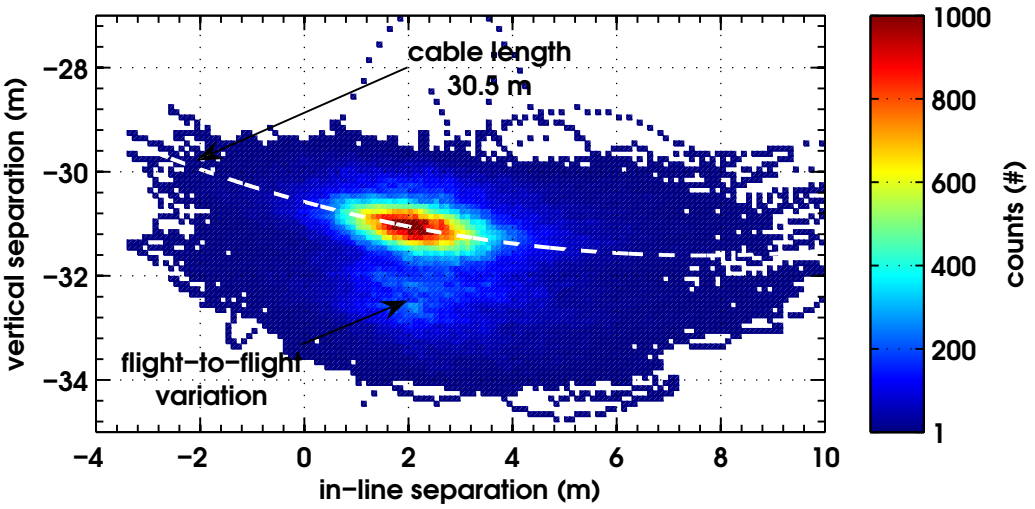

Figure 3.10: *Side-elevation view of the in-line positions of the bird GPS antenna relative to the helicopter GPS antenna for the Chowilla survey. The mean position of the towed bird GPS antenna is 2 m ahead of and 31 m below the GPS antenna of the helicopter. The bird oscillation follows a circle of radius 30.5 m centred on the hitching point of the helicopter (white line). The small peaks at the bottom of the distribution are possibly due to quantised 1 m errors produced when solving for vertical positions using GPS, and appear to be related to individual flights.*

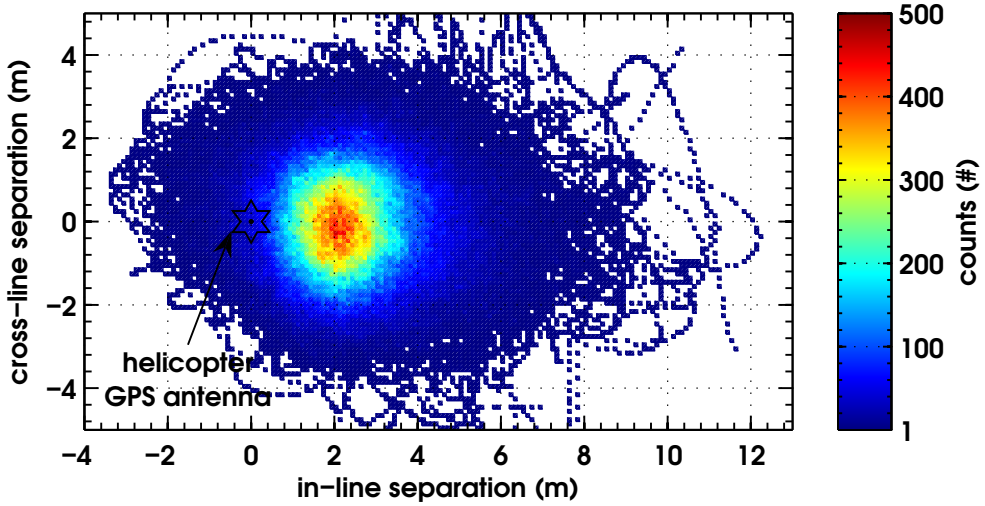

Figure 3.11: *Plan view of the distribution of the position of the GPS antenna of the bird in relation to the GPS antenna of the helicopter, for approximately 300 000 fiducial points (∼80 h). The bird GPS antenna clearly stays about 2 m directly in front of the helicopter GPS antenna, with 95% of the swings constrained to ±2 m in both the in-line and cross-line directions.*

known, but it could be due to errors in the vertical solution for one or both of the GPS antennas, a longer tow cable used for these flights, or a greater mean forward pitching of the towed bird during survey. The white line included in Figure 3.10 represents the path that the GPS antenna would make if the entire tow-cable bird system was rigidly mounted with no additional pitching of the bird allowed. The white line is an arc of a circle 30.5 m in radius, centred on the hitching point of the helicopter. The position of the helicopter hitch is estimated from photographs, see Appendix C.1.

Interestingly, the increased vertical offset of the GPS antennas has no great effect on their distribution in the in-line and cross-line directions. Figure 3.11 shows a plan view of the horizontal separation of the GPS antennas for all 300 000 plus data points. Although there is a large range of cross-line separations (-5 m to 5 m), the mean cross-line separation of the antennas is (0.0 ± 0.1) m, while its distribution is (0.0 ± 1.2) m. The mean cross-line and in-line separation of the GPS antennas must mark the point where the towed bird is expected to fly in a horizontal position beneath the helicopter, with both the transmitters and receivers a distance h above the ground and the laser altimeter pointing straight downwards to the earth. Any deviation from that point leads to pitching and rolling of the towed bird that affects the height of the transmitters and receivers, as well as the altitude measured by the laser altimeter. The radar altimeter, being attached to the undercarriage of the helicopter, is of course not affected.

Since the towed bird undergoes cross-line and in-line oscillations, it is important to consider their frequency. For every line in the survey, I divided the motion of the bird into in-line and cross-line motion, and measured the period of all oscillations. The distribution of the periods of oscillation are very well approximated by normal Gaussian curves, as shown in Figure 3.12. Using this analysis, the in-line and cross-line motions assume two statistically distinct mean periods of oscillation. For the in-line oscillation, the mean period is (8.97 ± 0.01) s, while the cross-line oscillation

has a mean period of (9.98 ± 0.01) s. Using basic physics (e.g. Fowles and Cassiday, 1993), with a constant drag force, the period of oscillation of a mass at the end of a rigid mounting is determined only by the vertical offset of the mass from the point of attachment. For the cases of in-line and cross-line motion, the vertical offset (helicopter to bird distance) of 30.5 m would lead to a simple pendulum period of 10.8 s. This period is larger than both the observed in-line and cross-line periods.

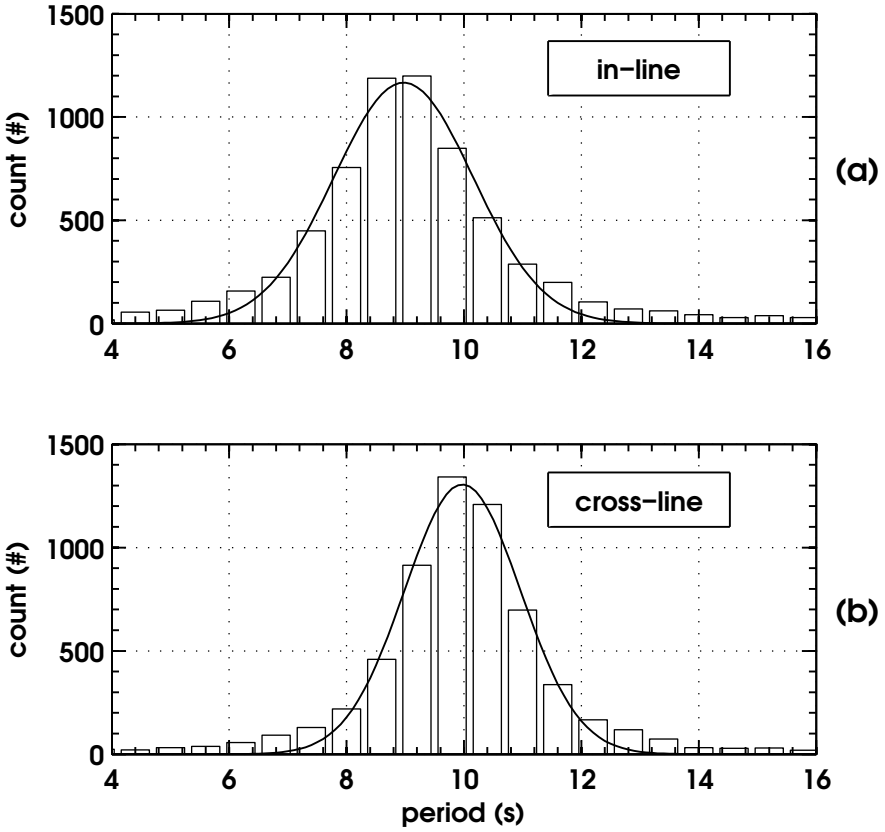

Figure 3.12: *Distribution of the periods of oscillation for the (a) in-line and (b) cross-line components of bird swing. In each, the histogram is superimposed by a fitted normal distribution. For the in-line oscillation, the distribution is (8.97± 0.35) s with a mean of (8.97± 0.01) s, while for the cross-line oscillation, the distribution is (9.98± 0.24) s, mean value of (9.98± 0.01) s.*

3.4.1 Radar Altimeter

Now that we have determined that the entire Chowilla dataset is subject to in-line and cross-line oscillations of different period, I will show its effect in the data. Figure 3.13 is a grid of β calculated from the 40 kHz in-phase and quadrature data using the radar altitude measured from the helicopter with a constant amount of 30 m subtracted from it. Bird swing is evident in this figure by "spottiness" in the value of β. On the map, β increases and decreases periodically over distances of about 320 m, consistent with a bird swing of 8 s at a speed of 40 m/s. Areas that should have consistent values of β, for example the dry lakes that are in the north (marked by an ellipse), clearly show periodic variation. On the NE side of the map is a small rectangle that is shown in more detail in the next figure.

Figure 3.14 is the detail of the small rectangle shown in Figure 3.13. It clearly shows the localised effect that bird swing has on the data. In this figure, white dots represent maximum forward swing of the towed bird in the in-line direction, while the black dots represent maximum backward swing. Since the towed bird is designed to be slung back while on survey, a forward swing brings it closer to the ground. The distance of separation of the receiver and image coil is less, thereby increasing the value of β. Conversely, a backward swing increases the height of the bird above the ground and reduces the value of β. This is shown in Figure 3.14 and is very clear for lines 10190 and 10210. Other lines in this figure show this clear relation between bird swing and β. In the next section, I will develop a model that shows how bird swing affects the calculation of β and devise a method of removing its effect from airborne data.

3.4.2 Laser Altimeter

Now I would like to discuss the other method of obtaining the altitude of the towed bird while it is on survey. Both RESOLVE and DIGHEM electromagnetic systems

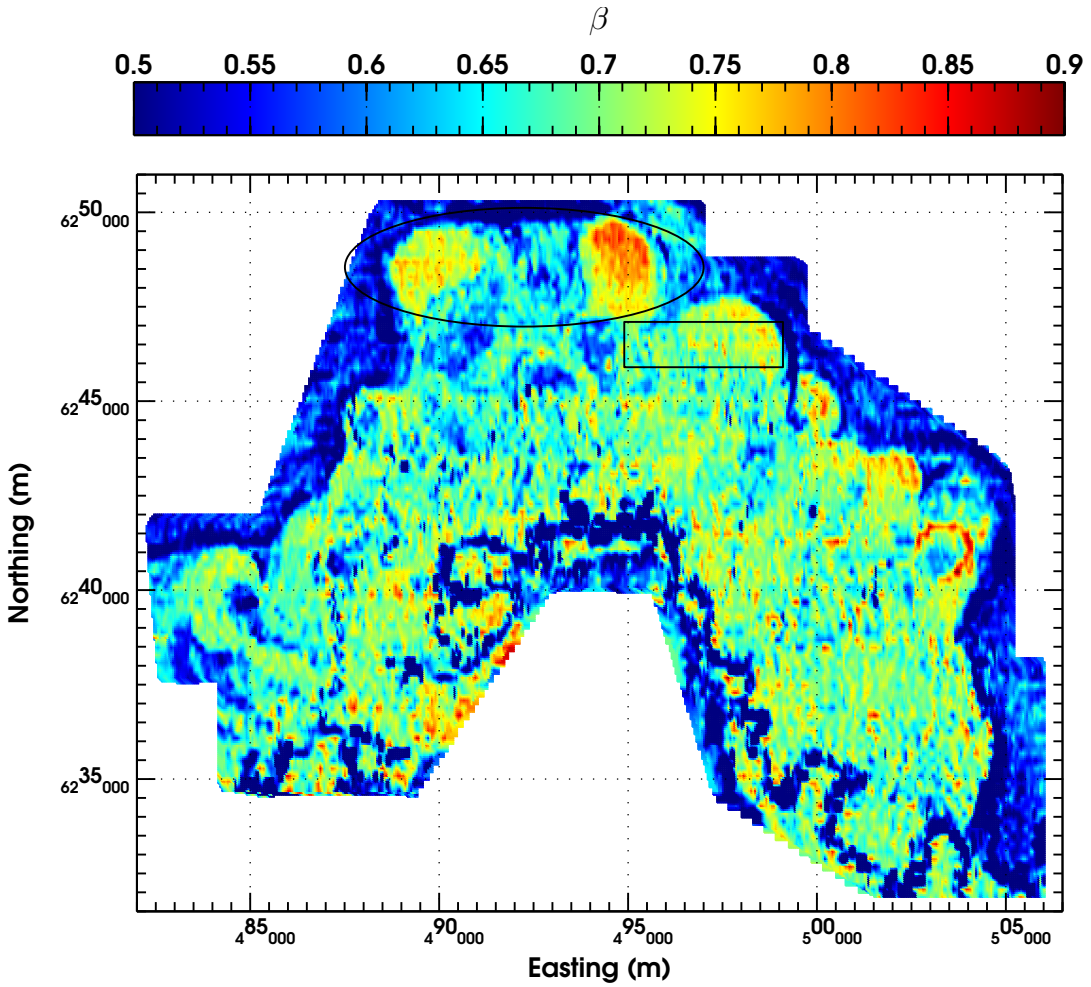

Figure 3.13: *Grid of β for the Chowilla Floodplain survey calculated from the 40 kHz in-phase and quadrature data. Flight direction is east-west and west-east. Bird swing is apparent in this graph from the "spottiness" in the data that is not coherent across flight lines.*

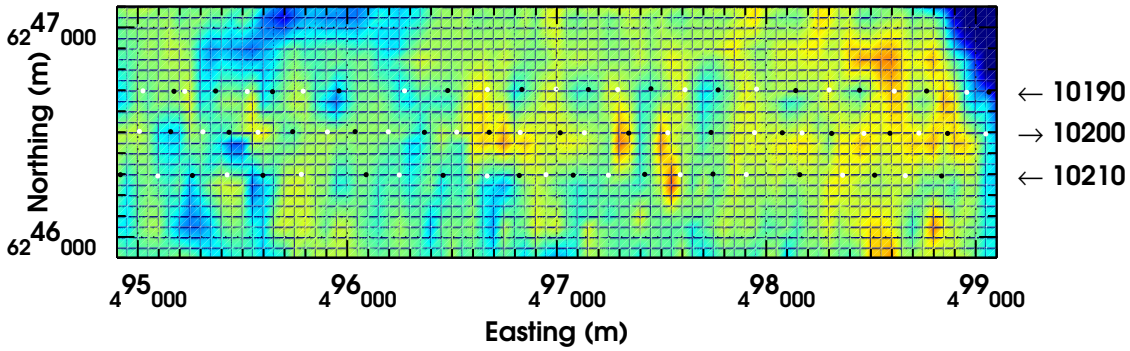

Figure 3.14: *Detail of the rectangle marked in the NE corner of Figure 3.13. Bird swing effect is clearly seen by increases and decreases in the value of β along lines. White dots represent the maximum forward in-line swing along the line, while black dots represent the maximum backward in-line swing. Line numbers and line direction are shown on the right-hand of the graph.*

frequently employ a laser altimeter mounted in the underside of the chassis of the towed system. This is pointed out in Figure C.3, the photo taken as the RESOLVE system is being lifted off the ground.

During an electromagnetic survey, the radar altimeter measures the altitude of the helicopter. The altitude of the bird is calculated by subtracting a constant amount of 30 m. The problem with this is that the bird swings during survey, which creates error in the altitude of the bird. The laser altimeter is designed to avoid this problem. It is mounted in the bird so that, when the bird is towed horizontally, the laser altimeter points directly down to the ground. As I have shown in this chapter, the bird pitches and rolls while it is being towed. When this happens, the laser altimeter measurement does not point vertically and its height is in error. Kratzer et al. (2007) call this error the slant range, and have successfully measured and corrected the slant range error in their test rig. I will discuss the laser altimeter error generated by system swing and give a correction for the altimeter reading based on measured pitch and roll.

The effect of bird swing on the laser altimeter largely arises due to the pitch and roll of the bird while it is on survey. Swinging of the tow cable, so long as it does not alter the attitude of the bird, will not affect the laser altimeter other than increasing or decreasing the actual altitude of the bird (which is precisely what we want to measure). For example, if the bird is swung back in an in-line swing, but somehow stays level during the swing duration, the measured altitude will accurately reflect the change. The value of β will not change because the decreased signal due to coupling will be compensated by the increased altitude. However, large values of bird pitch and roll (e.g. $>15^\circ$) will drastically affect measured altitude even though the coils may not change their separation from the ground very much. Evidence of this rotating motion can be seen in the data, and Figure 3.15 shows the grid of β calculated for the 40 kHz data using the laser altimeter. This grid is very similar to Figure 3.13, except that the overall value of β in Figure 3.13 is slightly lower

for the entire grid. This is most likely due to an overestimation error in the radar altimetry. Another, more significant difference between the two grids is in the value of β over the Murray River along the southern edges of the grid. The radar altimeter measures too large values of altitude near and over the Murray River which create abnormally low values of β. The laser altimeter, by contrast does not create this error. Since the altimeter error occurs near the edge of the Murray River, it may be due to the canopy effect discussed by Beamish (2002) and also by Brodie and Lane (2003). When looking at the laser and radar altimeter digital elevation maps near the edges of the Murray River, the difference between them is at times greater than 20 m. Brodie and Lane (2003) report canopy effect differences on the order of 6–10 m; so the differences seen here may be a new altimeter error, and I will discuss this in the next section.

As before, I have included a small detail of Figure 3.15 that shows a small section of the grid and the correlation between bird swing and β calculated with the laser altimeter. White dots in Figure 3.16 represent the maximum forward in-line swing of the towed bird, while black dots represent the maximum backward in-line swings. In general, forward swings are associated with increased values of β, while backward swings tend to decrease it. The relationship between swings and β using the laser altimeter is similar to, though not as obvious as, the relation between bird swing and β using radar altimetry.

3.4.3 Problems With Altimetry

As I mentioned in the last section, there is a discrepancy between the laser and radar altimetry near the Murray River along the southern edges of the grid in Figure 3.15. This can be most easily seen by a comparison of digital elevation maps (DEMs) computed using laser and radar altitudes. The method of computing a DEM is simple, as shown schematically in Figure 3.17. The height of the towed bird above the WGS84 ellipsoid is given by the bird's vertical GPS position h_{GPS}. The altitude

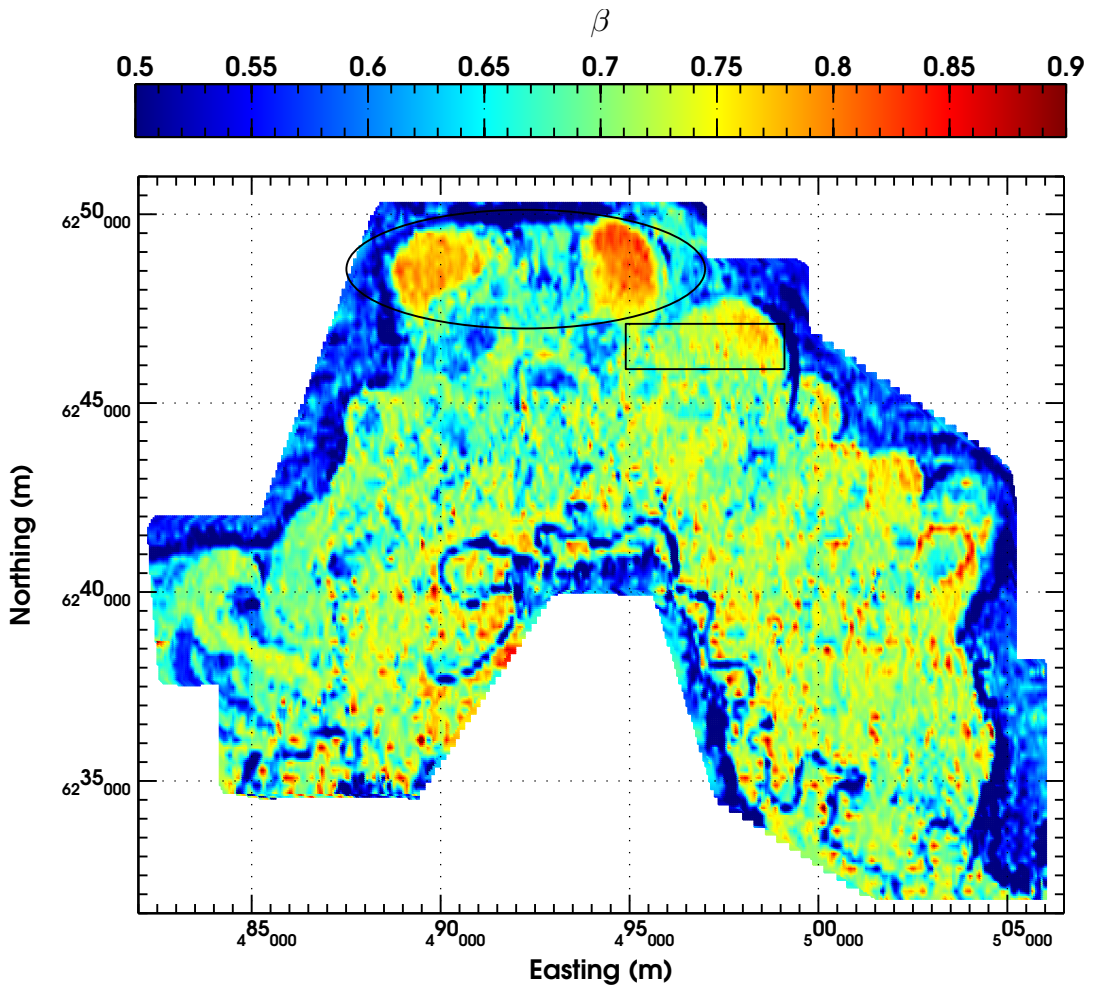

Figure 3.15: *Grid of β for the Chowilla Floodplain survey calculated from the 40 kHz in-phase and quadrature data using laser altimeter. The result is similar to the gridded data in Figure 3.13, with bird swing clearly evident in the data.*

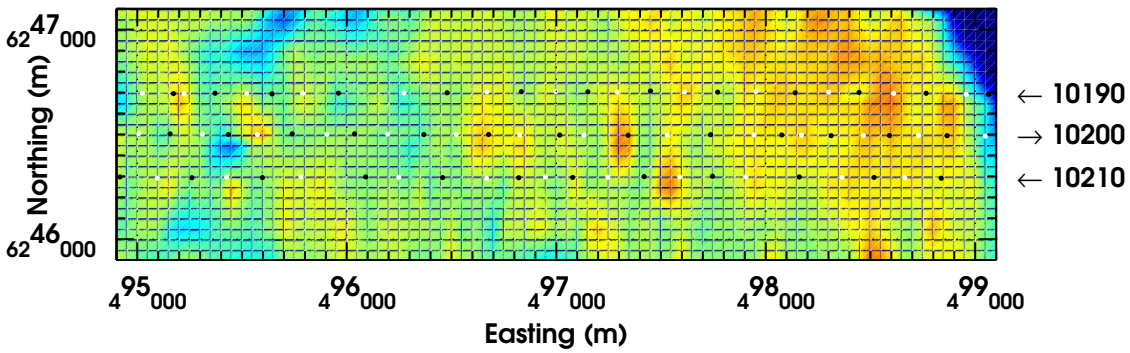

Figure 3.16: *Detail of the rectangle marked in the NE corner of Figure 3.15. Bird swing is again clearly evident in data along lines. White dots represent the maximum forward in-line swing along the line; black dots represent the maximum backward in-line swing.*

of the bird can be estimated from two different sources: laser h_l or radar h_r altimetry. The difference between GPS height above the ellipsoid and the measured altitude is the elevation of the surface of the earth above the ellipsoid. For laser altimetry, the DEM value at each fiducial is:

$$E_l = h_{GPS} - h_l, \tag{3.7}$$

where E_l is the elevation of the surface of the earth using the laser altimeter. Similarly, the elevation E_r of the surface of the earth above the ellipsoid, as measured with the radar altimeter is

$$E_r = h_{GPS} - h_r + 30 \text{ m}, \tag{3.8}$$

where a constant amount of 30 m is added to account for the fact that the radar altimeter is attached to the helicopter.

Figures 3.18 and 3.19 show the DEMs for the Chowilla Floodplain using the laser altimeter (equation (3.7)) and the radar altimeter (equation (3.8)), respectively. There is an obvious discrepancy between the two inside the area defined by the polygon shown on the southern edges of the grid, with differences between the laser and radar altimeter DEM calculations on the order of 20 m. The laser altimeter DEM in Figure 3.18 is reasonable, with the river being only a few metres below ground level. Figure 3.19 shows that sections of the river—or the river's edge—are 20 m above ground level. This error is either a result of 'canopy effect' (Brodie and Lane, 2003) due to trees near the river edge, or another source of error that is due to the river itself. I call this the 'watercourse effect' because it appears to occur only above and on the edges of the river, and is consistently larger in magnitude than 10 m. In the next chapter, I will show two other grids that display similar error in the DEM calculations. Again, these errors are present near bodies of water.

Regardless of which altimeter is chosen to transform airborne EM data into the $\phi\beta$ domain, it is important that the altitude used is accurate. In this section, I

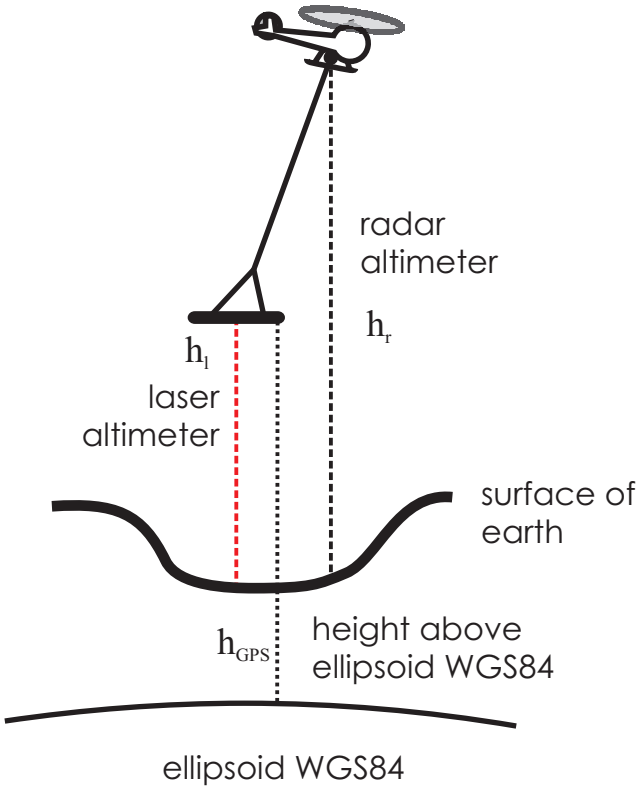

Figure 3.17: *Schematic for computing a digital elevation map (DEM) using bird GPS position (height above a reference ellipsoid) and measured altitude. Two maps can be produced: one using laser altimetry and one using radar altimetry.*

have shown that there are large differences between laser and radar altimeters along and around watercourses. Since β greatly depends on measured altitude, these differences will be readily apparent; which indeed they are around the Murray River in Figures 3.13 and 3.18.

3.5 Summary and Conclusion

I have introduced the topic of pendulum-like motion of the RESOLVE and DIGHEM survey instruments. I have shown that bird swing adds a fair amount of spurious information to the data collected using towed birds. I have chosen these systems not because they are particularly prone to bird swing, but rather because they have received a great deal of attention for land management (Coppa et al., 1998; George et al., 1998; de Broekert, 1996) and seawater bathymetry (Vrbancich, Fullagar and

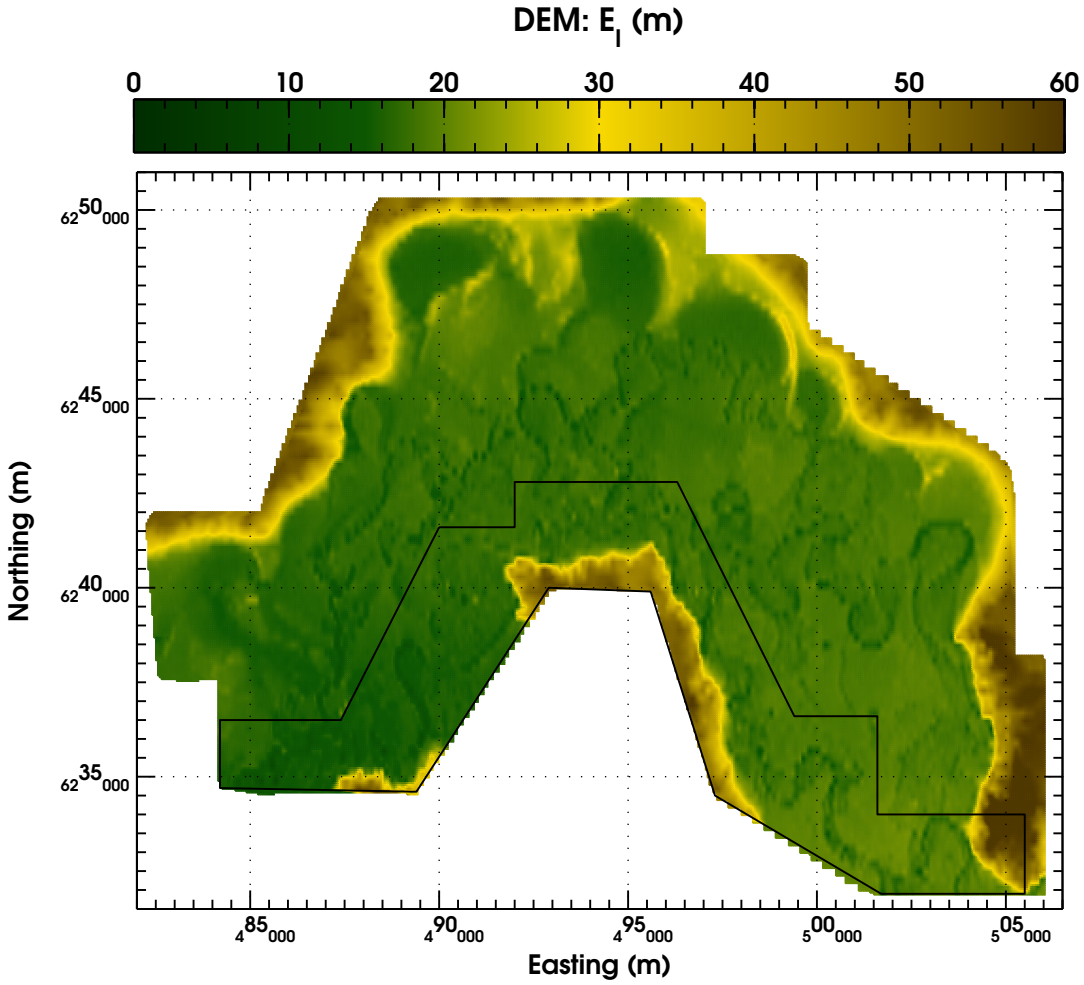

Figure 3.18: *Digital elevation map of Chowilla Floodplain calculated using the laser altimeter mounted in the underside of the towed bird (equation (3.7)). A large polygon is drawn along the southern edges of the figure to compare with the DEM using the radar altimeter (cf. Figure 3.19)*

.

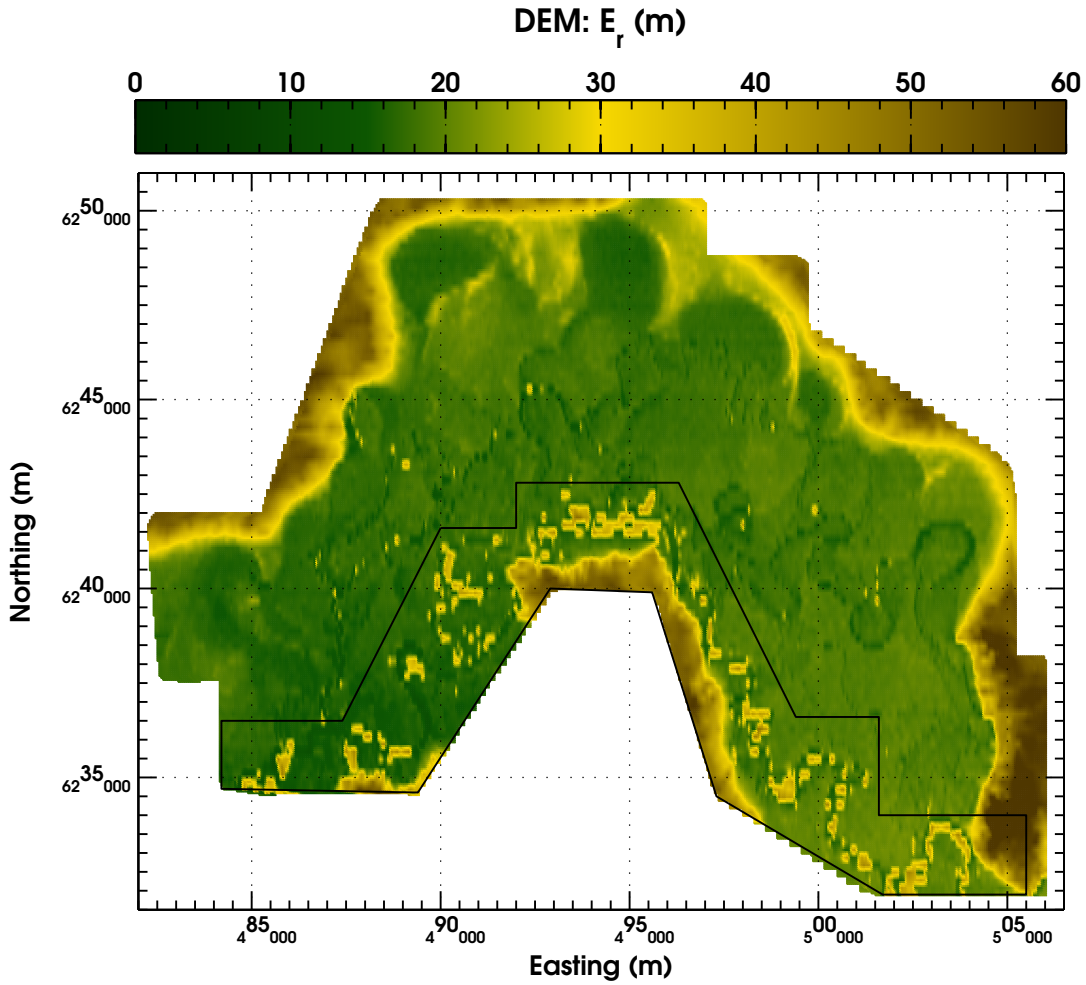

Figure 3.19: *DEM of Chowilla survey calculated using radar altimeter mounted on the underside of the helicopter (equation 3.8). The area inside the large polygon clearly shows the error in radar altimetry caused near and over the Murray River. Differences between the laser DEM and this one are on the order of 20 m.*

Macnae, 2000) in Australia, and I have been fortunate enough to obtain data sets from the CSIRO and DSTO. Bird swing that displays pendulum-like motion will result in every AEM system that employs a towed object (transmitter *or* receiver) to measure response.

When looking for systematic changes in the system response caused by altitude error or geometric coupling error, transforming the AEM data to the $\phi\beta$ domain is particularly useful. Essentially, transforming AEM data to β brings the data to a conductivity and frequency independent domain that compares the actual measured signal to what the signal should be if the earth was infinitely conductive. In that sense, then, β is an excellent tool for making comparisons based on geometric coupling. The utility of the β transformation has been exploited in this chapter to give unquestionable evidence that bird swing affects electromagnetic data. In turn, the information that we derive from the data such as apparent resistivity (conductivity) and apparent depth are affected by bird swing. This leads to consequent error in interpretation and is a particular problem when making conductivity predictions for land management. Electromagnetic data recorded at high frequency is most affected by geometric and altimeter error. Unfortunately, this corresponds to errors in near surface information: precisely in the area of greatest interest to land management.

So far, I have shown that bird swing is evident in AEM data regardless of whether a radar or laser altimeter is used for altitude determination. In the Chowilla Floodplain survey, I showed that repetitious changes in β are related to in-line bird swings that can be predicted from simultaneous measurement of helicopter and towed bird position. Horizontal separations in measured GPS antenna positions accurately reflect real swings of the towed bird relative to the helicopter. This was supported by video evidence when I measured the horizontal GPS separation through a manual picking routine. In the Sydney Harbour dataset, bird swing is the only physical occurrence that can affect the high frequency data so drastically as to cause an almost 10% change in β over sea water. Now that bird swing has been established, we must

strive to understand how it affects the data and, if possible, how its effects may be corrected. This is the subject of the next chapter.

Chapter 4

Modelling Bird Swing in AEM Systems

4.1 Introduction

In the last chapter I advanced the idea of bird swing and how it affects the measured response of an AEM system when it is on survey. I then established a link between observed fluctuations in the derived value of β and the actual, measured swinging of the towed bird. In this chapter I will create models of synthetic data and discuss how bird swing affects both actual and measured altitudes as well as the geometric coupling of the transmitting and receiving coils with the earth. As a first order correction for bird swing in historical data, I will derive some filters that correctly and efficiently remove bird swing artifacts from historical data. I will also present a method of correcting β based on measured pitch and roll of the bird and the physical dimensions of the towed object. The reason why I chose to focus on in-line rather than cross-line swings in Chapter 3 will be fully explained.

In studying the RESOLVE and DIGHEM^{VRES} systems, I have observed four dominant motions of oscillation. The first two come directly from the swinging of the main tow cable. This swing has both pitch and roll rotations that move the bird

fore-and-aft and side-to-side relative to the helicopter towing it. These motions were proven to exist in Section 3.4. The other two motions come from pitching of the towed bird about the point where the tow cable splits to a 'Y', resulting in further fore-and-aft motions, and a tube roll: a rolling motion of the towed bird about its main axis of symmetry. Their effect on AEM data is slightly less than cable swing, but is still present. In the first section of this chapter, I develop a model of bird swing and describe how it generalises the geometric coupling of the system to the earth in the inductive limit. All four types of motion are analysed and their relative effect is discussed. In Section 4.3, I develop a filter that corrects and removes bird swing error from the data when a radar altimeter is used to calculate ground clearance of the towed bird.

If the rigid chassis of the towed bird has some means of measuring its altitude above the earth, such as a rigidly mounted laser altimeter, then the range of the altimeter will have error in apparent height as a result of bird swing. This is the subject of Section 4.4, when I construct a model for the laser altimeter mounted in the underside of the RESOLVE system chassis and show how it too affects the measured response. I then develop a filter that removes bird swing from the measured response when using a laser altimeter to measure bird altitude.

In Section 4.6, I will give evidence of both cable swing and bird pitch from high-resolution photographs taken when the RESOLVE system was flown on survey in the Sunraysia district surrounding Mildura, Victoria. Finally, I will show that the RESOLVE system geometry can be modelled and its various pendulum-like motions could be roughly predicted if designing a new system.

4.2 Bird Swing Model: Radar Altimeter

Now that a relation between bird swing and β has been established, I will devise a model that attempts to explain how β changes with bird swing. Pitch of the bird

is defined as a rotation of the bird about an axis that runs parallel to the earth and through a diameter of the bird when viewed from above. A bird pitch will force the nose to move up or downwards. Roll is defined as a rotation of the bird through its central axis: an axis that runs down the length of the cylindrical body. A towed bird's geometric coupling to the earth can be changed in two ways: swinging of the main tow cable (thereby altering the altitude of the bird), and independent pitching and rolling of the towed bird (which alters the actual transmitter altitude for pitch, but not for roll). These two movements are not necessarily of the same frequency: in the Chowilla dataset, the in-line and cross-line oscillations measured represented movement of the bird relative to the helicopter, but we could not say anything about the pitching of the bird itself. The Sydney Harbour data showed high frequency oscillations of β that were superimposed on cable swing, but I have not yet linked those oscillations to bird pitch. Using G the geometric coupling coefficient of equation (3.5), we can generalise the calculation of β to include changes in both the height of the towed bird (h) and the geometric coupling of the receiver coil to the inductive limit image.

For an airborne survey that uses the helicopter-mounted radar altimeter for bird altitude, the contractor typically subtracts a constant amount of $\sim$30 m from the measured altimeter value. The difference is considered to be the altitude of the bird. Clearly, any sort of bird swing will result in an error in the calculation of bird altitude. Figure 4.1 shows a schematic of bird swing caused by the movement of the cable, similar to that measured in the last section. The backward in-line swing shown in this figure raises the bird from h_0 to altitude h. A forward swing lowers the bird so that $h_0 > h$.

The simplest way to mathematically describe the rotation of a vector is through the use of matrix multiplication in the manner described by Fitterman and Yin (2004). The matrix R that describes the rotation acts like an operator on a vector

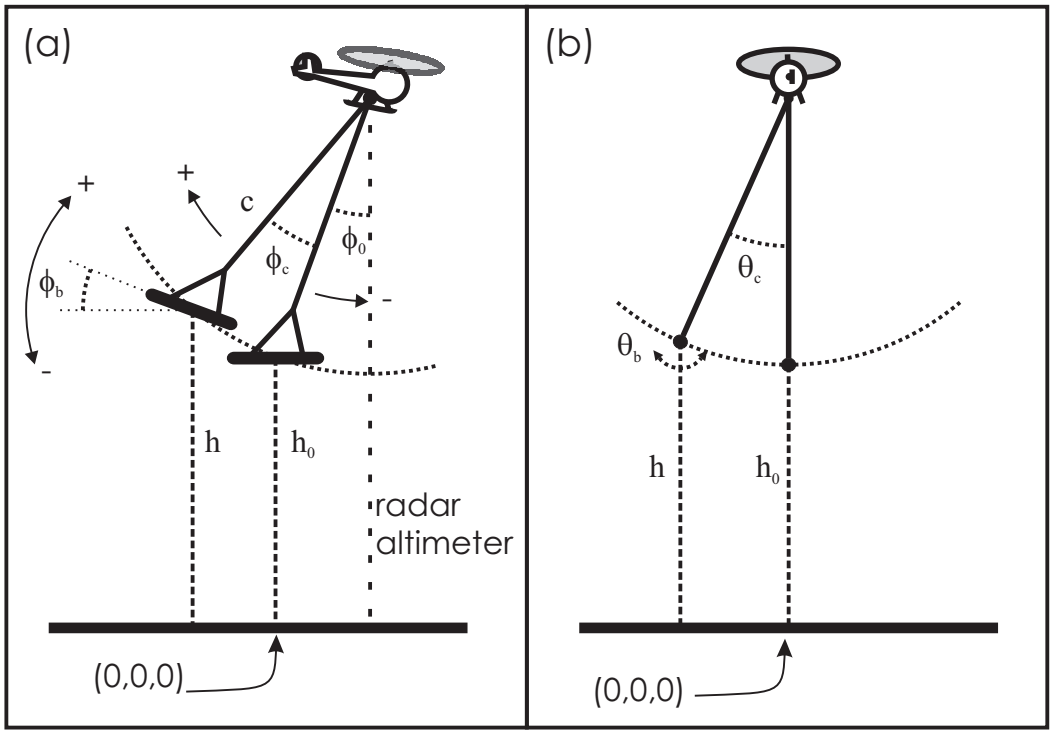

Figure 4.1: *Schematic of (a) fore-to-aft and (b) side-to-side bird swing caused by swinging of the cable. h_0 is the nominal altitude of the bird calculated from the radar altimeter mounted on the underside of the helicopter. In panel (a), h is the actual altitude of the bird caused by swinging the cable through ϕ_c. The bird can also pitch ϕ_b about its hitching point. In panel (b), the cable gets swung side-to-side through angle θ_c, and the bird can rotate through angle θ_b.*

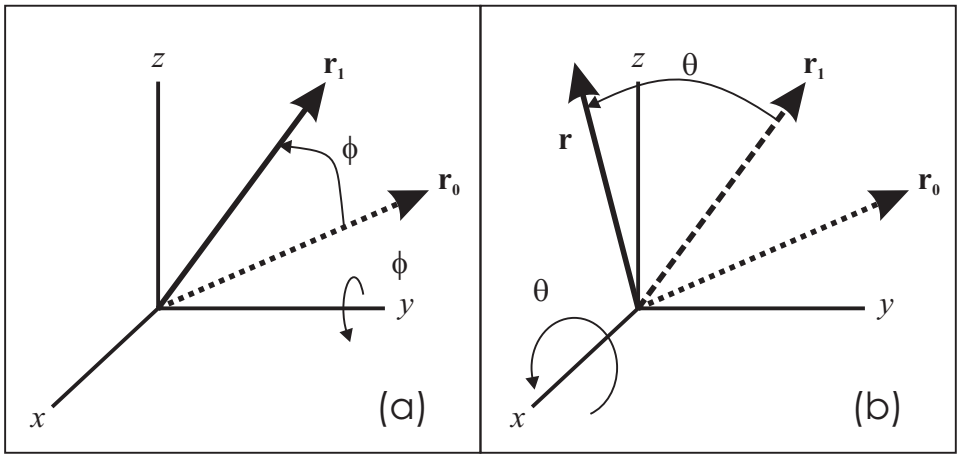

Figure 4.2: *Vector $\mathbf{r_0}$ gets rotated by matrix R: first by a pitch, then by a roll. The pitch is a rotation of angle ϕ about the y-axis (a). The roll is a rotation of angle θ about the x-axis in a counter-clockwise fashion when viewed down the axis (b). The resulting vector is $\mathbf{r}$.*

$\mathbf{r_0}$ in the following way:

$$R(\theta, \phi)\mathbf{r_0} = \mathbf{r}. \tag{4.1}$$

I define R by a pitch rotation R_{pitch} of angle ϕ about the y-axis, followed by a roll rotation R_{roll} of angle θ about the original x-axis (i.e. long axis of the bird). This is shown in Figure 4.2. The total rotation is a product of the two:

$$R(\theta, \phi) = R_{roll}\, R_{pitch},$$

and acts on the vector $\mathbf{r_0}$ from the left (i.e. pitch first, then roll).

The matrix for pitch R_{pitch} is expressed as

$$R_{pitch}(\phi) = \begin{pmatrix} \cos(\phi) & 0 & \sin(\phi) \\ 0 & 1 & 0 \\ -\sin(\phi) & 0 & \cos(\phi) \end{pmatrix},$$

while R_{roll} is defined as

$$R_{roll}(\theta) = \begin{pmatrix} 1 & 0 & 0 \\ 0 & \cos(\theta) & -\sin(\theta) \\ 0 & \sin(\theta) & \cos(\theta) \end{pmatrix},$$

so that R becomes

$$R(\theta, \phi) = \begin{pmatrix} \cos(\phi) & 0 & \sin(\phi) \\ 0 & 1 & 0 \\ -\sin(\phi) & 0 & \cos(\phi) \end{pmatrix} \begin{pmatrix} 1 & 0 & 0 \\ 0 & \cos(\theta) & -\sin(\theta) \\ 0 & \sin(\theta) & \cos(\theta) \end{pmatrix},$$

which simplifies to

$$R(\theta,\phi) = \begin{pmatrix} \cos(\phi) & 0 & \sin(\phi) \\ \sin(\phi)\sin(\theta) & \cos(\theta) & -\cos(\phi)\sin(\theta) \\ -\sin(\phi)\cos(\theta) & \sin(\theta) & \cos(\phi)\cos(\theta) \end{pmatrix}. \tag{4.2}$$

This general calculation of rotation can be used for the various motions of the tow cable and bird when it is on survey. Each motion can be considered independently, starting with the fore-to-aft and side-to-side swinging of the tow cable.

4.2.1 Swinging of the Tow Cable

In one common example, the length of the cable that attaches the towed bird to the helicopter is $c = 30.5$ m. As mentioned before, the bird is attached so that it is approximately horizontal while it is flown on survey. This is easily seen in Figure C.3 of Appendix C, which is a photo taken as the bird is lifted off the ground. Let us say that during survey, the cable is swung back so that most of the time it makes angle $\phi_0 = 20°$ with the vertical, shown in Figure 4.1a. Let us temporarily place the origin at the hitching point of the helicopter. The vector $\bar{\mathbf{c}}$ that describes the mean survey position of the bird is

$$\bar{\mathbf{c}} = R(0,\phi_0)(0\,\hat{\mathbf{i}} + 0\,\hat{\mathbf{j}} - c\,\hat{\mathbf{k}}),$$

which becomes, with $c = 30.5$ m and $\phi_0 = 20°$,

$$\bar{\mathbf{c}} = (-10.4\,\hat{\mathbf{i}} + 0\,\hat{\mathbf{j}} - 28.7\,\hat{\mathbf{k}})\,\text{m}.$$

I apply a transformation so that the origin is exactly 30 m beneath the bird in its mean survey position. In Figure 4.1, the distance h_0 is 30 m, and the radar altimeter

reads 58.7 m. The vector $\mathbf{h}$ from the origin to the helicopter hitch is

$$\mathbf{h} = (10.4\,\hat{\mathbf{i}} + 0\,\hat{\mathbf{j}} + 58.7\,\hat{\mathbf{k}})\,\mathrm{m},$$

so that the vector from the origin to the centre point of the bird after any pitching or rolling of the cable is

$$\mathbf{b} = \mathbf{h} + R(\theta_c, \phi_c)\bar{\mathbf{c}}, \tag{4.3}$$

where ϕ_c and θ_c are the pitch and roll of the cable at the hitching point on the helicopter.

In this configuration, any fore-to-aft swinging of the cable will raise and lower the bird. Side-to-side swinging will always raise it. The altitude h of the bird after any roll and swing will therefore be the $\hat{\mathbf{k}}$ component of vector $\mathbf{b}$, namely

$$h = (58.7 + 10.4\sin(\phi_c)\cos(\theta_c) - 28.7\cos(\phi_c)\cos(\theta_c))\,\mathrm{m}. \tag{4.4}$$

The new altitude h affects the coupling of the coils in the towed bird by changing their separation from the earth; this in turn affects β. Let us explore what happens to the system response and β when the bird swings and we are using the radar altimeter to measure altitude. When the bird swings back in Figure 4.1a, the response of the system must decrease because the bird is moved away from the earth. We do not perceive that the altitude has changed because we are actually measuring the separation of the helicopter from the earth. This implies that G must stay the same. Therefore, β must decrease as the bird is swung back.

The situation is the reverse when the bird is swung forward. The separation of the bird from the earth decreases, so $\frac{T^2}{R}$ in equation (3.6) increases while G stays the same, thereby increasing β.

We can predict how β changes in the following way. The response ratio $\frac{T^2}{R}$ is modelled using equation (3.5) with the altitude h computed in equation (4.4). This

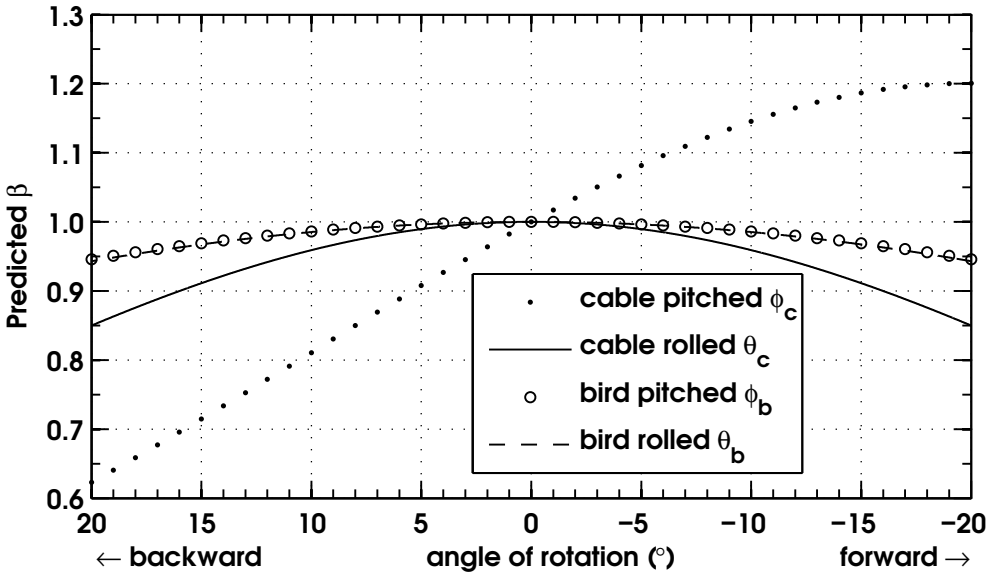

Figure 4.3: *Prediction of changes in β due to swinging of the tow cable and bird. The line marked by dots is due to fore-to-aft swinging of the tow cable with the bird remaining horizontal. The solid line is due to side to side swinging of the tow cable, bird horizontal. For the line marked with open circles, the bird pitches about its mid point. The dashed line is due to rolling the bird about its main axis.*

value is divided by $G_{nominal}$, the geometric factor that we expect from the bird at an altitude of 30 m. The result is β affected by bird swing. Figure 4.3 shows the effect of fore-to-aft swinging of the tow cable while the bird remains horizontal. Positive values of ϕ_c swing the tow cable to the aft while negative values swing the tow cable to the fore (cf. Figure 4.1). The ordinate is the ratio of the inductive limit response at the height h to the geometric factor $G_{nominal}$ of a horizontal bird at the nominal height of 30 m. From this figure, it is clear that forward swings increase β: backward swings decrease it. This is consistent with the relation between β and bird swing found in Chowilla (Section 3.4.1). Notice that in this figure, I have reversed the direction of the x-axis to make it appear more intuitive when comparing these results to the schematic in Figure 4.1a.

A different result is achieved when the cable swings from side to side. We allow only θ_c to change in Figure 4.1b. During this rotation, the transmitter and receiver coils are assumed to remain horizontal, and that the motion does not cause the bird

to tube roll about its central axis. The altitude of the bird for all side-to-side swings always increases, so the system response always decreases. Hence, our modelled β must also decrease. This is shown by the solid black line in Figure 4.3, where a tow cable roll of 20° causes a 15% decrease in β.

4.2.2 Pitch and Roll of the Bird

We can now generalise the motion of the bird to allow it to pitch about the centre point. This motion can be considered independently of changes in the altitude of the towed bird caused by cable swing. Rolling about the central axis of the bird body does not at all change its altitude: however, both rotations change the coupling of the transmitter-receiver pair to the earth. In panel (a) of Figure 4.1, I have shown the motion caused by bird pitch. In this figure, positive values of ϕ_b tilt the nose of the bird down while negative values tilt it upwards. For the example discussed here, the cable is in the mean position and the bird is allowed to pitch so that its centre nominal altitude of $h_0 = 30$ m, even though the transmitter and receiver are not.

The vector position of the transmitter is calculated by first finding the position of the centre of the bird. In this case it is 30 m above the origin, but in general it is the position given by vector $\mathbf{b}$, equation (4.3). The transmitter and receiver are separated by a distance d, so that the vector from the centre point to the transmitter, $\mathbf{t_0}$, is

$$\mathbf{t_0} = \Big(\frac{d}{2}\,\hat{\mathbf{i}} + 0\,\hat{\mathbf{j}} + 0\,\hat{\mathbf{k}}\Big).$$

After a pitch of angle ϕ_b, the transmitter vector is

$$\mathbf{t} = R(0, \phi_b)\mathbf{t_0},$$

which, after using equation (4.2) becomes

$$\mathbf{t} = \Big(\frac{d\cos(\phi_b)}{2}\,\hat{\mathbf{i}} + 0\,\hat{\mathbf{j}} - \frac{d\sin(\phi_b)}{2}\,\hat{\mathbf{k}}\Big).$$

The altitude of the transmitter is then the $\hat{\mathbf{k}}$ component of $\mathbf{t}$ plus h_0, i.e.

$$h = \Big(h_0 - \frac{d\sin(\phi_b)}{2}\Big). \tag{4.5}$$

The altitude of the receiver is h_0 minus the $\hat{\mathbf{k}}$ component of $\mathbf{t}$.

Pitch and roll of the bird alters the orientation of the dipole moment of the transmitter and receiver. We must generalise Figure 3.1 and equation (3.5) to account for these changes. The normal HCP pair consists of a transmitter and receiver pointing in the $\hat{\mathbf{k}}$ direction. After rotations of ϕ_b and θ_b, the transmitter will point in the direction of $\hat{\mathbf{r}}_{\mathbf{Tx}}$:

$$\hat{\mathbf{r}}_{\mathbf{Tx}} = R(\theta_b, \phi_b)(0\,\hat{\mathbf{i}} + 0\,\hat{\mathbf{j}} + 1\,\hat{\mathbf{k}}),$$

which can be expressed as

$$\hat{\mathbf{r}}_{\mathbf{Tx}} = \sin(\phi_b)\,\hat{\mathbf{i}} - \cos(\theta_b)\sin(\theta_b)\,\hat{\mathbf{j}} + \cos(\phi_b)\cos(\theta_b)\,\hat{\mathbf{k}}.$$

The receiver points in the same direction. The image of the transmitter in the earth has its $\hat{\mathbf{k}}$ component reversed in sign so that it points to

$$\hat{\mathbf{r}}_{\mathbf{image}} = \sin(\phi_b)\,\hat{\mathbf{i}} - \cos(\theta_b)\sin(\theta_b)\,\hat{\mathbf{j}} - \cos(\phi_b)\cos(\theta_b)\,\hat{\mathbf{k}}.$$

The orientation of the transmitter, receiver and image after rotations is shown in Figure 4.4.

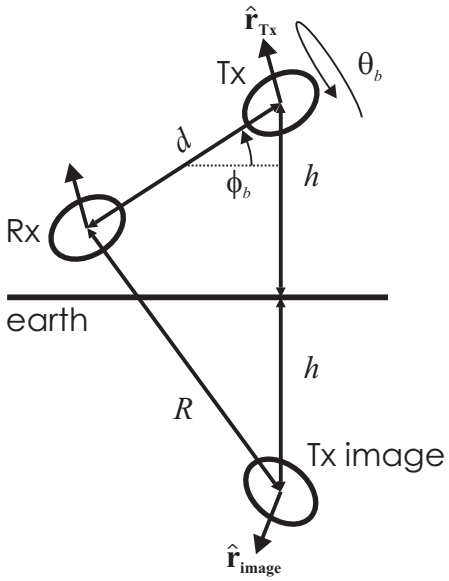

Figure 4.4: *Generalised method of images used to estimate the coupling coefficient at the inductive limit for a dipole pair above a conductive half space or thin sheet. The coil pair has been subject to pitch of ϕ_b and roll of θ_b. This changes the altitude h and the direction of the image dipole.*

We can now generalise the geometric factor G of equation (3.5) with the help of Figure 4.4 in order to predict how β changes with bird rotations. The distance of separation between the transmitter and receiver is still d, and the mutual inductance between them is still the mutual inductance of an HCP pair, equation (2.49). The image and receiver dipoles are now rotated and the distance between them has changed. The distance h in Figure 4.4 is the altitude calculated in equation (4.5), and the distance R is

$$R = \sqrt{{h_0}^2 + d^2 \cos^2(\phi_b)}.$$

The unit vector from the image to the receiver $\hat{\mathbf{r}}$ is

$$\hat{\mathbf{r}} = \frac{1}{R}(-d\cos(\phi_c)\,\hat{\mathbf{i}} + 0\,\hat{\mathbf{j}} + 2h_0\,\hat{\mathbf{k}}).$$

The mutual inductance M_{IR} between the image and the receiver is calculated using equation (2.48), where $\mathbf{a_1} = {a_1}^2\ \hat{\mathbf{r}}_{image}$, $\mathbf{a_2} = {a_2}^2\ \hat{\mathbf{r}}_{Tx}$ and $r = R$. The result is

given below:

$$M_{IR} = -\frac{{a_1}^2{a_2}^2}{\left(d^2\cos^2(\phi_b) + 4{h_0}^2\right)^{5/2}}\Big(d^2\cos^2(\phi_b)\big(3\cos^2(\phi_b) - 2\cos^2(\theta_b) - 2\big) + 4{h_0}^2\big(1 + \cos^2(\phi_b)\cos^2(\theta_b)\big)\Big).$$

The inductive limit geometric factor is the ratio of M_{IR} to M_{HCP} multiplied by 10^6:

$$G = \frac{10^6 d^3}{\left(d^2\cos^2(\phi_b) + 4{h_0}^2\right)^{5/2}}\Big(d^2\cos^2(\phi_b)\big(3\cos^2(\phi_b) - 2\cos^2(\theta_b) - 2\big) + 4{h_0}^2\big(1 + \cos^2(\phi_b)\cos^2(\theta_b)\big)\Big). \quad (4.6)$$

This is a general solution for the geometrical factor of a towed bird that is subject to an arbitrary pitch and roll. In this calculation, the bird is rotated about the centre point for pitch, and is rotated about the central or body axis for roll. The altitude h_0 is the instantaneous altitude of the centre of the bird.

Looking back to Figure 4.3 we see the effect of pitching the bird about its centre point with the centre of the bird held at 30 m (open circles). In this figure, positive rotation represents downward pitching of the nose of the bird, consistent with Figure 4.1. It is interesting to note that bird pitch always reduces G from the nominal horizontal coplanar value, so that β for a pitched bird is always less than β for a horizontal bird at the same altitude. This is because of the cosine-squared coupling of ϕ_b with G; and is controlled by the principle of reciprocity. If the transmitter is brought closer to the earth, the receiver is taken further away. The coupling would be the same if the transmitter was taken further away from the earth and the receiver was brought closer. Interestingly, roll is also cosine coupled to G. Any roll of the bird about its central axis reduces the coupling of the receiver to the image source. The effect is almost exactly alike for both motions as shown by the open circles and dashed line in Figure 4.3.

Figure 4.3 shows that altitude effect created by cable swing causes the greatest change to β. Fore-to-aft swings of only 20° can increase the value by 20% and decrease it by 40%. Side-to-side or cross-line swings have the next greatest effect, always reducing the coupling coefficient. Centre point pitching and tube rolling of the bird also reduce β, though to a far lesser extent.

4.2.3 Synthetic Examples of Rotation

In order to illustrate the principle of bird swing effect, I present some synthetic data for in-line (fore-to-aft) swings, cross-line (side-to-side) swings, bird pitch, bird roll, and a combination of in-line swing mixed with bird pitch. Both the in-line and cross-line swings have amplitudes of 3 m, consistent with some of the large swings seen in the Chowilla dataset. The period of oscillation of these swings is 9 s. The bird is made to pitch and roll 10° about its equilibrium point with a period of 2 s. The nominal altitude is survey altitude: 30 m. Figure 4.5 shows a prediction of how β changes with bird and cable swing. As seen from the figure, in-line cable swing has the greatest effect to the synthetic data. The swing both increases and decreases β. Bird pitch and bird roll have the next greatest effect, but note that the amplitude of these oscillations is 10°, twice that of the cable swings. The time scale on the main part of this figure makes it difficult to show the cosine-squared effect of bird pitch and roll, so I included a zoom-in of bird pitch in a smaller panel. The last section of the figure is an example of both in-line cable swing and bird pitch superimposed. This is shown in finer detail in Figure 4.6, so that both cable swing and bird pitch may be more finely examined.

Figure 4.6 is remarkable because it shows variation in synthetic β that is strikingly similar to the long and short period oscillations seen in Figure 3.6, when I was discussing Sydney Harbour data. This is strong evidence that supports my earlier claim that the short 1 s period variations in β over sea water are caused by 2 s pitches of the towed bird on survey. Furthermore, the 9–10 s oscillations in β are re-

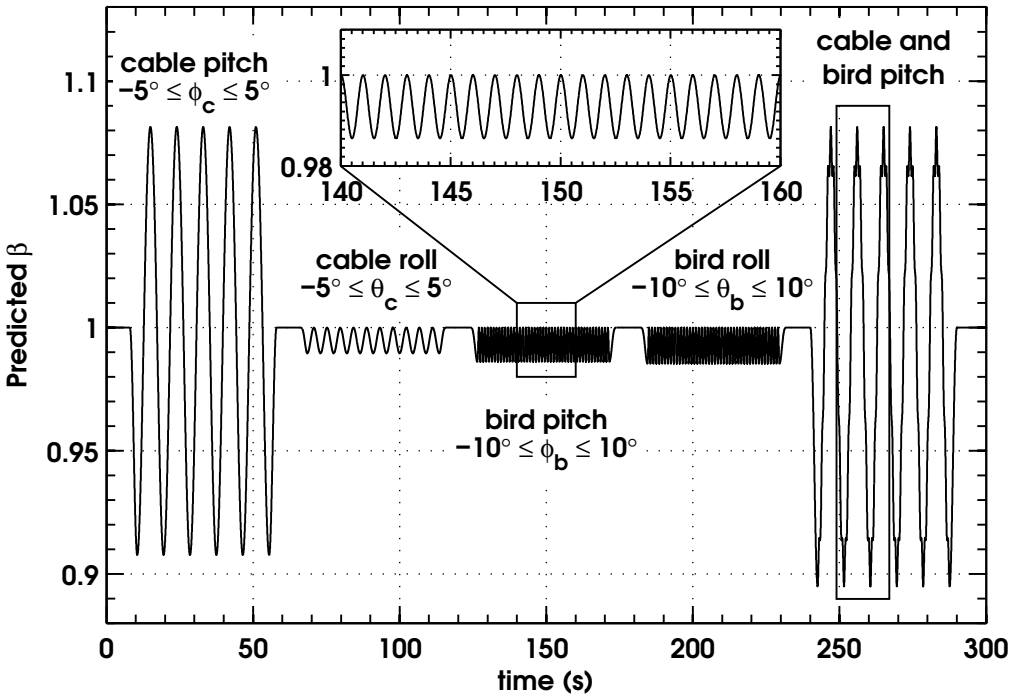

Figure 4.5: *Calculation of β for synthetic data. From 0 s to 60 s, the cable is swung fore-to-aft, period = 9 s, amplitude = $\pm 5°$; from 60 s to 120 s, the cable is swung side-to-side with the same period and amplitude. From 120 s to 180 s, the bird is pitched $\pm 10°$ with a period = 2 s. This is shown in greater detail in the sub-panel near the top of the figure. The bird is then rolled about its central axis, from 180 s to 230 s, with the same period and amplitude of oscillation. Finally, the entire system is subjected to a combination of fore-to-aft cable swing and bird pitching. A small rectangle in the right of the graph is the subject of Figure 4.6.*

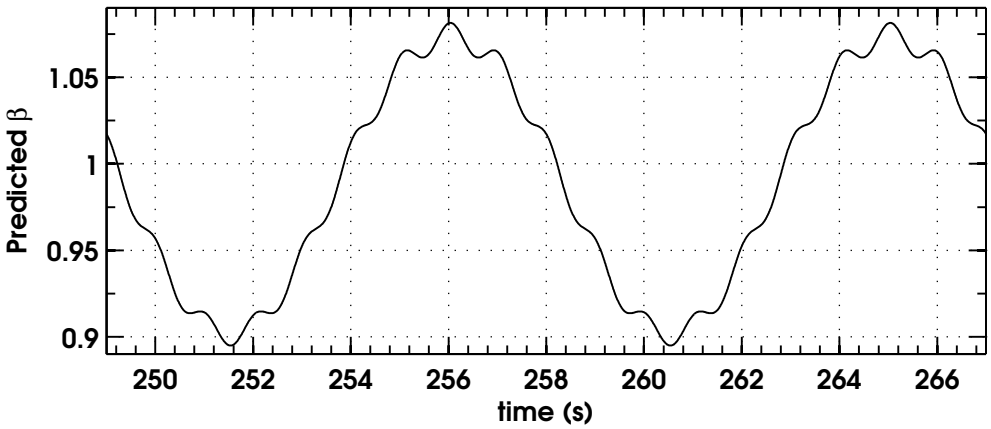

Figure 4.6: *Detail of Figure 4.5 from 249 s to 267 s. This figure clearly shows the effect of bird pitch (period of 2 s) superimposed over the in-line cable swing (period 9 s), and is remarkably similar to the plot of β versus time from the Sydney Harbour data (Figure 3.6, p. 72).*

produced faithfully by the 9 s in-line cable swings. Since there is about a 6% change in β over the large 9–10 s swings in the Sydney Harbour data, we can go back to Figure 4.3 and predict that the cable swings are on the order of $\pm 1.5°$. With a cable length of 30.5 m, an in-line swing of 1.5° corresponds to a horizontal displacement of about 0.9 m, which is consistent with the in-line GPS separation distances found from the Chowilla dataset.

Now that the relationship between bird swing and β has been firmly established, I will present a way to filter historical data as a first attempt at correcting it for bird swing. As with all filtering, care must be used to remove only spurious data. Injudicious use of filters can cause problems in final data, leading to incorrect analysis and erroneous conclusions. The filter that I have developed is presented in the next section.

4.3 Bird Swing Filter: Radar Altimeter

The method I use to correct survey data contaminated with system swing is to employ a non-linear filtering technique that is designed to remove only the components of 9.0 s and 4.5 s as predicted from the synthetic data. It is accomplished by representing the time series β data as a discrete time series, $F(n)$. At each sample n, I fit a cosine function of period $T_1 = 9.0$ s, one of period $T_2 = T_1/2$, a sine function of period T_2, a cosine function of $T_3 = T_1/3$. These functions are represented as ${}_bF_{\cos}(n)$ and ${}_bF_{\sin}(n)$, and are expressed as

$$ {}_bF_{\cos}(n) = \frac{\sum_{n'=0}^{89} \cos\Big(\frac{2b\pi n'}{T_b}\Big) F(n-n')}{\sum_{n'=0}^{89} \cos\Big(\frac{2b\pi n'}{T_b}\Big) \cos\Big(\frac{2b\pi n'}{T_b}\Big)}, \text{ and} \tag{4.7} $$

$$ {}_bF_{\sin}(n) = \frac{\sum_{n'=0}^{89} \sin\Big(\frac{2b\pi n'}{T_b}\Big) F(n-n')}{\sum_{n'=0}^{89} \sin\Big(\frac{2b\pi n'}{T_b}\Big) \sin\Big(\frac{2b\pi n'}{T_b}\Big)}. \tag{4.8} $$

In these equations, the index b is the divisor of the main period of the filter, so that $b = [1, 2, 3]$ for T_1, T_2, and T_3, respectively. Since the sampling frequency of the time series is 10 Hz, the 9 s cosine filter has 90 taps. The output of the filtering process is applied to the original signal F at each sample to give the corrected time series F_{radar} for β calculated with the radar altimeter:

$$F_{radar} = F + {}_1F_{\cos} - {}_2F_{\cos} + \sqrt{\left({}_2F_{\cos}\right)^2 + \left({}_2F_{\sin}\right)^2} + {}_3F_{\cos}, \tag{4.9}$$

where the index n is assumed implicitly.

The workings of the filtering process is shown in Figure 4.7. Panel (a) shows the original synthetic data and the result of the filtering process. In this example, the towed bird was subject to in-line cable swings of 9 s period, having an amplitude of $\phi_c = \pm 5°$ (0–60 s), followed by cross-line cable swings of the same period but having an amplitude of $\theta_c = \pm 10°$ (60–120 s). Synthetic data in panel (a) is shown in red, filtered data in black. After subtraction of the ${}_1F_{\cos}$ term, both in-line and cross-line components are seen to contain higher order terms, panel (b). The third term in equation (4.9), ${}_2F_{\cos}$, removes the cosine term of period T_2 but leaves a constant offset in the synthetic data. This is shown in red in panel (c), which also displays the final filtered data in thick black. The application of the square-root term removes the constant offset left behind, and the ${}_3F_{\cos}$ term removes still higher harmonics of the base frequency. Higher order terms can be added to the filtering process, but it is my opinion that the reduction in bird swing effects shown by equation (4.9) are sufficient.

A problem arises, however, when the cable swing filter is applied to synthetic data that contains oscillations due to bird pitch. This is shown in panel (a) of Figure 4.8. The 9 s filter removes the effect of cable swing, but does not affect bird pitch. The simplest way of dealing with this is to apply the filter again designed to filter the 2 s bird pitch effect from the data. Panel (b) clearly shows that this

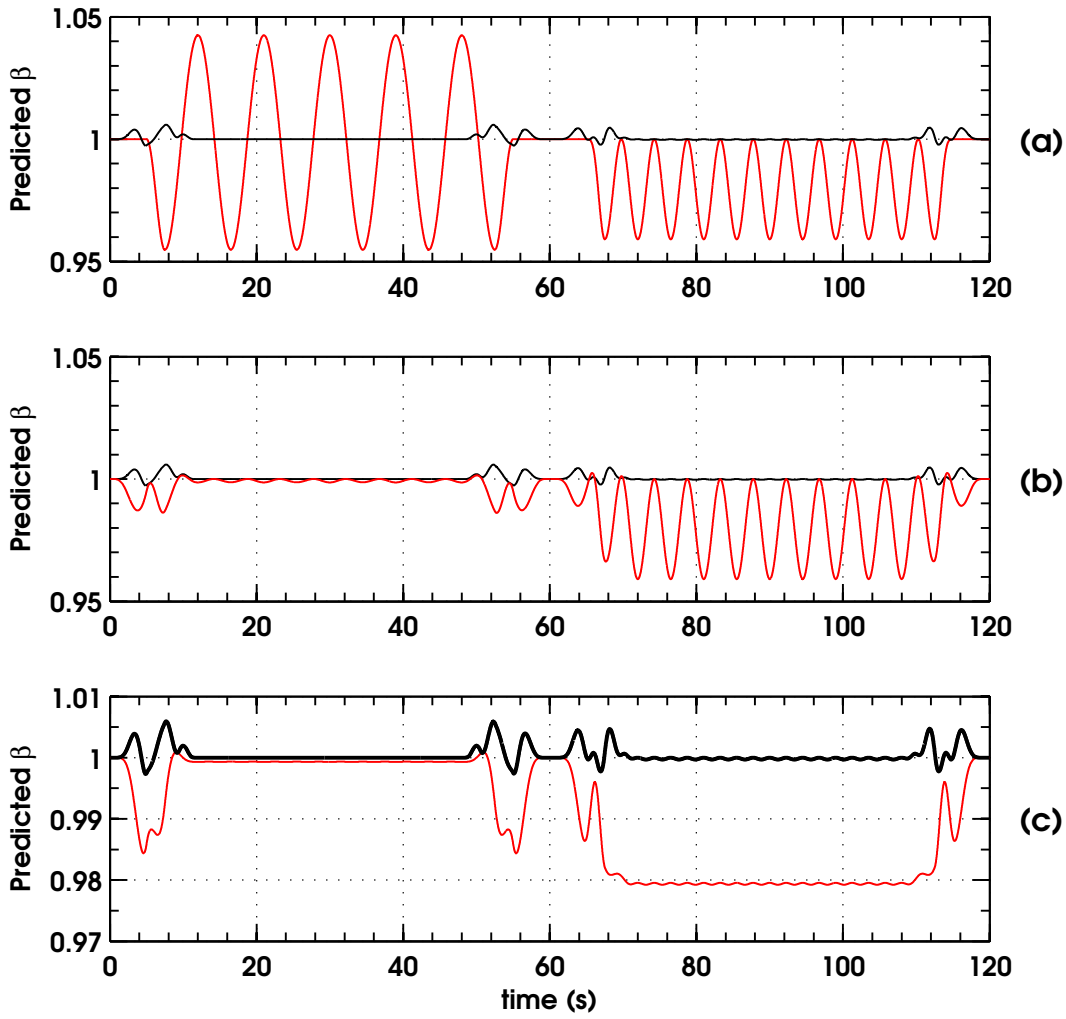

Figure 4.7: *Implementation of the filtering process on synthetic data (radar altimeter). Synthetic data shows β for in-line cable swings of $\phi_c = \pm 2.5°$, and period of 9 s (0–60 s) and cross-line cable swings of $\theta_c = \pm 10°$, period of 9 s (60–120 s). (a) Shows the original synthetic data (red) and the result of the filtering process (black). (b) The removal of the ${}_1F_{\cos}$ in equation (4.9) term from the synthetic data. The next step is the removal of the ${}_2F_{\cos}$ term (c), leaving the constant offsets in the synthetic data. The last two terms of equation (4.9) are shown in the repetition of the filtering process shown in thick black in panel (c).*

is effective on synthetic data. Now, I reiterate my warning about filtering data too much. A 9 s filter applied to real data will successfully eliminate cable swing effects from historical data, but it may also remove salient geophysical formations from the data set. For example, a 9 s filter removes all features that repeat over a distance of approximately 300 m from a typical RESOLVE survey. The 2 s filter will flatten 60 m features. When interpreting a grid obtained from an electromagnetic survey, the effect of the filtering process must be remembered.

4.3.1 Implementing the Bird Swing Filter

To finish with the analysis of bird swing when using the radar altimeter, I now present the 40 kHz β data from the Chowilla dataset. Figure 4.9 shows the output of the filter on the same detail shown in Figure 3.14. Bird and cable swing effects are largely eliminated from the data. Forward and backward swings of the cable are no longer associated with high and low values of β. Although there is some striping from line to line, this is not due to periodic bird swing. Most likely, it is related to

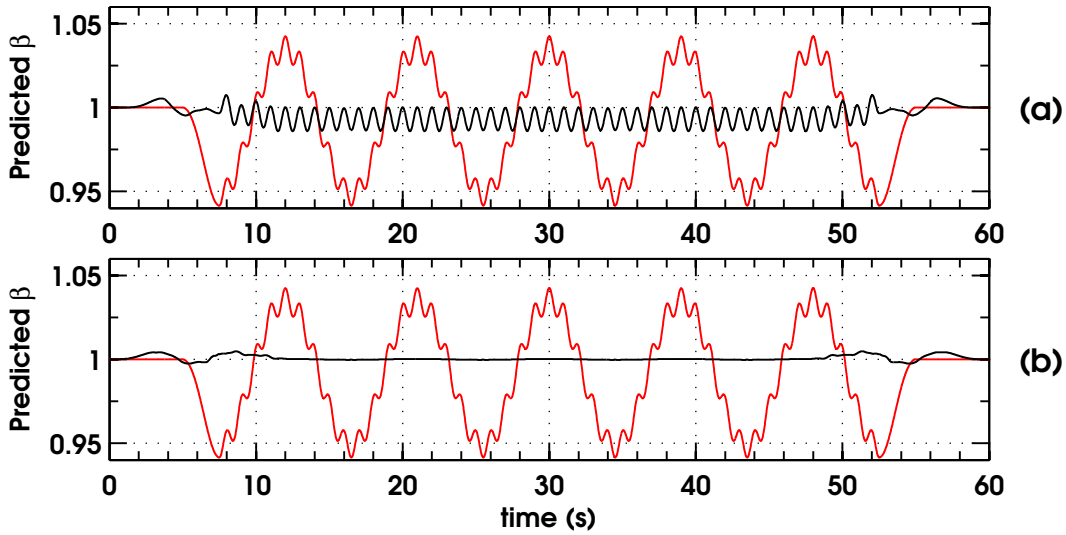

Figure 4.8: *Synthetic data that exhibits bird pitch ($\phi_b = \pm 10°$, period = 2 s), superimposed over in-line cable swing ($\phi_c = \pm 2.5°$, period of 9 s). Panel (a) shows the original synthetic data (red) with the output of the filtering process used with a period of 9 s (black). Bird pitch effects are not removed. Panel (b) shows the synthetic data (red), together with the 9 s filter process followed by the filter applied again with period of 2 s (black).*

the airspeed of the bird, affecting the drag acting on it and hence its average offset from the helicopter. Figure 4.9 also exhibits the problem that I mentioned earlier, loss of resolution of the data. How can we be sure that the filtered data still reflects reality? My only suggestion is to apply caution in the interpretation. The filtered data of β at 40 kHz for the entire dataset is presented in Figure 4.10. Clearly, the grid has lost a lot of its spottiness when compared to the original grid in Figure 3.13. Areas such as the dry lakes in the north of the survey are more coherent and much more clearly defined.

This brings the discussion back to Sydney Harbour and the dataset that first introduced evidence of bird swing. Instead of showing a section of just one line, Figure 4.11 shows a grid of β for the 25 800 Hz data for the entire survey. Although it is hard to see evidence of the 1 s oscillations in the gridded data, Figure 3.6 showed that they were there. The gridded data in Figure 4.11 is extremely useful for detecting the 9 s oscillations of β. After application of a 9 s filter and a 2 s, the bird and cable swing effects are completely eliminated from the data. The result is shown in Figure 4.12. Bird swing is eliminated, but the filtered grid shows remarkable line-to-line variation! Comparison to Figure 3.3 shows that the variation depends on flight-line direction, with lines flown to the northeast exhibiting strikingly lower values of β than those flown to the southwest. It is my conjecture that this must be related to air speed of the towed bird, since for high enough velocity, drag becomes proportional velocity squared (Fowles and Cassiday, 1993). A high drag in one direction due to a head wind and a low drag in the other caused by flying at constant ground speed with a tail wind would cause the towed bird to change its vertical separation from the helicopter. This would cause an almost constant offset error in the calculated altitude of the bird, and thus change the calculation of β.

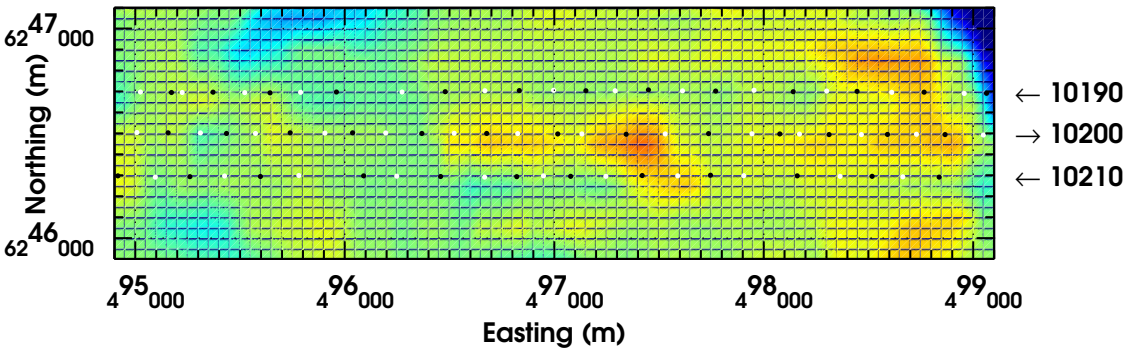

Figure 4.9: *Same detail as shown in Figure 3.14 with both the 9 s and the 2 s filter applied to the data. The filters remove most of the bird swing effects, at the cost of some loss of resolution.*

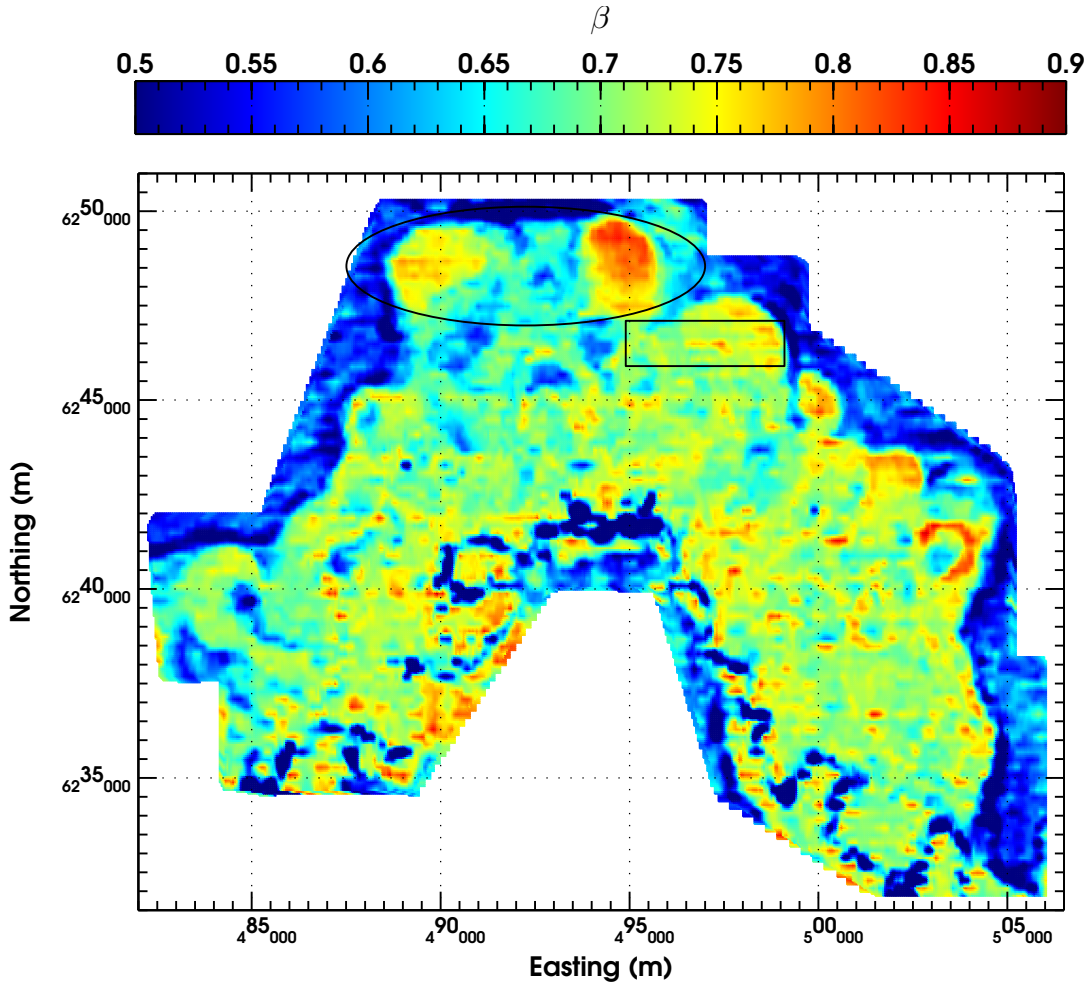

Figure 4.10: *Output of a 9 s filter followed by a 2 s filter (equation (4.9) applied to β(radar) of the 40 kHz data from the entire Chowilla dataset. Areas such as the dry lakes at the top of the figure are more defined and uniform in appearance. Spatial resolution is sacrificed for increased clarity of the image.*

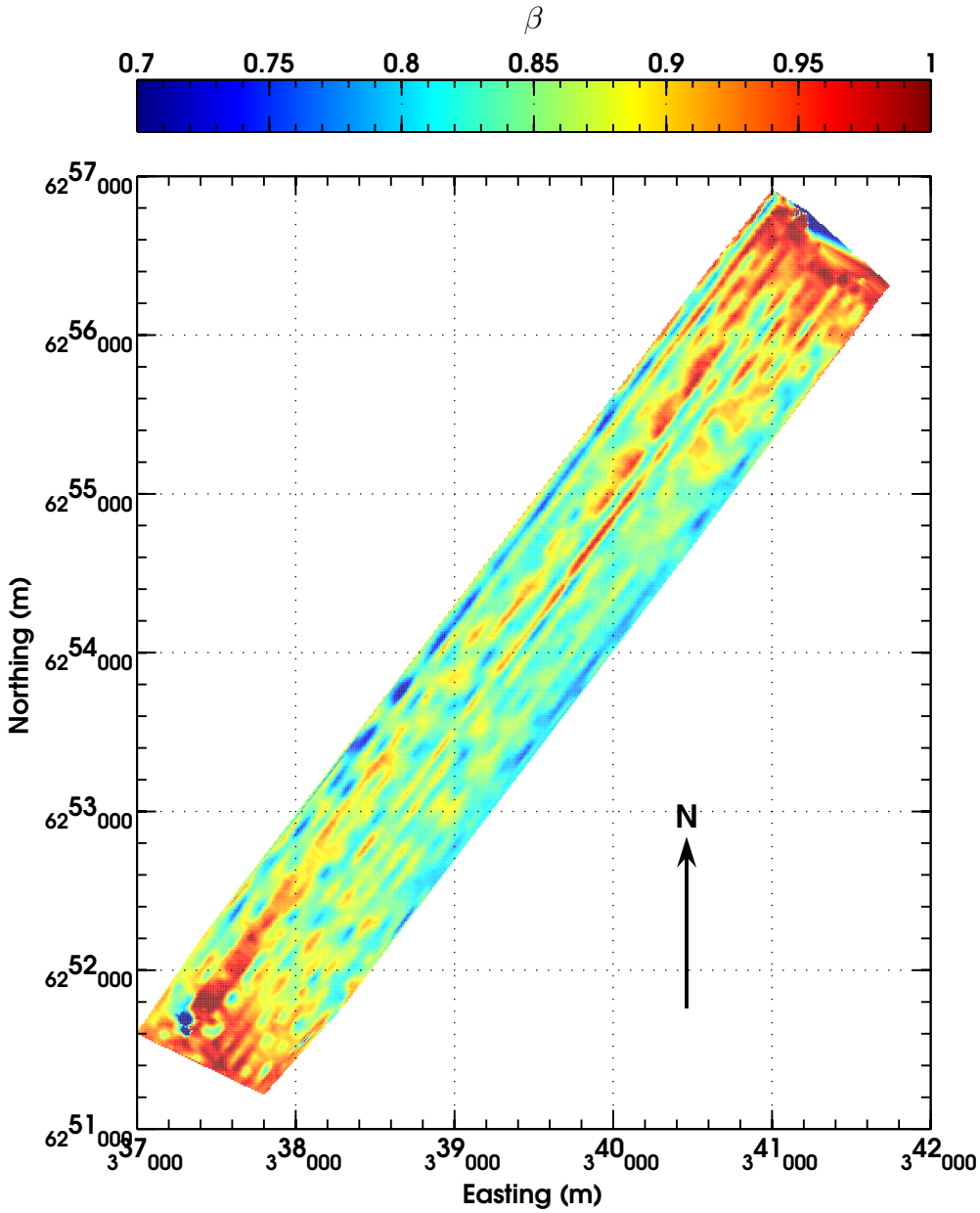

Figure 4.11: *Grid of β for the 25 800 Hz data from the Sydney Harbour dataset. This grid clearly shows the 9–10 s (300 m) oscillations due to cable swing.*

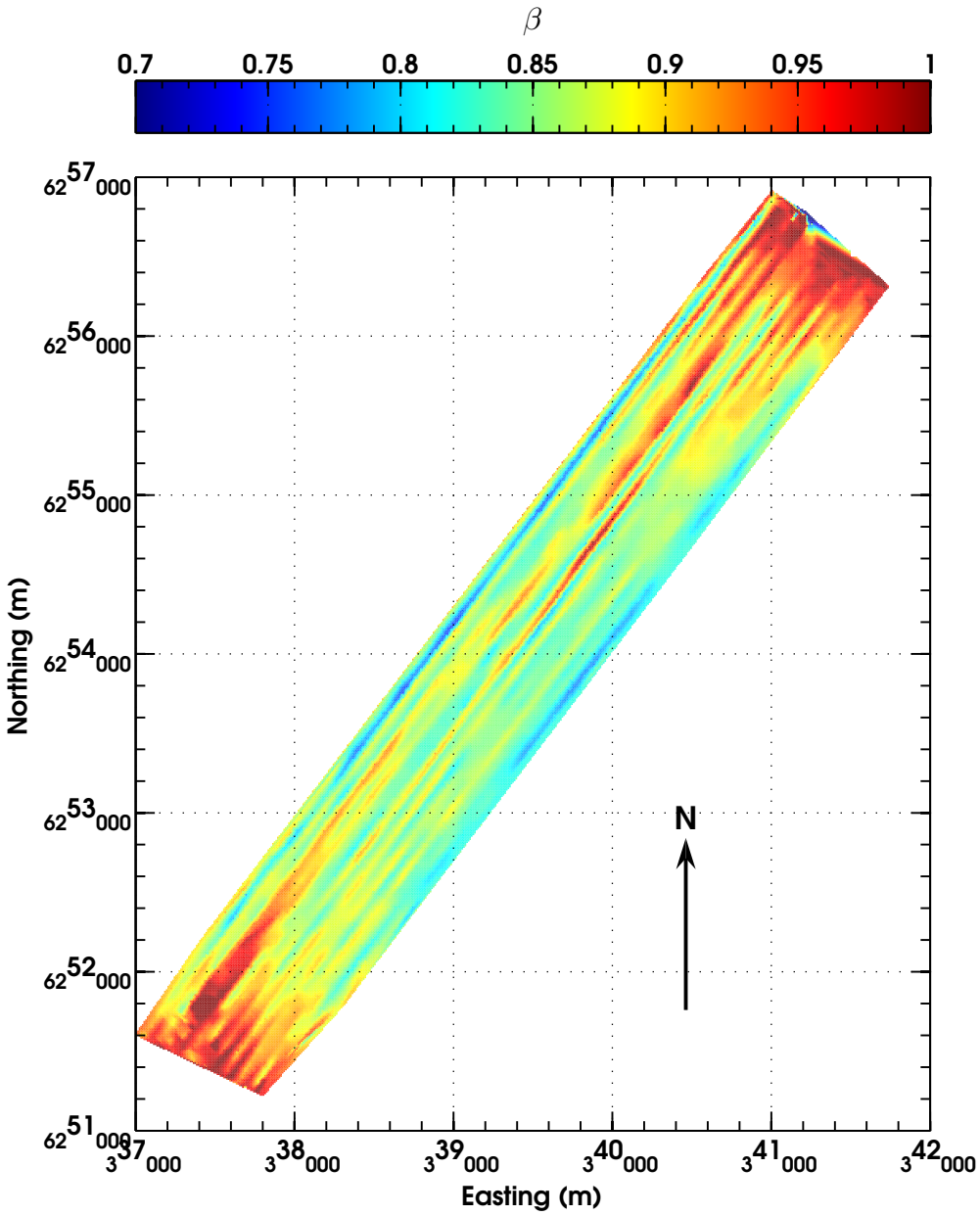

Figure 4.12: *Grid of 25 800 Hz β filtered with a 9 s filter, then with a 2 s filter applied after. Bird swing effects are eliminated, but the grid displays remarkable striping that depends on velocity and hence geometry.*

4.4 Bird Swing Model: Laser Altimeter

We can use the mathematical models derived in the last sections to model changes in β that occur during bird swing when the altitude is measured with a laser altimeter rigidly mounted on the bird. The laser altimeter used in RESOLVE surveys is typically mounted in the underside of the chassis of the bird near the nose. This is shown in Figure C.2, where I have marked the distance of the laser altimeter from the nose of the bird. If the bird does not pitch or roll when the tow cable swings, the laser altimeter will properly measure the altitude of the bird. Changes in system response due to altitude change will be balanced exactly by G calculated using the laser altitude, and β will not change at all. This is obviously the intention of system designers. Problems arise when the bird is subject to attitude changes. Not only does the geometric coupling change but the measured laser altitude changes as well. The change in laser altitude will not be a correct measurement of the altitude of the centre of the coil pair, and β will change. We can predict the change occurring using the same method as we did before.

4.4.1 Pitch and Roll of the Bird

When the bird is pitched and rolled about its centre point, the transmitter and receiver coils change their orientation according to the Figure 4.2. This results in the more generalised coupling of the coils with the earth as shown in Figure 4.4. Appropriately, we can use the more general computation of equation (4.6) to calculate the inductive limit coupling of the pitched and rolled bird to the earth beneath. The significant change from Section 4.2 is the measurement of h by the laser altimeter. A schematic of bird rotation and its implication for laser altimeter error is shown in Figure 4.13.

It is easy to see from the figure that bird pitch will cause the laser altimeter to over- and underestimate the measured altitude of the centre point of the bird. When

the cable is tilted back, as is normal on survey, negative tilting of the bird will raise the nose upwards away from the earth. The laser altimeter, mounted near the front of the bird, will yield an altitude too great. Tilt the nose downward and the laser altimeter will underestimate the altitude before it once again overestimates it. This peculiar behaviour is due to the fact that the laser altimeter is near the nose of the bird. If the laser altimeter was located directly beneath the centre point of the bird, it would always overestimate the altitude whenever the bird was pitched. By way of comparison, whenever the bird is forced into a roll, the laser altimeter will always overestimate the altitude of the centre of the bird.

We can model changes in β resulting from bird swing and altimeter error. As before, the cable is swung back ϕ_0 degrees so that the bird is towed horizontally and level with the earth during normal survey conditions. The actual and measured altitude of the centre of the bird is h_0, say 30 m. An origin is placed below the centre

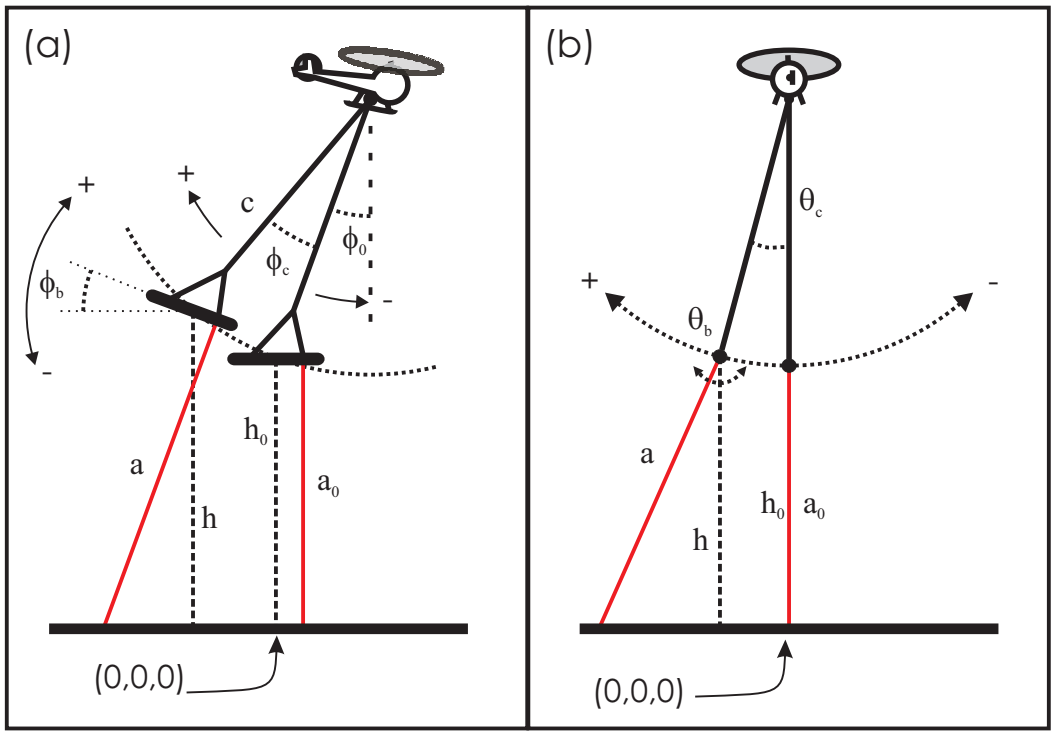

Figure 4.13: *Schematic of how bird swing creates altimeter error when using a laser altimeter. (a) Bird pitch causes the laser to both over- and underestimate the actual altitude h. In this panel, the measured laser altitude a is greater than h. (b) Roll always makes the laser altimeter overestimate the actual altitude of the bird.*

of the bird in its mean survey position, and we once again express the position of the centre point as vector $\mathbf{b} = \mathbf{h} + R(\theta_c, \phi_c)\bar{\mathbf{c}}$ (equation (4.3)). The altitude of the centre of the bird after any cable swinging will therefore be the $\hat{\mathbf{k}}$ component of $\mathbf{b}$. Let's say that the altimeter mounted underneath the bird points in the negative z-direction so that it points directly downward when the bird is level. We will call this vector $\hat{\mathbf{L}}_\mathbf{0}$. After an arbitrary pitch or roll of the bird, the laser altimeter vector $\hat{\mathbf{L}}$ points in the direction given by

$$\hat{\mathbf{L}} = R(\theta_b, \phi_b)\hat{\mathbf{L}}_\mathbf{0}.$$

This is expressed as

$$\hat{\mathbf{L}} = -\sin(\phi_b)\,\hat{\mathbf{i}} + \cos(\phi_b)\sin(\theta_b)\,\hat{\mathbf{j}} - \cos(\phi_b)\cos(\theta_b)\,\hat{\mathbf{k}}. \tag{4.10}$$

Inspection of Figure C.2 shows that the laser altimeter is offset from the centre of the bird by a small horizontal and vertical displacement. From measurement, the laser altimeter is horizontally offset from the midpoint of the bird by ∼2.6 m. The vertical offset from the middle of the bird is about 0.3 m. These distances are expressed as vector $\mathbf{a}$, so that when the bird pitches and rolls, the laser altimeter is located at $\mathbf{l}$, where

$$\mathbf{l} = \mathbf{b} + R(\theta_b, \phi_b)\mathbf{a}. \tag{4.11}$$

With the position of the laser altimeter described by equation (4.11) and the laser pointing in the direction given by equation (4.10), we can calculate what the altitude measured by the laser altimeter would be if the bird was towed over a flat earth. This is done by extending the unit vector $\hat{\mathbf{L}}$ from position $\mathbf{l}$ to the plane at $z = 0$ using a parametrisation of vector $\hat{\mathbf{L}}$:

$$\mathbf{L} = t\hat{\mathbf{L}},$$

where $\mathbf{L}$ is the vector from $\mathbf{l}$ to the point $(x,\ y,\ 0)$. This yields the system of equations,

$$\begin{pmatrix} tL_x = x - l_x \\ tL_y = y - l_y \\ tL_z = -l_z \end{pmatrix},$$

which is readily solved for t. Inspection reveals that $t = l_z/L_z$: the length of the vector and hence the measured altitude h' is

$$h' = \left|\frac{l_z}{L_z}\right| + 0.3\,\mathrm{m},$$

which will be in error whenever the bird is pitched or rolled. I have included the small distance of 0.3 m to account for the slight vertical offset of the laser altimeter from the midline of the bird. I can only assume that laser altimeters in actual survey systems have this vertical offset programmed into them.

The bird is towed at a nominal survey altitude of 30 m and slung behind the helicopter by ϕ_0 degrees, as shown in Figure 4.13. When the bird is level to the earth, the laser altimeter reads $h' = 30$ m, and β is therefore 1. This will hold for any swinging of the tow cable *provided the bird stays level*. Let the bird pitch $\pm 20°$ about its centre point while remaining at altitude 30 m. The response of the system changes just as it did in Section 4.2, but this time the laser altimeter records erroneous altitudes. To model β we use equation (4.6) for the response of the bird, and equation (3.5) for the calculation of G; β is their ratio. The result is shown in solid black in Figure 4.14. The direction of the x-axis is reversed in this graph to be more intuitive when using Figure 4.13 as a reference for swing. Values to the left of the graph mean that the nose of the bird has been pitched downwards. The laser altimeter is near the nose of the bird, so when it gets dipped down, the laser altimeter records smaller values of altitude, thereby increasing G. Bird pitch always reduces response, so β decreases. This continues until the laser altimeter records

larger and larger altitudes, decreasing G and increasing β. Eventually, altimeter error balances the change in response and the ratio is again 1.

In the case shown, this occurs when the bird is pitched about 14°. After that, both bird pitch and laser error combine to increase β well above the nominal value. For comparison, the model of β using bird pitch and radar altimetry is shown as a dashed line in Figure 4.14. For the same amount of pitch, the reduction due to geometric coupling is only about 5% at full swing (dashed line). The laser altimeter error creates an enormous 4–23% increase in the ratio for the same amount of pitch.

Error caused by bird roll is similar in effect. The dotted line in Figure 4.14 shows a symmetrical increase in β for tube rolls of the bird. Again, laser altimetry results in a drastic reduction of G creating large increases in β despite the reduction in response caused by the tube roll. For small values of roll, β can change a great deal (21% for a 20° roll). To show how these errors can affect β when a towed bird is subjected to pitch and roll similar to those seen in Chowilla and as predicted for Sydney Harbour, I will present some synthetic data representing bird swings.

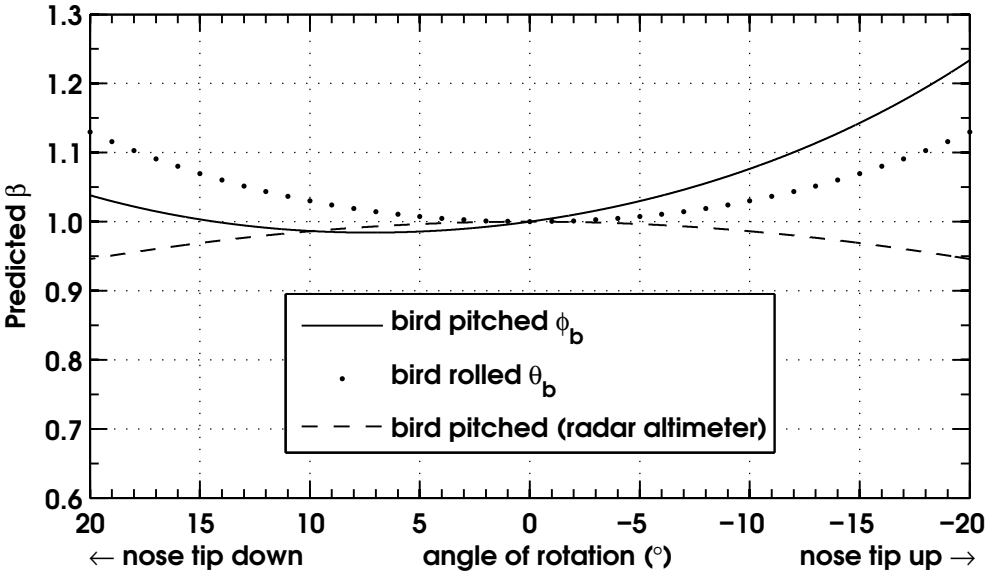

Figure 4.14: *Predicted β reflecting changes to the geometric coupling and altimeter error caused by bird rotations.*

4.4.2 Synthetic Examples of Rotation

The synthetic data that I will present in this section will be the one used by Davis et al. (2006). The model is a 30.5 m tow cable rigidly attached to the bird so that when the cable is pitched or rolled, the bird is also rotated. The tow cable is slung back ϕ_0 so that the bird is level to the earth. Further rotations of the cable move the bird from the 'normal' position.

From 0 s to 60 s, the cable is forced to rotate fore-to-aft with an amplitude of $\pm 7°$. The period of oscillation is 9 s. We can model the change in β the same way as before: backward swings of the cable will raise and rotate the bird, reducing the response. Therefore the value $\frac{T^2}{R}$ decreases. Forward swings lower the bird, increasing $\frac{T^2}{R}$. The laser altimeter only measures the altitude correctly when it goes through the 'normal' position. The incorrect values of altitude measured by the laser altimeter are used to calculate G in equation (3.5), and the ratio of $\frac{T^2}{R}$ to G gives predicted β. From 60 s to 120 s, the system is forced to roll or move side-to-side with the same amplitude and period as the fore-to-aft motions. Swings in either direction reduce the response of the signal but also cause the laser altimeter to overestimate the altitude of the bird.

The resulting predictions of β are shown in Figure 4.15. The cable begins with a backward swing that reduces β by 4% at full swing. Forward swings increase predicted β by a maximum of about 7.5%. Cable roll always increases β. This is in spite of the fact that the response is decreased. Evidently, the laser altimeter overestimation increases G to such an extent that it overpowers the decrease in response. Notice that the frequency of changes in β due to side-to-side swing are twice that of the changes due to in-line swing. Furthermore, for similar amplitude swings, rolling changes β by a mere 2% compared to a range of 11.5% for in-line swings. It is for this reason that I have neglected side-to-side swings in most of my analysis.

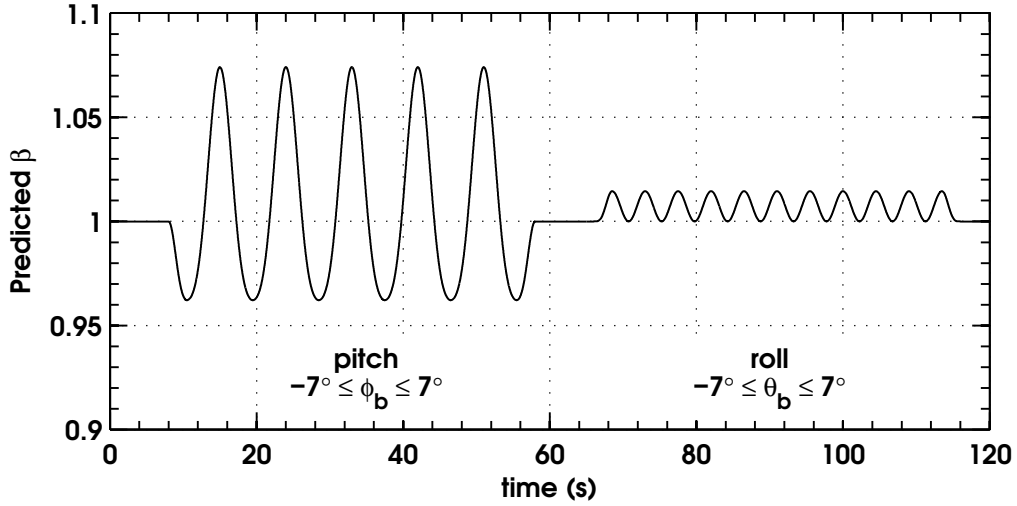

Figure 4.15: *Predicted β for synthetic data generated simulating bird and cable swings with a laser altimeter in the bird. From 0 s to 60 s, the bird is subject to pitch of amplitude $\pm 5^\circ$ and a period of 2 s. 60–120 s, $\pm 5^\circ$ roll about central axis with a period of 2 s. 120–180 s same pitch superimposed on fore-to-aft cable swing of amplitude $\pm 5^\circ$, period 9 s.*

4.5 Bird Swing Filter: Laser Altimeter

We can correct the data for bird swing by applying a similar filter to the one applied in Section 4.3. The cosine and sine terms of equations (4.7) and (4.8) are used exactly as before, but the filter is changed in its application of the terms. Whereas in the radar bird swing filter we added the magnitude of the T_2 term, here we must subtract it. The filter then becomes:

$$F_{laser} = F + {}_1F_{\cos} - {}_2F_{\cos} - \sqrt{\left({}_2F_{\cos}\right)^2 + \left({}_2F_{\sin}\right)^2} + {}_3F_{\cos}, \tag{4.12}$$

The result of application of the filter in equation (4.12) with a period of 9 s is shown in Figure 4.16. The filter acts on the synthetic data and removes the effect of both cable swing and bird rotation.

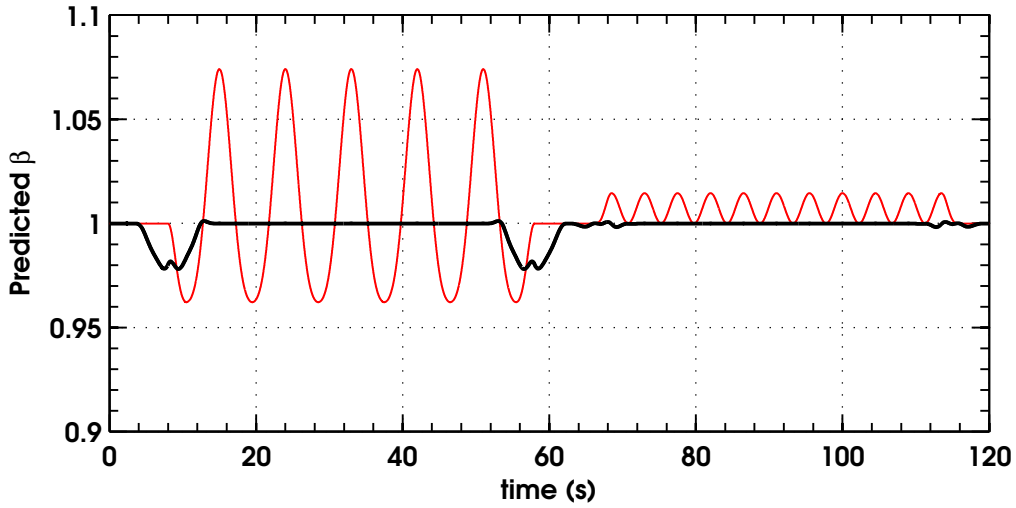

Figure 4.16: *Implementation of the 9 s bird swing filter on predicted β from the synthetic model (with laser altimeter). Original synthetic data is shown in red. Also shown is the output of the 9 s bird swing filter (thick black). Compare to Figure 4.7, where β was predicted using radar altimeter.*

4.5.1 Implementing the Bird Swing Filter

To sum up this section of the chapter and show the implementation of the swing filters applied to real data, I will present the result of applying equation (4.12) to β using the 40 kHz in-phase and quadrature responses with altitude measured by the laser altimeter from the Chowilla Floodplain. Figure 4.17 shows a grid of the filtered data. Bird swing is clearly reduced in effect in the data when compared to Figure 3.15. The dry lakes at the top of the grid are very clearly defined.

Comparison of β calculated with radar (Figure 4.10) and laser (Figure 4.17) altimetry shows several differences. The laser altimeter data is much flatter and less striped than radar altimeter data. This is most likely due to constant line to line altitude errors in the radar data due to variable airspeed and survey conditions, although I have done no tests to prove this. The laser altimeter does not seem to have this problem, but attaching it to the nose of the bird complicates true altitude estimation. It is my suggestion that the laser altimeter be placed directly under the central rotating point of the bird. If this is done, all bird swings will result in overestimating altitude and bird swing will be very easy to pick out of the data.

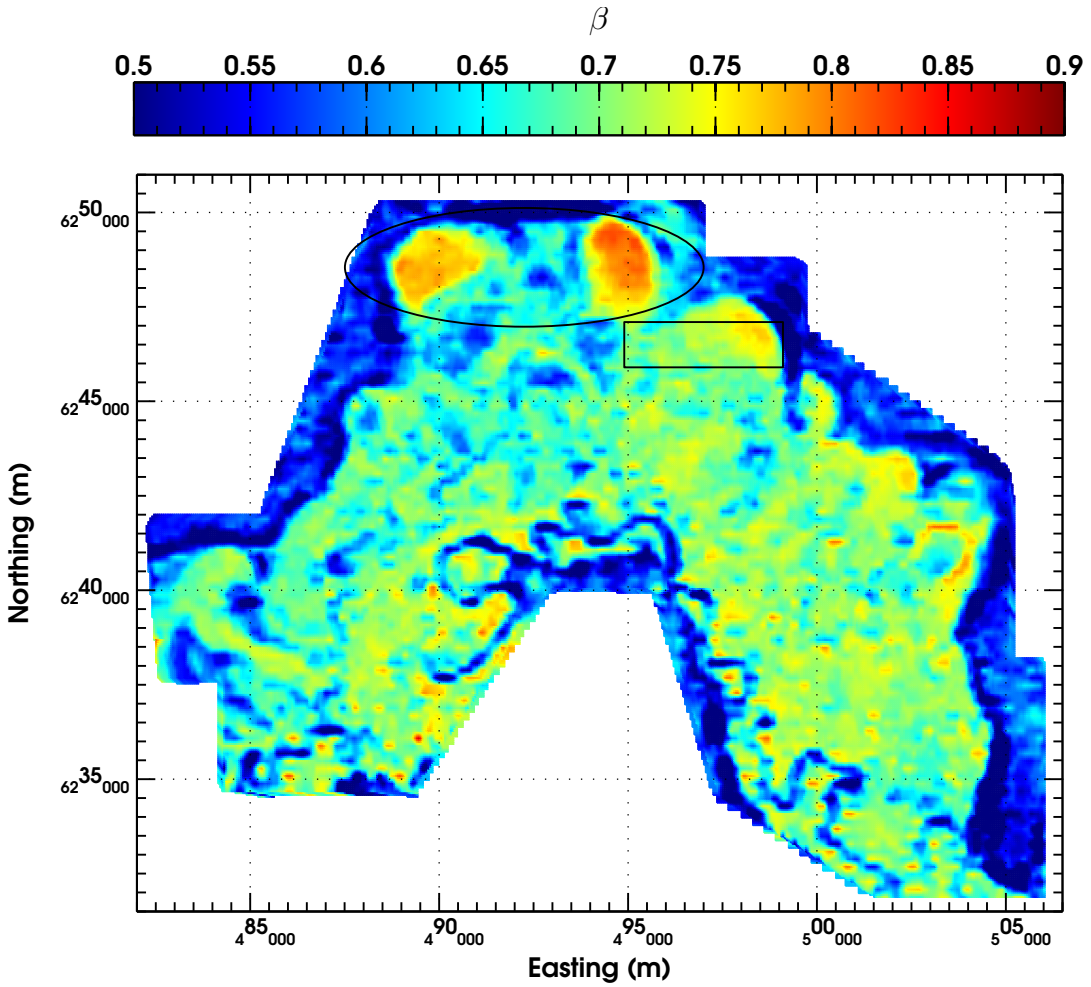

Figure 4.17: *Implementation of the 9 s bird swing filter on β calculated using laser altimetry and the response data from the 40 kHz component of the Chowilla Floodplain dataset. Bird swing is eliminated from the data with the inevitable loss of resolution.*

The radar altimeter seems to be very prone to error near and bordering the Murray River along the bottom part of the grid. This could be due to the canopy effect described by Brodie and Lane (2003), but it could also be a previously undiscussed 'watercourse' effect. It would be useful to determine the true cause, but it will not be explored in this thesis. When examining the laser altimeter, a pointing or range-finding type of laser altimeter must necessarily be very prone to bird swing error. I strongly suggest using a scanning laser altimeter that will more accurately measure the 'true' distance of the altimeter from the earth. With the laser altimeter mounted under the point of rotation of the bird, AEM data will be much less prone to error.

When attempting to find bird swing in AEM data, I strongly recommend β calculated using radar altimetry. Even with line to line striping, the radar altimeter is insensitive to errors caused by bird swing. Therefore, changes in response due to swing are easily discovered. This was most apparent in Sydney Harbour, but was easily discernable over the Chowilla Floodplain.

Analysis of the Chowilla data showed that the cable swings around a great deal during a survey. We can break the swings down into in-line and cross-line swings, and can even predict them from GPS data from the helicopter and towed bird. But this information does not predict bird swing, and in fact the only way to get that information is to actually measure it. Fortunately, this has occurred last year in September 2006, when the CSIRO contracted Fugro Airborne to conduct a RESOLVE HEM survey in the Sunraysia area just outside of Mildura, Victoria.

4.6 Sunraysia: RESOLVE

The Sunraysia dataset is unique to this thesis because the contractors provided a way to measure pitch, roll and yaw of the bird while it was on survey. They did this with 3 high accuracy GPS antennae mounted in a triangle pattern on the towed bird. Two GPS antennae were placed at opposite ends of a boom that can be mounted to the RESOLVE and usually houses a magnetometer. The last GPS antenna was placed near the tail of the bird. The position of the three GPS antennae is shown in Figure 4.18.

For this survey, the contractors used an internal computer or chip to calculate the pitch, yaw and roll of the towed bird 'on the fly'. In order to test that it was operating and really measuring these values, a team was assembled to sequentially photograph the RESOLVE system while it was on survey. The experiment was designed so that the team could take sub-second interval photographs of the RESOLVE system both along the direction of flight and perpendicular to it with high resolution digital cameras. Our success was varied, proving once again that video recording an HEM system on survey is extremely difficult. I managed to obtain some photo sequences

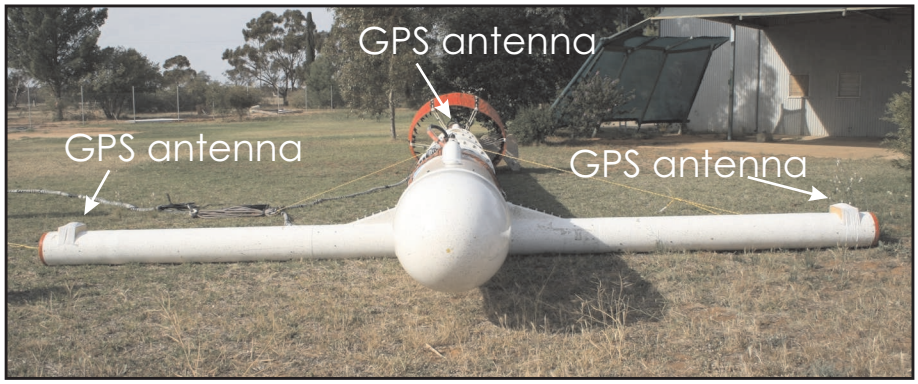

Figure 4.18: *Photograph of the 3 GPS antennae used to measure pitch, roll and yaw in the Sunraysia HEM survey. 2 GPS antennae are mounted on a boom near the front of the system, while the last is mounted on the chassis, near the back. Pitch, yaw and roll calculations are processed real-time.*

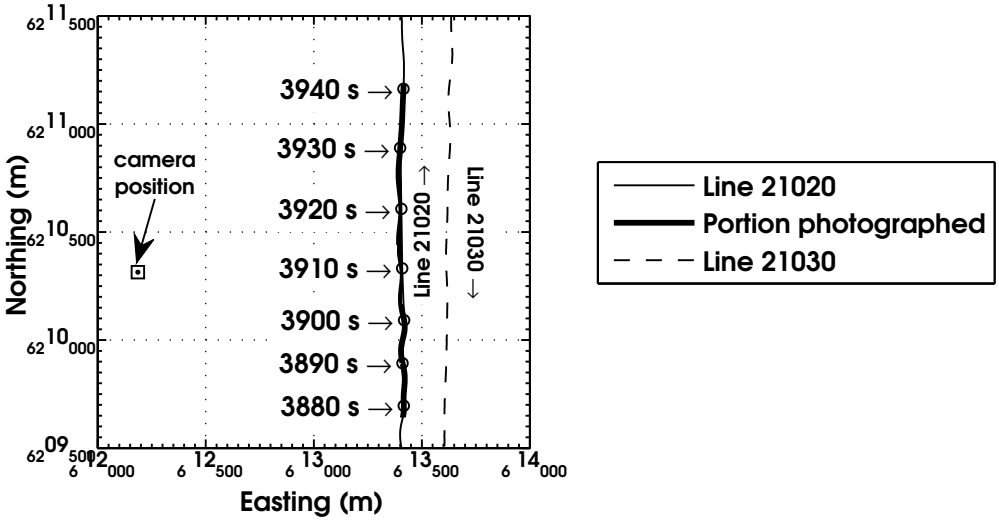

Figure 4.19: *Portions of lines 21020 and 21030 from the Sunraysia HEM survey. Marked in thick black is the section of line that was photographed at sub-second intervals. Open circles along this line mark 10 s intervals. Camera position was* $_{62}10_{314}$ *m North and* $_{6}12_{186}$ *m East.*

of the HEM system flown along one line, viewing perpendicularly to the line of flight. A portion of line 21020, together with the section that was photographed, is shown in Figure 4.19. The camera position is also marked. Luke Garde, a summer student at RMIT University manually picked the locations on each image of the nose, tail and hitching point of the bird, as well as the nose, GPS antenna and hitching point of the tow cable on the helicopter. An example of one such photograph and the points manually picked by Luke is shown in Figure 4.20. The video made from all the photographs is included in Appendix D.2.

In each frame, I calculated the apparent pitch of the bird and the in-line swing angle of the cable. Each photograph was date stamped, so I correlated the time that the photograph was taken to the GPS time recorded on the bird during survey.

Figure 4.21 shows the result of the analysis. The apparent bird pitch matches the measured bird pitch almost exactly from 3908 s to 3926 s. Looking back to Figure 4.19, this is where the helicopter and bird is almost due east of the camera position. For times earlier then 3908 s and later than 3926 s, the apparent bird pitch tends to underestimate the measured bird pitch due to parallax error. Looking at the dashed line in Figure 4.21, we see that once again the cable executes in-line swings with a period of around 9 s. This is consistent with the Chowilla dataset. During the period of least parallax, the mean cable position seems to be approximately 20°, consistent with my earlier predictions based on the rope lengths of the 'Y' section. Interestingly, this example shows that backward swings of the cable tend to cause the nose of the bird to plunge while forward swings tend to lift it. It seems that the rigid model of Section 4.4.2 is not entirely correct although it is evident that there is a correlation between cable swing and bird pitch. Furthermore, the bird tends to pitch with its own frequency of ∼2.5 s, and amplitudes of anywhere from 2° to 20°. This is strong evidence that supports my claim that the high frequency oscillations in β in Section 3.3 are due to bird rotation independent of cable swings. From this experiment, I believe that the 3 GPS antennae mounted on the bird yield accurate

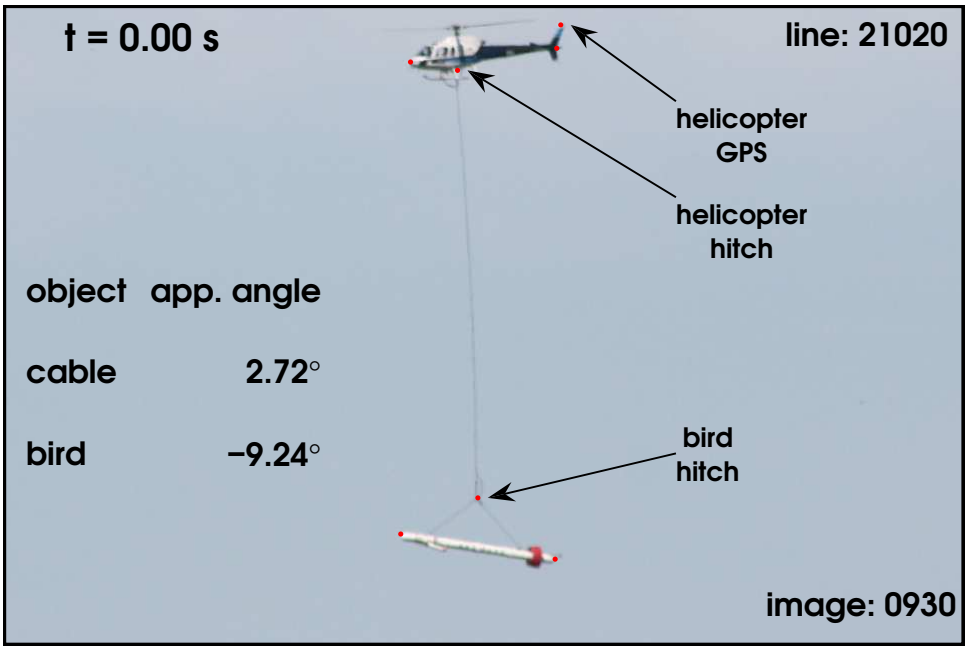

Figure 4.20: *Sample photograph used to analyse bird motion during line 21020 Sunraysia HEM survey. Points manually picked on helicopter were: GPS antenna, nose, tail and cable attachment. Points picked on bird were: nose, tail and the 'Y' point on the cable.*

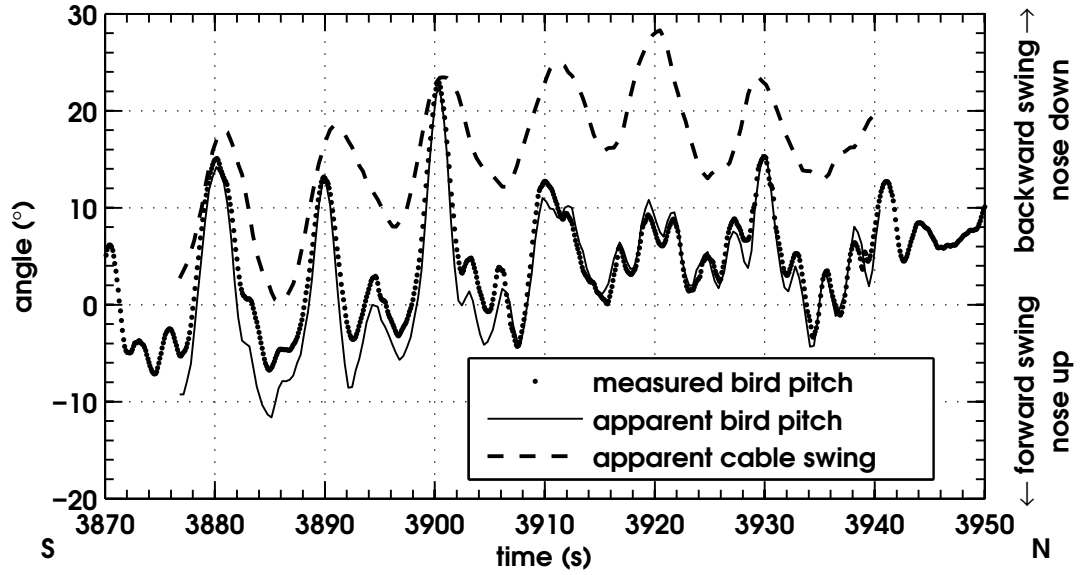

Figure 4.21: *Bird and cable swing measured for a section of Line 21020 from Sunraysia HEM survey. Bird pitch measured with triangular GPS antenna array provided by contractor (dots). Apparent bird pitch (solid) and in-line cable swing (dashed) measured from photographs are also shown.*

measurements of bird pitch.

4.6.1 Attempt at Predicting Roll

The 3 GPS antennae also provide a method to measure roll of the bird while it is on survey. I have said very little in the past two chapters on bird roll and in-line swings. This is partly to do with the models I have made that show that roll is slightly less important than pitch: but also it is because I have not been able to obtain reliable video evidence of cable and bird roll. It is very difficult to film the HEM system as it flies down the line. Despite these shortcomings, the Chowilla dataset proved that cross-line swings do occur. I assert that these cross-line cable swings also cause the bird to rotate. The roll measurements calculated from the 3 GPS antenna provide one way to measure roll, but I propose another based on simultaneous position solutions from the helicopter navigational and towed bird tracking GPS antennae.

The helicopter navigational GPS receiver typically provides horizontal resolution of 1 m, while the towed bird GPS receiver can be used in differential mode to provide horizontal positioning of typically <1 m. For my model we calculate roll by taking the inverse sine of the horizontal displacement of the helicopter and bird GPS antennae (Δx) divided by c the length of the tow cable, i.e.

$$\phi_c = \sin^{-1}\Big(\frac{\Delta x}{c}\Big). \tag{4.13}$$

Figure 4.22 shows a comparison of measured roll to that calculated using the helicopter and towed bird GPS antennae over the photographed section of line 21020.

It is clear from the figure that equation (4.13) yields roll values consistent with the measured values of roll. Angles calculated from the horizontal offsets of the survey GPS antennae are biased to the east, while the measured roll is biased slightly to the west. At this point, it is impossible to tell which is more accurate. This example shows that cross-line cable swing is responsible for rolling the towed bird,

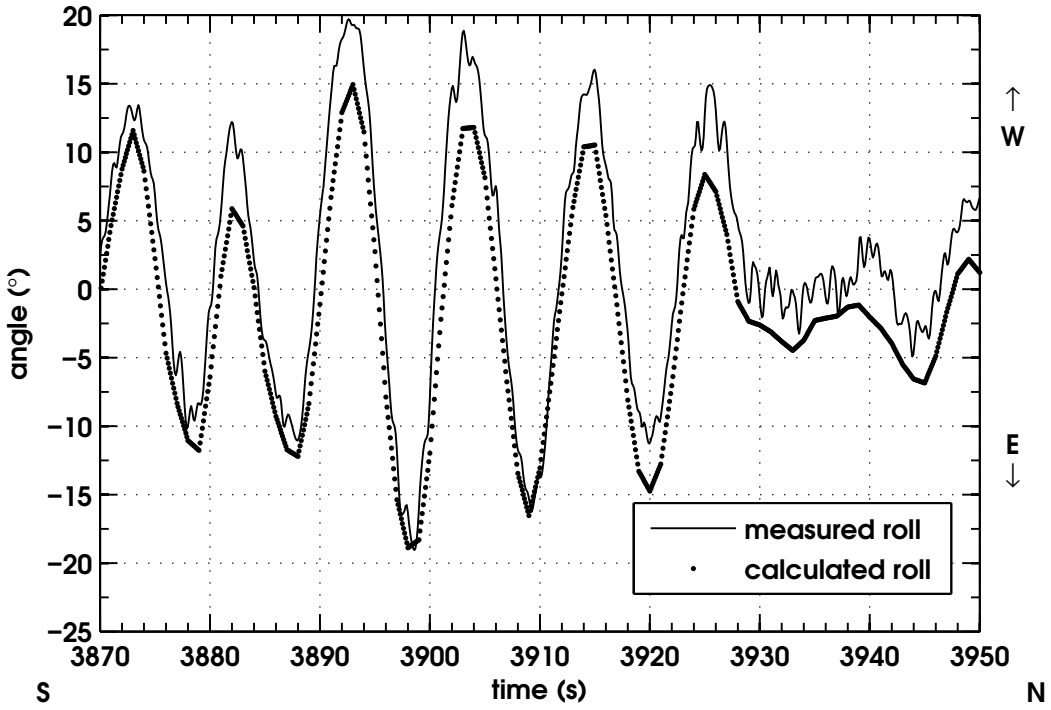

Figure 4.22: *Roll measured for a section of line 21020 from Sunraysia HEM survey. Bird roll measured with triangular GPS antenna array provided by contractor (solid line). Roll calculated (using equation (4.13)) due to cable swing inferred from horizontal helicopter and towed bird GPS antenna displacement (dots).*

but the solid line in Figure 4.22 also shows that there are higher frequency oscillations in rolling motion. I propose that these are the 'tube rolls' that I defined in the introduction to this chapter.

In order to determine the difference these two roll measurements make to the data, Figure 4.23 is a model of how β is affected by roll. I will use the altitude measured by the laser altimeter, and the earth is assumed to be infinitely conductive. The system response $\frac{T^2}{R}$ is given by a horizontal bird towed at an altitude of 30 m. β is modelled using the roll values to adjust both height and attitude of the towed bird from a flat level flight at 30 m. Panel (a) shows β for both measurements. The difference in the models is only great at extreme ranges of swing, which is exactly what we would expect. Furthermore, panel (b) shows the effect of administering the same bird swing filter (equation (4.9)) to both sets. Clearly, if we are using a bird swing filter, the choice is immaterial. But what if we are trying to predict

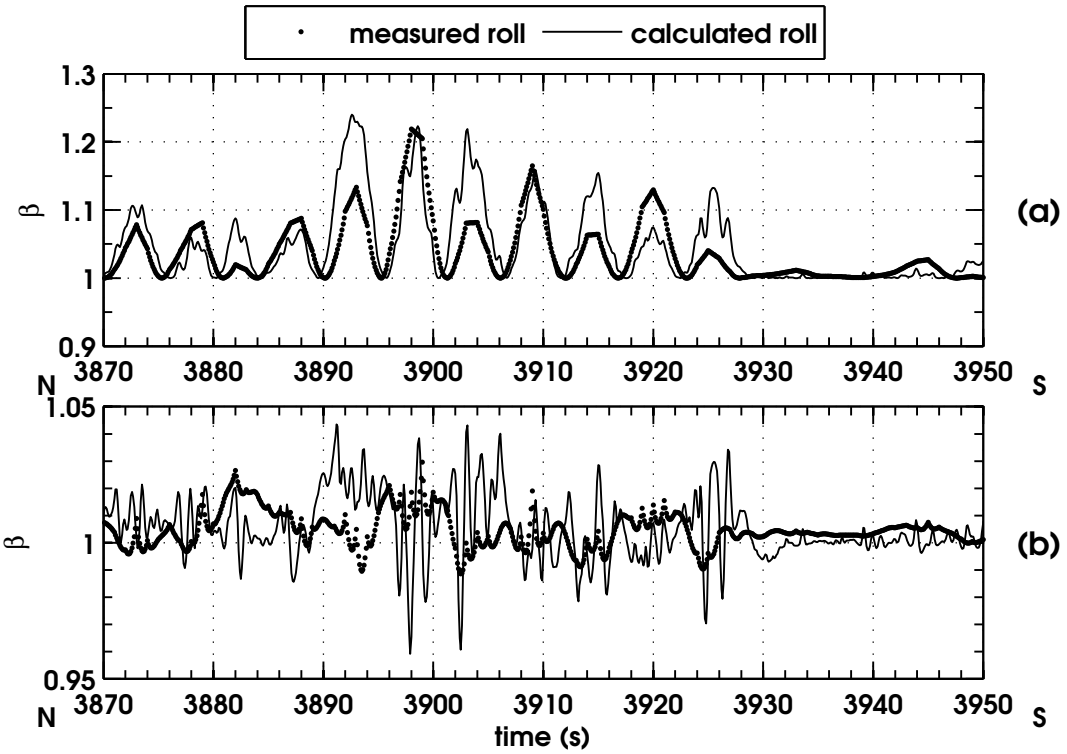

Figure 4.23: *(a) Predicted β using the response of a horizontal bird 30 m over a conductive half space and geometric factor based on measured (solid) and calculated (dots) roll (line 21020) affecting both cable swing and bird attitude. Differences up to 10% are seen. (b) Enlarged scale of β after application of a 10 s bird swing filter (equation (4.9)). Resulting differences are less than 5%.*

the system response based on roll measurements? Figure 4.23a shows that 10% differences appear due to the different methods of measuring roll. My suggestion is that further testing is done before we choose one method over the other. Clearly, the helicopter and towed bird GPS antenna method has merit, if only because these are routine position measurements and therefore add no extra cost to the survey.

In addition to the cost benefit of using my method of bird roll prediction, it also provides a very simple means as a check on the measured GPS roll angles. The dots in Figure 4.24 show that the roll angles measured with the triangular GPS array can be in error. At fiducial number 4452 on line 21030, the measured roll angle jumps from -20° to 10° in about 0.4 s. If we are to believe the measured roll angles, that means the bird slewed over at a rate of about 75°/s. This is not physically plausible since there are other such jumps at 4464 s and 4469 s. I have included my predicted

roll angles as a solid line in this figure, and they do not show any such motions. I believe that the jumps in measured roll are errors created by the algorithm used by the GPS receiver to calculate the angle. Furthermore, in the next section I will show that the bird pitch measurements experience similar jumps at exactly the same points in time.

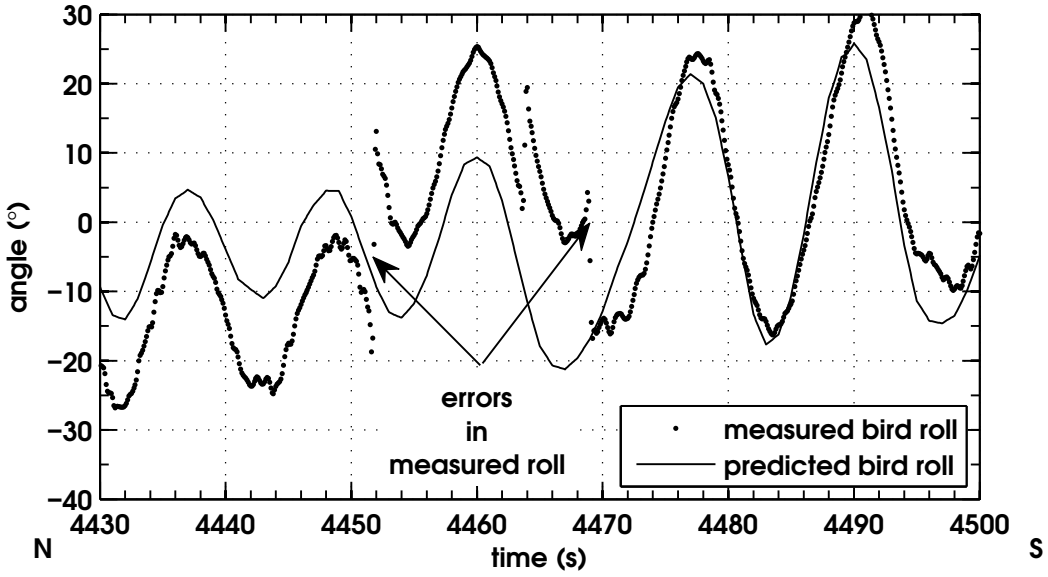

Figure 4.24: *Plot of measured and predicted bird roll angles versus time for a segment of line 21030 from the Sunraysia dataset. Measured bird roll (dots) predicts that the bird slews at a rate of about 75°/s at 4452 s, while predicted bird roll (solid) is smoothly varying. Similar jumps in measured roll occur at 4464 s and 4469 s.*

4.6.2 Attempt at Predicting Pitch

It is also possible to attempt to predict bird pitch from the helicopter and towed bird navigational GPS data, although as I will show, the results are limited. My prediction model relies on the rigid attachment model described in Section 4.4.2 and Davis et al. (2006).

In the rigid model, a cable of length c hangs from the hitching point of the helicopter (vector $\mathbf{c}$). At the bottom of the cable, the bird chassis is rigidly attached so that the nose points up at an angle of 20°: the model that I used in Figures 4.1 and 4.13. During normal survey conditions, the cable is swung back 20° and the

bird is towed horizontally. The GPS antenna on the towed bird is horizontally offset from the attachment point by ∼4.2 m (as shown in Figure C.2). This distance is vector $\mathbf{b_{GPS}}$ in Figure 4.25. The cable hitching point on the helicopter is offset from the helicopter navigation GPS antenna by about 7.7 m horizontally and 2.7 m vertically (vector $\mathbf{h_{GPS}}$). The helicopter is assumed to fly horizontally, which is not in general true. We say that the 'normal' position of the bird's GPS antenna is given by $\mathbf{r_0} = \mathbf{c} + \mathbf{b_{GPS}}$. To avoid confusion, a vector diagram is shown in Figure 4.25.

At every fiducial, we are given the position of the helicopter and bird GPS antennae, which I denote as vectors $\mathbf{h}$ and $\mathbf{b}$, respectively. The instantaneous position of the bird GPS $\mathbf{b}$ can also be determined by

$$\mathbf{b} = \mathbf{h} + \mathbf{h_{GPS}} + R(\theta_c, \phi_c)\mathbf{r_0}, \tag{4.14}$$

where $R(\theta_c, \phi_c)\mathbf{r_0}$ describes an arbitrary pitch and roll of the rigid towed bird using equation (4.2). After a pitch of ϕ_c and a roll of θ_c, the vector $\mathbf{r_0}$ points to vector $\mathbf{r}$, given by

$$\mathbf{r} = R(\theta_c, \phi_c)\mathbf{r_0},$$

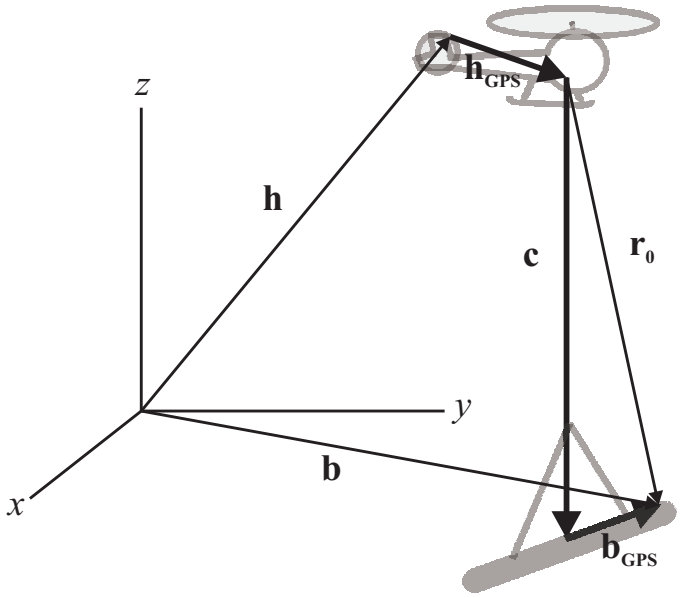

Figure 4.25: *Diagram showing how to predict pitch from helicopter and towed bird GPS position data.*

which is

$$\mathbf{r} = \begin{pmatrix} \cos(\phi_c) & 0 & \sin(\phi_c) \\ \sin(\phi_c)\sin(\theta_c) & \cos(\theta_c) & -\cos(\phi_c)\sin(\theta_c) \\ -\sin(\phi_c)\cos(\theta_c) & \sin(\theta_c) & \cos(\phi_c)\cos(\theta_c) \end{pmatrix} \begin{pmatrix} r_{0x} \\ r_{0y} \\ r_{0z} \end{pmatrix},$$

and evaluates to

$$\mathbf{r} = \begin{pmatrix} r_{0x}\cos(\phi_c) + r_{0z}\sin(\phi_c) \\ r_{0x}\sin(\phi_c)\sin(\theta_c) + r_{0y}\cos(\theta_c) - r_{0z}\cos(\phi_c)\sin(\theta_c) \\ -r_{0x}\sin(\phi_c)\cos(\theta_c) + r_{0y}\sin(\theta_c) + r_{0z}\cos(\phi_c)\cos(\theta_c) \end{pmatrix}. \tag{4.15}$$

Notice that the x-component of equation (4.15) has only the angle ϕ_c. All other quantities are known:

$$r_x = r_{0x}\cos(\phi_c) + r_{0z}\sin(\phi_c).$$

Solving this equation for ϕ_c yields

$$\phi_c = \tan^{-1}\left(\frac{r_x r_{0z}^2 + r_{0x}\sqrt{r_{0z}^2\left(r_{0x}^2 + r_{0z}^2 + r_x^2\right)}}{r_{0z}\left(r_x r_{0x} + \sqrt{r_{0z}^2\left(r_{0x}^2 + r_{0z}^2 + r_x^2\right)}\right)} \right). \tag{4.16}$$

The component r_x is given by equation (4.14):

$$r_x = b_x - h_x - h_{GPSx},$$

and we must take care using the arctangent function to pick the proper quadrant. Figure 4.26 shows my attempt at predicting the pitch of the rigid tow cable/bird model using equation (4.16). The thick red line is the pitch of the bird predicted from the simultaneous GPS data, but does not accurately reflect the pitch of the bird measured with the 3 GPS antennae mounted on the bird. This model and its predictions show that the independent pitching of the bird must be measured by at least two GPS antennae (mounted fore and aft of the bird) or by some other means.

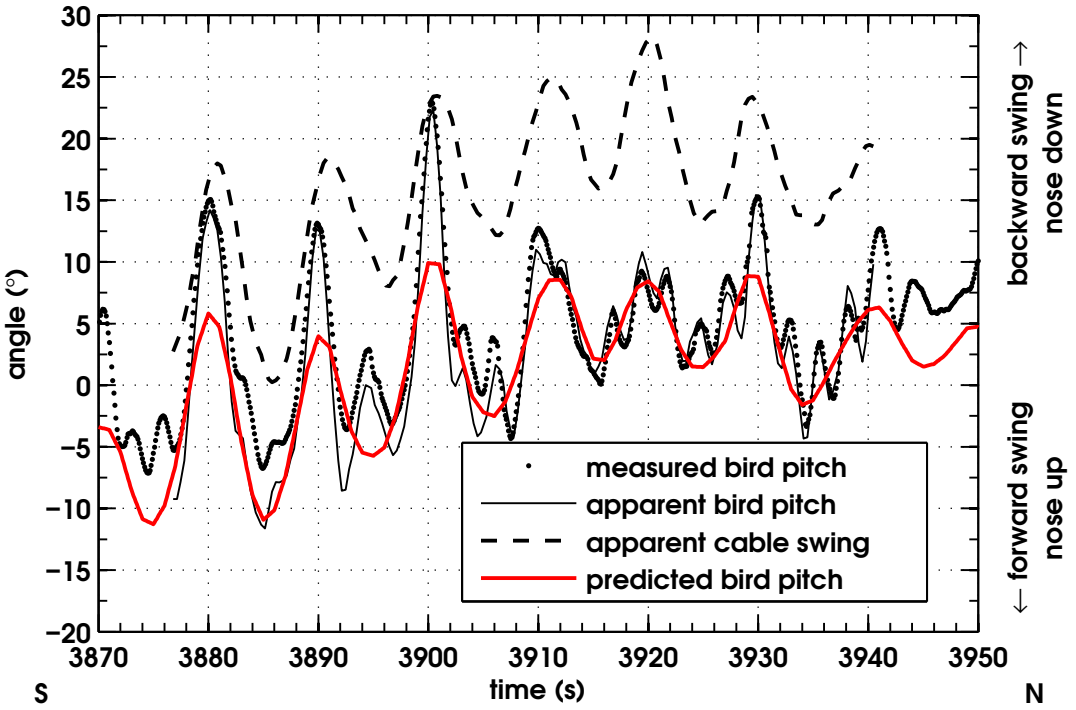

Figure 4.26: *Repetition of Figure 4.21 with the pitch predicted from a rigid model using equation (4.16) shown in thick red. Although the model follows the mia swinging of the towed bird, it cannot predict the actual pitch of the bird with any certainty.*

Although my method of bird pitch prediction does not accurately predict bird pitch, it is a convenient way to check the measured bird pitch angles provided by some other method. As an example of this utility, Figure 4.27 shows both the measured bird pitch and my predicted bird pitch versus time for a section of line 21030 from Sunraysia. It is easy to see a jump in measured bird pitch angles at fiducial 4452 s where the bird goes from -10° to 5° in about half a second. My predicted pitch angles vary smoothly over this time providing further evidence that the measured bird pitch is in error. Comparing with Figure 4.24 shows that a similar jump occurred at precisely the same time in the measured bird roll. I conclude that there are times when the algorithm that calculates bird pitch and roll from GPS position solutions gives misleading and erroneous angles. This is most likely due to information loss due to the rotation of the GPS antenna ground plates that

cause GPS satellites near the horizon to 'drop out'. The sudden loss of information presumably affects the position solution arrived at by the processor, which causes error in the measured roll and pitch values.

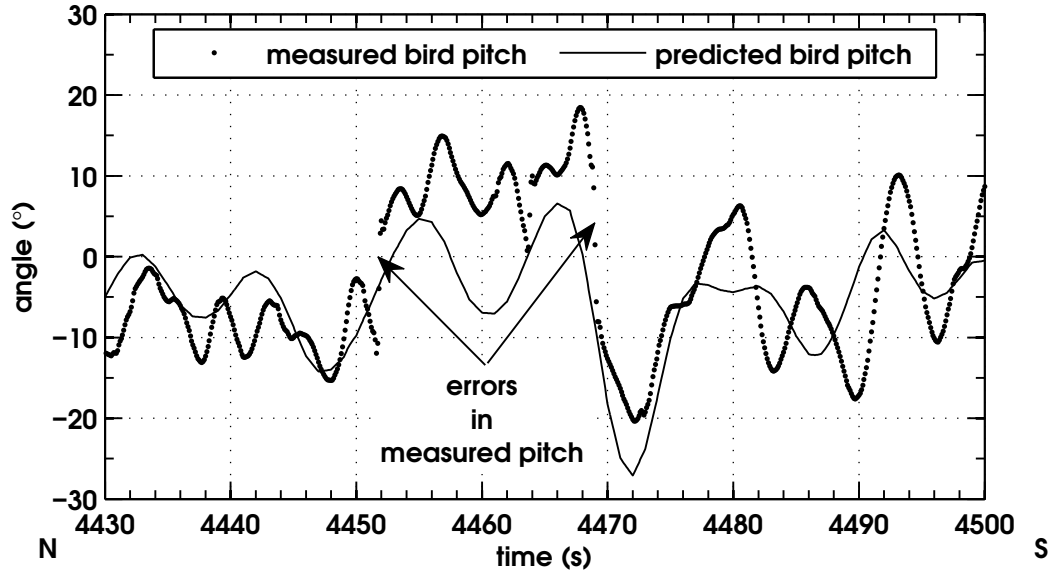

Figure 4.27: *Plot of measured (dots) and predicted (solid) bird pitch angles versus time for a segment of line 21030. Measured bird pitch reveals that the bird pitch changed by ∼15° in less than half a second. Predicted bird pitch (solid) shows a continuous and smooth change over the range of 4450 s to 4470 s. Comparison with Figure 4.24 shows that measured bird roll experienced similar jumps at the same times.*

4.6.3 Correcting β With Known Pitch and Roll

In this section, I present a final means of correcting β based on measured pitch and roll provided by the contractor. As shown in Section 4.4, bird pitch and roll changes the altitude measured by the altimeter. If we assume that a flat earth is beneath the towed bird, we can use the same model to calculate the altitude of the centre of the towed bird based on the altimeter reading and measured pitch and roll. Recall that equation (4.10) yields the direction of the laser altimeter after the bird is pitched by ϕ_b and rolled by θ_b. Let as take as origin the point on the plane $z = 0$ directly beneath the laser altimeter at each fiducial. The laser altimeter is therefore at the point $(0, 0, z_l)$, but points to the flat earth along vector $\hat{\mathbf{L}}$ (equation (4.10)), repeated

here:

$$\hat{\mathbf{L}} = -\sin(\phi_b)\,\hat{\mathbf{i}} + \cos(\phi_b)\sin(\theta_b)\,\hat{\mathbf{j}} - \cos(\phi_b)\cos(\theta_b)\,\hat{\mathbf{k}}.$$

The laser altimeter measures the distance D from the point $(0, 0, z_l)$ to the point $(x, y, 0)$ along vector $\mathbf{D}$. Thus we have

$$\mathbf{D} = x\,\hat{\mathbf{i}} + y\,\hat{\mathbf{j}} - z_l\,\hat{\mathbf{k}},$$

which may also be expressed as

$$\mathbf{D} = D\hat{\mathbf{L}}.$$

Taking the $\hat{\mathbf{k}}$ component of $\mathbf{D}$, we see that the actual altitude z_l of the laser altimeter above the flat earth is

$$z_l = D\cos(\phi_b)\cos(\theta_b),$$

which is consistent with Holladay et al. (1997).

Now that a corrected value of the laser altimeter altitude has been derived, the actual altitude of the centre of the bird remains to be found since we are assuming that the bird rotates about its centre point and central axis. The laser altimeter is separated from the centre of the bird by a horizontal distance of 2.6 m and after a pitch of ϕ_b, this translates into a vertical offset of $2.6\sin(\phi_b)$ m. This is because a positive pitching angle shifts the nose closer to the ground which means that the centre point of the bird is above the laser altimeter. The 'corrected' altitude of the centre of the bird is then

$$z_b = D\cos(\phi_b)\cos(\theta_b) + 2.6\sin(\phi_b)\ \text{m}.$$

Using the corrected altitude of the centre of the towed bird and the measured bird pitch and roll angles, I calculated β based on these values. In-phase and quadra-

ture signal response as measured by the system during survey are divided by the generalised geometric factor $G(\theta_b, \phi_b, z_l)$, now a function of pitch, roll and altitude (equation (4.6)).

The next 4 figures show the effectiveness of my response correction attempt. Figure 4.28 displays a grid of β for the 40 kHz component of the southeast section of the Sunraysia dataset using the laser altimeter. Bird swing can be seen in this figure by the spotting of the data, particularly over the reddish patch in the southwest corner of the figure. Figure 4.29 shows the same section of the Sunraysia set only with β calculated as discussed above, using equation (4.6).

The main difference between the two grids is that β in Figure 4.29 is reduced throughout the entire figure. Bird swing is not entirely eliminated from the data but it does seem to be reduced. It is clear from these two figures that geometric factor alone is not sufficient to remove bird swing from the data, even though it reduces the effect somewhat. The difference between original and 'corrected' β is shown in Figure 4.30. This grid shows that, in general, the original data is greater than the corrected data. Furthermore, bird swings are clearly shown in this figure by spots of yellow showing differences of approximately 5%. In other parts, such as the extreme east of the figure, the two grids differ by approximately -5%. As a comparison between 'corrected' β and filtered β, Figure 4.31 shows the same section of the survey with a 9 s bird swing filter applied to the data. Figure 4.31 and Figure 4.29 are remarkably similar in detail, with high-value β features clearly shown in both grids. The difference between them is that the filtered data will necessarily have some physical features removed from the data that should probably be present. Figure 4.29 does not try to remove anything extra from the data, but only to correct the existing data for bird swing using the available information.

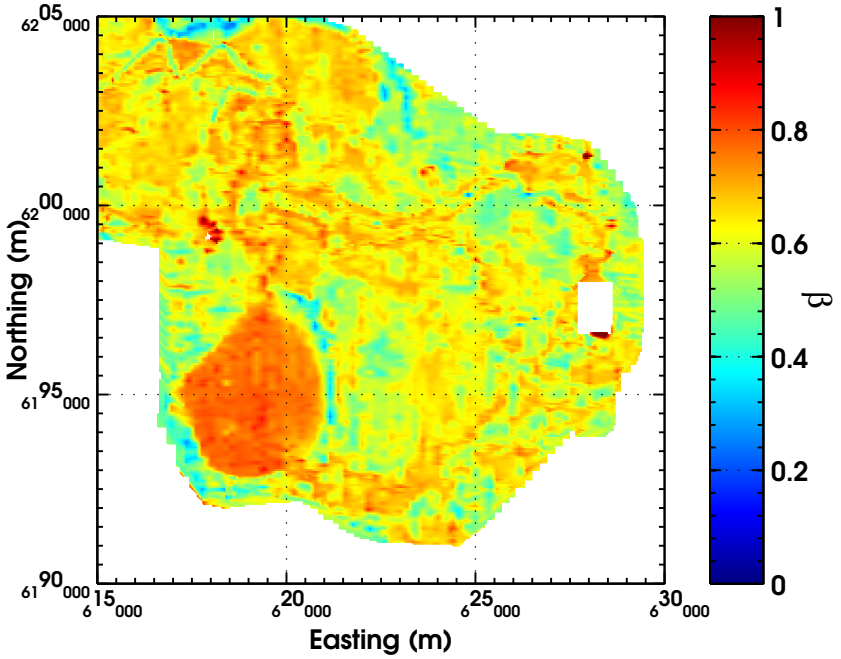

Figure 4.28: *Grid of β(laser) for a section of the 40 kHz component of the Sunraysia dataset. β was calculated with the laser altimeter as the height. Bird swing can be seen in this grid, particularly in the southwest corner of the figure.*

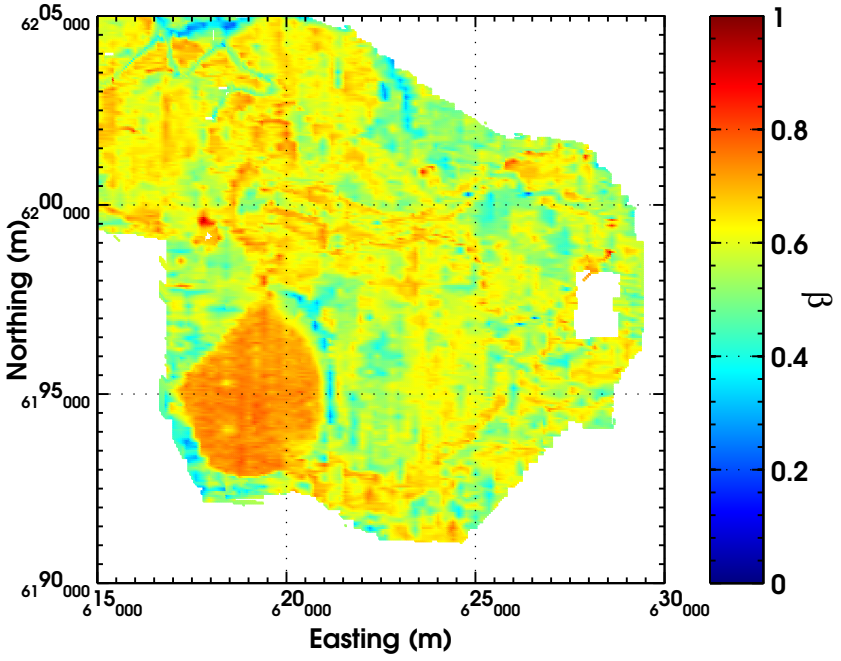

Figure 4.29: *Grid of same area with β 'corrected' using G calculated with measured pitch, roll and midpoint altitude.*

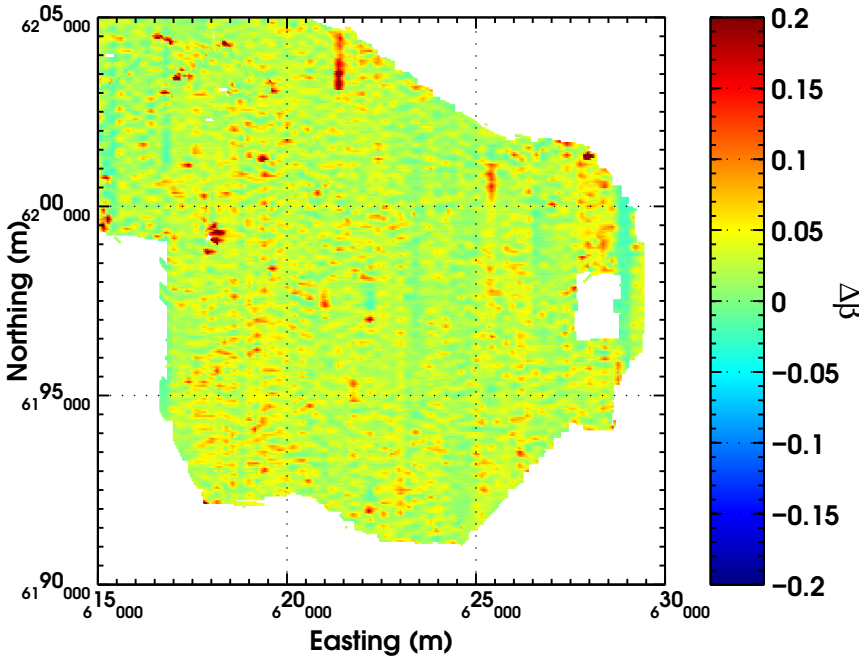

Figure 4.30: *Difference between original (Figure 4.28) and corrected (Figure 4.29) β for the southeast corner of the Sunraysia dataset.*

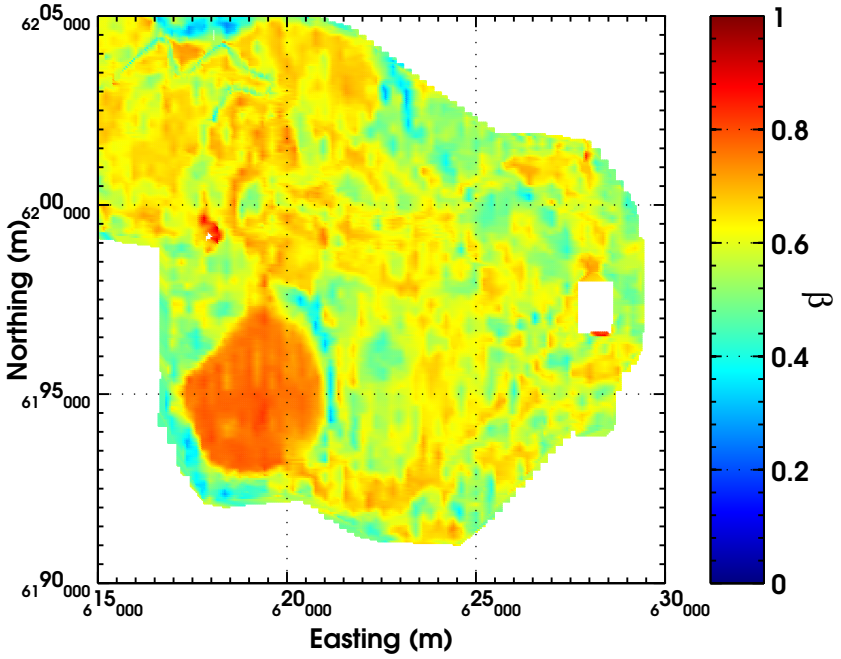

Figure 4.31: *Grid of β over the same southeast section of the Sunraysia survey, with β filtered with the laser altimeter bird swing filter set at 9 s (equation (4.12)).*

4.6.4 Problems with Altimetry

As mentioned in the last chapter, the laser and radar altimeters give differing values of altitude over and near watercourses. The situation is the same for the Sunraysia survey, with the radar altimeter recording incorrect altitudes over the Murray River. Figure 4.32 shows the DEM for the southeastern corner of the Sunraysia survey calculated using the laser altimeter and the bird's GPS position, equation (3.7). The same area is shown in Figure 4.33. The area inside the 6-sided polygon in the lower righthand side of the figure clearly shows that the radar altimeter is affected by the watercourse or the vegetation on its edges. I have included these figures to once again draw attention to some of the problems that accompany ground clearance measurement; and to show that the errors mentioned in Section 3.4.3 were not only apparent in the Chowilla dataset but can be found in the present case as well.

Closer examination of Figures 4.32 and 4.33 shows that there is also a constant offset in elevation between the two DEMs. The DEM calculated with the radar altimeter appears to be higher than the laser DEM. This is shown more clearly in Figure 4.34, which shows a histogram plot of the difference between the radar and laser altimeters ($h_r - h_l$) for the entire Sunraysia survey. This difference is most likely due to an error in the estimation of the separation distance between the helicopter and towed bird ($\sim$30 m).

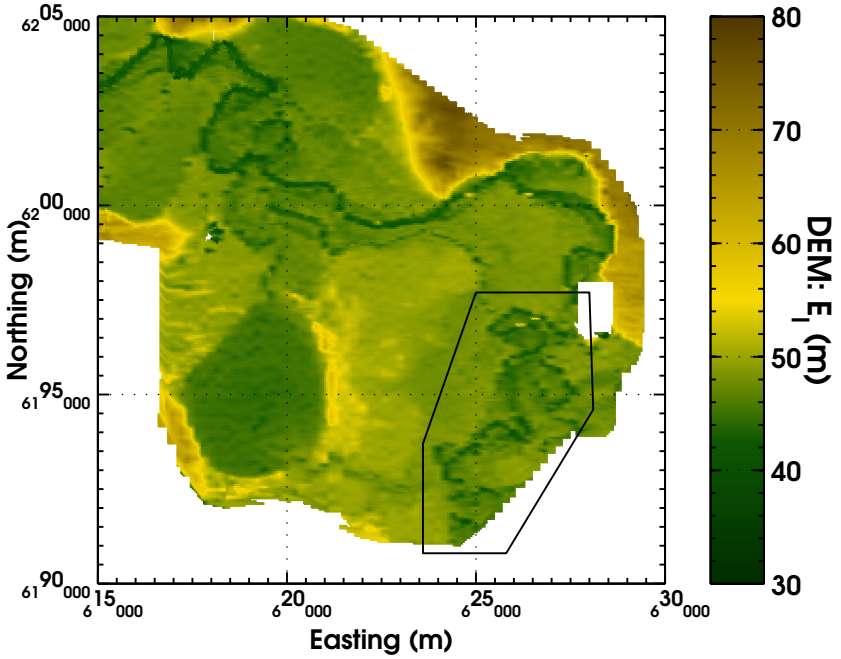

Figure 4.32: *Digital elevation map of the southeast section of the Sunraysia survey using the laser altimeter and bird's vertical GPS antenna position (equation (3.7)).*

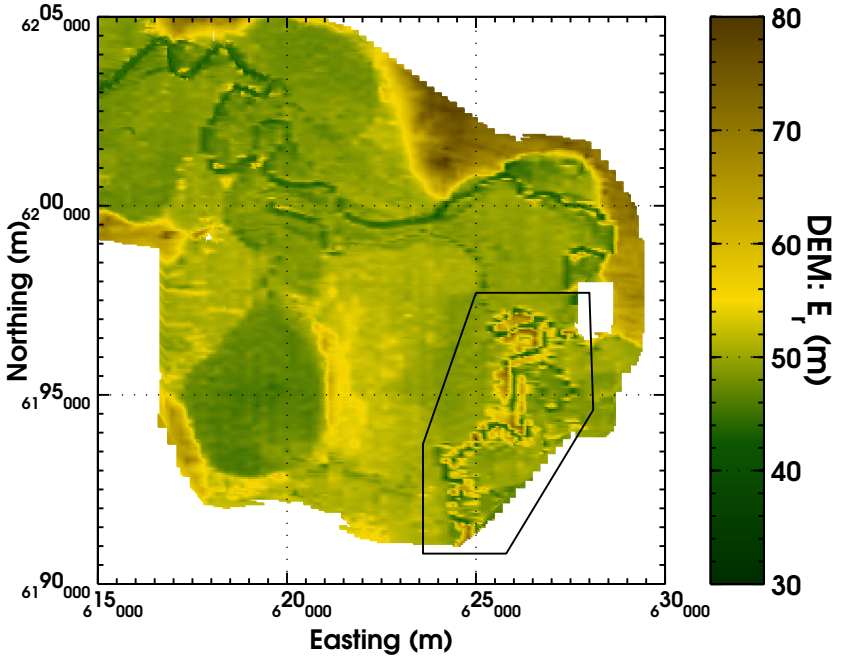

Figure 4.33: *DEM of the same section of Sunraysia using the radar altimeter (equation (3.8)). Inside the 6-sided polygon, the DEM shows that a section of the Murray River is 20 m higher than the surroundings.*

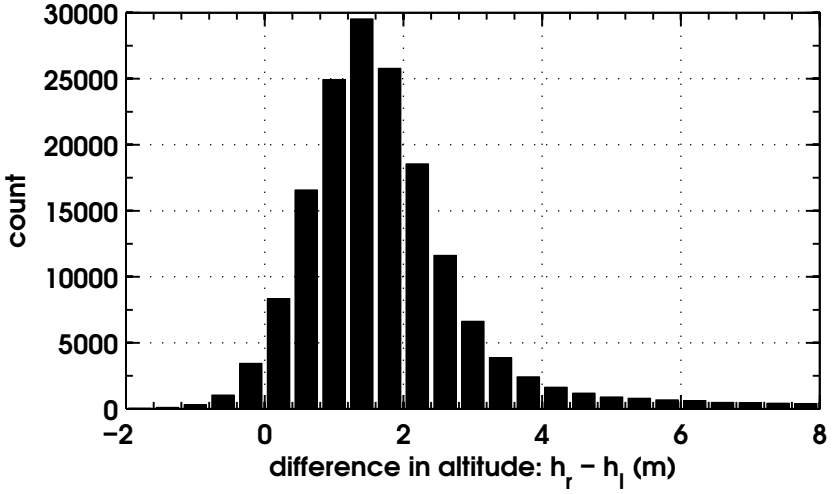

Figure 4.34: *Histogram plot of the difference between the radar and laser altimeters for the entire Sunraysia survey. The mean difference between the two altimeters is 2 m, but this graph shows that the most probable difference is 1.6 m to 1.8 m.*

4.7 Scale Model of the RESOLVE HEM System

In this chapter, I have developed models that divide the swinging of the HEM system into interdependent motions of the cable swinging fore-to-aft and side-to-side, and the bird rotating about its centre point and central axis. Although they have been investigated separately, the smaller bird motions are driven by and related to the cable motions. To investigate this relationship further, I made a scale model of the RESOLVE system and studied its movement when displaced from its rest position.

With the assistance of Luke Garde, I constructed a scale model of the RESOLVE HEM system using a 25 mm diameter PVC pipe of length 400 mm, string and LED lights. The 400 mm length of PVC pipe represented the 10.2 m length of the RESOLVE chassis; and from this I determined that the length of the string to represent the tow cable must be 1.25 m long to be a true length scale model of the 30.5 m tow cable. We attached the 'tow cable' to the ceiling and affixed 3 LED lights to the model as shown in Figure 4.35.

We video recorded the swinging of the model using a digital video recorder mounted on a tripod some 3 m away from the model. The model was set to swing-

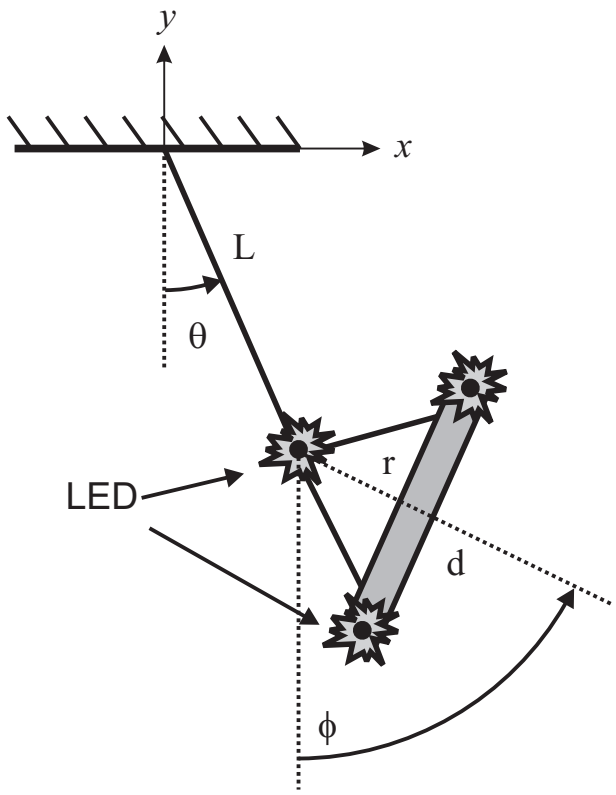

Figure 4.35: *Schematic of the model used to study the oscillatory behaviour of the RESOLVE HEM system.*

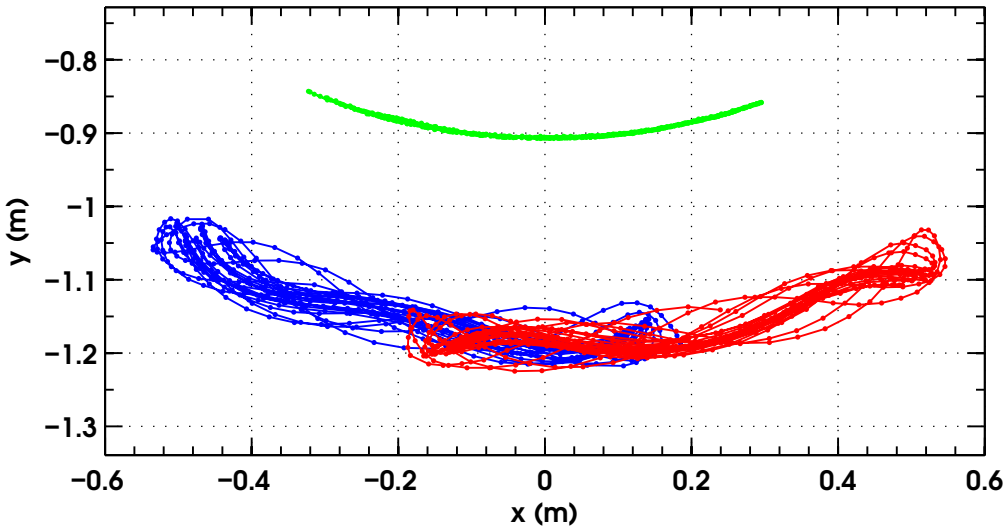

Figure 4.36: *x and y positions of the 3 LED lights attached to the RESOLVE model for one particular bird swing trial. Each point in the connected lines shows the position of the LED at a particular frame. Note the simple motion of the hitch and the Lissajous-like figures traced by the ends of the bird.*

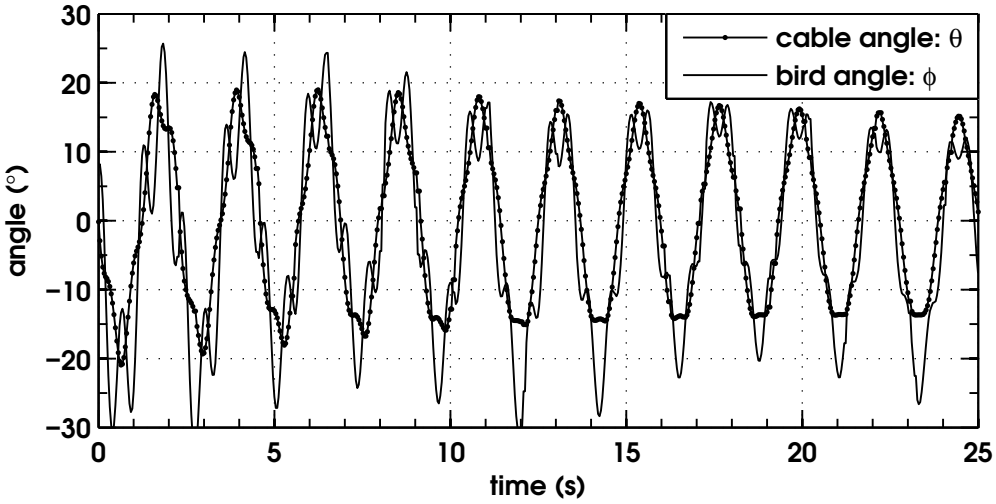

Figure 4.37: *Positions of the bird and cable converted and displayed as angles of rotation according to the schematic shown in Figure 4.35 versus time. The motion of the bird, and the extra 'kick' at the extremes are due to a momentum transfer from the swinging cable. Bird swing has higher frequency than cable swing.*

ing, and the video recording was ported over to a computer. I wrote a computer program in MATLAB® (The MathWorks, 2007) that recognised the LEDs based on image intensity and recorded their position in each frame. The original video segment and the derived video are presented in Appendix D.3. The x, y positions of the LED lights for the trial discussed in the Appendix are shown in Figure 4.36. Using the schematic shown in Figure 4.35, I converted the x, y positions of the cable and the bird into the angles θ and ϕ. A plot of these angles versus time is shown in Figure 4.37.

It is easy to see from Figure 4.37 that the bird swing is of a higher frequency than the cable swing for this trial cable length L and support length r. To examine the different effects that the distances L and r have on the period of the cable and bird, we ran several model trials with different lengths. The x, y positions were recorded and the angles calculated for each trial. As well, I examined the power spectrum of each angle versus time series and extracted the cable and bird oscillation frequency. The results of these experiments are displayed in Table 4.1.

Table 4.1: *Result of model bird swing trials. Changing L and r affects periods of cable (T_θ) and bird swing (T_ϕ). The last column shows the ratio of bird swings to cable swings.*

L (mm)	r (mm)	T_θ (s)	T_ϕ (s)	bird:cable
1150	95	2.27	0.75	3.0:1
905	270	2.15	0.53	4.1:1
840	95	2.04	0.75	2.7:1
465	95	1.57	0.72	2.1:1

It is clear that the period of the cable, that is the main swinging period of the system, increases with L. This is to be expected, since it is well established that pendulum period increases with length (e.g. Fowles and Cassiday, 1993), and this system is very much like a simple pendulum. It is also apparent from the table that increasing r decreases the period of oscillations for the bird (T_ϕ). This is also to be expected since the moment of inertia increases with increasing r, and hence reduces the period of oscillation of the second member.

4.7.1 Equations of Motion of the Towed Bird

As the final subject in this chapter I present a model of the simplest sort for the towed RESOLVE system. In this model, a cable of length L attaches to a 'Y' formation that splits off to suspend a rod of length d from the front and rear. The distance from the 'Y' join to the centre of the rod is length r. The planar motion of this system, neglecting yaw, can be constrained to two dimensions. The motion can be described by determining the equations of motion for the two coordinates. In the case shown in Figure 4.35, the coordinates are θ and ϕ. In general, they are functions of time, coupled together. The total mass M of the system is contained in the cylinder.

With the model described above, and shown in Figure 4.35, it is possible to write down the kinetic and potential energy of the system. The kinetic energy T of the

system is

$$T = \frac{ML^2\dot{\theta}^2}{2} + \frac{I\dot{\phi}^2}{2} + MLr\dot{\theta}\dot{\phi}\cos(\phi - \theta),$$

where I is the moment of inertia of the cylinder, r in the last term coincides with the distance to the centre of mass of the mass system, and the dots above the θ and ϕ variables represent a time derivative of the variable. The potential energy V of the system is much more simple to express:

$$V = -Mg\big(L\cos(\theta) + r\cos(\phi)\big),$$

where g is the acceleration due to gravity, 9.81 $\frac{\mathrm{m}}{\mathrm{s}^2}$.

From the kinetic and potential energy of the system, we can immediately state the Lagrangian equation of the system:

$$\mathcal{L} = T - V,$$

which becomes

$$\mathcal{L} = \frac{ML^2\dot{\theta}^2}{2} + \frac{I\dot{\phi}^2}{2} + MLr\dot{\theta}\dot{\phi}\cos(\phi - \theta) + Mg\big(L\cos(\theta) + r\cos(\phi)\big).$$

The generalised momentum of the first coordinate can be found by taking the derivative of the Lagrangian equation with respect to the time derivative of the first coordinate:

$$p_\theta = \frac{d\mathcal{L}}{d\dot{\theta}},$$

where p_θ is the generalised momentum of θ. Taking the derivative yields

$$p_\theta = ML^2\dot{\theta} + MLr\dot{\phi}\cos(\theta - \phi),$$

while keeping the same form for the ϕ coordinate yields

$$p_\phi = I\dot{\phi} + MLr\dot{\theta}\cos(\theta - \phi),$$

which is the generalised momentum of the second coordinate. These last two equations form a system of generalised momenta that may be solved to derive expressions for $\dot{\theta}$ and $\dot{\phi}$ as follows

$$\left\{ \begin{array}{l} \dot{\theta} = \dfrac{Ip_\theta - MLrp_\phi\cos(\phi-\theta)}{ML^2\big(I - Mr^2\cos^2(\phi-\theta)\big)} \\ \dot{\phi} = \dfrac{Lp_\phi - rp_\theta\cos(\phi-\theta)}{L\big(I - Mr^2\cos^2(\phi-\theta)\big)} \end{array} \right\}. \tag{4.17}$$

This forms the first two equations of motion for the system. The remaining two must come from the Hamiltonian equation $\mathcal{H}$ which is defined as

$$\mathcal{H} = T + V.$$

Using the results of equation (4.17) in the Hamiltonian equation above we arrive at

$$\mathcal{H} = \frac{1}{I - Mr^2\cos^2(\phi-\theta)}\left(\frac{Ip_\theta^2}{2ML^2} + \frac{p_\phi^2}{2} - \frac{r}{L}p_\theta p_\phi\cos(\phi-\theta)\right) - Mg\big(L\cos(\theta) + r\cos(\phi)\big).$$

The time rate of change of the generalised momenta is determined by taking the derivative of the Hamiltonian equation with respect to the coordinate, i.e. for the θ coordinate, we have

$$\dot{p_\theta} = \frac{d\mathcal{H}}{d\theta},$$

while for ϕ we have

$$\dot{p_\phi} = \frac{d\mathcal{H}}{d\phi}.$$

Taking the derivative of $\mathcal{H}$ with respect to θ, and taking the derivative of $\mathcal{H}$ with

respect to ϕ yields the system of equations

$$\left\{\begin{array}{l} \dot{p_\theta} = \dfrac{-2Mr^2\cos(\phi-\theta)\sin(\phi-\theta)}{\big(I - Mr^2\cos^2(\phi-\theta)\big)^2}\left(\dfrac{Ip_\theta^2}{2ML^2} + \dfrac{p_\phi^2}{2} - \dfrac{r}{L}p_\theta p_\phi\cos(\phi-\theta)\right) \\ \qquad + \dfrac{rp_\theta p_\phi\sin(\phi-\theta)}{L\big(I - Mr^2\cos^2(\phi-\theta)\big)} - MLg\sin(\theta) \\ \dot{p_\phi} = \dfrac{2Mr^2\cos(\phi-\theta)\sin(\phi-\theta)}{\big(I - Mr^2\cos^2(\phi-\theta)\big)^2}\left(\dfrac{Ip_\theta^2}{2ML^2} + \dfrac{p_\phi^2}{2} - \dfrac{r}{L}p_\theta p_\phi\cos(\phi-\theta)\right) \\ \qquad - \dfrac{rp_\theta p_\phi\sin(\phi-\theta)}{L\big(I - Mr^2\cos^2(\phi-\theta)\big)} - Mrg\sin(\phi) \end{array}\right\}. \tag{4.18}$$

Equations (4.17) and (4.18) form a system of coupled first-order differential equations that depend on L, and r. Noticing that the generalised momenta depend on I the moment of inertia, we can see that neither $\dot{\theta}$ nor $\dot{\phi}$ depend on the mass of the bird. The *distribution* of the mass, however, does affect them. This can be seen from equations (4.17), and realizing that the moment of inertia of a distributed mass is

$$I = \sum_{i=1}^{N} m_i r_i^2,$$

where N is the total number of mass elements, m_i is the mass of the i^{th} element, and r_i is its distance away from the object's centre of mass. For a RESOLVE system, it is simplest to assume that the chassis is a solid rod of uniform mass distribution and length $d = 10.2$ m. In that case, the moment of inertia is

$$I = \left(\frac{d^2}{12} + r^2\right)M,$$

where the first term arises from a rod of length d rotating about its central axis, and the second term arises due to the parallel axis theorem where the rod is actually rotating about the 'Y' on the tow cable, a distance r away (Fowles and Cassiday, 1993). Using this moment of inertia for a RESOLVE model where the cable length L is 27 m and the vertical displacement from the 'Y' to the centre of the chassis

is $r = 3.5$ m, displacing the bird by 5° yields Figure 4.38. The predicted cable swing has a period of approximately 12 s, which is longer than the 9–10 s observed in reality: the predicted bird pitch is about 4 times to every cable swing, which is consistent with the Sunraysia video.

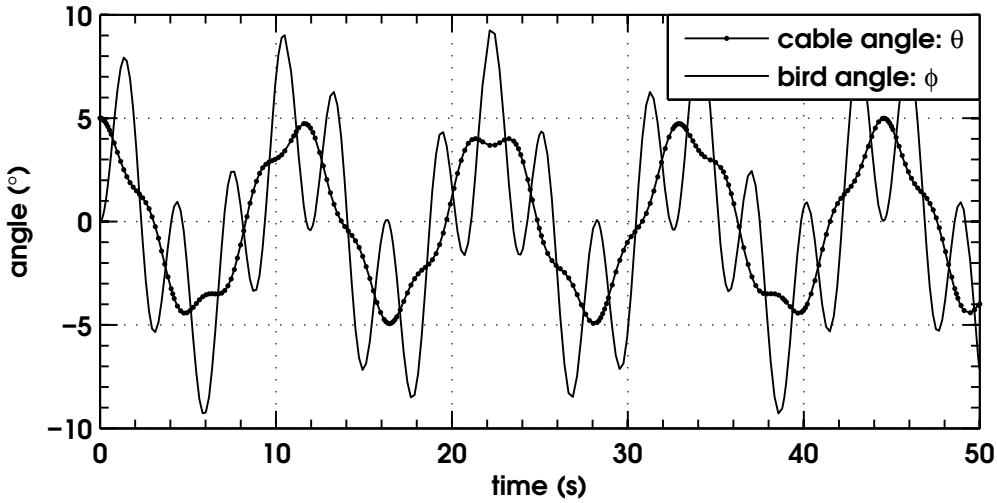

Figure 4.38: *Plot of cable (θ) and bird (ϕ) swing versus time as a result of numerically solving the system of differential equations (4.17) and (4.18) with $L = 27$ m, $r = 3.5$ m, $d = 10.2$ m and $\theta(0) = 5°$. Notice that the bird pitches approximately 4 times to every cable swing, similarly to what was seen in the Sunraysia video.*

The moment of inertia that I have chosen to illustrate for this model does not reflect the actual distribution of mass in the towed bird. Obviously, it is important to know the mass distribution and it is likely that it is something more like a few large point-like masses (due to the copper coils) placed inside a comparatively light cylindrical shell. My model is one of the simplest to consider and, it must be said, ignores the effect of air resistance. Equations of motion including drag become much more complicated and it was felt that the effort would outweigh the potential benefit.

4.8 Summary and Conclusion

I began this chapter by asserting that there is a relation between bird swing and system response based on the evidence from Chapter 3. In Section 4.2, I developed a

model that shows how bird swing affects system response when the radar altimeter mounted on the helicopter is used to estimate the altitude of the towed bird on survey. Radar altimeter measurement is insensible to bird swing, so when viewing β calculated using radar altitude estimates, bird swing readily shows up in the data. Any swing that lifts the bird away from the earth will reduce the response of the system; consequently β is reduced. Swings that reduce the separation of the bird from the earth increase the response and hence β.

Similar results are seen when a bird-mounted laser altimeter is used to measure bird altitude, although the effect on β is somewhat more complicated. Rotations of the bird due to cable swing and wind buffeting etc. cause the altimeter reading to be in error. This changes β in two ways. First, bird rotation changes the system response. The maximum amount that it can change by, in the inductive limit, is governed by the generalised geometrical factor derived in equation (4.6). Second, laser altimeter error enters the calculation of β by its inclusion in equation (4.6). The result of this combination was discussed in Section 4.4.

For both the radar altimeter and laser altimeter cases, I designed a filter that removes the effect of bird swing from β provided the main frequency of the oscillation is known. These filters, described by equation (4.9) for the case of the radar altimeter and equation (4.12) for the laser altimeter remove both the fundamental and the first harmonic frequency effects from β. The first harmonic frequency also contains a magnitude term that must be added to β calculated with radar altimeter data and subtracted from β calculated with the laser altimeter data. I have shown their efficacy in filtering β in the Sydney Harbour, Chowilla Floodplain and Sunraysia datasets, and am convinced that they can be used to enhance the final data from a survey.

By using sequential photographs to make a stop-action movie, I have determined the fundamental frequencies of the cable swing and bird pitch for the Sunraysia survey. My measurement of predicted bird and cable swing corroborate the mea-

surements of bird pitch and roll provided by the contractors. In my opinion, a third method needs to be tested before any more conclusions can be drawn. Using the simultaneous position solutions of the helicopter-mounted GPS antenna and the bird-mounted GPS antenna it is possible to predict roll of the bird to within about 5°. In my particular test on a section of line 21020 from the Sunraysia survey, there appeared to be a systematic difference of ∼2° between my prediction of bird roll and the measured roll provided by the contractors. Again, a third test should be applied to establish which method is more in error. Despite the fact that bird roll is very easily predicted from the GPS data, bird pitch predictions are not as successful. In Section 4.6.2, I showed that my bird pitch predictions were different from the measured and apparent bird swing predictions by about 5°; but there are times when the error is as great as 10°–12°. I conclude that bird pitch cannot be predicted from helicopter and bird GPS position solutions. The prediction is useful, however, as a check on the bird pitch values measured by the 3 GPS antenna array.

In this chapter, I studied the pendulum-like motion of a scale RESOLVE model. From analysis of the video recordings, I discovered that the bird swing period decreases with increased 'Y' attachment length, even though the period of the cable increases with increased length. Furthermore, the ratio of ∼4 bird swings to 1 cable swing is not unique to the system: it can be changed by altering the separation of the 'Y' attachment to the centre of the bird. I developed a simple mathematical model that predicts the behaviour of a rigid member that is attached to two cables and is allowed to rotate about their join. This is in essence a simplification of the classic double pendulum problem (e.g. Fowles and Cassiday, 1993), and the system of first-order differential equations has been presented here.

To close the chapter and my discussions of pendulum like behaviour of towed HEM systems, I present a few conclusions and recommendations for future researcher and field workers. First, I have substantively proven that the β domain is an excellent tool to investigate the effects of bird swing in data. It provides a means to test for

bird swing and is also an excellent domain to test for any corrections that are made to the data as a consequence of trying to eliminate it. Furthermore, bird swing is most easily seen when calculating β using the altitude estimated with the radar altimeter, and I strongly recommend using that as a first tool. System testing for bird swing is most readily accomplished over an area of uniform conductivity such as seawater. It provides an excellent basis for seeing the signature oscillations in β that indicate bird swing.

When using a laser altimeter to measure bird height above earth, it is important to keep in mind the position of the laser altimeter on the bird and its orientation. It is normal on the RESOLVE towed birds for the laser altimeter to be housed in the underside of the chassis, close to the nose. As I have shown in this chapter, this creates a sine type of error in the measured altitude when the bird swings, and it is not an accurate reflection of the separation of the centre of the transmitter and receiver coil pair. I therefore recommend that the laser altimeter is mounted as closely as possible to the rotation point of the bird. With this arrangement the laser altimeter error will only be an overestimate of the true altitude of the bird, effectively shifting the solid line in Figure 4.14 up and to the right so that it is symmetrical about a vertical line at the point $(0, 1)$. This simplifies the error predictions due to bird swing using the laser altimeter.

Pitch and roll measurement of a towed bird is a tricky problem. In the Sunraysia survey discussed in this chapter, the contractors used 3 GPS antennae mounted in a triangle configuration that enabled them to measure roll, pitch and yaw. While these measured values appeared to be reasonable, I have proven that there are times when they are in error. Furthermore, there does not appear to be any way to predict the times that the measured values will be in error. As a check on this, I recommend my method of checking measured bird pitch and roll based on helicopter and bird GPS position solutions. In addition, I believe that so long as $\pm 5^\circ$ errors are permitted in the measurement of bird roll, one GPS antenna may be removed from the 3 GPS

triangular array. This would leave just two GPS antennae, mounted fore and aft on the bird, to measure bird pitch and yaw.

I have attempted to correct EM system data with the measured bird pitch and roll values provided by the contractor, but my success was limited. The method that I used, based on the generalised method of images and corrected laser altitude does not yield a significant improvement to the same area that has had a bird swing filter applied to it. The main advantage of the method is that it offers a point-by-point calculation to the data rather than a time series filtered output. The bird swing filters are specifically designed to remove features that repeat with particular frequency. If there is a real repeating physical feature in the data that shares the same period as a bird swing, it will be removed. The point-by-point method will not do this. It is interesting to note that the generalised method of images offers the same order correction to the data as the correction derived by Fitterman and Yin (2004) for the HCP coil pair. They report that, like the generalised method of images, in-phase and quadrature data changes with pitch and roll angles via a cosine squared relation. I believe that, since Figure 4.29 is so little different from Figure 4.28, more care must be given to their $\frac{T_2}{BT_0}$ term, and we cannot simply assume that it goes to 0.5 as they suggest.

Finally, I have derived some equations of motion for the RESOLVE towed bird system in free space subject only to an initial displacement and the force of gravity. From these equations, it is possible to predict the fundamental frequencies of the cable and bird swings. In the simple example I have given, a cable of 27 m attached to a 'Y' member of cord that suspends a towed bird of 10.2 m length 3.5 m below the attachment has a cable swing period of $\sim$12 s and a bird pitch period of $\sim$3 s. These periods are close to the oscillations observed in the data and offer a simple first step to predicting bird and cable swing for future towed bird systems.

4.4 Bird Swing Model: Laser Altimeter

We can use the mathematical models derived in the last sections to model changes in β that occur during bird swing when the altitude is measured with a laser altimeter rigidly mounted on the bird. The laser altimeter used in RESOLVE surveys is typically mounted in the underside of the chassis of the bird near the nose. This is shown in Figure C.2, where I have marked the distance of the laser altimeter from the nose of the bird. If the bird does not pitch or roll when the tow cable swings, the laser altimeter will properly measure the altitude of the bird. Changes in system response due to altitude change will be balanced exactly by G calculated using the laser altitude, and β will not change at all. This is obviously the intention of system designers. Problems arise when the bird is subject to attitude changes. Not only does the geometric coupling change but the measured laser altitude changes as well. The change in laser altitude will not be a correct measurement of the altitude of the centre of the coil pair, and β will change. We can predict the change occurring using the same method as we did before.

4.4.1 Pitch and Roll of the Bird

When the bird is pitched and rolled about its centre point, the transmitter and receiver coils change their orientation according to the Figure 4.2. This results in the more generalised coupling of the coils with the earth as shown in Figure 4.4. Appropriately, we can use the more general computation of equation (4.6) to calculate the inductive limit coupling of the pitched and rolled bird to the earth beneath. The significant change from Section 4.2 is the measurement of h by the laser altimeter. A schematic of bird rotation and its implication for laser altimeter error is shown in Figure 4.13.

It is easy to see from the figure that bird pitch will cause the laser altimeter to over- and underestimate the measured altitude of the centre point of the bird. When

the cable is tilted back, as is normal on survey, negative tilting of the bird will raise the nose upwards away from the earth. The laser altimeter, mounted near the front of the bird, will yield an altitude too great. Tilt the nose downward and the laser altimeter will underestimate the altitude before it once again overestimates it. This peculiar behaviour is due to the fact that the laser altimeter is near the nose of the bird. If the laser altimeter was located directly beneath the centre point of the bird, it would always overestimate the altitude whenever the bird was pitched. By way of comparison, whenever the bird is forced into a roll, the laser altimeter will always overestimate the altitude of the centre of the bird.

We can model changes in β resulting from bird swing and altimeter error. As before, the cable is swung back ϕ_0 degrees so that the bird is towed horizontally and level with the earth during normal survey conditions. The actual and measured altitude of the centre of the bird is h_0, say 30 m. An origin is placed below the centre

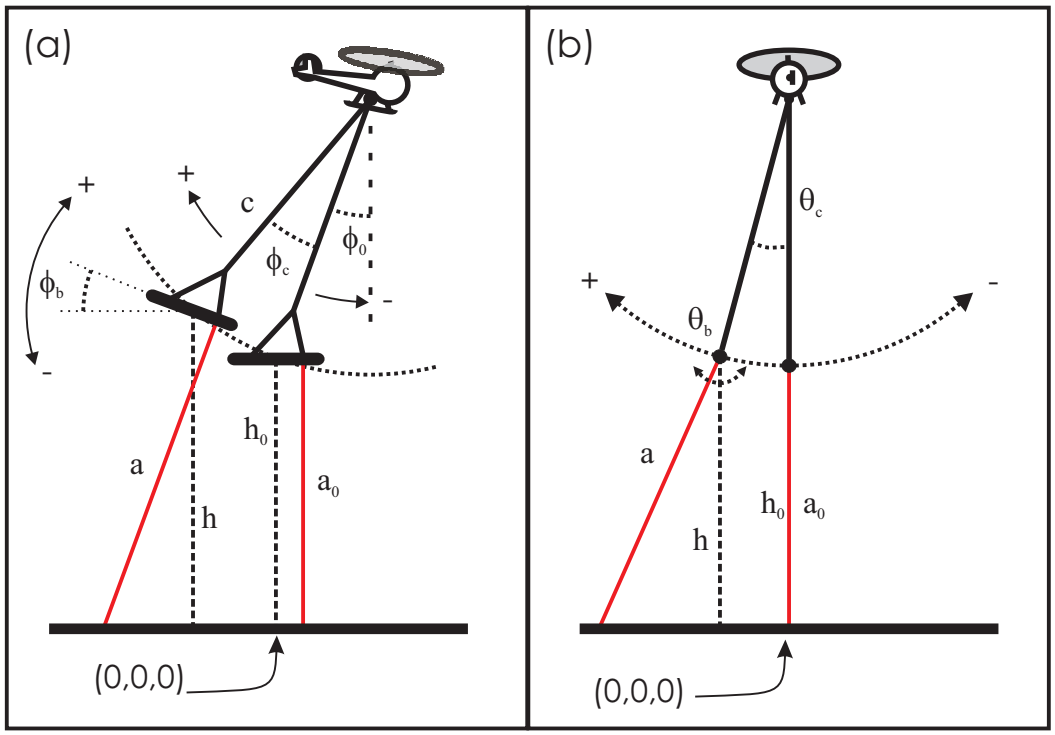

Figure 4.13: *Schematic of how bird swing creates altimeter error when using a laser altimeter. (a) Bird pitch causes the laser to both over- and underestimate the actual altitude h. In this panel, the measured laser altitude a is greater than h. (b) Roll always makes the laser altimeter overestimate the actual altitude of the bird.*

of the bird in its mean survey position, and we once again express the position of the centre point as vector $\mathbf{b} = \mathbf{h} + R(\theta_c, \phi_c)\bar{\mathbf{c}}$ (equation (4.3)). The altitude of the centre of the bird after any cable swinging will therefore be the $\hat{\mathbf{k}}$ component of $\mathbf{b}$. Let's say that the altimeter mounted underneath the bird points in the negative z-direction so that it points directly downward when the bird is level. We will call this vector $\hat{\mathbf{L}}_\mathbf{0}$. After an arbitrary pitch or roll of the bird, the laser altimeter vector $\hat{\mathbf{L}}$ points in the direction given by

$$\hat{\mathbf{L}} = R(\theta_b, \phi_b)\hat{\mathbf{L}}_\mathbf{0}.$$

This is expressed as

$$\hat{\mathbf{L}} = -\sin(\phi_b)\,\hat{\mathbf{i}} + \cos(\phi_b)\sin(\theta_b)\,\hat{\mathbf{j}} - \cos(\phi_b)\cos(\theta_b)\,\hat{\mathbf{k}}. \tag{4.10}$$

Inspection of Figure C.2 shows that the laser altimeter is offset from the centre of the bird by a small horizontal and vertical displacement. From measurement, the laser altimeter is horizontally offset from the midpoint of the bird by ∼2.6 m. The vertical offset from the middle of the bird is about 0.3 m. These distances are expressed as vector $\mathbf{a}$, so that when the bird pitches and rolls, the laser altimeter is located at $\mathbf{l}$, where

$$\mathbf{l} = \mathbf{b} + R(\theta_b, \phi_b)\mathbf{a}. \tag{4.11}$$

With the position of the laser altimeter described by equation (4.11) and the laser pointing in the direction given by equation (4.10), we can calculate what the altitude measured by the laser altimeter would be if the bird was towed over a flat earth. This is done by extending the unit vector $\hat{\mathbf{L}}$ from position $\mathbf{l}$ to the plane at $z = 0$ using a parametrisation of vector $\hat{\mathbf{L}}$:

$$\mathbf{L} = t\hat{\mathbf{L}},$$

where $\mathbf{L}$ is the vector from $\mathbf{l}$ to the point $(x,\ y,\ 0)$. This yields the system of equations,

$$\begin{pmatrix} tL_x = x - l_x \\ tL_y = y - l_y \\ tL_z = -l_z \end{pmatrix},$$

which is readily solved for t. Inspection reveals that $t = l_z/L_z$: the length of the vector and hence the measured altitude h' is

$$h' = \left|\frac{l_z}{L_z}\right| + 0.3\,\mathrm{m},$$

which will be in error whenever the bird is pitched or rolled. I have included the small distance of 0.3 m to account for the slight vertical offset of the laser altimeter from the midline of the bird. I can only assume that laser altimeters in actual survey systems have this vertical offset programmed into them.

The bird is towed at a nominal survey altitude of 30 m and slung behind the helicopter by ϕ_0 degrees, as shown in Figure 4.13. When the bird is level to the earth, the laser altimeter reads $h' = 30$ m, and β is therefore 1. This will hold for any swinging of the tow cable *provided the bird stays level*. Let the bird pitch $\pm 20°$ about its centre point while remaining at altitude 30 m. The response of the system changes just as it did in Section 4.2, but this time the laser altimeter records erroneous altitudes. To model β we use equation (4.6) for the response of the bird, and equation (3.5) for the calculation of G; β is their ratio. The result is shown in solid black in Figure 4.14. The direction of the x-axis is reversed in this graph to be more intuitive when using Figure 4.13 as a reference for swing. Values to the left of the graph mean that the nose of the bird has been pitched downwards. The laser altimeter is near the nose of the bird, so when it gets dipped down, the laser altimeter records smaller values of altitude, thereby increasing G. Bird pitch always reduces response, so β decreases. This continues until the laser altimeter records

larger and larger altitudes, decreasing G and increasing β. Eventually, altimeter error balances the change in response and the ratio is again 1.

In the case shown, this occurs when the bird is pitched about 14°. After that, both bird pitch and laser error combine to increase β well above the nominal value. For comparison, the model of β using bird pitch and radar altimetry is shown as a dashed line in Figure 4.14. For the same amount of pitch, the reduction due to geometric coupling is only about 5% at full swing (dashed line). The laser altimeter error creates an enormous 4–23% increase in the ratio for the same amount of pitch.

Error caused by bird roll is similar in effect. The dotted line in Figure 4.14 shows a symmetrical increase in β for tube rolls of the bird. Again, laser altimetry results in a drastic reduction of G creating large increases in β despite the reduction in response caused by the tube roll. For small values of roll, β can change a great deal (21% for a 20° roll). To show how these errors can affect β when a towed bird is subjected to pitch and roll similar to those seen in Chowilla and as predicted for Sydney Harbour, I will present some synthetic data representing bird swings.

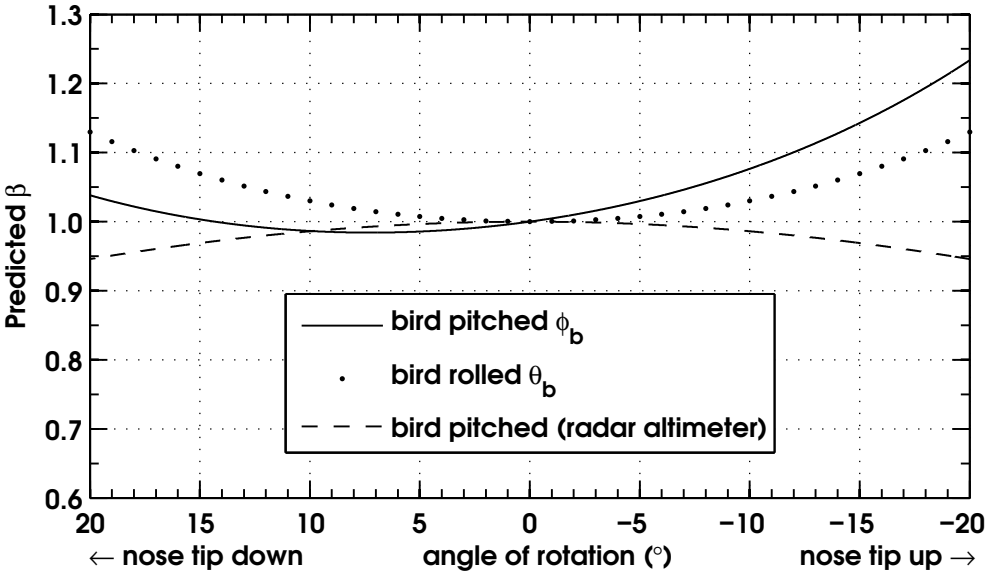

Figure 4.14: *Predicted β reflecting changes to the geometric coupling and altimeter error caused by bird rotations.*

4.4.2 Synthetic Examples of Rotation

The synthetic data that I will present in this section will be the one used by Davis et al. (2006). The model is a 30.5 m tow cable rigidly attached to the bird so that when the cable is pitched or rolled, the bird is also rotated. The tow cable is slung back ϕ_0 so that the bird is level to the earth. Further rotations of the cable move the bird from the 'normal' position.

From 0 s to 60 s, the cable is forced to rotate fore-to-aft with an amplitude of $\pm 7°$. The period of oscillation is 9 s. We can model the change in β the same way as before: backward swings of the cable will raise and rotate the bird, reducing the response. Therefore the value $\frac{T^2}{R}$ decreases. Forward swings lower the bird, increasing $\frac{T^2}{R}$. The laser altimeter only measures the altitude correctly when it goes through the 'normal' position. The incorrect values of altitude measured by the laser altimeter are used to calculate G in equation (3.5), and the ratio of $\frac{T^2}{R}$ to G gives predicted β. From 60 s to 120 s, the system is forced to roll or move side-to-side with the same amplitude and period as the fore-to-aft motions. Swings in either direction reduce the response of the signal but also cause the laser altimeter to overestimate the altitude of the bird.

The resulting predictions of β are shown in Figure 4.15. The cable begins with a backward swing that reduces β by 4% at full swing. Forward swings increase predicted β by a maximum of about 7.5%. Cable roll always increases β. This is in spite of the fact that the response is decreased. Evidently, the laser altimeter overestimation increases G to such an extent that it overpowers the decrease in response. Notice that the frequency of changes in β due to side-to-side swing are twice that of the changes due to in-line swing. Furthermore, for similar amplitude swings, rolling changes β by a mere 2% compared to a range of 11.5% for in-line swings. It is for this reason that I have neglected side-to-side swings in most of my analysis.

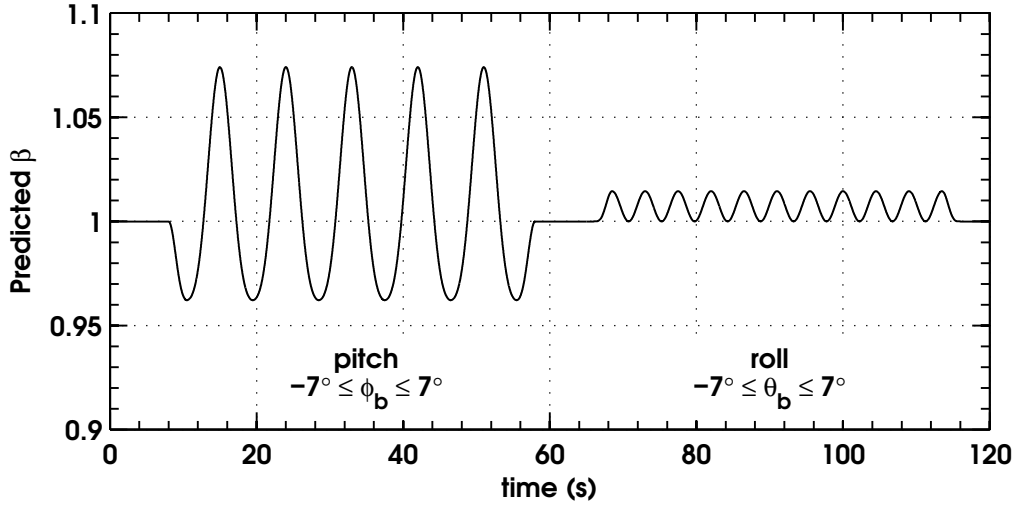

Figure 4.15: *Predicted β for synthetic data generated simulating bird and cable swings with a laser altimeter in the bird. From 0 s to 60 s, the bird is subject to pitch of amplitude $\pm 5^\circ$ and a period of 2 s. 60–120 s, $\pm 5^\circ$ roll about central axis with a period of 2 s. 120–180 s same pitch superimposed on fore-to-aft cable swing of amplitude $\pm 5^\circ$, period 9 s.*

4.5 Bird Swing Filter: Laser Altimeter

We can correct the data for bird swing by applying a similar filter to the one applied in Section 4.3. The cosine and sine terms of equations (4.7) and (4.8) are used exactly as before, but the filter is changed in its application of the terms. Whereas in the radar bird swing filter we added the magnitude of the T_2 term, here we must subtract it. The filter then becomes:

$$F_{laser} = F + {}_1F_{\cos} - {}_2F_{\cos} - \sqrt{\left({}_2F_{\cos}\right)^2 + \left({}_2F_{\sin}\right)^2} + {}_3F_{\cos}, \tag{4.12}$$

The result of application of the filter in equation (4.12) with a period of 9 s is shown in Figure 4.16. The filter acts on the synthetic data and removes the effect of both cable swing and bird rotation.

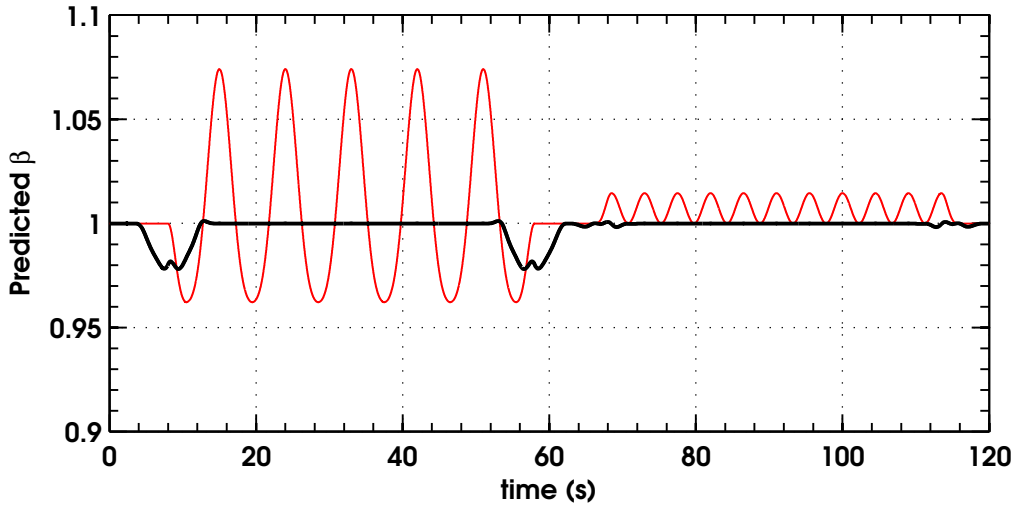

Figure 4.16: *Implementation of the 9 s bird swing filter on predicted β from the synthetic model (with laser altimeter). Original synthetic data is shown in red. Also shown is the output of the 9 s bird swing filter (thick black). Compare to Figure 4.7, where β was predicted using radar altimeter.*

4.5.1 Implementing the Bird Swing Filter

To sum up this section of the chapter and show the implementation of the swing filters applied to real data, I will present the result of applying equation (4.12) to β using the 40 kHz in-phase and quadrature responses with altitude measured by the laser altimeter from the Chowilla Floodplain. Figure 4.17 shows a grid of the filtered data. Bird swing is clearly reduced in effect in the data when compared to Figure 3.15. The dry lakes at the top of the grid are very clearly defined.

Comparison of β calculated with radar (Figure 4.10) and laser (Figure 4.17) altimetry shows several differences. The laser altimeter data is much flatter and less striped than radar altimeter data. This is most likely due to constant line to line altitude errors in the radar data due to variable airspeed and survey conditions, although I have done no tests to prove this. The laser altimeter does not seem to have this problem, but attaching it to the nose of the bird complicates true altitude estimation. It is my suggestion that the laser altimeter be placed directly under the central rotating point of the bird. If this is done, all bird swings will result in overestimating altitude and bird swing will be very easy to pick out of the data.

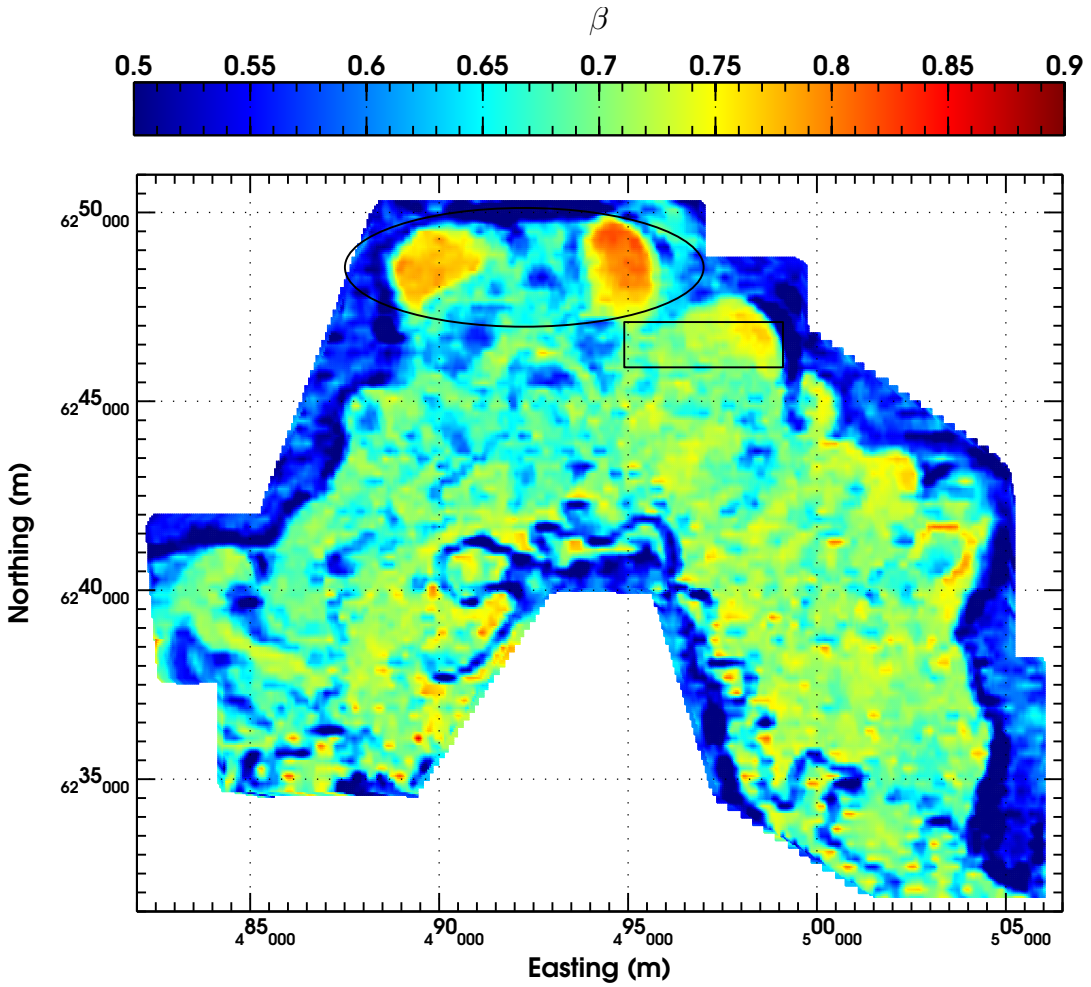

Figure 4.17: *Implementation of the 9 s bird swing filter on β calculated using laser altimetry and the response data from the 40 kHz component of the Chowilla Floodplain dataset. Bird swing is eliminated from the data with the inevitable loss of resolution.*

The radar altimeter seems to be very prone to error near and bordering the Murray River along the bottom part of the grid. This could be due to the canopy effect described by Brodie and Lane (2003), but it could also be a previously undiscussed 'watercourse' effect. It would be useful to determine the true cause, but it will not be explored in this thesis. When examining the laser altimeter, a pointing or range-finding type of laser altimeter must necessarily be very prone to bird swing error. I strongly suggest using a scanning laser altimeter that will more accurately measure the 'true' distance of the altimeter from the earth. With the laser altimeter mounted under the point of rotation of the bird, AEM data will be much less prone to error.

When attempting to find bird swing in AEM data, I strongly recommend β calculated using radar altimetry. Even with line to line striping, the radar altimeter is insensitive to errors caused by bird swing. Therefore, changes in response due to swing are easily discovered. This was most apparent in Sydney Harbour, but was easily discernable over the Chowilla Floodplain.

Analysis of the Chowilla data showed that the cable swings around a great deal during a survey. We can break the swings down into in-line and cross-line swings, and can even predict them from GPS data from the helicopter and towed bird. But this information does not predict bird swing, and in fact the only way to get that information is to actually measure it. Fortunately, this has occurred last year in September 2006, when the CSIRO contracted Fugro Airborne to conduct a RESOLVE HEM survey in the Sunraysia area just outside of Mildura, Victoria.

4.6 Sunraysia: RESOLVE

The Sunraysia dataset is unique to this thesis because the contractors provided a way to measure pitch, roll and yaw of the bird while it was on survey. They did this with 3 high accuracy GPS antennae mounted in a triangle pattern on the towed bird. Two GPS antennae were placed at opposite ends of a boom that can be mounted to the RESOLVE and usually houses a magnetometer. The last GPS antenna was placed near the tail of the bird. The position of the three GPS antennae is shown in Figure 4.18.

For this survey, the contractors used an internal computer or chip to calculate the pitch, yaw and roll of the towed bird 'on the fly'. In order to test that it was operating and really measuring these values, a team was assembled to sequentially photograph the RESOLVE system while it was on survey. The experiment was designed so that the team could take sub-second interval photographs of the RESOLVE system both along the direction of flight and perpendicular to it with high resolution digital cameras. Our success was varied, proving once again that video recording an HEM system on survey is extremely difficult. I managed to obtain some photo sequences

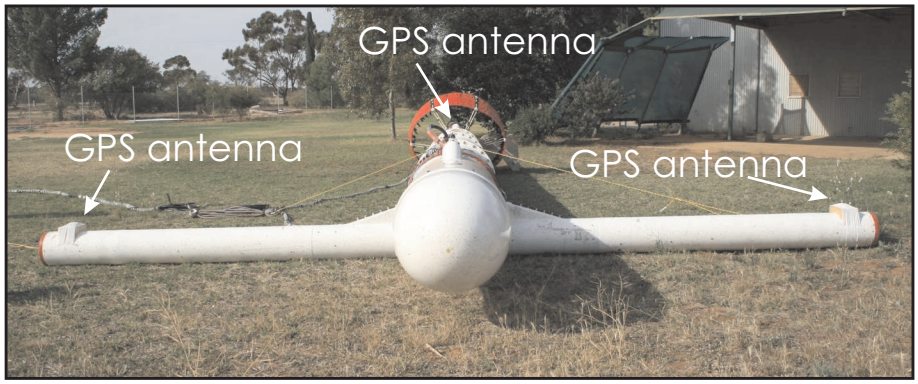

Figure 4.18: *Photograph of the 3 GPS antennae used to measure pitch, roll and yaw in the Sunraysia HEM survey. 2 GPS antennae are mounted on a boom near the front of the system, while the last is mounted on the chassis, near the back. Pitch, yaw and roll calculations are processed real-time.*

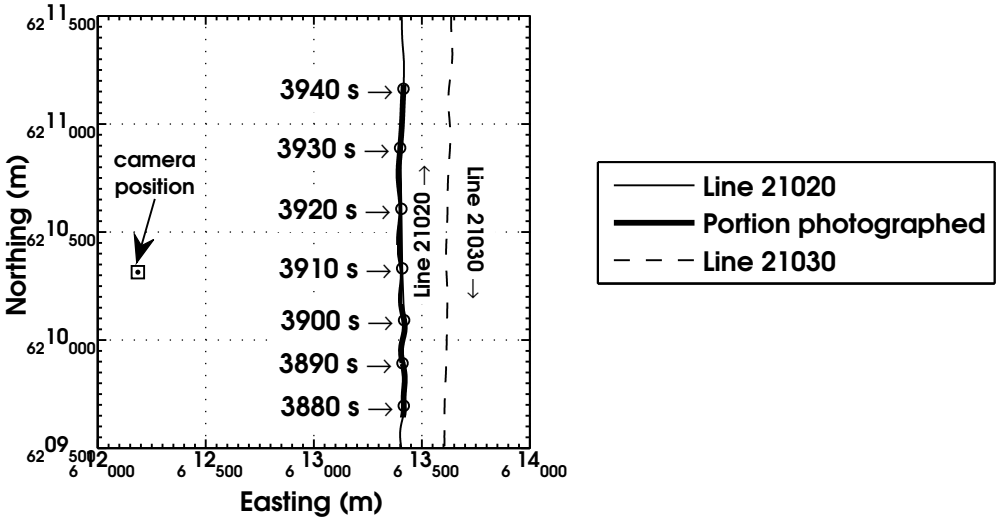

Figure 4.19: *Portions of lines 21020 and 21030 from the Sunraysia HEM survey. Marked in thick black is the section of line that was photographed at sub-second intervals. Open circles along this line mark 10 s intervals. Camera position was* $_{62}10_{314}$ *m North and* $_{6}12_{186}$ *m East.*

of the HEM system flown along one line, viewing perpendicularly to the line of flight. A portion of line 21020, together with the section that was photographed, is shown in Figure 4.19. The camera position is also marked. Luke Garde, a summer student at RMIT University manually picked the locations on each image of the nose, tail and hitching point of the bird, as well as the nose, GPS antenna and hitching point of the tow cable on the helicopter. An example of one such photograph and the points manually picked by Luke is shown in Figure 4.20. The video made from all the photographs is included in Appendix D.2.

In each frame, I calculated the apparent pitch of the bird and the in-line swing angle of the cable. Each photograph was date stamped, so I correlated the time that the photograph was taken to the GPS time recorded on the bird during survey.

Figure 4.21 shows the result of the analysis. The apparent bird pitch matches the measured bird pitch almost exactly from 3908 s to 3926 s. Looking back to Figure 4.19, this is where the helicopter and bird is almost due east of the camera position. For times earlier then 3908 s and later than 3926 s, the apparent bird pitch tends to underestimate the measured bird pitch due to parallax error. Looking at the dashed line in Figure 4.21, we see that once again the cable executes in-line swings with a period of around 9 s. This is consistent with the Chowilla dataset. During the period of least parallax, the mean cable position seems to be approximately 20°, consistent with my earlier predictions based on the rope lengths of the 'Y' section. Interestingly, this example shows that backward swings of the cable tend to cause the nose of the bird to plunge while forward swings tend to lift it. It seems that the rigid model of Section 4.4.2 is not entirely correct although it is evident that there is a correlation between cable swing and bird pitch. Furthermore, the bird tends to pitch with its own frequency of ∼2.5 s, and amplitudes of anywhere from 2° to 20°. This is strong evidence that supports my claim that the high frequency oscillations in β in Section 3.3 are due to bird rotation independent of cable swings. From this experiment, I believe that the 3 GPS antennae mounted on the bird yield accurate

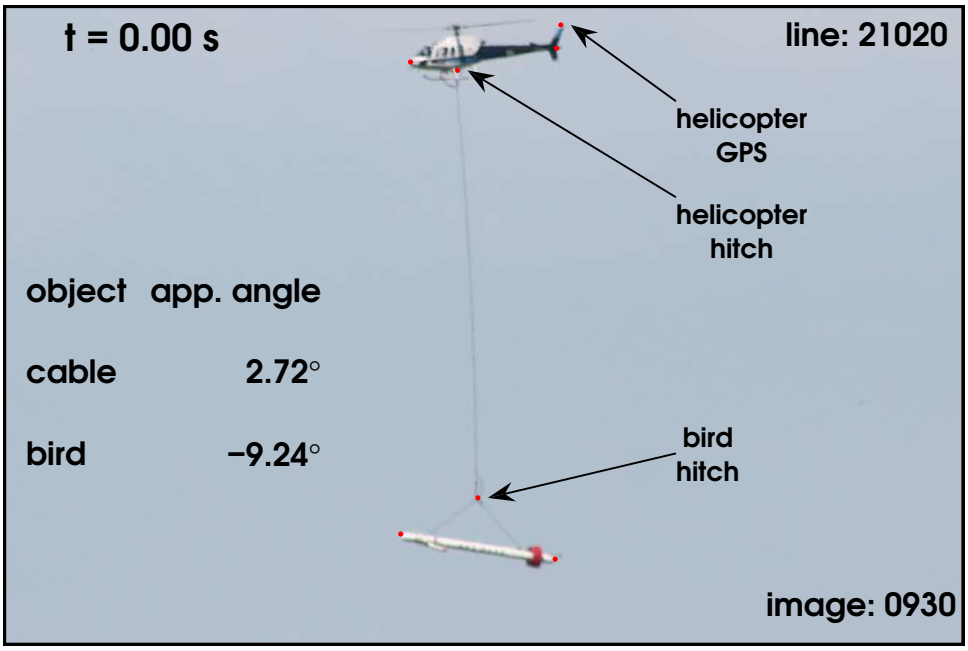

Figure 4.20: *Sample photograph used to analyse bird motion during line 21020 Sunraysia HEM survey. Points manually picked on helicopter were: GPS antenna, nose, tail and cable attachment. Points picked on bird were: nose, tail and the 'Y' point on the cable.*

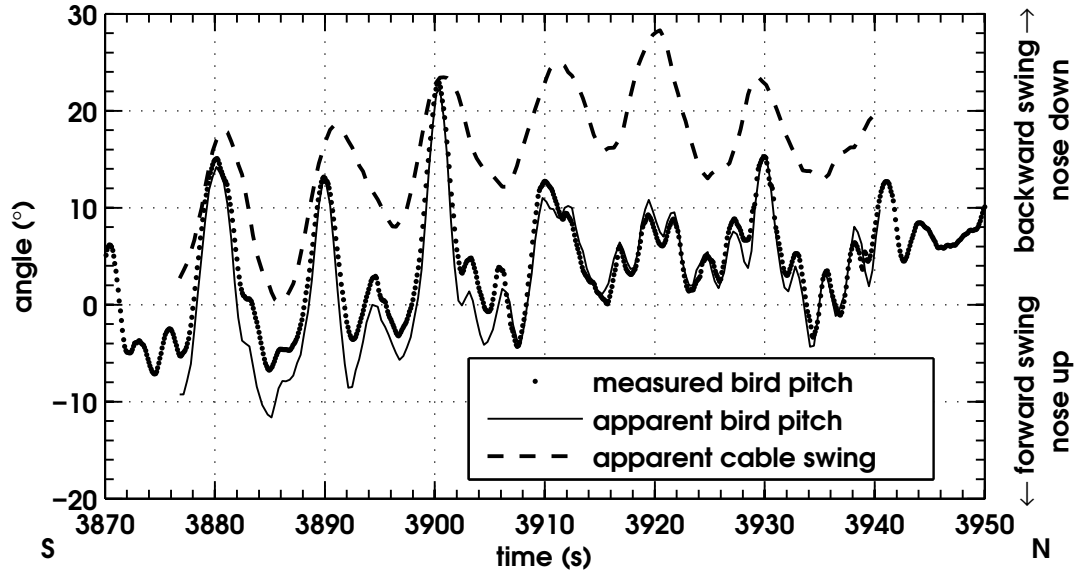

Figure 4.21: *Bird and cable swing measured for a section of Line 21020 from Sunraysia HEM survey. Bird pitch measured with triangular GPS antenna array provided by contractor (dots). Apparent bird pitch (solid) and in-line cable swing (dashed) measured from photographs are also shown.*

measurements of bird pitch.

4.6.1 Attempt at Predicting Roll

The 3 GPS antennae also provide a method to measure roll of the bird while it is on survey. I have said very little in the past two chapters on bird roll and in-line swings. This is partly to do with the models I have made that show that roll is slightly less important than pitch: but also it is because I have not been able to obtain reliable video evidence of cable and bird roll. It is very difficult to film the HEM system as it flies down the line. Despite these shortcomings, the Chowilla dataset proved that cross-line swings do occur. I assert that these cross-line cable swings also cause the bird to rotate. The roll measurements calculated from the 3 GPS antenna provide one way to measure roll, but I propose another based on simultaneous position solutions from the helicopter navigational and towed bird tracking GPS antennae.

The helicopter navigational GPS receiver typically provides horizontal resolution of 1 m, while the towed bird GPS receiver can be used in differential mode to provide horizontal positioning of typically <1 m. For my model we calculate roll by taking the inverse sine of the horizontal displacement of the helicopter and bird GPS antennae (Δx) divided by c the length of the tow cable, i.e.

$$\phi_c = \sin^{-1}\Big(\frac{\Delta x}{c}\Big). \tag{4.13}$$

Figure 4.22 shows a comparison of measured roll to that calculated using the helicopter and towed bird GPS antennae over the photographed section of line 21020.

It is clear from the figure that equation (4.13) yields roll values consistent with the measured values of roll. Angles calculated from the horizontal offsets of the survey GPS antennae are biased to the east, while the measured roll is biased slightly to the west. At this point, it is impossible to tell which is more accurate. This example shows that cross-line cable swing is responsible for rolling the towed bird,

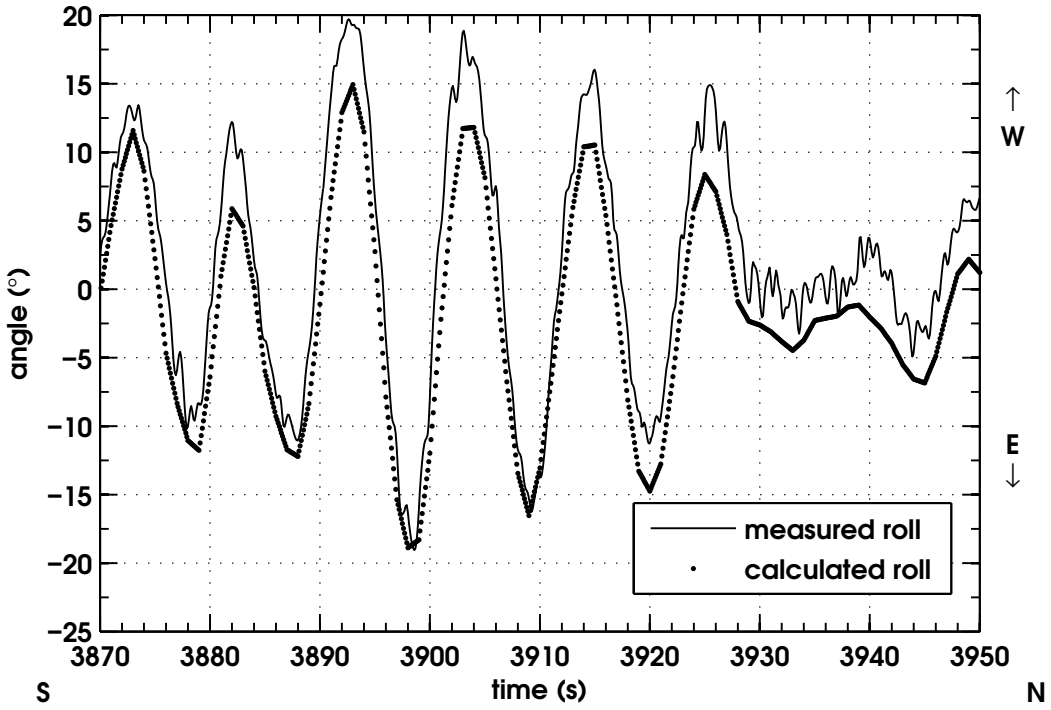

Figure 4.22: *Roll measured for a section of line 21020 from Sunraysia HEM survey. Bird roll measured with triangular GPS antenna array provided by contractor (solid line). Roll calculated (using equation (4.13)) due to cable swing inferred from horizontal helicopter and towed bird GPS antenna displacement (dots).*

but the solid line in Figure 4.22 also shows that there are higher frequency oscillations in rolling motion. I propose that these are the 'tube rolls' that I defined in the introduction to this chapter.

In order to determine the difference these two roll measurements make to the data, Figure 4.23 is a model of how β is affected by roll. I will use the altitude measured by the laser altimeter, and the earth is assumed to be infinitely conductive. The system response $\frac{T^2}{R}$ is given by a horizontal bird towed at an altitude of 30 m. β is modelled using the roll values to adjust both height and attitude of the towed bird from a flat level flight at 30 m. Panel (a) shows β for both measurements. The difference in the models is only great at extreme ranges of swing, which is exactly what we would expect. Furthermore, panel (b) shows the effect of administering the same bird swing filter (equation (4.9)) to both sets. Clearly, if we are using a bird swing filter, the choice is immaterial. But what if we are trying to predict

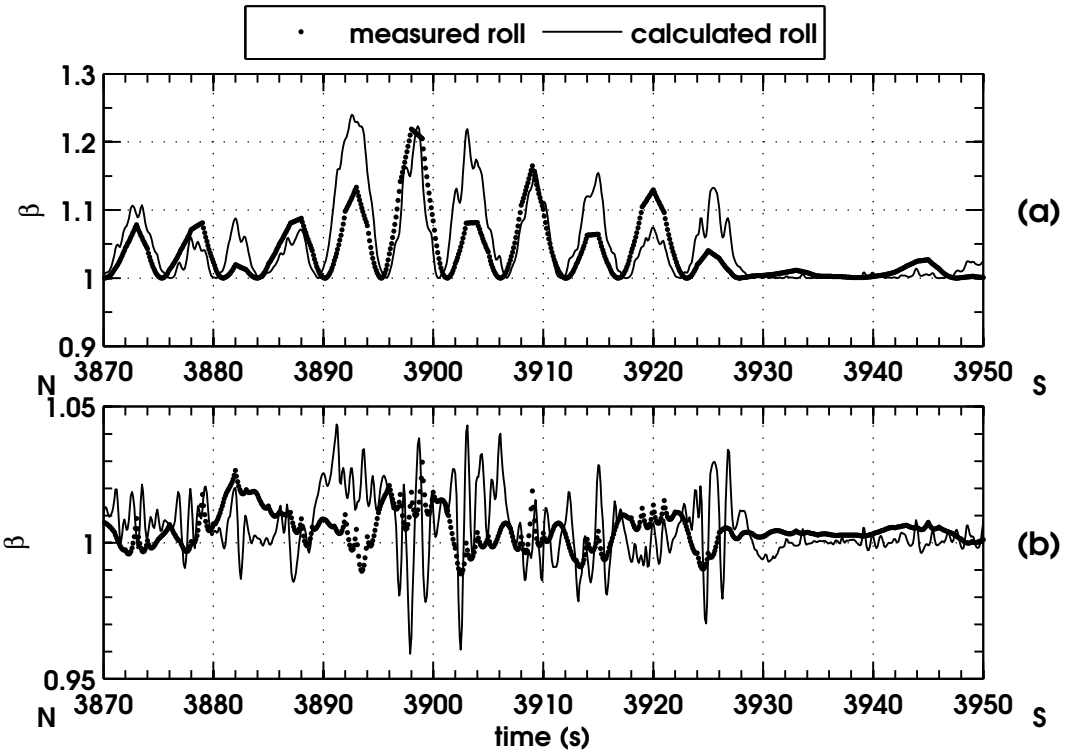

Figure 4.23: *(a) Predicted β using the response of a horizontal bird 30 m over a conductive half space and geometric factor based on measured (solid) and calculated (dots) roll (line 21020) affecting both cable swing and bird attitude. Differences up to 10% are seen. (b) Enlarged scale of β after application of a 10 s bird swing filter (equation (4.9)). Resulting differences are less than 5%.*

the system response based on roll measurements? Figure 4.23a shows that 10% differences appear due to the different methods of measuring roll. My suggestion is that further testing is done before we choose one method over the other. Clearly, the helicopter and towed bird GPS antenna method has merit, if only because these are routine position measurements and therefore add no extra cost to the survey.

In addition to the cost benefit of using my method of bird roll prediction, it also provides a very simple means as a check on the measured GPS roll angles. The dots in Figure 4.24 show that the roll angles measured with the triangular GPS array can be in error. At fiducial number 4452 on line 21030, the measured roll angle jumps from -20° to 10° in about 0.4 s. If we are to believe the measured roll angles, that means the bird slewed over at a rate of about 75°/s. This is not physically plausible since there are other such jumps at 4464 s and 4469 s. I have included my predicted

roll angles as a solid line in this figure, and they do not show any such motions. I believe that the jumps in measured roll are errors created by the algorithm used by the GPS receiver to calculate the angle. Furthermore, in the next section I will show that the bird pitch measurements experience similar jumps at exactly the same points in time.

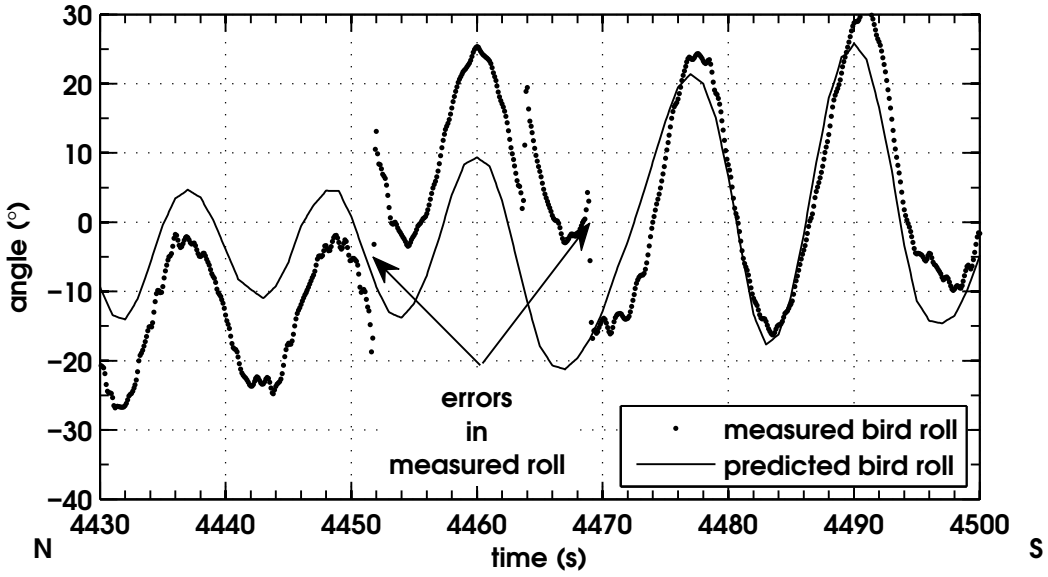

Figure 4.24: *Plot of measured and predicted bird roll angles versus time for a segment of line 21030 from the Sunraysia dataset. Measured bird roll (dots) predicts that the bird slews at a rate of about 75°/s at 4452 s, while predicted bird roll (solid) is smoothly varying. Similar jumps in measured roll occur at 4464 s and 4469 s.*

4.6.2 Attempt at Predicting Pitch

It is also possible to attempt to predict bird pitch from the helicopter and towed bird navigational GPS data, although as I will show, the results are limited. My prediction model relies on the rigid attachment model described in Section 4.4.2 and Davis et al. (2006).

In the rigid model, a cable of length c hangs from the hitching point of the helicopter (vector $\mathbf{c}$). At the bottom of the cable, the bird chassis is rigidly attached so that the nose points up at an angle of 20°: the model that I used in Figures 4.1 and 4.13. During normal survey conditions, the cable is swung back 20° and the

bird is towed horizontally. The GPS antenna on the towed bird is horizontally offset from the attachment point by ∼4.2 m (as shown in Figure C.2). This distance is vector $\mathbf{b_{GPS}}$ in Figure 4.25. The cable hitching point on the helicopter is offset from the helicopter navigation GPS antenna by about 7.7 m horizontally and 2.7 m vertically (vector $\mathbf{h_{GPS}}$). The helicopter is assumed to fly horizontally, which is not in general true. We say that the 'normal' position of the bird's GPS antenna is given by $\mathbf{r_0} = \mathbf{c} + \mathbf{b_{GPS}}$. To avoid confusion, a vector diagram is shown in Figure 4.25.

At every fiducial, we are given the position of the helicopter and bird GPS antennae, which I denote as vectors $\mathbf{h}$ and $\mathbf{b}$, respectively. The instantaneous position of the bird GPS $\mathbf{b}$ can also be determined by

$$\mathbf{b} = \mathbf{h} + \mathbf{h_{GPS}} + R(\theta_c, \phi_c)\mathbf{r_0}, \tag{4.14}$$

where $R(\theta_c, \phi_c)\mathbf{r_0}$ describes an arbitrary pitch and roll of the rigid towed bird using equation (4.2). After a pitch of ϕ_c and a roll of θ_c, the vector $\mathbf{r_0}$ points to vector $\mathbf{r}$, given by

$$\mathbf{r} = R(\theta_c, \phi_c)\mathbf{r_0},$$

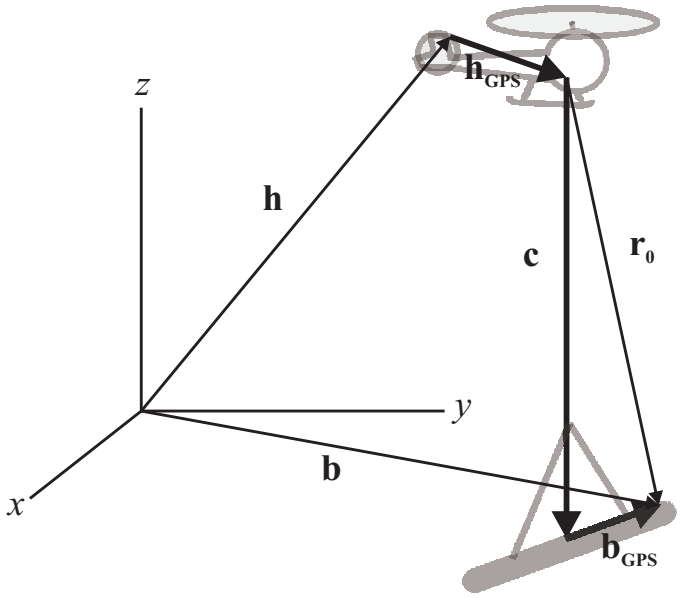

Figure 4.25: *Diagram showing how to predict pitch from helicopter and towed bird GPS position data.*

which is

$$\mathbf{r} = \begin{pmatrix} \cos(\phi_c) & 0 & \sin(\phi_c) \\ \sin(\phi_c)\sin(\theta_c) & \cos(\theta_c) & -\cos(\phi_c)\sin(\theta_c) \\ -\sin(\phi_c)\cos(\theta_c) & \sin(\theta_c) & \cos(\phi_c)\cos(\theta_c) \end{pmatrix} \begin{pmatrix} r_{0x} \\ r_{0y} \\ r_{0z} \end{pmatrix},$$

and evaluates to

$$\mathbf{r} = \begin{pmatrix} r_{0x}\cos(\phi_c) + r_{0z}\sin(\phi_c) \\ r_{0x}\sin(\phi_c)\sin(\theta_c) + r_{0y}\cos(\theta_c) - r_{0z}\cos(\phi_c)\sin(\theta_c) \\ -r_{0x}\sin(\phi_c)\cos(\theta_c) + r_{0y}\sin(\theta_c) + r_{0z}\cos(\phi_c)\cos(\theta_c) \end{pmatrix}. \tag{4.15}$$

Notice that the x-component of equation (4.15) has only the angle ϕ_c. All other quantities are known:

$$r_x = r_{0x}\cos(\phi_c) + r_{0z}\sin(\phi_c).$$

Solving this equation for ϕ_c yields

$$\phi_c = \tan^{-1}\left(\frac{r_x r_{0z}^2 + r_{0x}\sqrt{r_{0z}^2\left(r_{0x}^2 + r_{0z}^2 + r_x^2\right)}}{r_{0z}\left(r_x r_{0x} + \sqrt{r_{0z}^2\left(r_{0x}^2 + r_{0z}^2 + r_x^2\right)}\right)} \right). \tag{4.16}$$

The component r_x is given by equation (4.14):

$$r_x = b_x - h_x - h_{GPSx},$$

and we must take care using the arctangent function to pick the proper quadrant. Figure 4.26 shows my attempt at predicting the pitch of the rigid tow cable/bird model using equation (4.16). The thick red line is the pitch of the bird predicted from the simultaneous GPS data, but does not accurately reflect the pitch of the bird measured with the 3 GPS antennae mounted on the bird. This model and its predictions show that the independent pitching of the bird must be measured by at least two GPS antennae (mounted fore and aft of the bird) or by some other means.

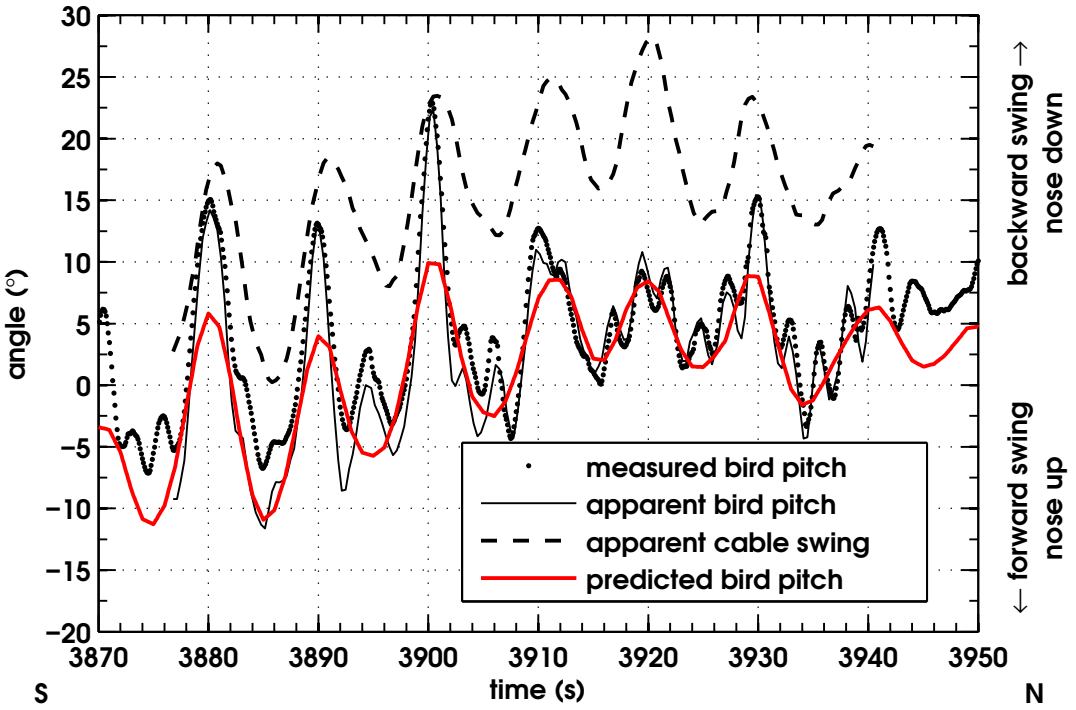

Figure 4.26: *Repetition of Figure 4.21 with the pitch predicted from a rigid model using equation (4.16) shown in thick red. Although the model follows the mia swinging of the towed bird, it cannot predict the actual pitch of the bird with any certainty.*

Although my method of bird pitch prediction does not accurately predict bird pitch, it is a convenient way to check the measured bird pitch angles provided by some other method. As an example of this utility, Figure 4.27 shows both the measured bird pitch and my predicted bird pitch versus time for a section of line 21030 from Sunraysia. It is easy to see a jump in measured bird pitch angles at fiducial 4452 s where the bird goes from -10° to 5° in about half a second. My predicted pitch angles vary smoothly over this time providing further evidence that the measured bird pitch is in error. Comparing with Figure 4.24 shows that a similar jump occurred at precisely the same time in the measured bird roll. I conclude that there are times when the algorithm that calculates bird pitch and roll from GPS position solutions gives misleading and erroneous angles. This is most likely due to information loss due to the rotation of the GPS antenna ground plates that

cause GPS satellites near the horizon to 'drop out'. The sudden loss of information presumably affects the position solution arrived at by the processor, which causes error in the measured roll and pitch values.

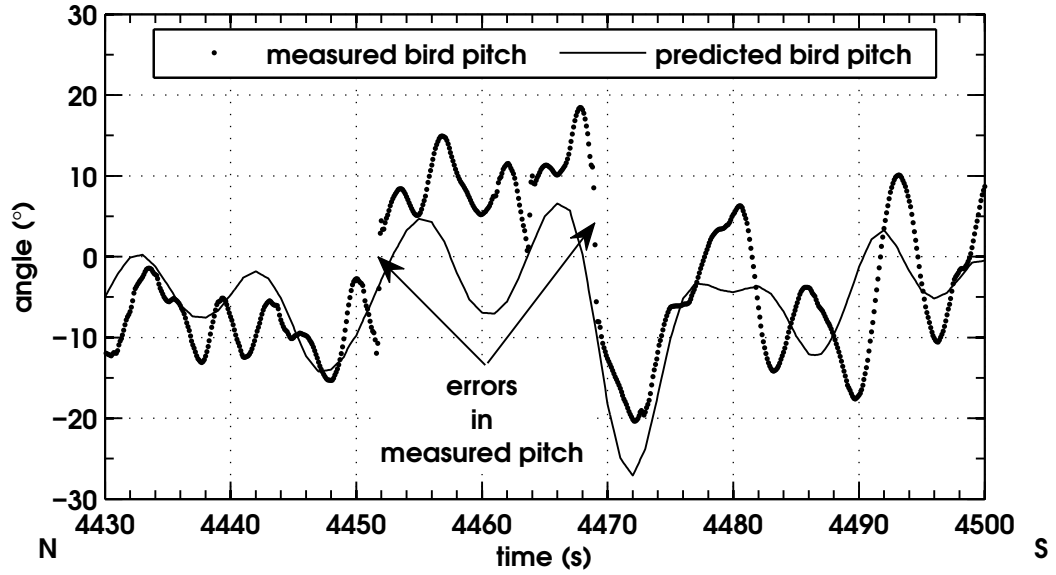

Figure 4.27: *Plot of measured (dots) and predicted (solid) bird pitch angles versus time for a segment of line 21030. Measured bird pitch reveals that the bird pitch changed by ∼15° in less than half a second. Predicted bird pitch (solid) shows a continuous and smooth change over the range of 4450 s to 4470 s. Comparison with Figure 4.24 shows that measured bird roll experienced similar jumps at the same times.*

4.6.3 Correcting β With Known Pitch and Roll

In this section, I present a final means of correcting β based on measured pitch and roll provided by the contractor. As shown in Section 4.4, bird pitch and roll changes the altitude measured by the altimeter. If we assume that a flat earth is beneath the towed bird, we can use the same model to calculate the altitude of the centre of the towed bird based on the altimeter reading and measured pitch and roll. Recall that equation (4.10) yields the direction of the laser altimeter after the bird is pitched by ϕ_b and rolled by θ_b. Let as take as origin the point on the plane $z = 0$ directly beneath the laser altimeter at each fiducial. The laser altimeter is therefore at the point $(0, 0, z_l)$, but points to the flat earth along vector $\hat{\mathbf{L}}$ (equation (4.10)), repeated

here:

$$\hat{\mathbf{L}} = -\sin(\phi_b)\,\hat{\mathbf{i}} + \cos(\phi_b)\sin(\theta_b)\,\hat{\mathbf{j}} - \cos(\phi_b)\cos(\theta_b)\,\hat{\mathbf{k}}.$$

The laser altimeter measures the distance D from the point $(0, 0, z_l)$ to the point $(x, y, 0)$ along vector $\mathbf{D}$. Thus we have

$$\mathbf{D} = x\,\hat{\mathbf{i}} + y\,\hat{\mathbf{j}} - z_l\,\hat{\mathbf{k}},$$

which may also be expressed as

$$\mathbf{D} = D\hat{\mathbf{L}}.$$

Taking the $\hat{\mathbf{k}}$ component of $\mathbf{D}$, we see that the actual altitude z_l of the laser altimeter above the flat earth is

$$z_l = D\cos(\phi_b)\cos(\theta_b),$$

which is consistent with Holladay et al. (1997).

Now that a corrected value of the laser altimeter altitude has been derived, the actual altitude of the centre of the bird remains to be found since we are assuming that the bird rotates about its centre point and central axis. The laser altimeter is separated from the centre of the bird by a horizontal distance of 2.6 m and after a pitch of ϕ_b, this translates into a vertical offset of $2.6\sin(\phi_b)$ m. This is because a positive pitching angle shifts the nose closer to the ground which means that the centre point of the bird is above the laser altimeter. The 'corrected' altitude of the centre of the bird is then

$$z_b = D\cos(\phi_b)\cos(\theta_b) + 2.6\sin(\phi_b)\ \text{m}.$$

Using the corrected altitude of the centre of the towed bird and the measured bird pitch and roll angles, I calculated β based on these values. In-phase and quadra-

ture signal response as measured by the system during survey are divided by the generalised geometric factor $G(\theta_b, \phi_b, z_l)$, now a function of pitch, roll and altitude (equation (4.6)).

The next 4 figures show the effectiveness of my response correction attempt. Figure 4.28 displays a grid of β for the 40 kHz component of the southeast section of the Sunraysia dataset using the laser altimeter. Bird swing can be seen in this figure by the spotting of the data, particularly over the reddish patch in the southwest corner of the figure. Figure 4.29 shows the same section of the Sunraysia set only with β calculated as discussed above, using equation (4.6).

The main difference between the two grids is that β in Figure 4.29 is reduced throughout the entire figure. Bird swing is not entirely eliminated from the data but it does seem to be reduced. It is clear from these two figures that geometric factor alone is not sufficient to remove bird swing from the data, even though it reduces the effect somewhat. The difference between original and 'corrected' β is shown in Figure 4.30. This grid shows that, in general, the original data is greater than the corrected data. Furthermore, bird swings are clearly shown in this figure by spots of yellow showing differences of approximately 5%. In other parts, such as the extreme east of the figure, the two grids differ by approximately -5%. As a comparison between 'corrected' β and filtered β, Figure 4.31 shows the same section of the survey with a 9 s bird swing filter applied to the data. Figure 4.31 and Figure 4.29 are remarkably similar in detail, with high-value β features clearly shown in both grids. The difference between them is that the filtered data will necessarily have some physical features removed from the data that should probably be present. Figure 4.29 does not try to remove anything extra from the data, but only to correct the existing data for bird swing using the available information.

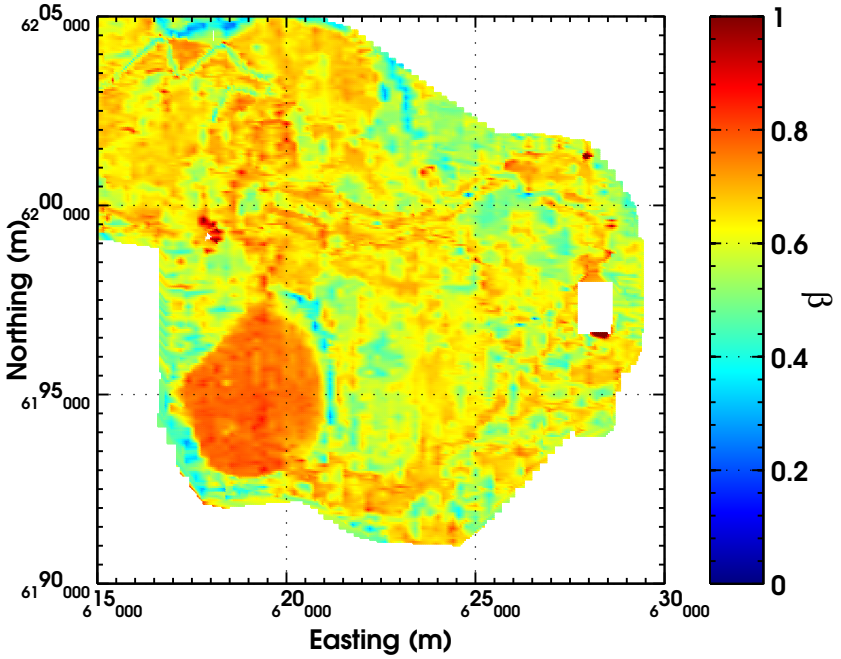

Figure 4.28: *Grid of β(laser) for a section of the 40 kHz component of the Sunraysia dataset. β was calculated with the laser altimeter as the height. Bird swing can be seen in this grid, particularly in the southwest corner of the figure.*

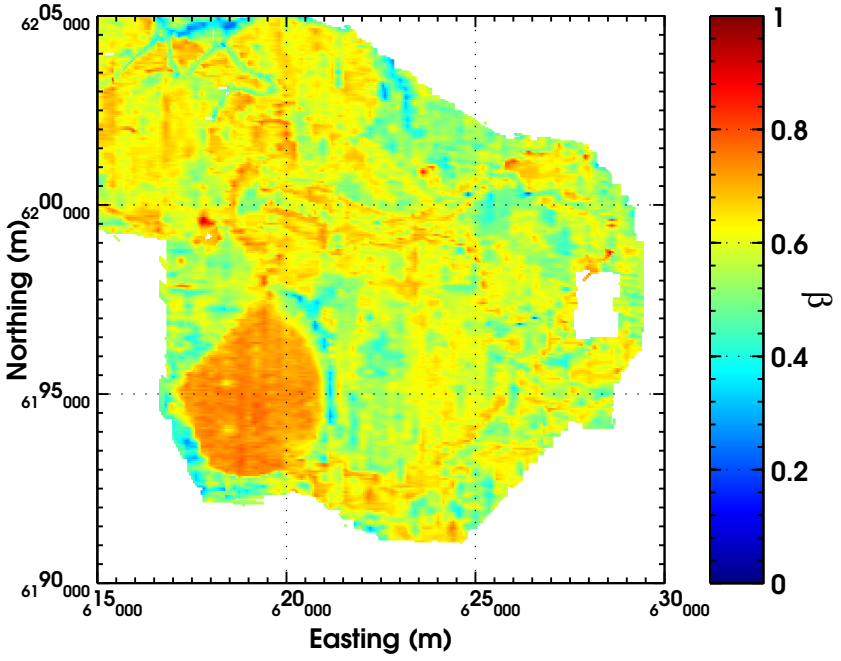

Figure 4.29: *Grid of same area with β 'corrected' using G calculated with measured pitch, roll and midpoint altitude.*

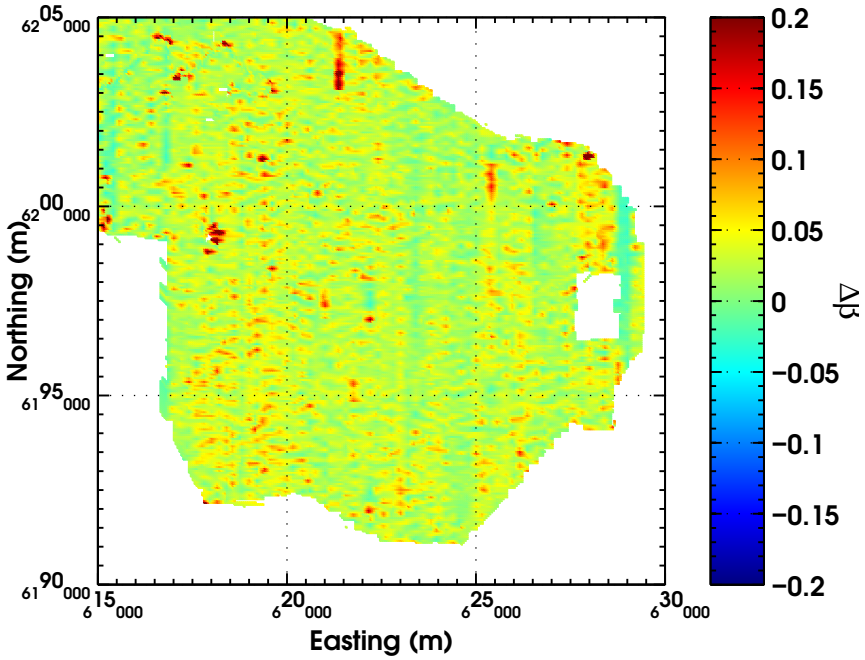

Figure 4.30: *Difference between original (Figure 4.28) and corrected (Figure 4.29) β for the southeast corner of the Sunraysia dataset.*

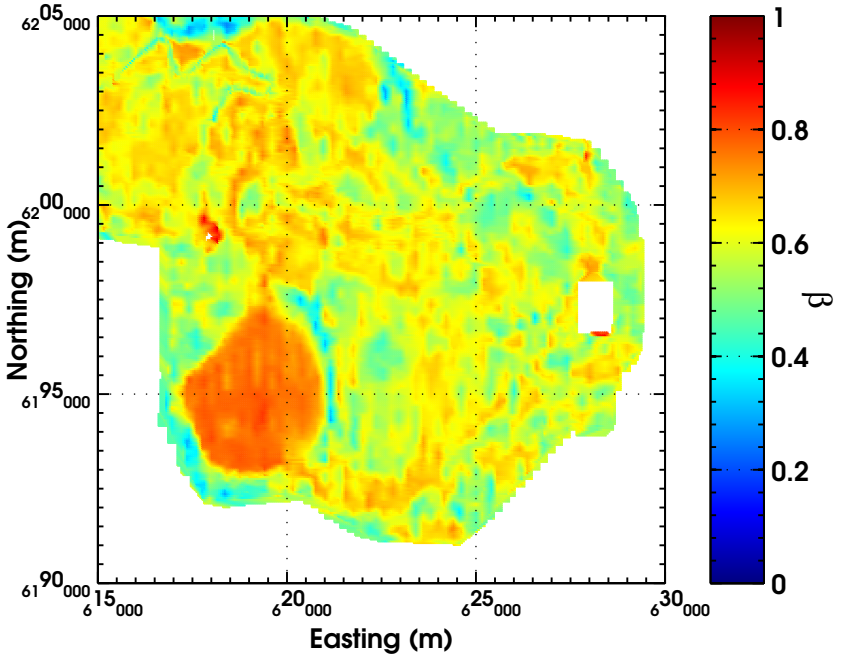

Figure 4.31: *Grid of β over the same southeast section of the Sunraysia survey, with β filtered with the laser altimeter bird swing filter set at 9 s (equation (4.12)).*

4.6.4 Problems with Altimetry

As mentioned in the last chapter, the laser and radar altimeters give differing values of altitude over and near watercourses. The situation is the same for the Sunraysia survey, with the radar altimeter recording incorrect altitudes over the Murray River. Figure 4.32 shows the DEM for the southeastern corner of the Sunraysia survey calculated using the laser altimeter and the bird's GPS position, equation (3.7). The same area is shown in Figure 4.33. The area inside the 6-sided polygon in the lower righthand side of the figure clearly shows that the radar altimeter is affected by the watercourse or the vegetation on its edges. I have included these figures to once again draw attention to some of the problems that accompany ground clearance measurement; and to show that the errors mentioned in Section 3.4.3 were not only apparent in the Chowilla dataset but can be found in the present case as well.

Closer examination of Figures 4.32 and 4.33 shows that there is also a constant offset in elevation between the two DEMs. The DEM calculated with the radar altimeter appears to be higher than the laser DEM. This is shown more clearly in Figure 4.34, which shows a histogram plot of the difference between the radar and laser altimeters ($h_r - h_l$) for the entire Sunraysia survey. This difference is most likely due to an error in the estimation of the separation distance between the helicopter and towed bird ($\sim$30 m).

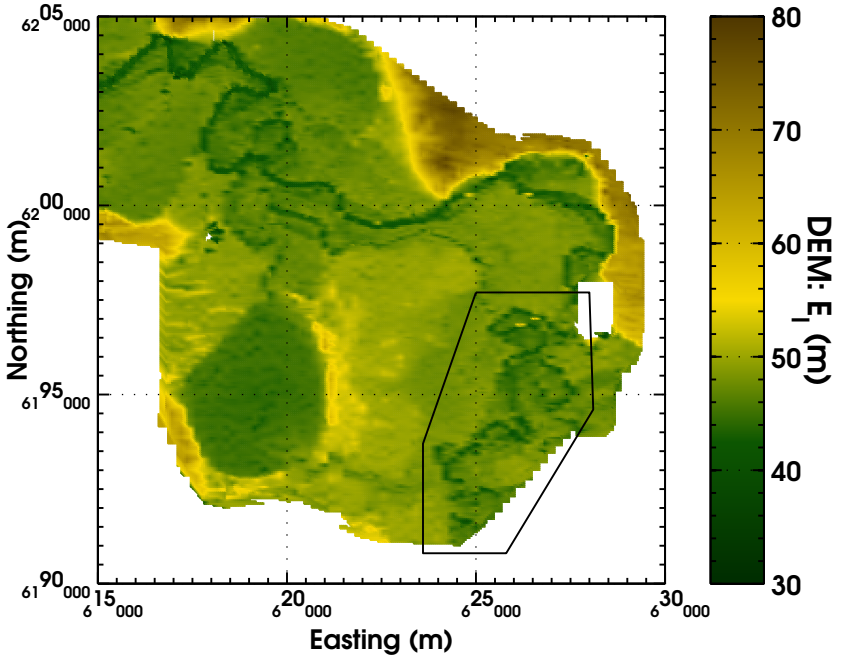

Figure 4.32: *Digital elevation map of the southeast section of the Sunraysia survey using the laser altimeter and bird's vertical GPS antenna position (equation (3.7)).*

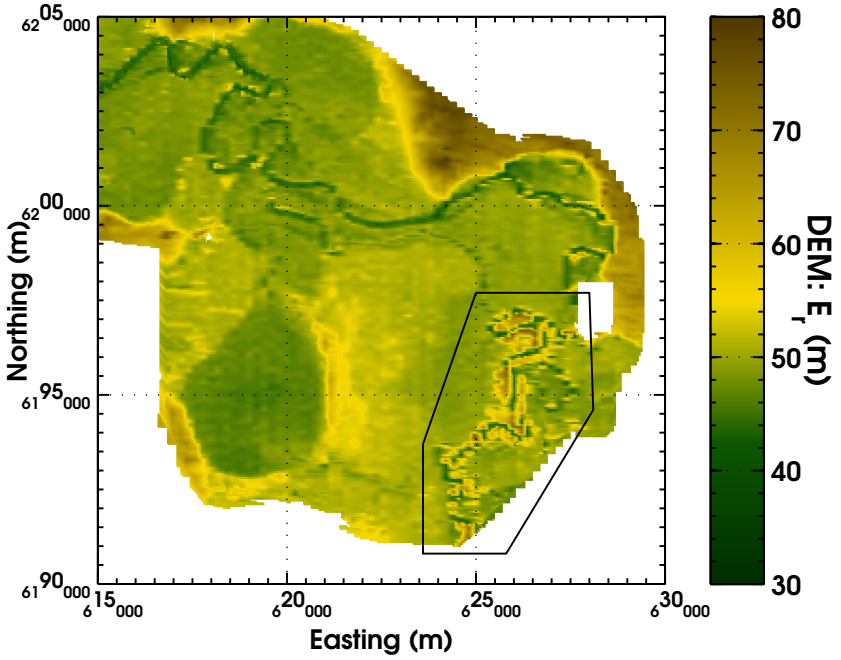

Figure 4.33: *DEM of the same section of Sunraysia using the radar altimeter (equation (3.8)). Inside the 6-sided polygon, the DEM shows that a section of the Murray River is 20 m higher than the surroundings.*

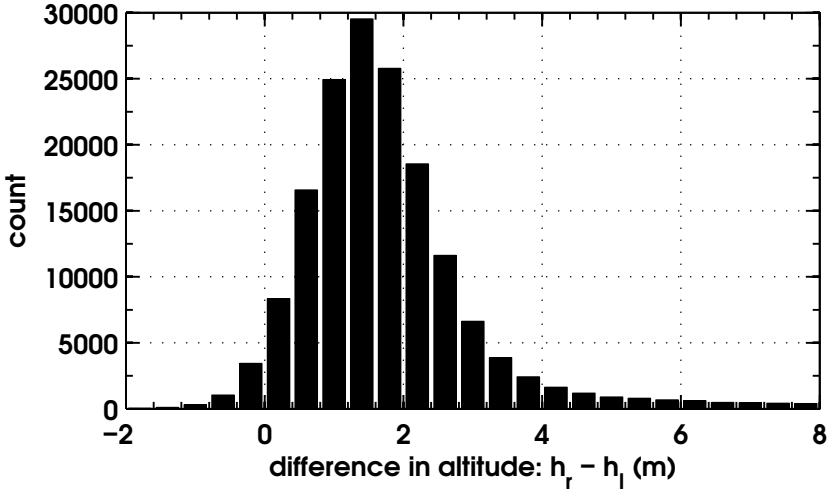

Figure 4.34: *Histogram plot of the difference between the radar and laser altimeters for the entire Sunraysia survey. The mean difference between the two altimeters is 2 m, but this graph shows that the most probable difference is 1.6 m to 1.8 m.*

4.7 Scale Model of the RESOLVE HEM System

In this chapter, I have developed models that divide the swinging of the HEM system into interdependent motions of the cable swinging fore-to-aft and side-to-side, and the bird rotating about its centre point and central axis. Although they have been investigated separately, the smaller bird motions are driven by and related to the cable motions. To investigate this relationship further, I made a scale model of the RESOLVE system and studied its movement when displaced from its rest position.

With the assistance of Luke Garde, I constructed a scale model of the RESOLVE HEM system using a 25 mm diameter PVC pipe of length 400 mm, string and LED lights. The 400 mm length of PVC pipe represented the 10.2 m length of the RESOLVE chassis; and from this I determined that the length of the string to represent the tow cable must be 1.25 m long to be a true length scale model of the 30.5 m tow cable. We attached the 'tow cable' to the ceiling and affixed 3 LED lights to the model as shown in Figure 4.35.

We video recorded the swinging of the model using a digital video recorder mounted on a tripod some 3 m away from the model. The model was set to swing-

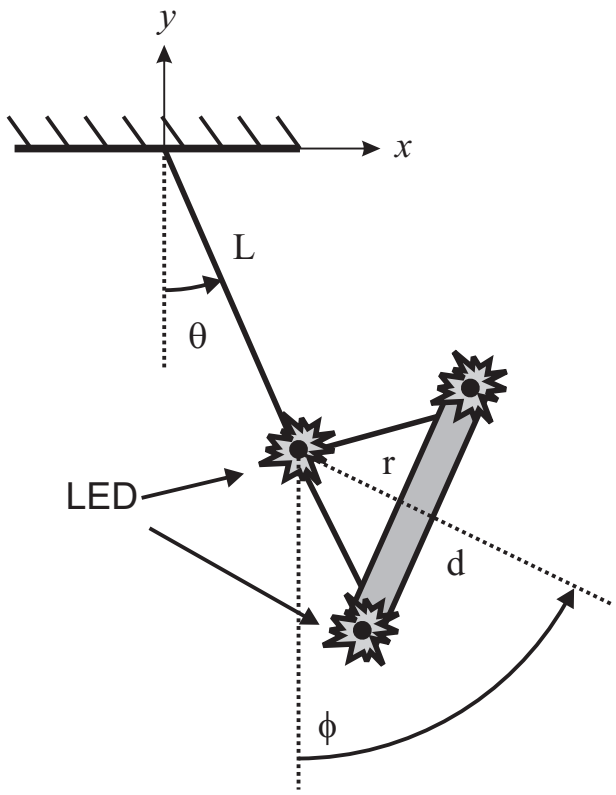

Figure 4.35: *Schematic of the model used to study the oscillatory behaviour of the RESOLVE HEM system.*

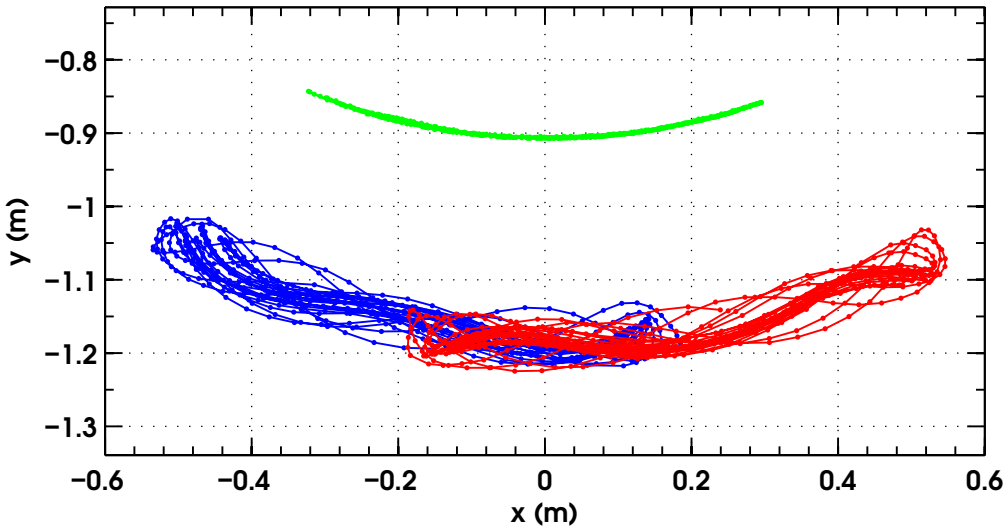

Figure 4.36: *x and y positions of the 3 LED lights attached to the RESOLVE model for one particular bird swing trial. Each point in the connected lines shows the position of the LED at a particular frame. Note the simple motion of the hitch and the Lissajous-like figures traced by the ends of the bird.*

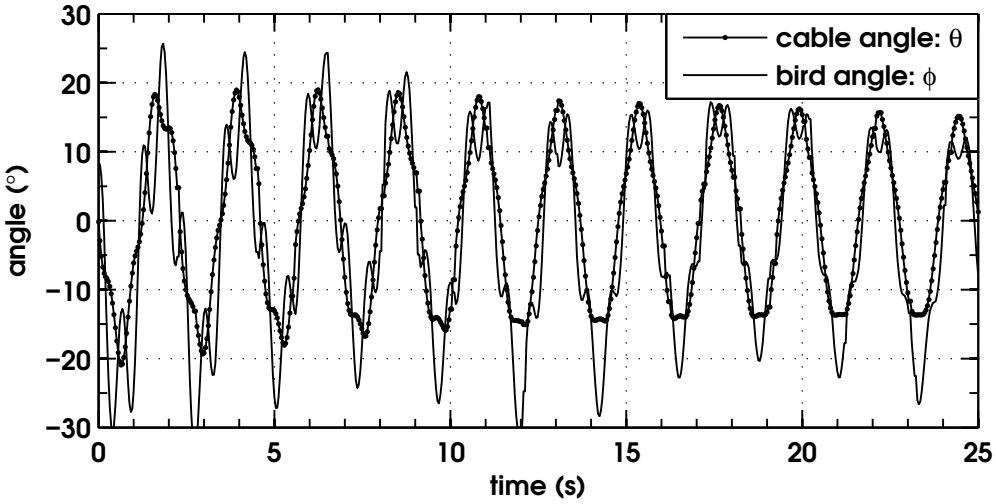

Figure 4.37: *Positions of the bird and cable converted and displayed as angles of rotation according to the schematic shown in Figure 4.35 versus time. The motion of the bird, and the extra 'kick' at the extremes are due to a momentum transfer from the swinging cable. Bird swing has higher frequency than cable swing.*

ing, and the video recording was ported over to a computer. I wrote a computer program in MATLAB® (The MathWorks, 2007) that recognised the LEDs based on image intensity and recorded their position in each frame. The original video segment and the derived video are presented in Appendix D.3. The x, y positions of the LED lights for the trial discussed in the Appendix are shown in Figure 4.36. Using the schematic shown in Figure 4.35, I converted the x, y positions of the cable and the bird into the angles θ and ϕ. A plot of these angles versus time is shown in Figure 4.37.

It is easy to see from Figure 4.37 that the bird swing is of a higher frequency than the cable swing for this trial cable length L and support length r. To examine the different effects that the distances L and r have on the period of the cable and bird, we ran several model trials with different lengths. The x, y positions were recorded and the angles calculated for each trial. As well, I examined the power spectrum of each angle versus time series and extracted the cable and bird oscillation frequency. The results of these experiments are displayed in Table 4.1.

Table 4.1: *Result of model bird swing trials. Changing L and r affects periods of cable (T_θ) and bird swing (T_ϕ). The last column shows the ratio of bird swings to cable swings.*

L (mm)	r (mm)	T_θ (s)	T_ϕ (s)	bird:cable
1150	95	2.27	0.75	3.0:1
905	270	2.15	0.53	4.1:1
840	95	2.04	0.75	2.7:1
465	95	1.57	0.72	2.1:1

It is clear that the period of the cable, that is the main swinging period of the system, increases with L. This is to be expected, since it is well established that pendulum period increases with length (e.g. Fowles and Cassiday, 1993), and this system is very much like a simple pendulum. It is also apparent from the table that increasing r decreases the period of oscillations for the bird (T_ϕ). This is also to be expected since the moment of inertia increases with increasing r, and hence reduces the period of oscillation of the second member.

4.7.1 Equations of Motion of the Towed Bird

As the final subject in this chapter I present a model of the simplest sort for the towed RESOLVE system. In this model, a cable of length L attaches to a 'Y' formation that splits off to suspend a rod of length d from the front and rear. The distance from the 'Y' join to the centre of the rod is length r. The planar motion of this system, neglecting yaw, can be constrained to two dimensions. The motion can be described by determining the equations of motion for the two coordinates. In the case shown in Figure 4.35, the coordinates are θ and ϕ. In general, they are functions of time, coupled together. The total mass M of the system is contained in the cylinder.

With the model described above, and shown in Figure 4.35, it is possible to write down the kinetic and potential energy of the system. The kinetic energy T of the

system is

$$T = \frac{ML^2\dot{\theta}^2}{2} + \frac{I\dot{\phi}^2}{2} + MLr\dot{\theta}\dot{\phi}\cos(\phi - \theta),$$

where I is the moment of inertia of the cylinder, r in the last term coincides with the distance to the centre of mass of the mass system, and the dots above the θ and ϕ variables represent a time derivative of the variable. The potential energy V of the system is much more simple to express:

$$V = -Mg\big(L\cos(\theta) + r\cos(\phi)\big),$$

where g is the acceleration due to gravity, 9.81 $\frac{\mathrm{m}}{\mathrm{s}^2}$.

From the kinetic and potential energy of the system, we can immediately state the Lagrangian equation of the system:

$$\mathcal{L} = T - V,$$

which becomes

$$\mathcal{L} = \frac{ML^2\dot{\theta}^2}{2} + \frac{I\dot{\phi}^2}{2} + MLr\dot{\theta}\dot{\phi}\cos(\phi - \theta) + Mg\big(L\cos(\theta) + r\cos(\phi)\big).$$

The generalised momentum of the first coordinate can be found by taking the derivative of the Lagrangian equation with respect to the time derivative of the first coordinate:

$$p_\theta = \frac{d\mathcal{L}}{d\dot{\theta}},$$

where p_θ is the generalised momentum of θ. Taking the derivative yields

$$p_\theta = ML^2\dot{\theta} + MLr\dot{\phi}\cos(\theta - \phi),$$

while keeping the same form for the ϕ coordinate yields

$$p_\phi = I\dot{\phi} + MLr\dot{\theta}\cos(\theta - \phi),$$

which is the generalised momentum of the second coordinate. These last two equations form a system of generalised momenta that may be solved to derive expressions for $\dot{\theta}$ and $\dot{\phi}$ as follows

$$\left\{ \begin{array}{l} \dot{\theta} = \dfrac{Ip_\theta - MLrp_\phi\cos(\phi-\theta)}{ML^2\big(I - Mr^2\cos^2(\phi-\theta)\big)} \\ \dot{\phi} = \dfrac{Lp_\phi - rp_\theta\cos(\phi-\theta)}{L\big(I - Mr^2\cos^2(\phi-\theta)\big)} \end{array} \right\}. \tag{4.17}$$

This forms the first two equations of motion for the system. The remaining two must come from the Hamiltonian equation $\mathcal{H}$ which is defined as

$$\mathcal{H} = T + V.$$

Using the results of equation (4.17) in the Hamiltonian equation above we arrive at

$$\mathcal{H} = \frac{1}{I - Mr^2\cos^2(\phi-\theta)}\left(\frac{Ip_\theta^2}{2ML^2} + \frac{p_\phi^2}{2} - \frac{r}{L}p_\theta p_\phi\cos(\phi-\theta)\right) - Mg\big(L\cos(\theta) + r\cos(\phi)\big).$$

The time rate of change of the generalised momenta is determined by taking the derivative of the Hamiltonian equation with respect to the coordinate, i.e. for the θ coordinate, we have

$$\dot{p_\theta} = \frac{d\mathcal{H}}{d\theta},$$

while for ϕ we have

$$\dot{p_\phi} = \frac{d\mathcal{H}}{d\phi}.$$

Taking the derivative of $\mathcal{H}$ with respect to θ, and taking the derivative of $\mathcal{H}$ with

respect to ϕ yields the system of equations

$$\left\{\begin{array}{l} \dot{p_\theta} = \dfrac{-2Mr^2\cos(\phi-\theta)\sin(\phi-\theta)}{\big(I - Mr^2\cos^2(\phi-\theta)\big)^2}\left(\dfrac{Ip_\theta^2}{2ML^2} + \dfrac{p_\phi^2}{2} - \dfrac{r}{L}p_\theta p_\phi\cos(\phi-\theta)\right) \\ \qquad + \dfrac{rp_\theta p_\phi\sin(\phi-\theta)}{L\big(I - Mr^2\cos^2(\phi-\theta)\big)} - MLg\sin(\theta) \\ \dot{p_\phi} = \dfrac{2Mr^2\cos(\phi-\theta)\sin(\phi-\theta)}{\big(I - Mr^2\cos^2(\phi-\theta)\big)^2}\left(\dfrac{Ip_\theta^2}{2ML^2} + \dfrac{p_\phi^2}{2} - \dfrac{r}{L}p_\theta p_\phi\cos(\phi-\theta)\right) \\ \qquad - \dfrac{rp_\theta p_\phi\sin(\phi-\theta)}{L\big(I - Mr^2\cos^2(\phi-\theta)\big)} - Mrg\sin(\phi) \end{array}\right\}. \tag{4.18}$$

Equations (4.17) and (4.18) form a system of coupled first-order differential equations that depend on L, and r. Noticing that the generalised momenta depend on I the moment of inertia, we can see that neither $\dot{\theta}$ nor $\dot{\phi}$ depend on the mass of the bird. The *distribution* of the mass, however, does affect them. This can be seen from equations (4.17), and realizing that the moment of inertia of a distributed mass is

$$I = \sum_{i=1}^{N} m_i r_i^2,$$

where N is the total number of mass elements, m_i is the mass of the i^{th} element, and r_i is its distance away from the object's centre of mass. For a RESOLVE system, it is simplest to assume that the chassis is a solid rod of uniform mass distribution and length $d = 10.2$ m. In that case, the moment of inertia is

$$I = \left(\frac{d^2}{12} + r^2\right)M,$$

where the first term arises from a rod of length d rotating about its central axis, and the second term arises due to the parallel axis theorem where the rod is actually rotating about the 'Y' on the tow cable, a distance r away (Fowles and Cassiday, 1993). Using this moment of inertia for a RESOLVE model where the cable length L is 27 m and the vertical displacement from the 'Y' to the centre of the chassis

is $r = 3.5$ m, displacing the bird by 5° yields Figure 4.38. The predicted cable swing has a period of approximately 12 s, which is longer than the 9–10 s observed in reality: the predicted bird pitch is about 4 times to every cable swing, which is consistent with the Sunraysia video.

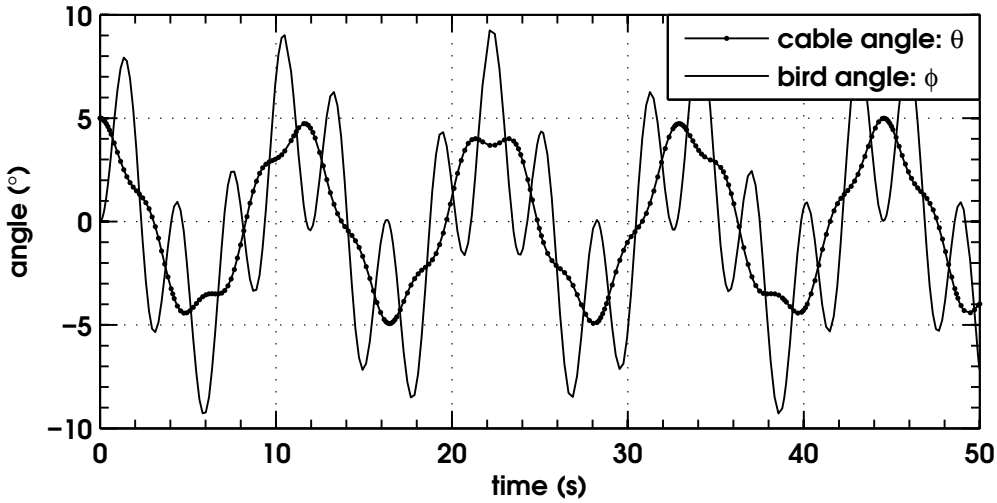

Figure 4.38: *Plot of cable (θ) and bird (ϕ) swing versus time as a result of numerically solving the system of differential equations (4.17) and (4.18) with $L = 27$ m, $r = 3.5$ m, $d = 10.2$ m and $\theta(0) = 5°$. Notice that the bird pitches approximately 4 times to every cable swing, similarly to what was seen in the Sunraysia video.*

The moment of inertia that I have chosen to illustrate for this model does not reflect the actual distribution of mass in the towed bird. Obviously, it is important to know the mass distribution and it is likely that it is something more like a few large point-like masses (due to the copper coils) placed inside a comparatively light cylindrical shell. My model is one of the simplest to consider and, it must be said, ignores the effect of air resistance. Equations of motion including drag become much more complicated and it was felt that the effort would outweigh the potential benefit.

4.8 Summary and Conclusion

I began this chapter by asserting that there is a relation between bird swing and system response based on the evidence from Chapter 3. In Section 4.2, I developed a

model that shows how bird swing affects system response when the radar altimeter mounted on the helicopter is used to estimate the altitude of the towed bird on survey. Radar altimeter measurement is insensible to bird swing, so when viewing β calculated using radar altitude estimates, bird swing readily shows up in the data. Any swing that lifts the bird away from the earth will reduce the response of the system; consequently β is reduced. Swings that reduce the separation of the bird from the earth increase the response and hence β.

Similar results are seen when a bird-mounted laser altimeter is used to measure bird altitude, although the effect on β is somewhat more complicated. Rotations of the bird due to cable swing and wind buffeting etc. cause the altimeter reading to be in error. This changes β in two ways. First, bird rotation changes the system response. The maximum amount that it can change by, in the inductive limit, is governed by the generalised geometrical factor derived in equation (4.6). Second, laser altimeter error enters the calculation of β by its inclusion in equation (4.6). The result of this combination was discussed in Section 4.4.

For both the radar altimeter and laser altimeter cases, I designed a filter that removes the effect of bird swing from β provided the main frequency of the oscillation is known. These filters, described by equation (4.9) for the case of the radar altimeter and equation (4.12) for the laser altimeter remove both the fundamental and the first harmonic frequency effects from β. The first harmonic frequency also contains a magnitude term that must be added to β calculated with radar altimeter data and subtracted from β calculated with the laser altimeter data. I have shown their efficacy in filtering β in the Sydney Harbour, Chowilla Floodplain and Sunraysia datasets, and am convinced that they can be used to enhance the final data from a survey.

By using sequential photographs to make a stop-action movie, I have determined the fundamental frequencies of the cable swing and bird pitch for the Sunraysia survey. My measurement of predicted bird and cable swing corroborate the mea-

surements of bird pitch and roll provided by the contractors. In my opinion, a third method needs to be tested before any more conclusions can be drawn. Using the simultaneous position solutions of the helicopter-mounted GPS antenna and the bird-mounted GPS antenna it is possible to predict roll of the bird to within about 5°. In my particular test on a section of line 21020 from the Sunraysia survey, there appeared to be a systematic difference of ∼2° between my prediction of bird roll and the measured roll provided by the contractors. Again, a third test should be applied to establish which method is more in error. Despite the fact that bird roll is very easily predicted from the GPS data, bird pitch predictions are not as successful. In Section 4.6.2, I showed that my bird pitch predictions were different from the measured and apparent bird swing predictions by about 5°; but there are times when the error is as great as 10°–12°. I conclude that bird pitch cannot be predicted from helicopter and bird GPS position solutions. The prediction is useful, however, as a check on the bird pitch values measured by the 3 GPS antenna array.

In this chapter, I studied the pendulum-like motion of a scale RESOLVE model. From analysis of the video recordings, I discovered that the bird swing period decreases with increased 'Y' attachment length, even though the period of the cable increases with increased length. Furthermore, the ratio of ∼4 bird swings to 1 cable swing is not unique to the system: it can be changed by altering the separation of the 'Y' attachment to the centre of the bird. I developed a simple mathematical model that predicts the behaviour of a rigid member that is attached to two cables and is allowed to rotate about their join. This is in essence a simplification of the classic double pendulum problem (e.g. Fowles and Cassiday, 1993), and the system of first-order differential equations has been presented here.

To close the chapter and my discussions of pendulum like behaviour of towed HEM systems, I present a few conclusions and recommendations for future researcher and field workers. First, I have substantively proven that the β domain is an excellent tool to investigate the effects of bird swing in data. It provides a means to test for

bird swing and is also an excellent domain to test for any corrections that are made to the data as a consequence of trying to eliminate it. Furthermore, bird swing is most easily seen when calculating β using the altitude estimated with the radar altimeter, and I strongly recommend using that as a first tool. System testing for bird swing is most readily accomplished over an area of uniform conductivity such as seawater. It provides an excellent basis for seeing the signature oscillations in β that indicate bird swing.

When using a laser altimeter to measure bird height above earth, it is important to keep in mind the position of the laser altimeter on the bird and its orientation. It is normal on the RESOLVE towed birds for the laser altimeter to be housed in the underside of the chassis, close to the nose. As I have shown in this chapter, this creates a sine type of error in the measured altitude when the bird swings, and it is not an accurate reflection of the separation of the centre of the transmitter and receiver coil pair. I therefore recommend that the laser altimeter is mounted as closely as possible to the rotation point of the bird. With this arrangement the laser altimeter error will only be an overestimate of the true altitude of the bird, effectively shifting the solid line in Figure 4.14 up and to the right so that it is symmetrical about a vertical line at the point $(0, 1)$. This simplifies the error predictions due to bird swing using the laser altimeter.

Pitch and roll measurement of a towed bird is a tricky problem. In the Sunraysia survey discussed in this chapter, the contractors used 3 GPS antennae mounted in a triangle configuration that enabled them to measure roll, pitch and yaw. While these measured values appeared to be reasonable, I have proven that there are times when they are in error. Furthermore, there does not appear to be any way to predict the times that the measured values will be in error. As a check on this, I recommend my method of checking measured bird pitch and roll based on helicopter and bird GPS position solutions. In addition, I believe that so long as $\pm 5^\circ$ errors are permitted in the measurement of bird roll, one GPS antenna may be removed from the 3 GPS

triangular array. This would leave just two GPS antennae, mounted fore and aft on the bird, to measure bird pitch and yaw.

I have attempted to correct EM system data with the measured bird pitch and roll values provided by the contractor, but my success was limited. The method that I used, based on the generalised method of images and corrected laser altitude does not yield a significant improvement to the same area that has had a bird swing filter applied to it. The main advantage of the method is that it offers a point-by-point calculation to the data rather than a time series filtered output. The bird swing filters are specifically designed to remove features that repeat with particular frequency. If there is a real repeating physical feature in the data that shares the same period as a bird swing, it will be removed. The point-by-point method will not do this. It is interesting to note that the generalised method of images offers the same order correction to the data as the correction derived by Fitterman and Yin (2004) for the HCP coil pair. They report that, like the generalised method of images, in-phase and quadrature data changes with pitch and roll angles via a cosine squared relation. I believe that, since Figure 4.29 is so little different from Figure 4.28, more care must be given to their $\frac{T_2}{BT_0}$ term, and we cannot simply assume that it goes to 0.5 as they suggest.

Finally, I have derived some equations of motion for the RESOLVE towed bird system in free space subject only to an initial displacement and the force of gravity. From these equations, it is possible to predict the fundamental frequencies of the cable and bird swings. In the simple example I have given, a cable of 27 m attached to a 'Y' member of cord that suspends a towed bird of 10.2 m length 3.5 m below the attachment has a cable swing period of $\sim$12 s and a bird pitch period of $\sim$3 s. These periods are close to the oscillations observed in the data and offer a simple first step to predicting bird and cable swing for future towed bird systems.

Chapter 5

Calibration of AEM Systems Using a Ground Loop

5.1 Introduction

The last two chapters have dealt with the pendulum-like motion of towed HEM birds and the effect the swinging has on recorded EM data. Both the RESOLVE and DIGHEM HEM systems are frequency domain systems: the transmitters output a sinusoidal signal that constantly induces eddy currents in the earth. I will now turn our attention to time domain AEM systems which will, of course, experience the same pendulum effects as frequency domain systems. Time domain EM systems (TDEM) operate by generating in the transmitter a current pulse or ramp that in turn creates an electromagnetic pulse that travels to and penetrates the earth. The physics of TDEM systems is similar to the frequency domain case, with the ground producing eddy currents which generate electromagnetic fields that transmit outwards. A towed receiver intercepts a portion of the secondary field and converts it to a measurable voltage. Instead of measuring in-phase and quadrature portions of the secondary field, a TDEM receiver measures the secondary signal from a pulse as a sequential series of voltages. In modern, digitally controlled TDEM systems, the

transmitter current is controlled by a microprocessor that produces a waveform of a certain predefined shape. Although some time domain receivers record the secondary response continuously, I will only refer to systems that record during the off-time. A switch in the microprocessor then synchronises the receiver. A time delay allows the EM pulse to travel to the ground and set up the secondary response, as well as to ensure that there is minimal voltage applied to the transmitter before the receiver is turned on. Once the delay time has passed, the microprocessor turns the receiver on and begins recording the voltage drop across the receiving coil. The time series of recorded voltages is binned according to the design of the system. Typically, the bins are spaced logarithmically in time, i.e. the time measurement window gets wider as time passes. These windows are often called 'channels' or 'delays'. After the voltage receiving is complete, the transmitter gets turned on again with the transmitting current run in the opposite direction: this is called the negative half cycle of the waveform. The receiver is turned on again, and the secondary response recorded for this portion of the cycle. Once the negative half cycle is complete, the process begins all over again. Airborne time domain EM systems generally operate at base frequencies of around 30 Hz to 50 Hz, i.e. 30–50 complete waveforms per second. A schematic timing diagram of a time domain EM system is shown in Figure 5.1. The example shown in this figure has a square or castellated current waveform. The first part of figure shows the positive on-time of the current, followed by a short delay time. The receiver then records voltage and bins them according to the times t_1, t_2, t_3 and t_4. These are the decay times and they occur during the transmitter off-time. The cycle then repeats in the negative sense.

The secondary response measured by the receiver yields information about the conductivity structure of the earth. We can determine this structure in much the same way that conductivity structure is determined in the frequency domain case. For example, we can compare the decay time voltages to type curves known for a specific geometry, or we can invert the data using modelling programs (Oldenburg

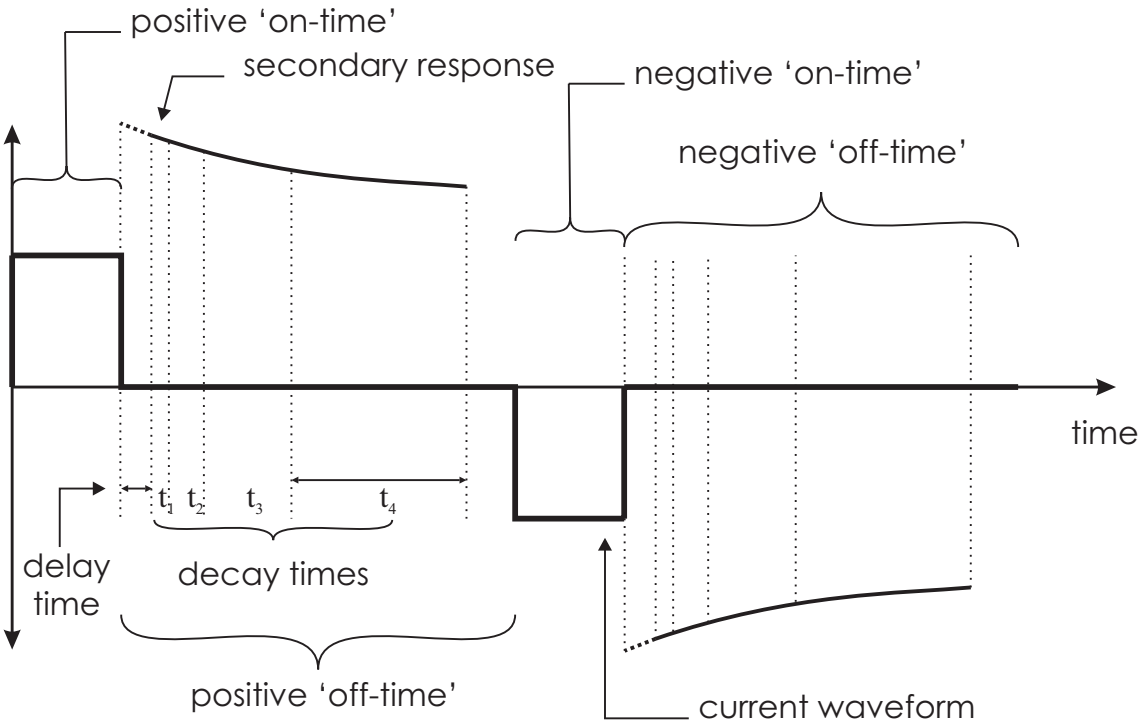

Figure 5.1: *Schematic of a nominal time domain transmitter current waveform, delay time and receiver time windows. A complete cycle is made of a positive on-time, a delay, the positive off-time whereby the receiver records the secondary signal, a negative on-time, delay, and the negative off-time.*

and Li, 2005; Raiche, 1998). As with the frequency domain case, difficulties arise in interpretation when there are problems with the calibration of the system. In this chapter, I will explore some of the calibration issues that occur in time domain airborne EM systems and explain my attempt at resolving these problems.

5.1.1 Calibration Problems in Time Domain AEM Systems

Time domain systems are repeated pulse or ramp systems. After every half cycle, the receiver records voltages and averages them into decay windows or channels. The positive and negative half cycle voltages are then averaged together, with the sign reversed on the negative half cycle. Several of the cycles are then averaged together—known as stacking—and the resulting decay voltages are recorded at one fiducial. In such a process as this, accurate timing is essential, and the complete cycle process must be known precisely. For example, we must know how much time

has passed between when the transmitter current is shut off and when the first receiver gate opens. We need to know how long each gate is for the decay voltage measurement, what shape the transmitter current has during the excitation stage, how long it takes to turn off, and what its peak current is. The transmitter and receiver information needs to be correlated back to the actual survey and logistics information. As I will show in the next two chapters, it turns out that some of that information is not well known. For example, some transmitter current waveforms have a different shape from the one reported by the contractor. Other waveforms have instability in their peak current output. Still others are not known, as is the case when the receiver is so close to the transmitter loop that it is impossible to turn the receiver on during the on-time. The correction method that I propose in this chapter deals specifically with the 'waveform' problem.

Geometrical errors are also possible. For example, system geometry is important: we need to know the separation distance of the transmitter and receiver to get an idea of how to model the response. Ground clearance and position also need to be known in order to generate accurate conductivity structure maps. The problems of laser and radar altimetry are no less important for time domains systems as they are for frequency domain, as is the pendulum problem. In a fixed wing towed bird system like GEOTEM (Fugro Airborne Surveys, 2005*a*), the position of the bird is often estimated to be 30–60 m down and 100–120 m back from the navigation GPS antenna that is mounted on the airplane. Smith (2001) tried to account for the bird's pendulum motions using the measurement of the total field produced by the transmitter during the on-time. For the VTEM system (Witherly et al., 2004), a helicopter towed bird time domain EM system, the transmitter and receiver are considered to be coincident loop and are estimated to be 35 m below the helicopter (similar to the RESOLVE system). These variables combine to create what I call geometrical calibration errors. In theory, it should be possible to correct an AEM system for these errors.

Calibration of AEM systems can be problematic. For most systems, accurate calibration cannot be achieved on the ground. The main reason for this is because the system geometry cannot be reproduced while the aircraft used for towing the receiver is in the hangar or on the airstrip. For some fixed-wing systems, transmitters cannot be run at full power on the ground because they rely on the rushing air of flight to provide adequate cooling. Although helicopter EM systems operating in the frequency domain can be calibrated with sets of loops of known response, the procedure can fail when the calibration is attempted near conductive or magnetic ground. For time domain electromagnetic systems, one of the greatest difficulties is determining transmitter waveform due to over-range on the sensitive receiver electronics which are suited to off-time measurement. In addition to this, it is often difficult to determine precisely when the transmitter has been turned off and the receiver turned on.

As a means of checking the response signal and geometry of time domain towed bird systems, I tested the idea of using a closed loop of accurately known electrical properties that is positioned on, but insulated from, the ground. In this chapter I will show the results of my experiments, but first I will give an explanation of the concept of using a ground loop to calibrate AEM systems.

5.2 Calibration of AEM Systems Using a Ground Loop—Concept

Using a ground loop to check for system operation is not new. In Fountain's (1998) review article, he mentions that ground loops were laid out on frozen lakes in Canada to test for a secondary response. Another method, for the Input system, was to fly the system over large lakes of known resistivity (Nelson, 1973). Prior to that, Becker (1969) employed conductive rings to calibrate the Input time domain system. He compared the system response of the conductive ring to the electrical response of an

RC network, and used Fourier analysis to compute theoretical calibration curves. Indeed, Gupta Sarma et al. (1976) suggested the simplification of assuming every conductor is a simple one-turn wire loop when assessing the performance of an AEM system over a variety of conductors. The manner of calibration which I propose is similar. An airborne time domain system can be calibrated by flying the system over a closed multi-turn loop of known resistance and inductance. The transmitter's magnetic pulse generates an eddy current in the ground loop described by Faraday's law of induction. The magnitude of the eddy current produced in the ground loop is determined by the shape of the current waveform in the transmitter and the mutual magnetic inductance coupling the transmitter to the ground loop. The eddy current generated in the ground loop decays at a constant exponential rate determined by the resistance R and total self inductance L of the ground loop. Both of these values can be measured or estimated. The electromagnetic field generated by the eddy current, called the secondary field, is then detected by the receiving loop of the EM system. The magnitude of the secondary response is determined both by the geometric mutual magnetic inductance coupling the receiver to the ground loop and the amount of current flowing in the ground loop. Since magnetic inductance is determined by geometry, the signal measured in the receiver is a function of the positions of all three loops. This is shown schematically in Figure 5.2. The mutual magnetic inductance of each loop pair (if known) can be calculated using the principles described in Section 2.7.

The ground loop position is known by ensuring that it is accurately surveyed when it is laid out. This is achieved by obtaining the position of each corner with a GPS receiver and making sure that the loop wire is straight when it is deployed. The position of the transmitter is generally known or approximated. If the system is mounted on a fixed wing aircraft, we can for example estimate that the transmitter loop is symmetric about the GPS antenna, and the separation of the transmitter from the earth is measured with a laser or radar altimeter when it is on survey. The

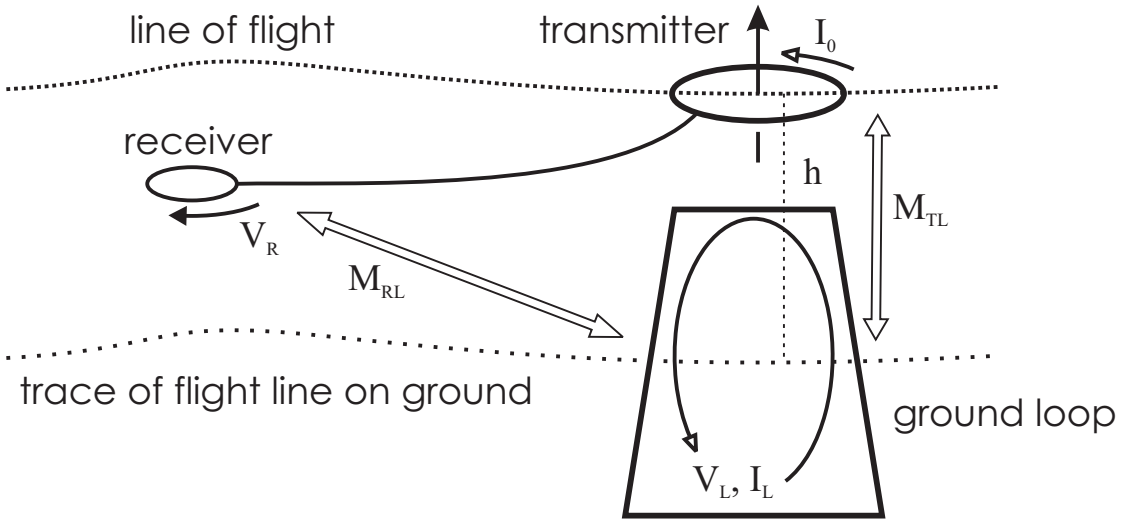

Figure 5.2: *Diagram of the concept of calibrating an AEM system using a ground loop. The height of the transmitter above the ground loop is measured using an altimeter (or GPS positions). The mutual inductance between transmitter and the ground loop, and between the ground loop and receiver is calculated.*

altimeter measurement can be in error and corrected for as discussed in Section 4.4.1. The receiver position with respect to the aircraft is often not well known, is likely a function of airspeed, changes continuously due to bird swing and therefore must be derived from the nominal geometry claimed by the contractor (e.g. Witherly et al., 2004). Although in systems such as TEMPEST, the receiver position is predicted based on the primary field, this calibration method will always be limited by the lack of knowledge of the geometry of the towed bird.

By measuring the voltage across a resistor that is in series with the ground loop, it is possible to calculate the current flowing in it as a result of the excitation from the transmitter pulse during flyover. This can predict (hence, calibrate) the waveform of the transmitter current if no other conductors are present, since the current in the ground loop is proportional to $\frac{\partial I}{\partial t}$ of the current waveform. As a further check on transmitter and receiver location, it is possible to tie the voltage measurement with an accurate GPS clock. This allows synchronisation between the transmitter (whose position is monitored with the AEM system's navigational GPS receiver) and the current flowing in the ground loop.

Calculating mutual inductances and receiver responses requires certain assumptions about the geometry of the system. Differences in the measured receiver voltages compared to expected voltages can be attributed to errors in waveform, delay time onset, altitude measurement and overall geometry (which changes continuously because of bird swing). Even so, the ground loop technique is an attractive idea for calibration. Wire loops are easy to lay out, very inexpensive and can be left on the calibration line for the duration of the survey. Their electrical properties are very well understood and highly configurable (i.e. it is easy to change the resistance and self inductance of the loop). Multichannel data loggers are relatively inexpensive and configurable GPS receivers are easily obtained. But, it turns out that the task of calibration is not so simple to carry out in practice.

5.3 Mathematical Derivation of the Calibration

Before I discuss the results of my experiments for calibrating time domain systems, I will present the theory of the calibration process. The derivation is similar to Section 2.8. This time, the current in the transmitter is not a repeating sine wave but is permitted to be a more general function of time, i.e. $I_T \rightarrow I_T(t)$.

Using the general function $I_T(t)$ for the current in the transmitter, we can use the derivation discussed in Section 2.8 to obtain the differential equations for this situation. As discussed before, the current in the transmitter generates a magnetic field that is proportional in magnitude to the strength of the current flowing in the loop. Because the transmitter current is changing with time, this creates a time-varying magnetic flux that flows through the ground loop. This in turn creates an emf in the ground loop according to equation (2.45), repeated here for convenience:

$$\mathcal{E} = -\frac{\partial \Phi}{\partial t}.$$

Using the above equation expressed in a more useful way (such as equation (2.74)),

we see that the emf in the ground loop due to the transmitter current is simply (e.g. Grant and West, 1965)

$$\mathcal{E}_L(t) = -M_{TL}\frac{\partial}{\partial t}I_T(t), \tag{5.1}$$

where the subscript L refers to the ground loop and M_{TL} is the mutual inductance between the transmitter and the ground loop.

Since the emf generated in the loop is equal to the potential drops across the loop due its resistance and self-reactance, we have the following relation in the loop:

$$\mathcal{E}_L(t) = R_L I_L(t) + L_L\frac{d}{dt}I_L(t).$$

Rewriting the above equation to include equation (5.1), and dropping the subscript $_L$ from the resistance R and the self induction L, we have the following first-order differential equation describing the current in the ground loop

$$\frac{d}{dt}I_L(t) + \frac{R}{L}I_L(t) = \frac{-M_{TL}}{L}\frac{d}{dt}I_T(t). \tag{5.2}$$

I have changed the partial derivative to a full one on the transmitter current $I_T(t)$ since it can be assumed that amplitude changes due to system translation are slow compared to the changes in transmitter current. Equation (5.2) gives us the first equation of this time domain system. The second equation, that describing the emf generated in the receiver from the ground loop current, also obeys Faraday's Law. It is therefore simple to write the expression of the emf in the receiver:

$$\mathcal{E}_R(t) = -M_{RL}\frac{d}{dt}I_L(t), \tag{5.3}$$

where the subscript R implies the receiver, M_{RL} is the mutual inductance between the receiver and the ground loop, and again I use a full derivative in time.

Together, equations (5.2) and (5.3) determine the measurable ground loop current and receiver voltage. In a time domain geophysical survey, it is the latter

quantity that is measured in order to determine the conductivity structure of the earth. Provided we know the waveform of the transmitter current, we can determine what voltages should be measurable at the receiver due to the geometry of the survey set-up and the electrical properties of the ground loop.

The time domain calibration scheme shown in Figure 5.2 is described by the set of equations

$$\left\{ \begin{array}{c} \frac{d}{dt} I_L(t) = -\frac{R}{L} I_L(t) - \frac{M_{TL}}{L} \frac{d}{dt} I_T(t) \\ \mathcal{E}_R(t) = -M_{RL} \frac{d}{dt} I_L(t) \end{array} \right\}. \tag{5.4}$$

I believe the simplest way to solve the equations above is to view them as an input/output system determined by the transmitter current (input) and the measurable receiver voltage (output). To analyse this we can use the formalism of the Laplace transform operating on a function $F(t)$ of time, and transforming to the Laplace space s (i.e. $\mathfrak{L}\big[F(t)\big]$) to solve the differential equations. The Laplace transform is discussed, for example, in Simmons (1991), and is valid for piecewise continuous and differentiable equations. It is particularly useful for applications where we wish to determine the response of a system to a sudden impulse or change in variables. For this derivation, I assume that the transmitter current $I_T(t)$ is a function that has derivatives everywhere in positive time except for a few places where it is permitted to be discontinuous. With this in mind, we will assume that both $I_T(t)$ and $\frac{d}{dt} I_T(t)$ exist, and that we can always determine $\frac{d}{dt} I_T(t)$ from $I_T(t)$. Therefore, I will carry the derivative of the transmitter current out of the system of equations and replace $\frac{d}{dt} I_T(t)$ with the simple notation $I'_T(t)$ to imply that we know the derivative at all points in time. Thus equation (5.4) becomes

$$\left\{ \begin{array}{c} \frac{d}{dt} I_L(t) = -\frac{R}{L} I_L(t) - \frac{M_{TL}}{L} I'_T(t) \\ \mathcal{E}_R(t) = -M_{RL} \frac{d}{dt} I_L(t) \end{array} \right\},$$

and applying the Laplace transform yields

$$\left\{ \begin{array}{l} s\mathfrak{L}\big[I_L(t)\big] = -\dfrac{R}{L}\mathfrak{L}\big[I_L(t)\big] - \dfrac{M_{TL}}{L}\mathfrak{L}\big[I'_T(t)\big] \\ \mathfrak{L}\big[\mathcal{E}_R(t)\big] = -sM_{RL}\mathfrak{L}\big[I_L(t)\big] \end{array} \right\}. \tag{5.5}$$

5.3.1 Ground Loop Response

The upper expression in equation (5.5) describes the current induced in the ground loop through Faraday induction from the field produced by the current in the AEM transmitter. Collecting terms of $\mathfrak{L}\big[I_L(t)\big]$ yields

$$\mathfrak{L}\big[I_L(t)\big]\left(s + \frac{R}{L}\right) = -\frac{M_{TL}}{L}\,\mathfrak{L}\big[I'_T(t)\big].$$

The current in the ground loop can now be written explicitly. By taking the inverse Laplace transform of both sides, and taking advantage of the fact that the inverse Laplace transform of a Laplace transform is simply the argument, the current in the ground loop becomes

$$I_L(t) = -\frac{M_{TL}}{L}\,\mathfrak{L}^{-}\left[\frac{1}{s + \dfrac{R}{L}}\mathfrak{L}\big[I'_T(t)\big]\right], \tag{5.6}$$

where the term in the square brackets on the right-hand side represents the convolution of the *incidial* or *impulse* response (defined later) with the waveform (Simmons, 1991). I now change the general assumption on the transmitter current waveform and force it to become a function that starts from 0 A at time $t \leq 0$ s and assumes a peak current of I_T sometime after $t = 0$ s. The transmitter current waveform then becomes

$$I_T(t) = \begin{cases} 0 & \text{if } t < 0, \\ I_T\, i_T(t) & \text{if } t \geq 0, \end{cases}$$

where $i_T(t)$ is a piecewise continuous function determined for any time t. Using this result, equation (5.6) becomes

$$I_L(t) = -\frac{I_T M_{TL}}{L}\,\mathfrak{L}^{-}\left[\frac{1}{s+\dfrac{R}{L}}\mathfrak{L}\left[i'_T(t)\right]\right]. \tag{5.7}$$

This is the general expression for the current induced in the ground loop due to a transmitter current of peak value I_T, whose shape is determined by $i_T(t)$. The convolution term describes the temporal behaviour of the ground loop for all positive times.

Let's assume that the current in the transmitter is suddenly turned on at time $t = 0$. We can immediately see the current response of the ground loop by using equation (5.7). Let $i_T(t)$ be represented by the Heaviside step distribution:

$$i_T(t) = U(t) = \begin{cases} 0 & \text{if } t < 0, \\ 1 & \text{if } t \geq 0. \end{cases}$$

With this determination, the time derivative of the transmitter current is

$$i'_T(t) = U'(t) = \begin{cases} \delta(t) & \text{if } t = 0, \\ 0 & \text{otherwise.} \end{cases} \tag{5.8}$$

The Laplace transform of the Dirac delta function is 1 (e.g. Spiegel, 1995), so equation (5.7) becomes

$$I_L(t) = -\frac{M_{TL} I_T}{L}\,\mathfrak{L}^{-}\left[\frac{1}{s+\dfrac{R}{L}}\right],$$

which, after performing the inverse Laplace transform, yields

$$I_L(t) = -\frac{M_{TL} I_T}{L} e^{-tR/L};$$

the ground current exponentially decays with characteristic time $\tau = \frac{L}{R}$ from a discontinuity at $t = 0$ whose limit from the positive side is $\frac{-M_{TL} I_T}{L}$ and is proportional to the size of the current step in the transmitter. This is known as the *incidial* response of the ground loop to the transmitter current if we are looking at the transmitter current waveform $I_T(t)$ as the main input and also as the *impulse* response of the ground loop, if we regard the time rate of change of the transmitter current $I_T'(t)$ as the main input to the system. Regardless of paradigm, the fundamental lesson to be learned is that no matter what the waveform of the transmitter current is, the ground loop will always respond with an exponentially decaying current after excitation.

5.3.2 Receiver Response

Examination of the lower expression of equation (5.5) shows that the emf in the receiver behaves in an analogous manner to the ground loop current. Solving the top expression of equation (5.5) for $\mathfrak{L}\big[I_L(t)\big]$, using equation (5.7) as the expression of $I_L(t)$, and substituting them into the bottom expression of equation (5.5), yields

$$\mathfrak{L}\big[\mathcal{E}_R(t)\big] = \frac{M_{RL} M_{TL} I_T}{L} \left(\frac{s}{s + \dfrac{R}{L}} \mathfrak{L}\big[i_T'(t)\big] \right). \tag{5.9}$$

As with the ground loop current, the presence of the pole at $s = \frac{-R}{L}$ implies that the emf in the receiver decays exponentially with the rate determined by the electrical properties of the ground loop. The presence of an s in the numerator indicates an impulse in the receiver response at $t = 0$ s. Using equation (5.8) to describe the step

in the transmitter current, the incidial or impulse response of the receiver is

$$\mathcal{E}_R(t) = \frac{M_{RL}M_{TL}I_T}{L}\Big(\delta(t) - \frac{R}{L}e^{\frac{-tR}{L}}\Big),$$

which, using $\tau = \frac{L}{R}$, can be expressed as

$$\mathcal{E}_R(t) = \frac{M_{RL}M_{TL}I_T}{L}\Big(\delta(t) - \frac{1}{\tau}e^{\frac{-t}{\tau}}\Big).$$

This result is consistent with Liu (1998), who used the step operator in the transmitter current waveform to compare the effectiveness of arbitrarily shaped current waves and hence determine their resolving ability when a target is buried under conductive overburden. The factor $\frac{M_{RL}M_{TL}}{L}$ is the inductive limit of the system response and is analogous to the coupling coefficient defined in equation (2.81).

Going back to equation (5.9) and taking the inverse Laplace transform of both sides of the equation yields

$$\mathcal{E}_R(t) = \frac{M_{RL}M_{TL}I_T}{L}\,\mathfrak{L}^{-}\left[\frac{s}{s+\dfrac{R}{L}}\mathfrak{L}\big[i'_T(t)\big]\right].$$

This is the general solution of the receiver response to any waveform. The term in square brackets is the total transient system response which is determined by the electrical properties of the ground loop and the shape of the transmitting current waveform. In signal processing terms, it is known as the transfer function (Lyons, 1997). It represents the convolution of the impulse response of the system to the time derivative of the waveform of the transmitter current. As with the induced current in the ground loop, the receiver emf will always decay exponentially with time constant $\tau = \frac{L}{R}$.

In practical systems, the transmitter current is repeated with period T. The secondary response is sampled in channels or time windows and the result is then

stacked over a number of half waveforms (or cycles) of period $\frac{T}{2}$ in order to reduce signal noise. Following the derivation of Stolz and Macnae (1998), but using my formalism, the windowed response at time $t = \frac{t_k + t_{k+1}}{2}$ due to sampling the repetitive receiver emf from $t = [t_k, t_{k+1}]$ is

$$\mathcal{E}_R(t_k, t_{k+1}, T) = \frac{M_{RL} M_{TL} I_T}{L} \frac{\tau\left(e^{\frac{-t_k}{\tau}} - e^{\frac{-t_{k+1}}{\tau}}\right)}{\left(t_{k+1} - t_k\right)} \frac{1}{\left(1 + e^{\frac{-T}{2\tau}}\right)} \mathfrak{L}^{-} \left[\frac{s}{s + \frac{R}{L}} \mathfrak{L}\left[i'_T(t)\right] \right]. \quad (5.10)$$

The first term represents the geometric coupling; the second term accounts for the integration of $e^{\frac{-t}{\tau}}$ from t_k to t_{k+1}, the third term is the result of a Taylor series that factors the repetitive nature of the transmitter current waveform and the fourth term is the transfer function that convolves the impulse response to the transmitter waveform (or, in this case, $\frac{d}{dt} I_T(t)$).

5.4 Calibration of the AeroTEM System

5.4.1 Description of the System

The first AEM calibration that I will present is of the AeroTEM II helicopter-borne time domain system (Aeroquest International, 2005). AeroTEM is a coincident loop system, meaning that the receiver z-coil is in the plane of and concentric to the transmitter loop. It has been in service in different configurations since 1999 (Balch, 2004; Balch and Boyko, 2003; Balch et al., 2002). The transmitter current waveform for this system is a triangular half pulse, operating between 25–150 Hz. For this experiment, the system was operated at 125 Hz with a 0.004 s half pulse and a peak current of ∼270 A. The positive half-cycle of the transmitter current waveform, along with the off-time receiver time windows, is shown in Figure 5.3a.

The time derivative of the current waveform is shown in panel (b); it results in a series of step functions whose height is equal to the slope of the current waveform for each section.

The last panel (c) in Figure 5.3 shows a model of the emf induced in the receiver as a result of the secondary coupling with the transmitter loop through the ground loop when the entire system is 30 m above the centre of an 80×80 m loop with resistance of 1.35 Ω and self inductance of 695 μH. Using equation (5.10), we can predict the emf that should be measured by the receiver due to the secondary field produced by the ground loop. The channel or window times for the AeroTEM system (provided by the contractor) are given in Table 5.1.

Table 5.1: *Off-time window times for the AeroTEM II system measured from the beginning of the transmitter waveform.*

Channel	Start Time (ms)	End Time (ms)	Time Window Width(μs)
1	1.19411	1.22188	27.8
2	1.22188	1.24965	27.8
3	1.24965	1.27742	27.8
4	1.27742	1.30519	27.8
5	1.30519	1.33296	27.8
6	1.33296	1.36073	27.8
7	1.36073	1.41627	55.5
8	1.41627	1.47181	55.5
9	1.47181	1.52735	55.5
10	1.52735	1.58289	55.5
11	1.58289	1.69397	111
12	1.69397	1.80505	111
13	1.80505	1.94390	139
14	1.94390	2.13829	194
15	2.13829	2.44376	305
16	2.44376	2.91585	472
17	2.91585	3.66564	750

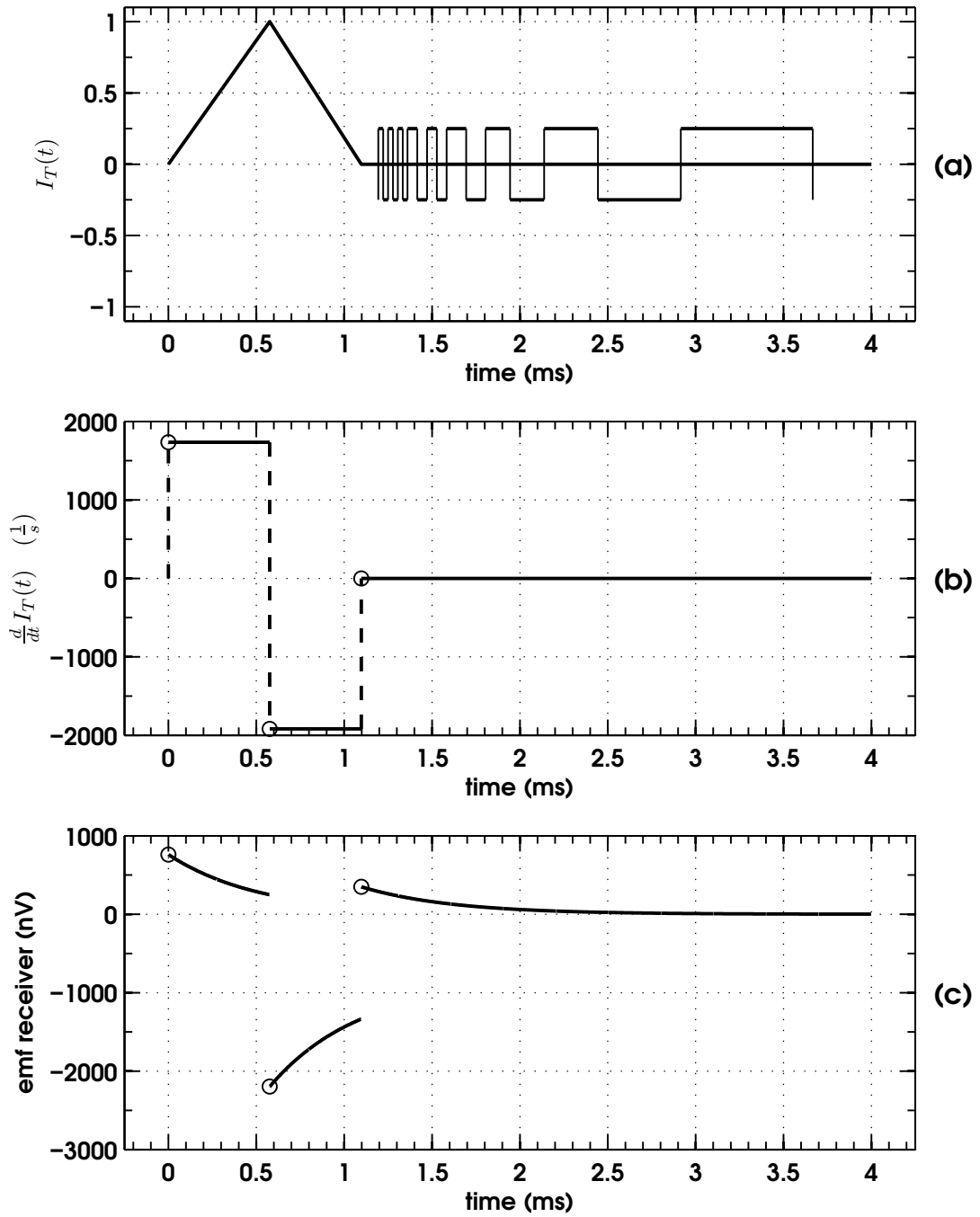

Figure 5.3: *(a) AeroTEM transmitter current waveform, normalised to 1, versus time for a positive half cycle. Also included are the off-time receiver voltage measurement windows. (b) $\frac{d}{dt}I_T(t)$, the first derivative of the current profile results in a series of step functions whose height is determined by the slope of the waveform in (a). (c) Predicted response in the receiver coil when the AeroTEM system is 30 m directly above the centre of the loop.*

5.4.2 Description of the Experiment

The values reported of the resistance and self inductance of an 80×80 m loop were measured by the contractor for the purpose of this calibration experiment. The AeroTEM system was slung beneath a helicopter using a (nominal) 55 m cable. The altitude of the transmitter and receiver are predicted from the altitude of the helicopter, as measured with a radar altimeter, minus the cable length. The transmitter loop is an octagon of point-to-point diameter of 5 m, and typically is flown at survey heights of 30 m (Aeroquest International, 2005). For this altitude, it is a reasonable approximation to model the receiver coil as a dipole receiver.

Position of the towed bird system was predicted from the measured position of a GPS antenna mounted on the helicopter. The bird's easting and northing, although not known precisely, is assumed to be that of the helicopter. Data was stacked and recorded every 0.1 s. Knowing the instantaneous 3-dimensional positions of the transmitter, receiver and ground loop, we can predict the emf of the receiver based on the transmitter waveform and receiver averaging windows of Table 5.1.

In this experiment, the AeroTEM system was flown 9 different times over a ground loop whose corner positions were accurately measured. The flight lines, in diagonals across the square loop, are shown in Figure 5.4. The loop, whose coordinates are given in Table 5.2 was laid out over resistive ground in South Africa. As an example of the response measured by the receiver as the AeroTEM system is flown over the ground loop, Figure 5.5 shows the response for line 8 (marked with open circles in Figure 5.4).

5.4.3 Results and Discussion

Using the flight path recovered from the flyover, the altitude of the bird predicted from the radar altimeter, and the time windows provided by the contractor, I calculated the expected response for line 8. The result of my calculation, together with

Table 5.2: *Coordinates of the corners of the loop for the AeroTEM calibration test (UTM Zone 35, WGS84).*

Easting (m)	Northing (m)
$_{5}92_{820}$	$_{71}29_{300}$
$_{5}92_{900}$	$_{71}29_{300}$
$_{5}92_{900}$	$_{71}29_{220}$
$_{5}92_{820}$	$_{71}29_{220}$

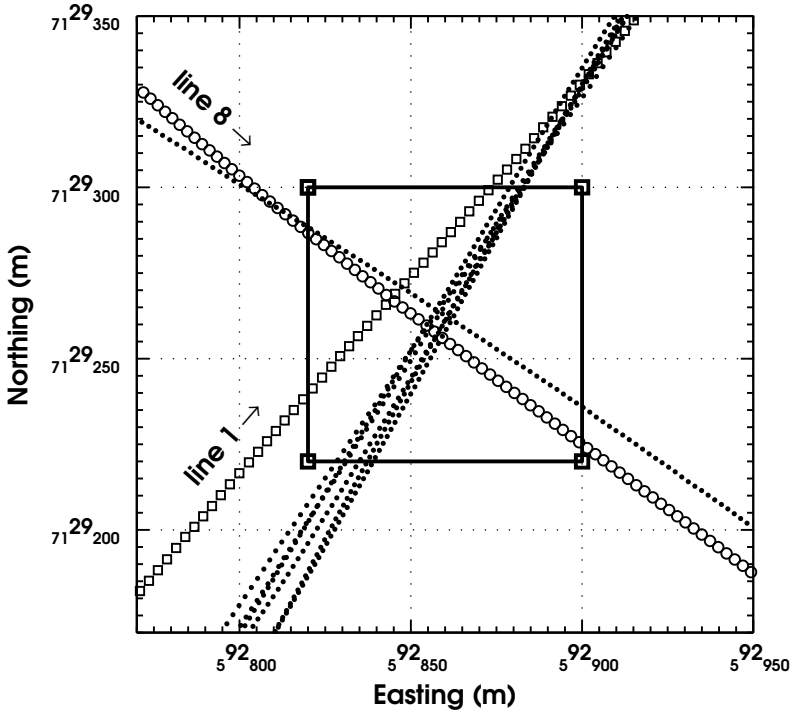

Figure 5.4: *Plot of the 9 flight lines flown by AeroTEM over an 80×80 m ground loop of resistance $R = 1.35\ \Omega$ and total self inductance $L = 695\ \mu H$. Line 8 is marked with open circles, while line 1 is marked with open squares.*

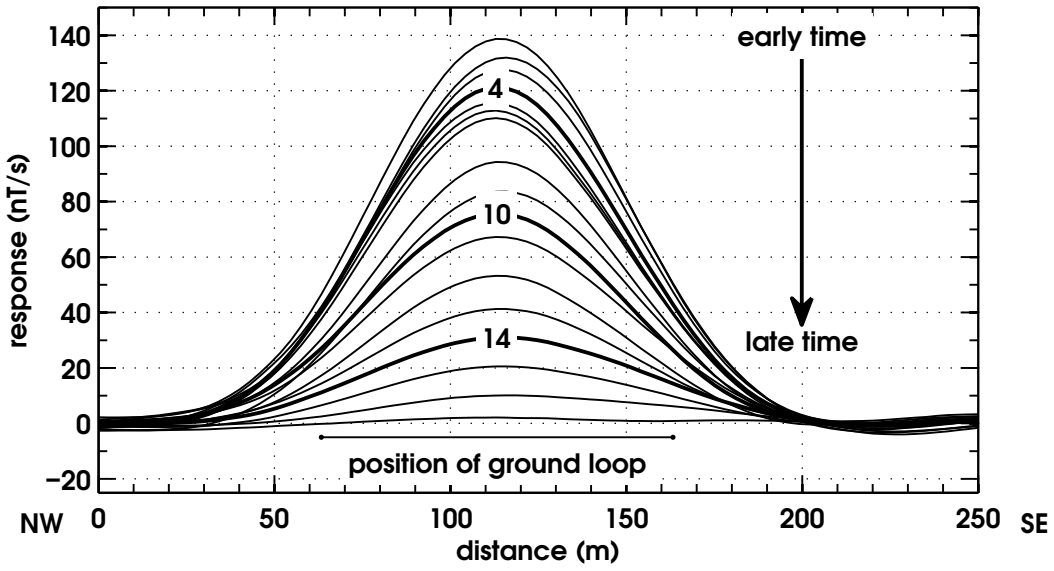

Figure 5.5: *Responses measured in the receiver versus distance flown as the AeroTEM system is towed over the ground loop. Highlighted are channels 4, 10 and 14. The ground loop edges are marked in the bottom of the figure. This example is taken from line 8 (cf. Figure 5.4).*

the measured responses for channels 4, 10 and 14 are shown in Figure 5.6. At first glance, the curves appear to be surprisingly dissimilar. The predicted curves are much narrower and have higher peak values than the measured data. Furthermore, the peak of the predicted curves appear earlier in distance along the line than the measured values. I believe there are three main factors that account for these differences. The first one is averaging: in addition to waveform stacking, contractors may average a number of full waveforms together to give the measured response at one fiducial. How many full repetitions of the waveform are taken depends on the system and is rarely reported. This type of averaging, which is really filtering to smooth out the data, broadens and flattens peaks in the data; and this process has most likely been applied to the data provided here. The second problem with the data arises due to the fact that the GPS antenna is attached to the helicopter, but is assumed to be towed directly underneath it. The responses that I present in Figure 5.6 are calculated in this way. The spatial shift in peak response shows that the spatial (GPS) positions of the helicopter are not the spatial positions of

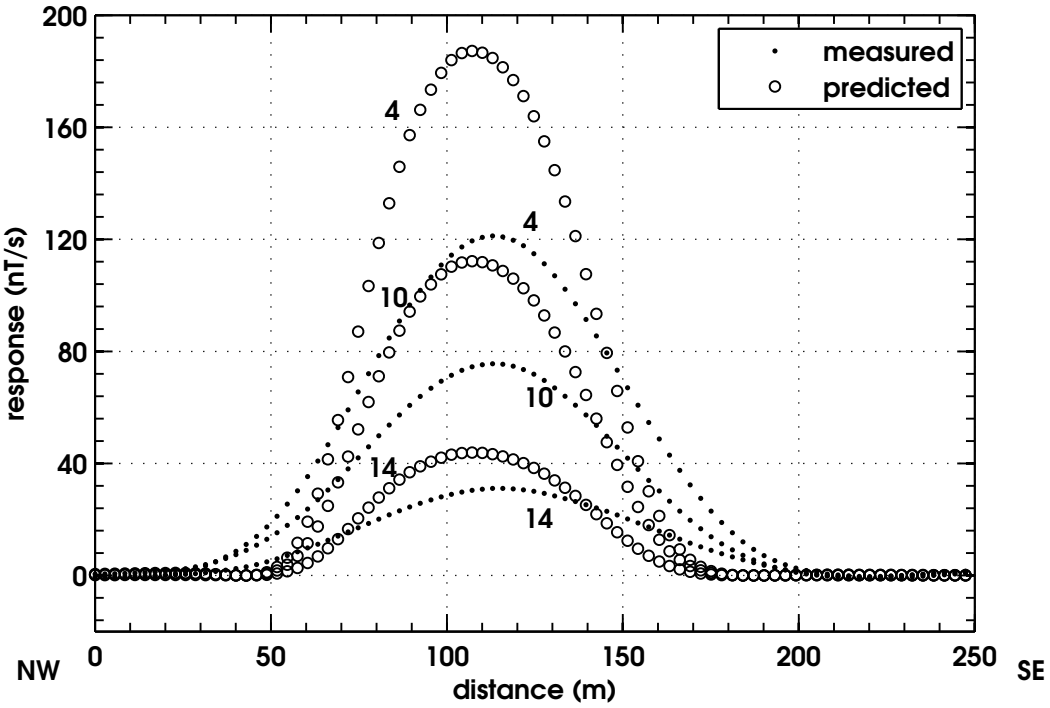

Figure 5.6: *Measured (dots) and predicted (open circles) AeroTEM responses for channels 4, 10 and 14 versus distance for line 8. Predicted peaks are not only shifted spatially from the measured responses, they are much narrower and have higher peak value than the measured response for the same decay time.*

the towed bird. The final factor is amplitude caused by altitude. The altitude of the towed bird above the ground loop is predicted from the measured altitude of the helicopter.

Under the assumption that the predicted and measured responses differed according to a change in altitude (Δh), a spatial shift in distance along the line (Δd) and the number of taps (n) in a boxcar filter applied to the data (Lyons, 1997), I minimised the difference between the two curves in a least squares sense. I chose to fit channel 10 because it is a mid-time channel that starts at a time that is approximately one decay constant τ after the transmitter current shut-off. By minimising the error E between measured and predicted curves according to the relation

$$E = \sum_{i=1}^{N} \left(F_P(\Delta h, \Delta d, n)_i - F_i \right)^2, \tag{5.11}$$

where $F_P(\Delta h, \Delta d, n)_i$ is the predicted data based on the changes in altitude, distance along line and number of taps in the averaging window at every point i, and F_i is the measured response at every point, the predicted curve can be matched to the measured data. The calculation of minimum error was conducted using a least squares curve fitting algorithm that is part of the function `lsqcurvefit.m`; a standard function of the MATLAB Optimisation Toolbox (The MathWorks, 2007). The result of the minimisation process, applied to channel 10 of line 8, is shown in Figure 5.7a. The predicted data was fitted to the measured data by applying changes of $\Delta h = 1.94$ m, $\Delta d = -3.3$ m, and $n = 19$ (filtering data for 1.9 s in a boxcar filter). For channel 10, all predicted points fit the measured data within 2% of the peak response of ∼120 nT/s. Once the corrections in $\Delta h, \Delta d$ and n have been found for channel 10, the same process is applied to all the channels. For the sake of clarity, I have only plotted channels 4, 10 and 14. These were chosen because they are representative of early, mid and late time channels.

It is easy to see that while the predicted response for channel 10 fits the measured data, the corrections applied to the predicted responses of the earlier and later time channels do not agree quite as well. The predicted system responses for channels 4 and 14 are consistently greater than what was actually measured for those channels. There are two easy explanations for this: the transmitter current waveform is not what the contractors say it is (e.g. it's shorter), or the actual timing window for channel 4 is later in time than reported. Unfortunately, neither explanation can be proven for this test, but changes of only 5 μs in window timing for early channels can create as much as 20% difference in measured responses. If the window times reported by the contractor in Table 5.1 are incorrect, large differences will appear between measured and predicted response.

An interesting difference between measured and predicted response arises when calibrating line 1, marked with open squares in Figure 5.4. Without changing bird

altitude, distance along line, or averaging, the measured and predicted responses are shown in Figure 5.8. As was the case in Figure 5.6, the measured responses for line 1 do not match the predictions: the predicted responses are narrower, shifted in distance along the line and larger in amplitude. Applying the corrections obtained from line 8 ($\Delta h = 1.94$ m, $\Delta d = -3.3$ m, and $n = 19$) to the predicted responses for line 1 does not make the measured and predicted responses agree; and Figure 5.9 shows that the predicted responses are now much lower in amplitude than the measured responses. While this could point to a receiver gain issue, it is much more likely that the altitude adjustment for line 8 is not applicable to line 1. Instead, it is more reasonable to apply a separate set of fitting parameters to the predictions for line 1. The result is shown in Figure 5.10, where I have forced a fit between the measurement and prediction for channel 10 of line 1. The parameter changes are: $\Delta h = -1.3$ m, $\Delta d = -3.2$ m, and $n = 24$.

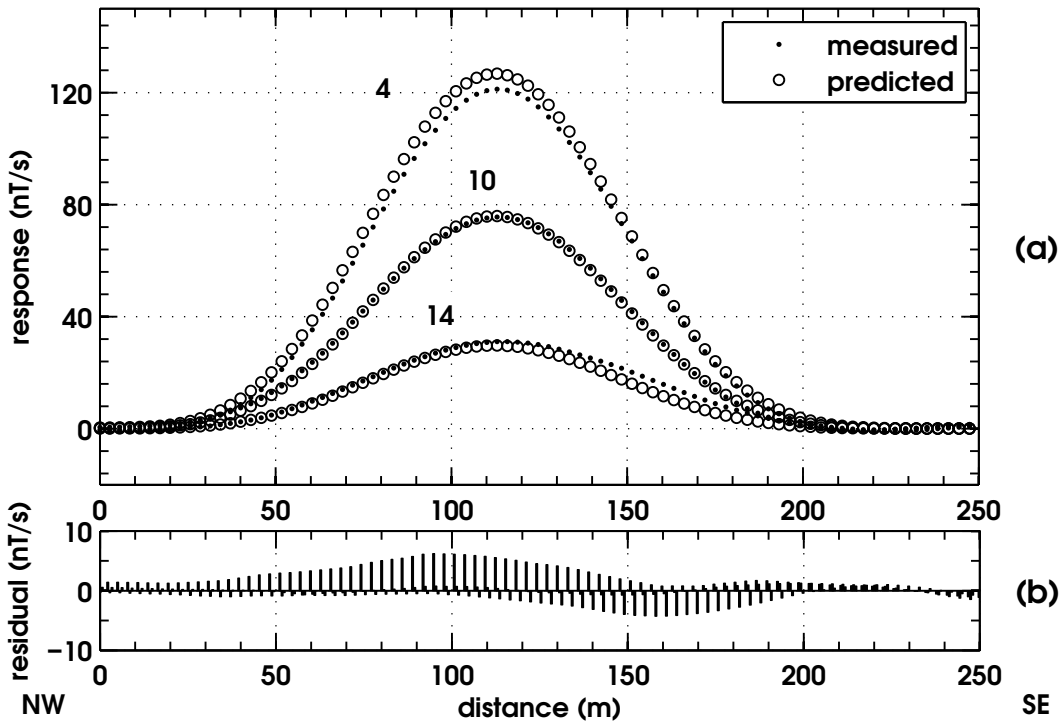

Figure 5.7: *(a) Fitted predicted data (open circles) compared to measured data (dots), for all channels of line 8 (AeroTEM). The minimisation process was applied to channel 10 using $\Delta h = 1.94$ m, $\Delta d = -3.3$ m, and $n = 19$ (filtering data for 1.9 s with a boxcar filter), and the data re-predicted for all other channels. (b) Histogram of the residual of each channel at an enlarged vertical scale.*

The parameters for line 1 are sufficiently different from line 8 that I was inspired to calculate fitting parameters for channel 10 of all 9 lines flown over the ground loop. In each case, I minimised the error E of equation (5.11) by allowing $\Delta h, \Delta d$, and n to change and recomputing the predicted response. The results of the minimisation process for each line are displayed in Table 5.3.

Table 5.3 is instrumental in showing that the calibration method proposed has limitations. The secondary response from line to line changes so much that practical corrections to altitude, distance along line and even windowing need to be changed in order to fit predicted to measured responses for channel 10. In light of the results of Chapter 3, where I conclusively proved that towed birds swing while on survey, this is hardly surprising; and the required changes in altitude and distance along line reflect that swinging and changes in airspeed create positional error in towed birds. An altitude change of ± 2.6 m is consistent with an 18° bird swing for a 55 m tow cable, and I showed in Section 3.4 that swings of that magnitude are likely.

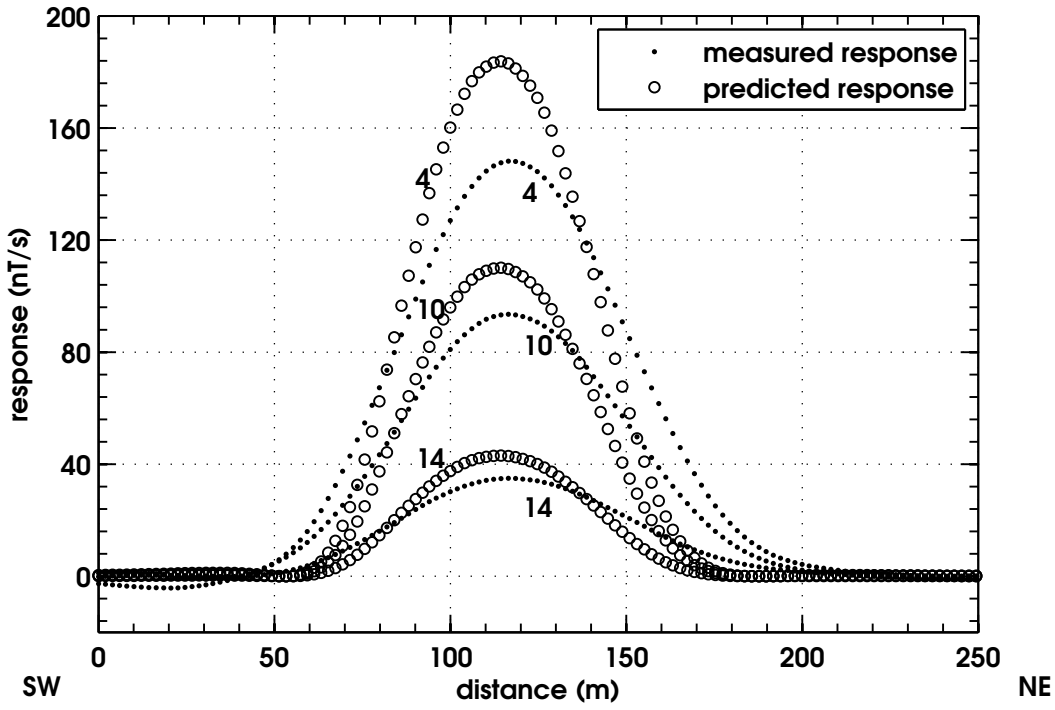

Figure 5.8: *Predicted (open circles) and measured AeroTEM response (dots) for line 1, (cf. Figure 5.4). Channels 4, 10, and 14 are shown.*

Table 5.3: *Calculated $\Delta h, \Delta d$, and n for each line of the AeroTEM II calibration test.*

Line	Δh	Δd	n
1	-1.3	-3.2	24
2	-2.8	1.8	14
3	0.56	-8.4	16
4	-0.3	-4.1	16
5	-6.7	-11	19
6	-1.6	-0.5	15
7	1.4	-3.5	20
8	1.9	-3.3	19
9	-0.2	-6.2	19
mean	-1.0 ± 2.6	-4.2 ± 3.9	18 ± 3

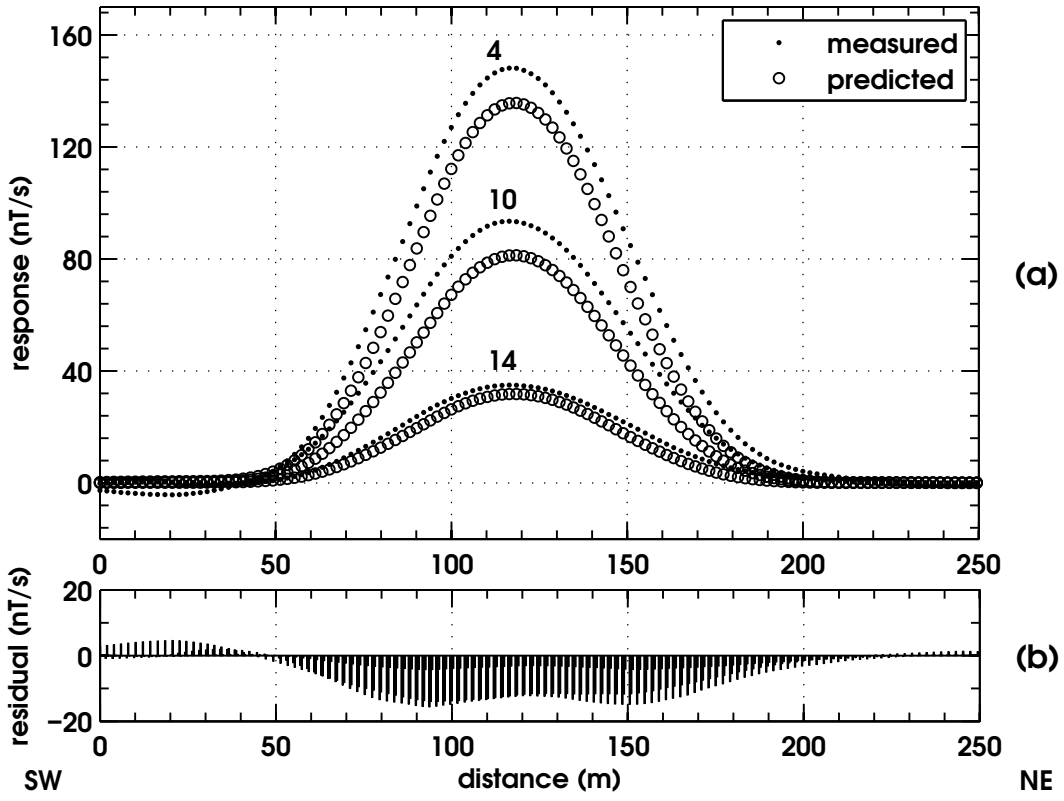

Figure 5.9: *(a) Predicted (open circles) and measured AeroTEM response (dots) for line 1, using the calibration corrections obtained for line 8. The predicted and measured responses still do not agree, as shown in (b), the difference between measured and predicted responses at each fiducial.*

The offsets of the towed bird behind the helicopter predicted by Δd are also readily explained. Towed birds are towed *behind* the aircraft; no offset between helicopter GPS position and bird position would be more surprising! But what of the last column in Table 5.3? Changes in the number of taps needed to filter the predicted responses to match measured is curious. I believe that this is due to a geometrical positioning error that is mistaken for an averaging error. Line 1, marked in open squares in Figure 5.4, is the best example of this. Line 1 is flown from the southwest corner of the figure to the northeast corner, covering only a small fraction of the northwest corner of the ground loop. Any slight deviation of the towed bird from the flight path marked by the helicopter GPS positions constitutes a large change

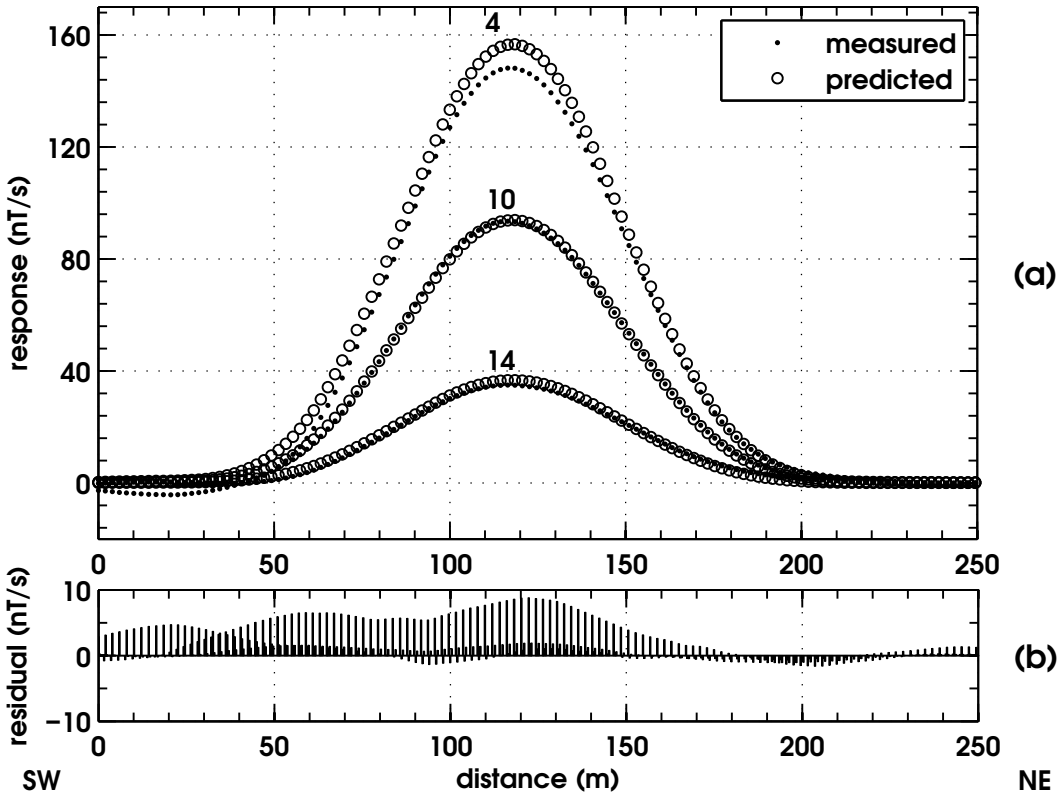

Figure 5.10: *(a) Predicted (open circles) and measured AeroTEM response (dots) for line 1, using the calibration corrections of $\Delta h = -1.3$ m, $\Delta d = -3.2$ m and $n = 24$ (2.4 s moving average). Even though there is agreement for channel 10, the measured response in the other channels is consistently lower than predicted; shown in (b). The residuals between measured and predicted response here are half what they were in Figure 5.9.*

in the duration of the secondary response. Evidence of bird swing from Chapter 3 showed that cross-line bird swing happens concurrently with in-line swing, so this is likely to happen. In this case, the bird most likely slung to the right when looking in the direction of the flight path. The AEM system was therefore positively coupling with the ground loop for a longer period of time during the flight; this manifests as a need for increased averaging in the predicted response.

5.5 Calibration of the HoistEM System

As the second example of using a ground loop to check the calibration of a time domain system, the HoistEM helicopter time domain system (Boyd, 2004) was flown over ground loops composed of single-core household wire placed on resistive ground near Paraburdoo in the Pilbara region of Western Australia. Most of the field work done for this test was conducted by Don Hunter and Andrew Boyd, so I would like to take this opportunity to thank them for their help.

5.5.1 Description of the System

The HoistEM system is a relatively new system that was first introduced in Australia in 1999 and has recently had success at detecting a high grade manganese deposit under regolith cover (Boyd, 2004; Hashemi and Meyers, 2004). It has also been assessed by DSTO to not only accurately estimate the depth of seawater in the Sydney Harbour (Vrbancich and Fullagar, 2004; Vrbancich and Fullagar, 2007*a*), but also to estimate the thickness of sediment lying on the sea floor in shallow coastal waters (Vrbancich and Fullagar, 2007*b*). A novel design, the HoistEM system consists of a hexagonal single-turn transmitter of radius 12 m. The support frame is constructed from the masts from windsurfing boards and carbon composite parts.

Receiver

The receiver for the HoistEM system is a 20-bit, A/D converter that samples in window widths of 112.7 μs (Boyd, 2004). Each of these windows is divided into 4 sub-windows of width 25.325 μs and an 'integration' or 'dead-space' of 11.4 μs. The sampling and stacking scheme is as follows. The first 12 delay channels are all one sample window wide (25.325 μs), starting 5.0654 ms after the transmitter current turns on. After that, there are 2 channels that are the full 112.7 μs window wide, even though they actively measure for 101.3 μs. The remaining channels stack an increasing number of 112.7 μs receiver windows, starting at 2 for delay channel 15, through to 17 receiver windows at delay channel 27. The sampling schematic for the HoistEM system is computed in Appendix E, and the result is displayed in Table 5.4.

Table 5.4: *Mid-point and channel width for the 27 receiving windows used on the HoistEM system. Time is measured from the start of the on-time of the half cycle.*

Channel	Mid-time (μs)	Width (μs)	Channel	Mid-time (μs)	Width (μs)
1	5 078.063	25.325	15	5 735.900	202.600
2	5 103.387	25.325	16	6 017.650	303.900
3	5 128.712	25.325	17	6 412.100	405.200
4	5 154.038	25.325	18	6 919.250	506.500
5	5 190.762	25.325	19	7 539.100	607.800
6	5 216.087	25.325	20	8 271.650	709.100
7	5 241.413	25.325	21	9 116.900	810.400
8	5 266.738	25.325	22	10 074.850	911.700
9	5 303.462	25.325	23	11 145.500	1 013.000
10	5 328.788	25.325	24	12 328.850	1 114.300
11	5 354.113	25.325	25	13 624.900	1 215.600
12	5 379.438	25.325	26	15 033.650	1 316.900
13	5 454.150	101.300	27	16 724.150	1 722.100
14	5 566.850	101.300			

Waveform

The HoistEM transmitter current waveform is a 25% duty-cycle modified square wave, powered by a 25 horsepower motor mounted on one skid of the helicopter doing the survey (Boyd, 2004). Vrbancich and Fullagar (2007*a*) describe the HoistEM current pulse as quasi-trapezoidal with an exponential rise-time of approximately 500 μs, followed by a fast 40 μs linear shut-off at 5 ms. Peak currents are reported to be about 300–340 A (Boyd, 2004; Vrbancich and Fullagar, 2007*a*). Because HoistEM is a concentric-loop system, the receiver has to be shut-off during the transmitter turn-on and turn-off to prevent damage to the circuitry; there is no way to monitor the waveform during survey. A diagram of the positive half-cycle of the proposed transmitter current waveform is displayed in panel (a) of Figure 5.11.

The second panel of Figure 5.11 shows the first derivative of the transmitter current waveform with respect to time. The sharp turn-off at 5 ms generates a large negative peak in $\frac{d}{dt}I_t(t)$. Panel (c) shows the response at the receiver due to the system being held 30 m above the centre of a 100×100 m 3-turn loop of wire 1 mm in diameter. If the receiver was able to measure and discriminate primary from secondary signal during the on-time and shut-off, it would measure the waveform here. The secondary response due to the shut-off (for this model) is so large that it is not shown on this scale: an arrow is place in the panel to mark the existence of the response.

Another interesting feature of the derivations above, that I skipped over in Section 5.4, is the current in the ground loop. The derivation for the ground loop current induced from the current in the transmitter is given in equation (5.7): it represents the convolution of an exponential decay with the time rate of change of the HoistEM current waveform. Using the positive half cycle of the transmitter current presented in Figure 5.11a, the form of the predicted current in the ground loop is shown in Figure 5.12. As expected, it has very much the same shape as $\frac{d}{dt}I_T(t)$ from the transmitter (Figure 5.11b), but is of opposite sign and possesses a

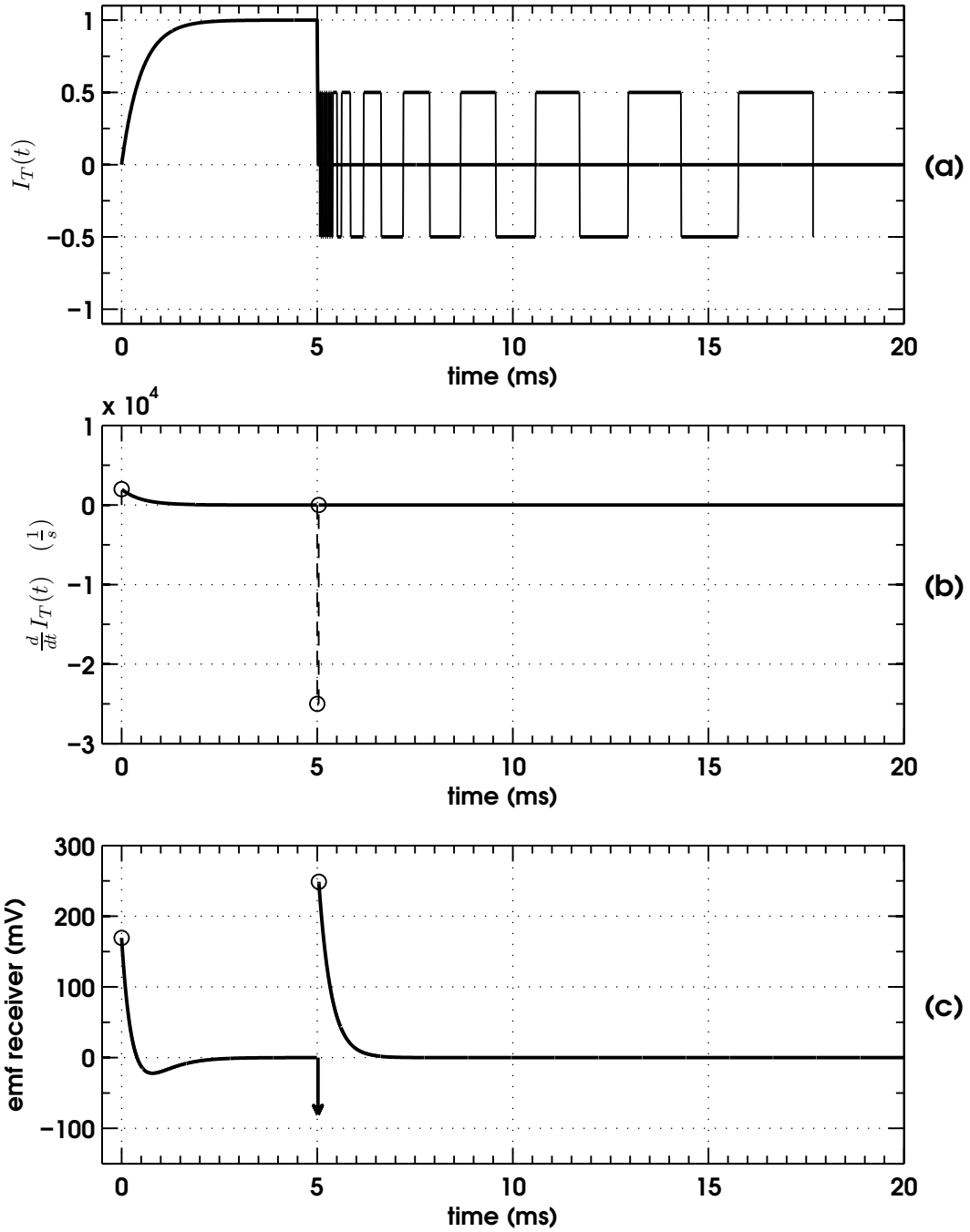

Figure 5.11: *(a) HoistEM transmitter current waveform (normalised to 1), as described by Boyd (2004). Here the current is normalised to 1, even though peak currents are ∼300–340 A. (b) $\frac{d}{dt} I_T(t)$, the first derivative of the transmitter current waveform. The sharp shut-off makes an extremely large jump at t=5 ms. (c) Predicted response of the HoistEM receiver when the HoistEM system is 30 m above the centre of a 100×100 m (3 turn) loop.*

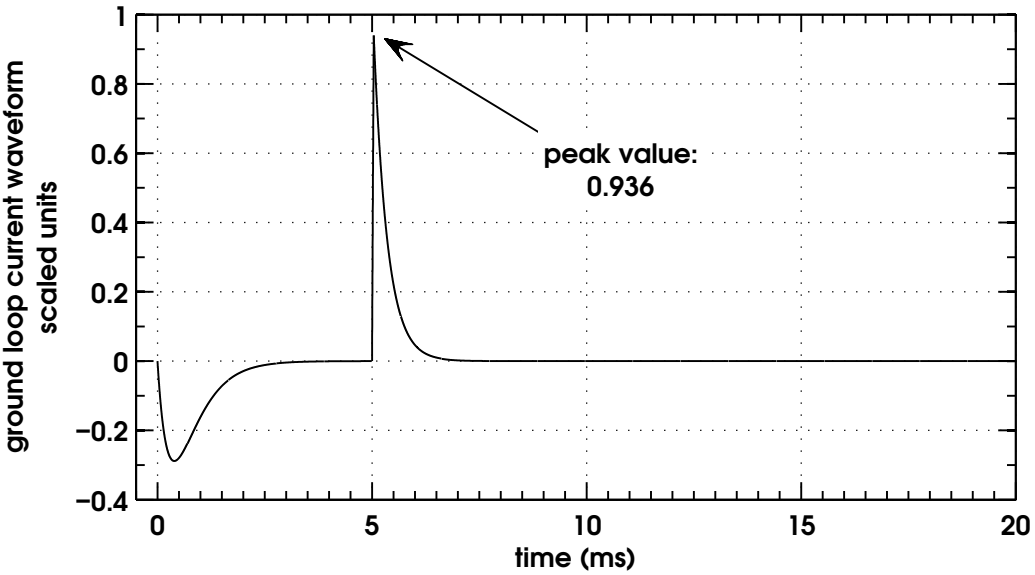

Figure 5.12: *Current waveform predicted in a 100×100 m 3-turn ground loop of decay constant $\tau = 0.296$ ms as a result from one positive half-cycle when HoistEM system is 30 m directly above the centre of the loop. Peak predicted current is about 350 mA.*

finite peak at the current shut-off time of 5.04 ms. The peak current at 5.04 ms is predicted to be 0.936 of the value of $\frac{I_T M_{TL}}{L}$ and, as determined by the time constant τ of the loop, quickly decays to nothing.

5.5.2 Description of the Experiment

The HoistEM calibration tests were conducted in July 2003. Common household wire, single core and sheathed in groups of three insulated strands, was laid out in a roughly 100×100 m loop. The three strands in the household wire bundle were connected to make a 3 turn loop of resistance 25.7 Ω. A small 1 Ω resistor was used to close the ground loop, thus making its total resistance 26.7 Ω. By using the method of Section 2.7.6, the total self-inductance of the loop was estimated to be 7.91 mH, and the characteristic time of the loop was thus τ=0.296 ms. The coordinates of the loop for the resistive ground fly-over experiment are given in the top half of Table 5.5. A photograph of the resistive hilltop where the loop was laid out is shown in Figure 5.13.

Table 5.5: *GPS locations of the ground loop used for the resistive terrain HoistEM calibration test near Paraburdoo, Western Australia (ADG84, Zone 50).*

Easting (m)	Northing (m)	Altitude (m)
$_{5}73_{544}$	$_{74}37_{492}$	428
$_{5}73_{451}$	$_{74}37_{500}$	428
$_{5}73_{445}$	$_{74}37_{401}$	429
$_{5}73_{541}$	$_{74}37_{394}$	429

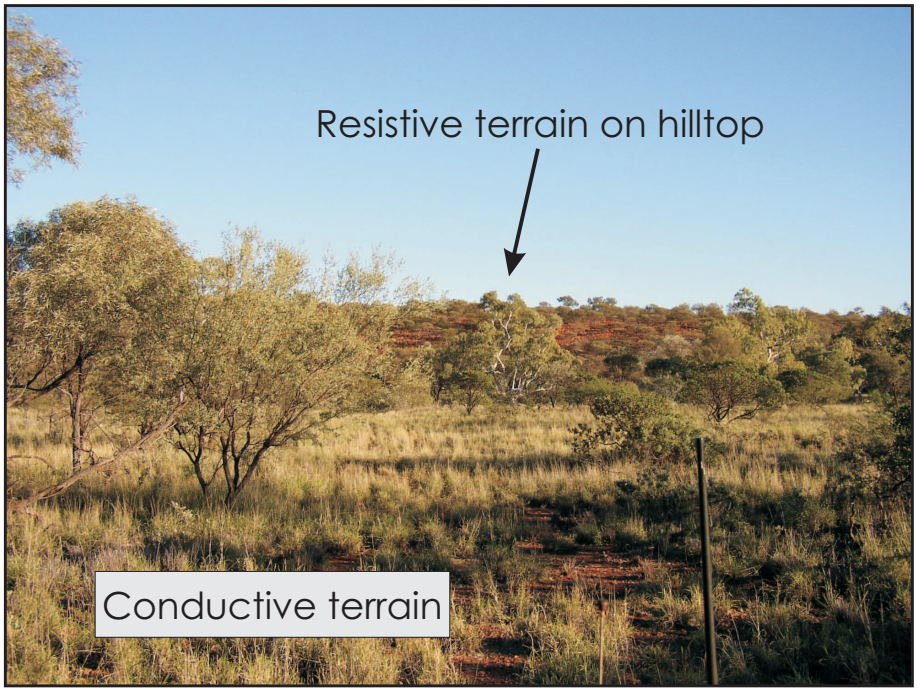

Figure 5.13: *Photograph of resistive ridge outside Paraburdoo, Western Australia, for the HoistEM ground loop calibration test.*

Measurement of the Current Induced in the Ground Loop

The HoistEM experiment is different from the AeroTEM experiment of Section 5.4 because a data acquisition (DAS) unit was attached across the 1 Ω resistor used to close the loop. The DAS used was a 2-channel Roland Edirol UA-5 USB analog to digital converter. Designed for audio capture, the Edirol UA-5 records at 96 000 samples/s at 24-bit precision, although it is band limited to -2 dB at 20 Hz and 20 000 Hz. In order to calibrate the UA-5 DAS, a reference sine wave of known frequency and V_{RMS} was fed into the second channel. The voltage measured across

the 1 Ω resistor in the ground loop thus directly translates to measured induced current.

Flight Lines

Once the ground loop and DAS were connected and working properly, the operating HoistEM system was flown over the ground loop in north-south and south-north lines. The three flight lines that are pertinent to this thesis, along with the position of the ground loop, are shown in Figure 5.14. A photograph taken of the HoistEM system in July 2003 is shown in Figure 5.15.

5.5.3 Results and Discussion

Measuring the current induced in the ground loop allows for a 2 part calibration for the HoistEM system. By comparing the measured current to the predicted current, it is possible to calibrate for the system's altitude above the ground loop before the measured and predicted secondary responses are calculated. The reference and ground loop signals measured by the Edirol UA-5 during the HoistEM flyover (line 1) are shown in Figure 5.16.

The current induced in the ground loop has already been discussed; and the form of the ground loop current was shown in Figure 5.12. The peak current in the ground loop, neglecting the terms $\frac{I_T M_{TL}}{L}$ outside the convolution term of equation (5.7), was shown to be 0.936. Using the flight path recovery ($\mathbf{r}$) and the GPS positions of the ground loop ($\mathbf{r}'$), as well as the peak transmitter currents measured by the HoistEM system during survey ($I_{T(peak)}(t)$), the peak ground loop current was predicted as a function of positions $\mathbf{r}$ and $\mathbf{r}'$ and time t:

$$I_{L(peak)}(\mathbf{r}, \mathbf{r}', t) = 0.936 \frac{M_{TL}(\mathbf{r}) I_{T(peak)}(t)}{L(\mathbf{r}')}.$$

The HoistEM transmitter was assumed to be $\Delta h = 20$ m below the bottom of the

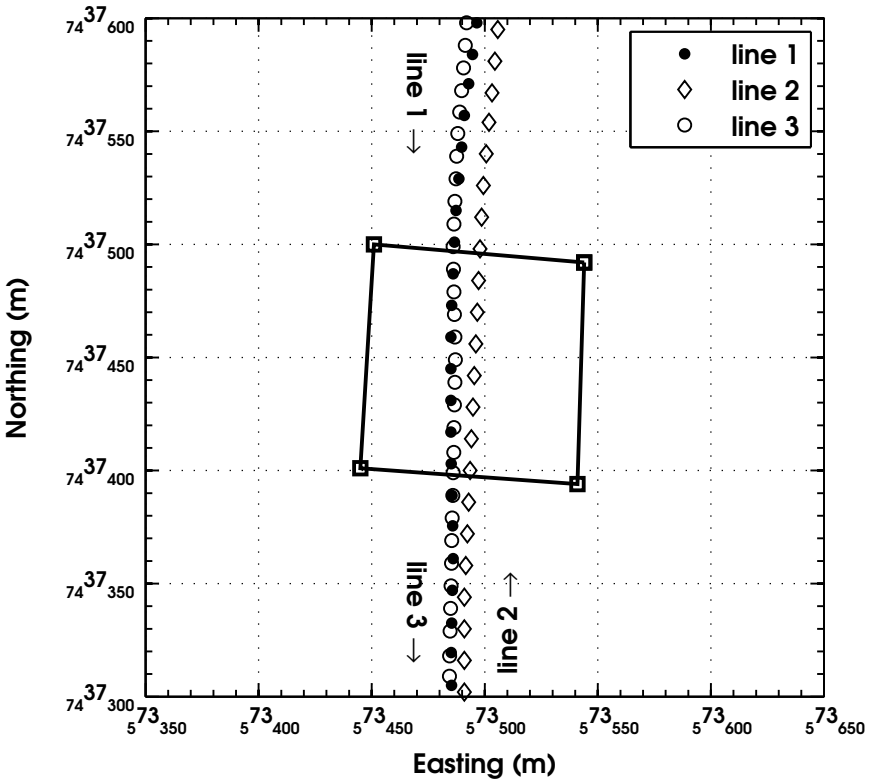

Figure 5.14: *HoistEM flight lines 1 (dots, flying north-south), 2 (open circles, flying south-north), and 3 (diamonds, flying north-south) are shown in the area around the ground loop laid out on resistive terrain. Corners of the ground loop are marked with open squares.*

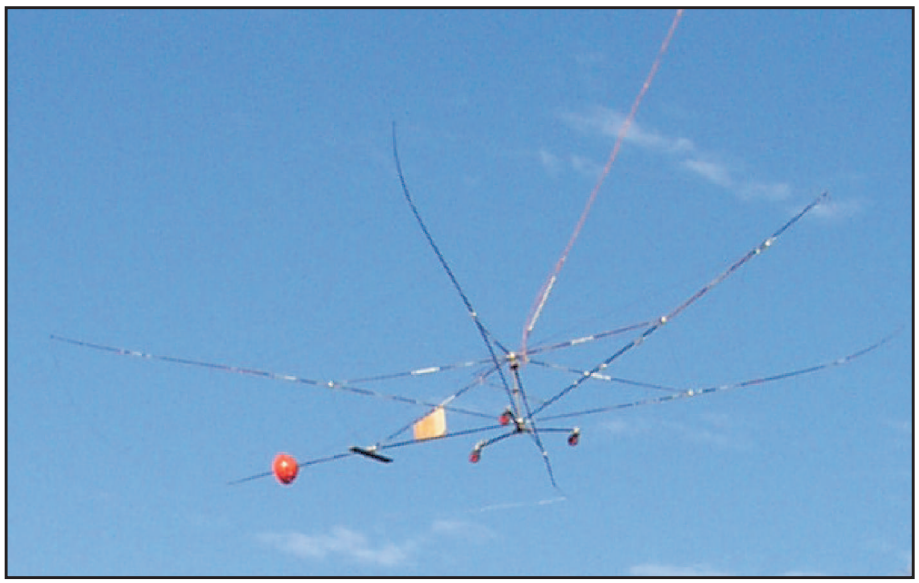

Figure 5.15: *Photograph taken of the HoistEM system in July 2003.*

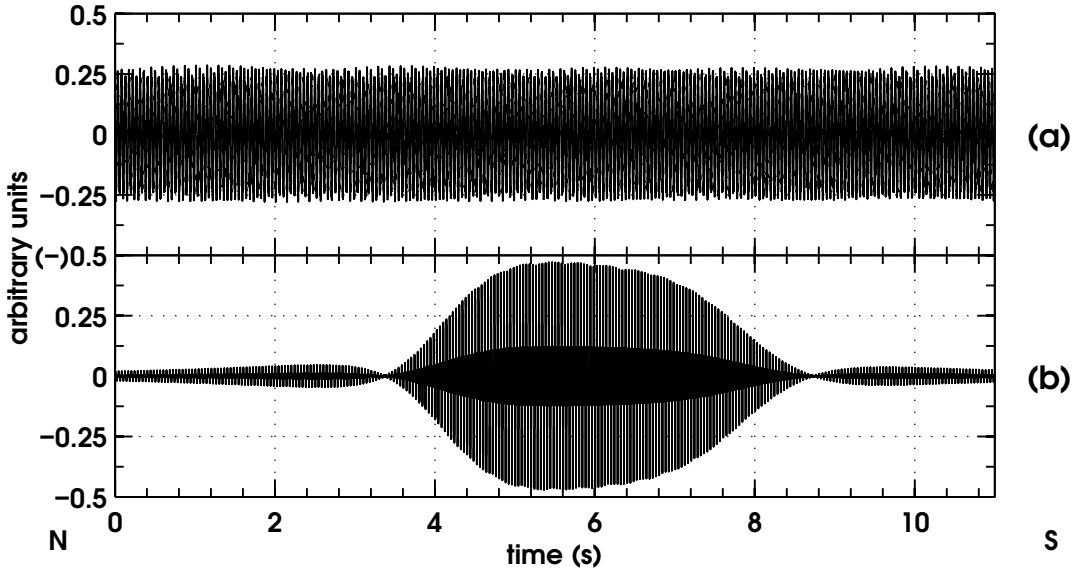

Figure 5.16: *(a) Reference signal and (b) induced current in ground loop, measured with the Edirol UA-5, for line 1 (HoistEM). The reference signal was a 22 Hz sine wave with an input V_{RMS} of 0.138 V and a measured (channel) RMS of 0.168. Details of each waveform cannot be seen at this horizontal scale.*

helicopter. Because the ground loop was laid out on a hill, I chose to use horizontal GPS positions and the radar altimeter to calculate the peak ground current. Due to the fact that the current measured with the Edirol UA-5 used a timer independent of the HoistEM system, I arbitrarily moved the predicted ground loop peak current curve to match the actual, measured current. Additionally, I altered the vertical offset Δh, thereby changing $M_{TL}(\mathbf{r})$, so that the predicted curve matched the peaks of the measured. The prediction, together with the calibrated, measured ground loop current is shown in Figure 5.17.

The peak current predicted to be induced in the ground loop is marked by the two curves in red, while the actual measured current is the trace in black. Unfortunately, the time scale in this figure is too large to be able to see the detail of the measured current: I will return to it later. Excellent agreement between measured and predicted results is achieved by arbitrarily shifting the curve in time and by changing the altimeter offset. Instead of a value of 21 m, Δh has been changed to 19.3 m below the helicopter. A fascinating feature of this figure is the presence of

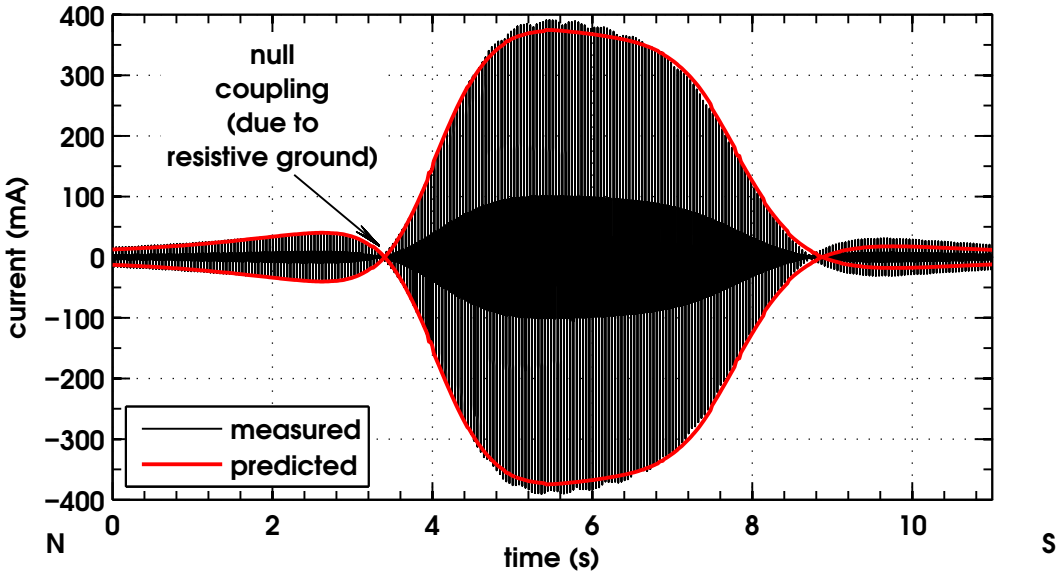

Figure 5.17: *Measured current induced in ground loop (black) as a result of the HoistEM flyover (line 1). The red curves are the predicted values of* $I_{L(peak)}(\mathbf{r}, \mathbf{r}', t)$*, calculated from measured peak transmitter current, estimated ground loop self induction and flight path recovery. Clear nulls in induced current are a result of zero total magnetic flux through the loop.*

the very clear null couplings at 3.4 s and 8.8 s. These points mark the time when the HoistEM transmitter straddles the ground loop in such a way as to create zero net magnetic flux through the ground loop. At these times, the emf and induced current are negligible. The fact that the nulls are so clear is a testament to the resistive nature of the earth on this hilltop for, as we will see later, this is not always the case. The main implication of the resistive nulls in the ground loop response is that we can be reasonably confident that the signal measured in the receiver is due to the ground loop itself and not the earth underneath it.

Figure 5.17 is important for three reasons. First, the null couplings showed us that the ground on this hilltop is reasonably resistive. Second, it allowed us to actually measure and see the interaction between the transmitter current and the ground loop current (the subject of Chapter 6), and finally, it allowed us to determine that the vertical offset between the helicopter and the transmitter loop for this particular line is $\Delta h = 19.3$ m. This vertical offset fixes the altitudinal

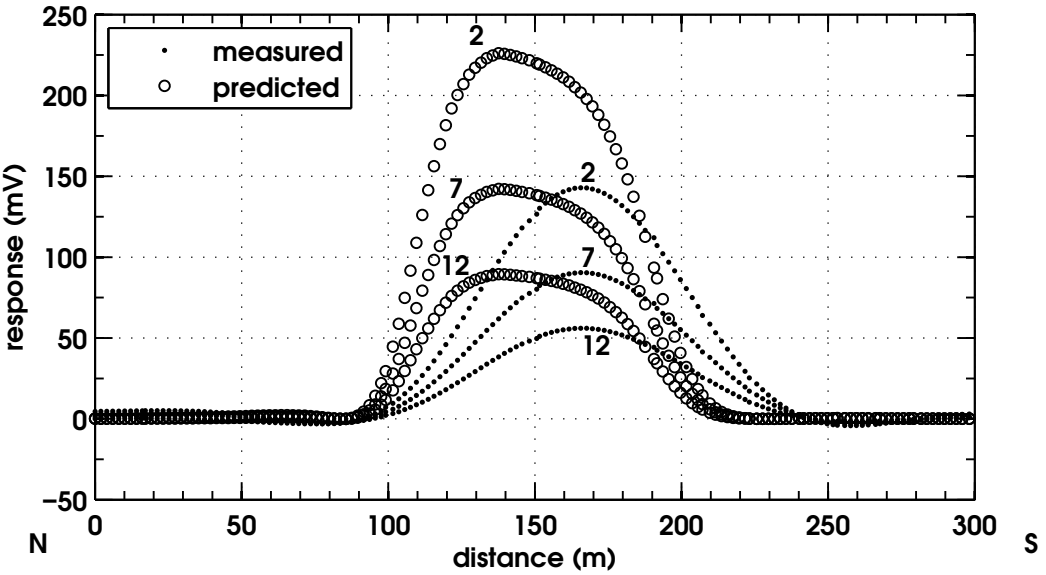

Figure 5.18: *Measured (dots) and predicted (open circles) HoistEM receiver response for channels 2, 7 and 12, line 1. Disagreement between the measured and predicted responses are similar to the AeroTEM case, except that here we can only change position of the peaks by sliding them along the line and by averaging.*

geometry of the transmitter and receiver. With this in mind, Figure 5.18 shows the predicted receiver responses and the actual measured responses for delay channels 2, 7 and 12 in the HoistEM receiver as it was flown over the ground loop.

Clearly, the measured and predicted responses do not match. Not only are the shapes of the responses different (the predicted responses are flatter on the top), but they are shifted in distance. The peaks of the measured responses are shifted about 20 m down the line from the predicted peaks. Forcing predicted channel 7 to fit measured channel 7 by changing n, the number of points in an average applied to the data, and Δd, the shift in distance along the line does not help the agreement. Figure 5.19 shows the result of the process in attempting to force channels 7 to fit and applying the corrections to channels 2 and 12. Both curves are a similar shape, and the peaks match spatially, but there is clearly a problem with amplitude, most probably associated with the HoistEM receiver amplitude gains. This was reported by Vrbancich and Fullagar (2004), when they said that they had to use unrealistic values for the conductivity of seawater in Sydney Harbour

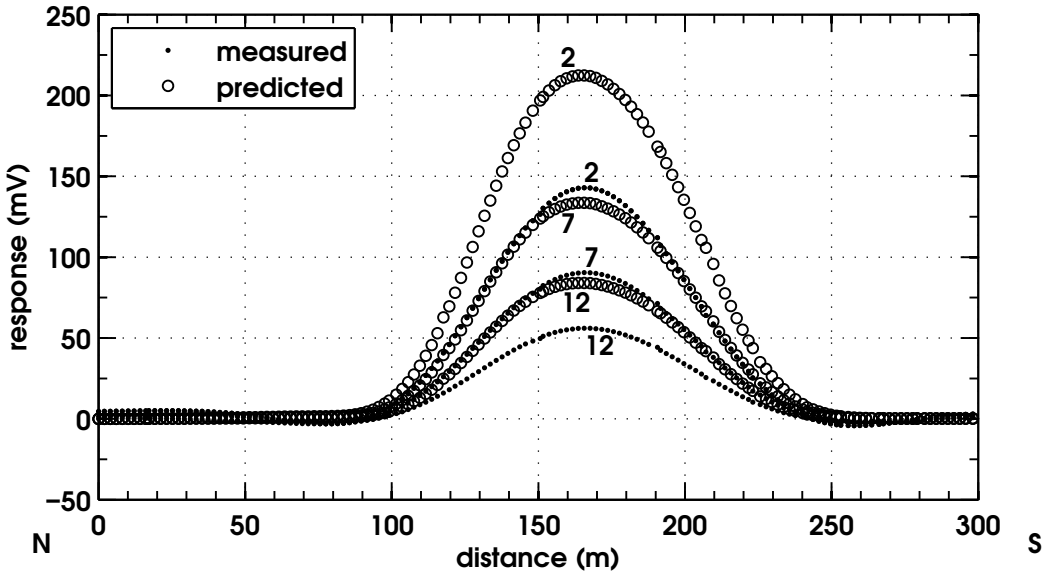

Figure 5.19: *Measured (dots) and predicted (open circles) HoistEM response (line 1) after an average of 1.7 s and a line shift of 18.5 m was applied to the predicted response. Curves are of the right width, and in the right place, but amplitudes do not match!*

to fix data. In that paper, they changed the altitude of the survey to account for the amplitude differences. Figure 5.17 showed that the measured altitude of the HoistEM system was being properly measured, within 2 m or so; we now know that if the Sydney Harbour system was identical to that being used here, their assumption was probably incorrect. By allowing for a change in the amplitude, and searching for the minimum in error between the measured curve and the fitted one (in a calculation like equation (5.11)), we can recalibrate the receiver of the HoistEM system.

The equation to minimise is the difference between the measured and predicted curves by allowing the analytic prediction to be changed by n, the amount of averaging, Δd the shift of the predicted curve along the x-axis and, A a change in amplitude (in this case, $A < 1$):

$$E = \sum_{i=1}^{N} \left(F_P(n, \Delta d, A)_i - F_i \right)^2,$$

where $F_P(n, \Delta d, A)$ is the modified predicted response at each fiducial for delay channel 7. I found that E is minimised for $n = 17$ (averaging for 1.7 s), $\Delta d = 18.5$ m and $A = 0.647$. The result of the same correction applied to each delay channel is shown in Figure 5.20a. Applying the same correction to each channel shows remarkable agreement between measured and predicted values. For each channel, the difference between the predicted and measured curves is less than 5 mV, which implies that the timing windows are most likely correct. This result is in excellent contrast to the AeroTEM calibration trial where the corrections for one channel did not exactly apply to the others. Another interesting feature of Figure 5.20b is the sinusoidal nature of the residual or differences between measured and predicted responses. During this flyover, the Hoist was being towed at a groundspeed of about 20 m/s, so the range 0–300 m represents about 15 s of flying. The period in the residual is therefore about 3 s. While a period of 3 s is much too fast for the in-line bird swing (RESOLVE was about 9 s with a 30 m cable), it may be due to the transmitter or the bird pitching or rolling (RESOLVE bird pitch was about 2–2.5 s).

Taking the calibration factors of $n = 17$, $\Delta d = 18.5$ m and $A = 0.649$ obtained from line 1, and applying them to the predicted responses for line 2 yields a slight disagreement between measured and predicted response. The result, displayed in Figure 5.21, shows that although the peaks match in position along the line, width and shape, their amplitudes do not agree. The disagreement is simply rectified by allowing the vertical offset between radar altimeter and transmitter position to be changed. By changing Δh from 19.3 m to 16.9 m, the predicted responses are much closer to the measured. This is shown in Figure 5.22a, and the agreement between measured and predicted curves is excellent. By keeping the distance shift, the number of seconds averaging and the amplitude gain factor, the corrections obtained from matching one delay channel on a previous line make the predictions

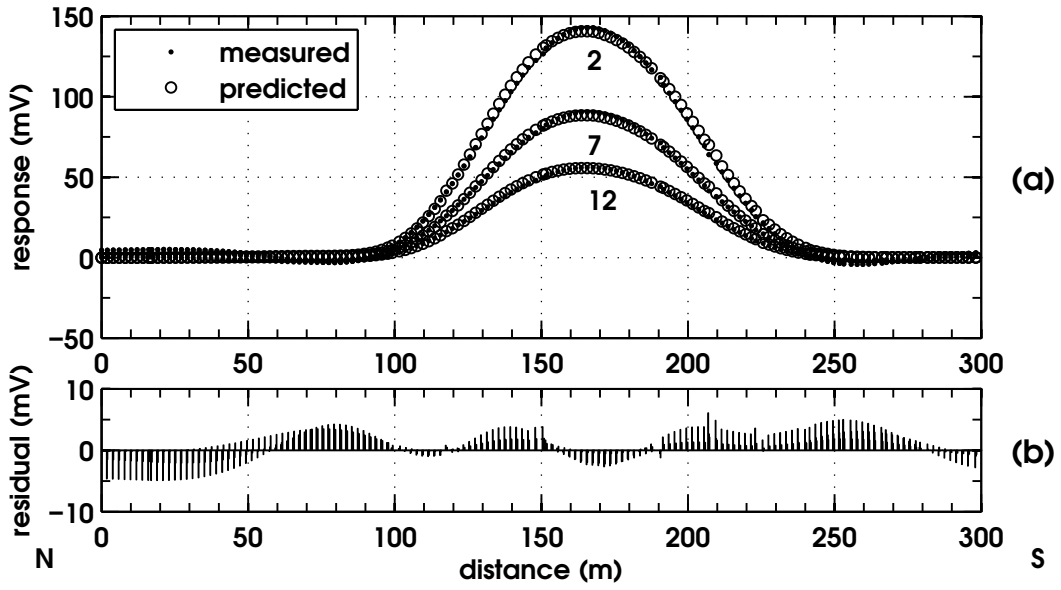

Figure 5.20: *(a) Measured (dots) and predicted (open circles) HoistEM response after an average of 1.7 s, a line shift of 18.5 m, and an amplitude scaling of* $A = 0.694$ *is applied to the predicted response of line 1. Each predicted delay channel fits the measured response quite well, with the residuals for each delay channel* $<$ *5 mV (b).*

match the results on another line. Interestingly, the sinusoidal oscillation in residuals in panel (b) is again present, indicating a possible remaining geometry error in the calculation (bird swing). In order to ensure that the altitude change of 2.4 m between lines was reasonable, we turn to the current measured in the ground loop during the line 2 flyover. Figure 5.23 shows the peak current predicted in the ground loop using $\Delta h = 19.3$ m (blue) and using $\Delta h = 16.9$ m (red). Clearly, the choice of using $\Delta h = 16.9$ m is more reasonable.

It appears from these experiments that at the time they were conducted, the HoistEM system suffered from a problem in its receiver gains. Only after adjusting them to about 65% of their nominal value could they be made to agree with the measured responses, and this finding is corroborated by Vrbancich and Fullagar (2004). Apart from the by now familiar in-line offset (in this case 18.5 m behind the helicopter GPS antenna) and the expected radar altimetry errors of $\sim$2.5 m, the HoistEM system appears to yield excellent results in terms of predicted to mea-

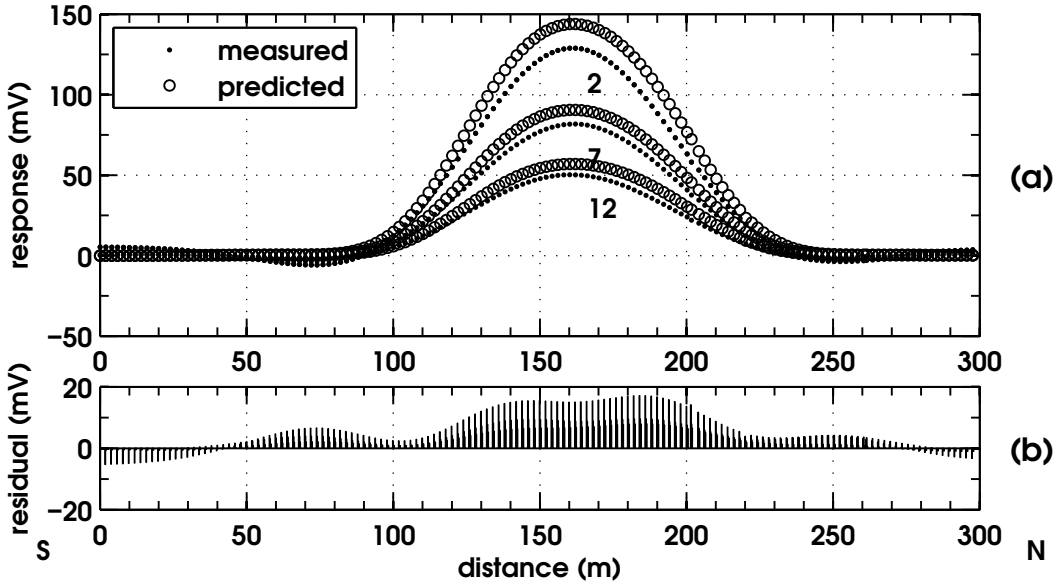

Figure 5.21: *(a) Measured (dots) and predicted (open circles) HoistEM after the calibration factors from line 1 are applied to the predicted response for line 2. Peaks match in width, position and shape; however, amplitudes are incorrect. (b) Residuals between predicted and measured response for all three delay channels. Residuals here are ∼2 times as great as in Figure 5.20.*

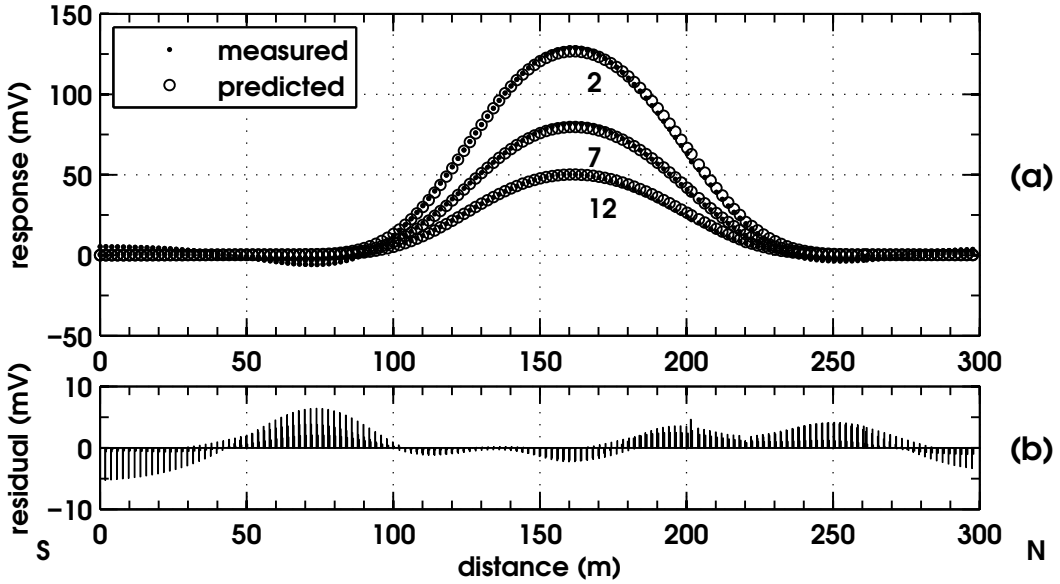

Figure 5.22: *(a) Measured (dots) and predicted (open circles) HoistEM receiver response after changing the radar altimeter to transmitter vertical offset from $\Delta h =$ 19.3 m to $\Delta h =$ 16.9 m for line 2. Now there is excellent agreement between the measured and predicted responses (b), where the residuals for each channel over the centre of the loop are below 5 mV.*

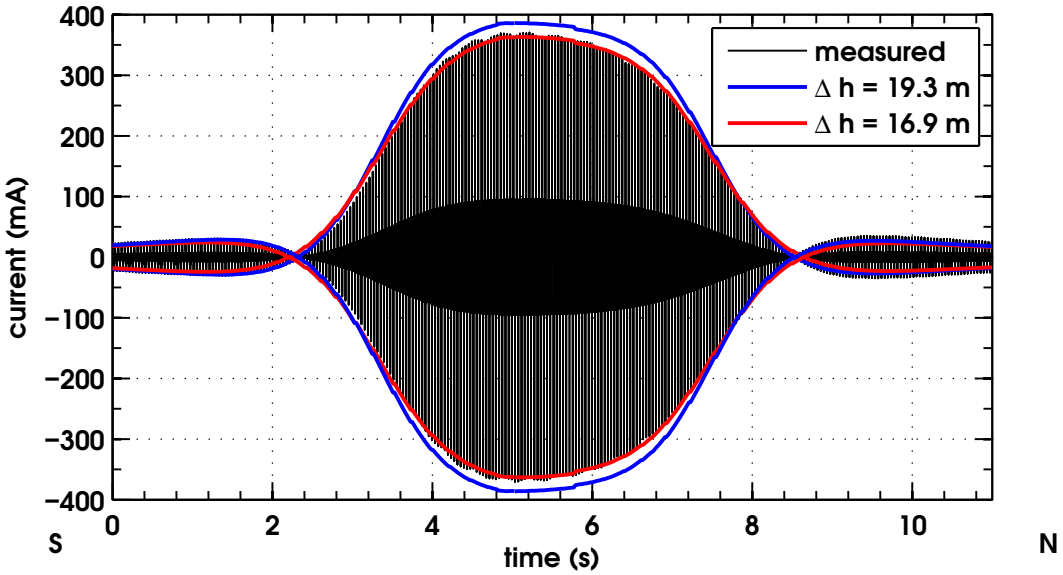

Figure 5.23: *Current measured in the ground loop as the HoistEM was flown over (line 2, black), as well as peak currents predicted by changing the vertical offset between measured radar altimeter and transmitter from* $\Delta h = 19.3$ *m (blue lines) to* $\Delta h = 16.9$ *m (red lines).*

sured responses. The greatest discrepancy between the predicted and the measured responses is the presence of stacking and filtering in the measured data. Whilst waveform stacking is a useful and expected process for a contractor to apply to the raw data, there was also some averaging applied to the data that served to spread the measured data out by about 1.7 s. It may be that the stacking process has the effect of filtering and spreading the data, and since I have not been able to find any mention in the literature of filtering in the HoistEM response, I will assume that this is the case. In their paper, Vrbancich and Fullagar (2007*a*) stress the need for accurately calibrated data to do meaningful interpretation. The series of tests conducted here shows clearly that in 2003, the main calibration error was receiver gains.

5.5.4 Changing the Ground Loop Resistance

An interesting change to the HoistEM system experiment was to change the resistance of the ground calibration loop. During the flyover marked as line 3 in

Figure 5.14, the 1 Ω resistor was removed and the leads from the Edirol UA-5 were connected to the ends of the ground loop. This made the total resistance of the loop equal to approximately 12 000 Ω: the input impedance of the Edirol UA-5. This effectively lowered the decay constant τ from 0.298 ms to about 0.6 μs. With such a short time constant, we should not expect to receive any signal at the receiver: it should all have decayed away, even 14 μs after the shut-off. Yet, as can be seen in Figure 5.24, there is an airborne response measured in at least the first 4 delay channels. More interestingly, channel 2 measures a negative response and channel 1 is about 100 mV greater in signal strength during this flyover than in line 2 (cf. Figure 5.22). In the next Chapter, I will analyse this anomalous result in more detail; it is mentioned here for completeness.

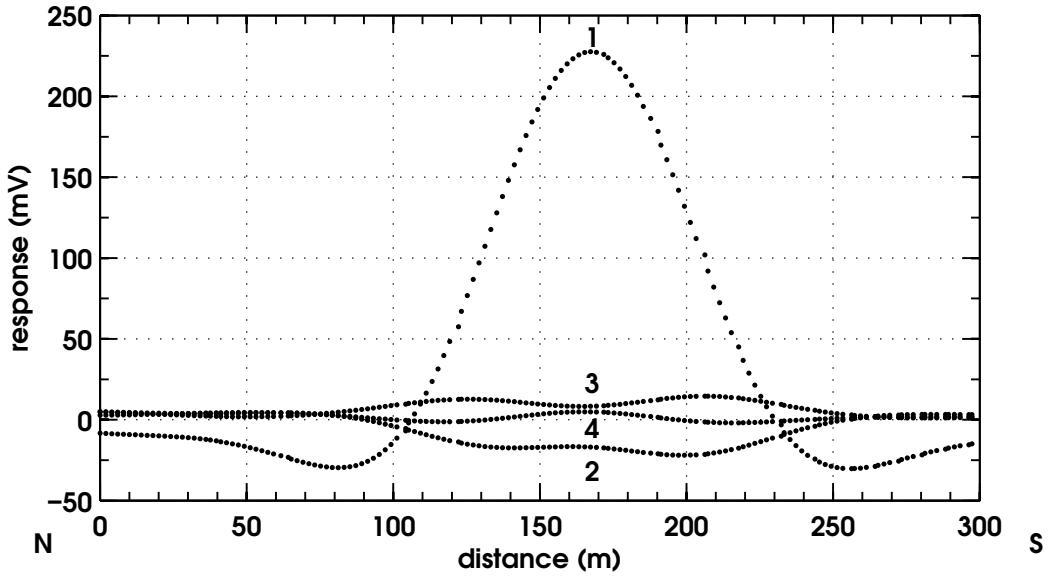

Figure 5.24: *Measured HoistEM response in the first 4 channels for line 3 (shown with open circles in Figure 5.14) Channel 2, although very low in amplitude, is of opposite sign to channels 1 and 3.*

5.6 Calibration of the VTEM System

5.6.1 Description of the System

The next time domain AEM system that I will discuss is the VTEM system of Geotech Airborne (Geotech Ltd, 2005), and flown over a ground loop in Botswana in 2004. The VTEM system is a helicopter-borne time domain system whose transmitter (in 2004) had 4 turns of wire in a dodecahedron of 26 m in diameter. The receiver, a vertical axis coil of 100 turns, was positioned in the centre of the loop and had a diameter of 1.1 m (Witherly et al., 2004). The base frequency for this test was 25 Hz in a trapezoidal half cycle with approximately 45% duty cycle. In 2004, VTEM was powered from the alternator of the helicopter with a peak transmitter current of 120 A. The waveform increased linearly from 0 A to 120 A in 1 ms, maintained for 7 ms, then shut off to 0 A in 1 ms. The off-time measurements at the receiver, clocked to 50 000 Hz, started 9.08 ms after the start of the transmitter waveform. Voltage measurements were binned into 26 delay channels as described in Table 5.6. A photograph of the VTEM system, taken in Sudbury, Ontario in 2005 is shown in Figure 5.25. Lateral position of the bird is estimated from the GPS antenna position of the helicopter (mounted on the tail), while vertical position is estimated by subtracting 45 m from the altitude of the helicopter, measured with a radar altimeter mounted on the underside of the helicopter.

The waveform described above is shown in panel (a) of Figure 5.26, along with a schematic of the delay windows used in the 2004 ground loop tests. Panel (b) shows the time rate of change of the proposed transmitter current—this is proportional in magnitude to the time rate of change of the magnetic field. Finally, in the last panel of Figure 5.26, the response of the VTEM system (if it were capable of measuring during the entire on-time at full gain) 30 m above a 4 turn ground loop of 100 m to a side with resistance $R = 2.89\ \Omega$ and self inductance $L = 13.4$ mH.

Table 5.6: *Mid-point and channel width for the 26 receiving windows used on the VTEM system in Botswana in 2004. Time is measured from the start of the transmitter waveform.*

Channel	Mid-time (μs)	Width (μs)	Channel	Mid-time (μs)	Width (μs)
1	9 090	20	14	9 920	160
2	9 110	20	15	10 090	180
3	9 130	20	16	10 300	240
4	9 150	20	17	10 560	280
5	9 180	40	18	10 860	320
6	9 220	40	19	11 200	360
7	9 260	40	20	11 620	480
8	9 310	60	21	12 140	560
9	9 370	60	22	12 740	640
10	9 440	80	23	13 420	720
11	9 530	100	24	14 260	960
12	9 640	120	25	15 300	1 120
13	9 770	140	26	16 500	1 280

Figure 5.25: *Photograph of the VTEM system during take-off in Sudbury, Ontario in 2005.*

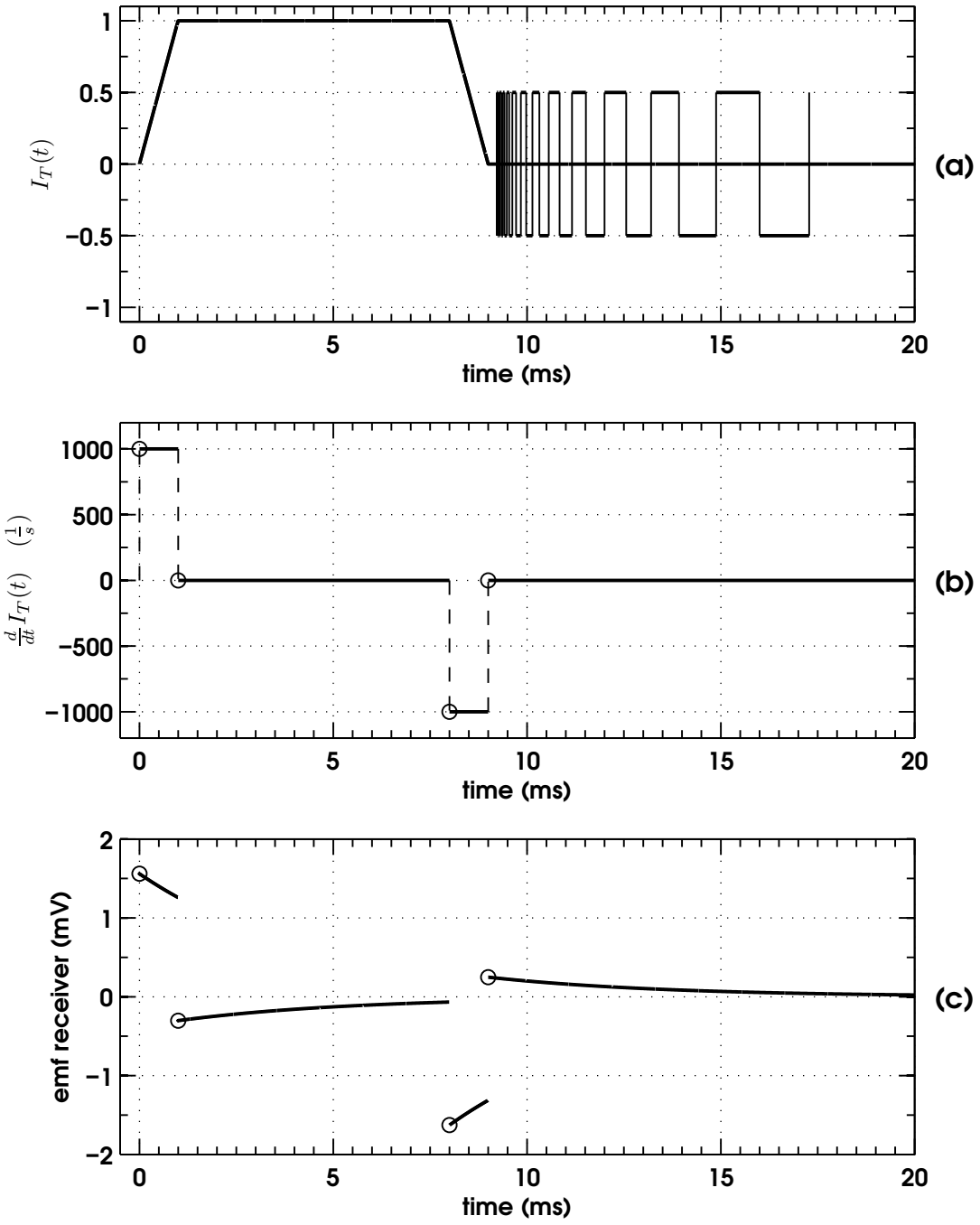

Figure 5.26: *(a) Nominal VTEM current waveform, normalised to a peak current of 120 A. Timing windows are shown with dotted lines. (b) First time derivative of the transmitter current waveform, $\frac{d}{dt}I_T(t)$. (c) Predicted response at the VTEM receiver, 30 m above a 4 turn 100×100 m loop with resistance $R = 2.89\ \Omega$ and self inductance $L = 13.4$ mH, $\tau = 4.64$ ms.*

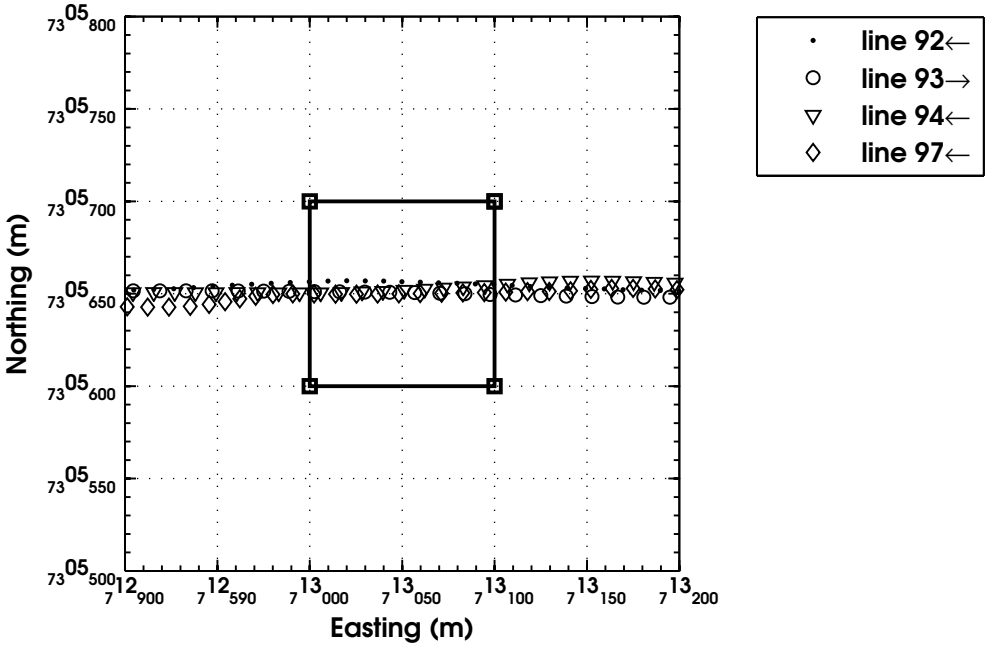

Figure 5.27: *Flight path of 4 representative lines (92, 93, 94 and 97) flown over the ground loop (marked with open squares) in Botswana with the VTEM system. Direction of lines flown shown in legend in upper right-hand corner.*

5.6.2 Description of the Experiment

The VTEM calibration tests that I present in this thesis were conducted in 2004 over resistive ground in Botswana for Rio Tinto (data particulars supervised by Condor Consulting). The ground loop was a 100×100 m loop of wire, laid out in 4 turns. Unfortunately, neither the resistance nor the self inductance of the loop was measured for this experiment, so absolute calibration of the VTEM system with these results is impossible. The responses measured by the VTEM system during flyover are extremely instructive.

The VTEM system was flown a total of 12 times over the 4-turn ground loop placed on resistive ground in Botswana. For 8 lines flown, the ground loop was closed in a short circuit, exactly like the AeroTEM tests. A further 4 lines were flown with the ground loop held in open circuit (i.e. the ends were not attached). The flight path of the helicopter for 4 representative lines is shown in Figure 5.27, while the coordinates of the ground loop are given in Table 5.7.

Table 5.7: *Loop coordinates the VTEM calibration test (UTM Zone 34N, WGS84).*

Easting (m)	Northing (m)	Altitude (m)
$_{7}13_{100}$	$_{73}05_{700}$	1 045
$_{7}13_{000}$	$_{73}05_{700}$	1 045
$_{7}13_{000}$	$_{73}05_{600}$	1 045
$_{7}13_{100}$	$_{73}05_{600}$	1 045

5.6.3 Results and Discussion

Measuring τ

Since the resistance and the self inductance of the loop were not measured for this test, calculation of the characteristic ground loop decay constant is impossible for this series of tests. However, looking at the response of the receiver as it is flown over the ground loop gives some indication of how to proceed. Figure 5.28 shows the receiver response for the ground loop flyover of line 94. All channels are shown, with early delays yielding the largest response and the late delay channels measuring the smallest response. The response of the ground loop is very obvious in this graph, starting at 100 m and finishing by 220 m. The system's response to the ground itself is easily seen between 0–80 m and 230–300 m, and is about 12% of the overall signal strength at early time. In order to find the decay constant of the ground loop for this particular line, I took the mean of the signal measured for each delay channel over the peak ground loop responses from 130–180 m, marked with solid vertical lines in Figure 5.28. Using delay channels 14–26, I fitted an exponential decay to the measured data in a least squares sense. The result is shown in Figure 5.29, with a decay constant of $\tau = 4.62$ ms.

It is clear in Figure 5.29 that a fitted exponential decay closely matches the measured data from channels 14–26. The measured response at the earlier time channels 1–13 are just as easily seen to not match the exponential decay of 4.62 ms. This is clearly shown in the small inset of Figure 5.29, which shows the first 14 delay channels. The extra signal measured in the early times is due to non-zero conductivity

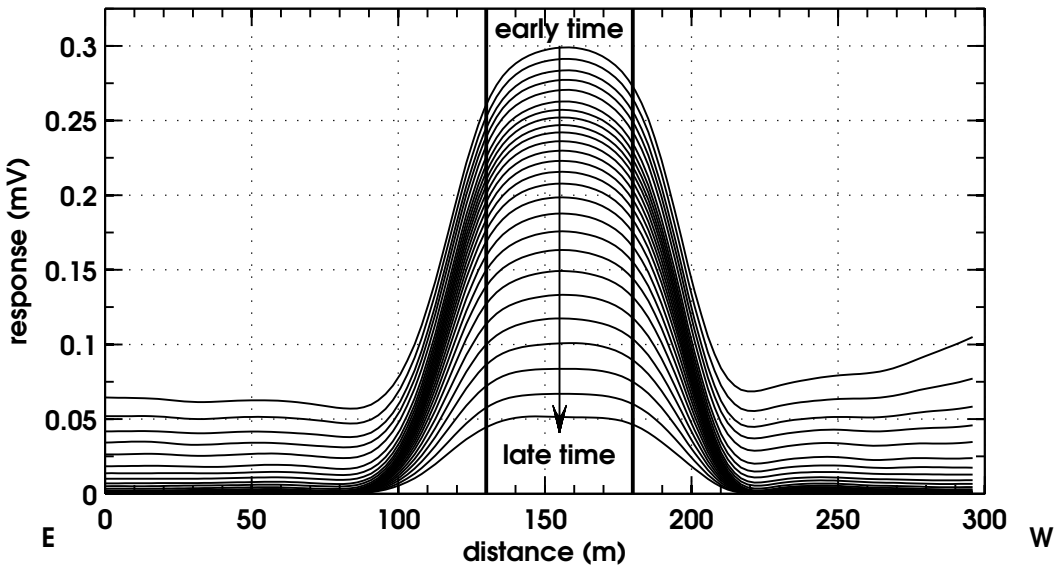

Figure 5.28: *Voltage measured by the VTEM receiver for line 94 (shown with triangles in Figure 5.27). Ground loop response is easily seen from 100 m to 220 m. Vertical lines at 130 m and 180 m mark boundaries of the response used to calculate a mean loop response.*

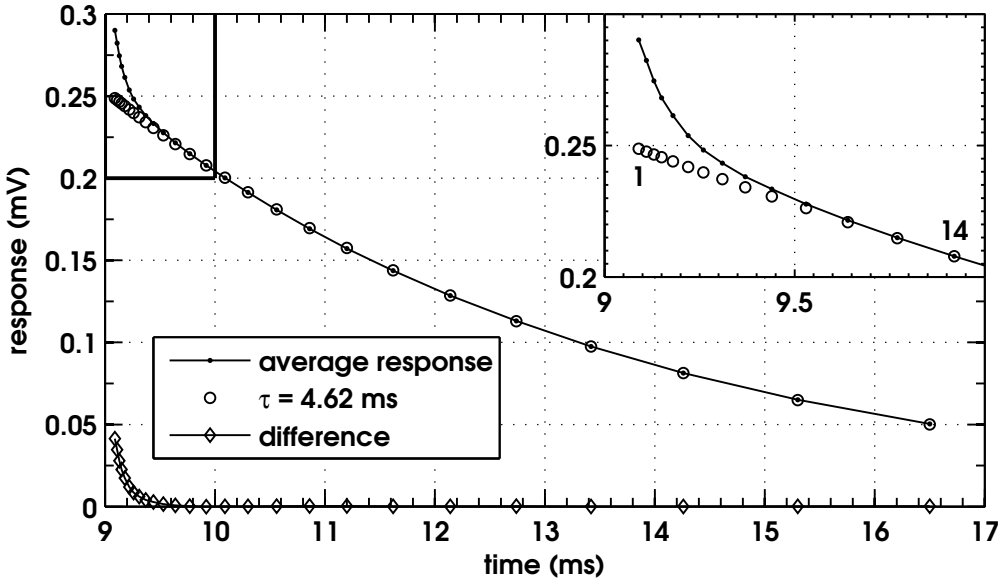

Figure 5.29: *Mean decay response measured over the loop (solid dots) compared to an exponential decay of characteristic time $\tau = 4.62$ ms forced to fit VTEM channel 14 (open circles). The difference between the measured and fitted values is shown in the bottom of the graph (open diamonds). Inset on right hand side of figure shows the earliest 14 channels: misfit between average and fitted voltages is due to ground conductivity.*

of the ground. At late times, the ground response has mostly faded away and only the loop response is left. Using this procedure, I fitted exponential decays to the mean response of the system to the ground loop for most of the other lines flown. The values of τ are shown in Table 5.8.

Table 5.8: *Decay constant τ calculated by fitting an exponential curve to the decay response over the centre of the loop.*

Line Number	τ (ms)
91	4.70
92	4.69
93	4.66
94	4.62
181	4.62
182	4.57
mean	4.64±0.05

Response Fitting

Using the mean value of τ (4.64 ms), I calculated a reasonable resistance and self-inductance for a 4-turn ground loop made from single core wire. For a wire of $\sim$9.3 mm^2 cross-sectional area (which is approximately 7 AWG wire), the resistance of 1 600 m is 2.89 Ω, while the self inductance of a 100 × 100 m 4-turn loop is 13.4 mH. Using these values of R and L, I predicted the response at the receiver by using the helicopter GPS positions and the measured radar altimeter minus 45 m vertical offset. The measured and predicted results for channel 14 of line 94 are shown in Figure 5.30, where there is a clear disagreement between measured and predicted values.

Because the resistance and self inductance of the ground loop were not measured, it is impossible to calibrate the receiver of the VTEM system for any of the lines flown. To move forward, I forced the predicted response of channel 14 to match the actual response by adjusting for transmitter altitude, distance offset along the line flown and amplitude gain in a least squares sense. Similarly to the curve-fitting

method of Section 5.5, I minimised

$$E = \sum_{i=1}^{N} \left(F_P(\Delta h, \Delta d, A)_i - F_i \right)^2,$$

where F_P is the predicted response as a function of change in system altitude (Δh), change in position along line (Δd), and an amplitude gain factor (A), and F_i is the measured response for the fly-over. The parameters for line 94 are $\Delta h = -50.1$ m, $\Delta d = -7.04$ m and $A = 1.25$. Using these values, I applied the corrections to all delay channels of the line. The result of the curve fitting for channels 1, 14, 20 and 26 are shown in panel (a) of Figure 5.31, with the residuals or differences of fit for channels 14, 20 and 26 shown in panel (b).

Although the values for $\Delta d, \Delta h$ and A seem reasonable, it is important to remember that they were arbitrary; and the excellent agreement between measured and predicted delay channels is simply because channel 14 was forced to fit the measured values. It is still reasonable to assume that a good fit achieved for one line should obtain a similarly good fit for another line. However, by looking at the measured response for channels 1, 14, 20 and 26 of line 93 in Figure 5.32, it is clear here that changing altitude and distance along the line is not sufficient to make the predicted curves match the measured ones. The lopsided shape of the loop response suggests that the transmitter and receiver were pitched during the flyover.

By keeping the amplitude gain $A = 1.25$, I fitted the predicted response to the measured response by altering not only Δd and Δh, as before, but also allowing a constant pitch θ_b of the transmitter and receiver (since they are concentric and tied together) by minimising Equation (5.12)

$$E = \sum_{i=1}^{N} \left(F_P(\Delta h, \Delta d, \theta_b)_i - F_i \right)^2, \tag{5.12}$$

where $F_P(\Delta h, \Delta d, \theta_b)_i$ are the predicted responses calculated by changing the fitting parameters and F_i are the measured responses. The parameters for line 93 are

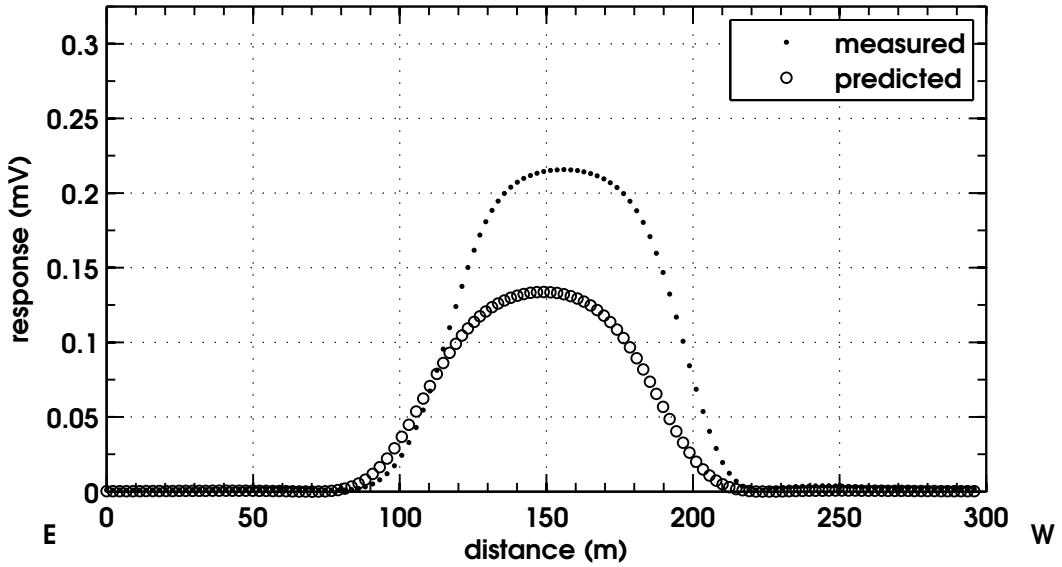

Figure 5.30: *Measured (solid dots) and predicted (open circles) VTEM response for channel 14 of line 94 (shown with open triangles in Figure 5.27.*

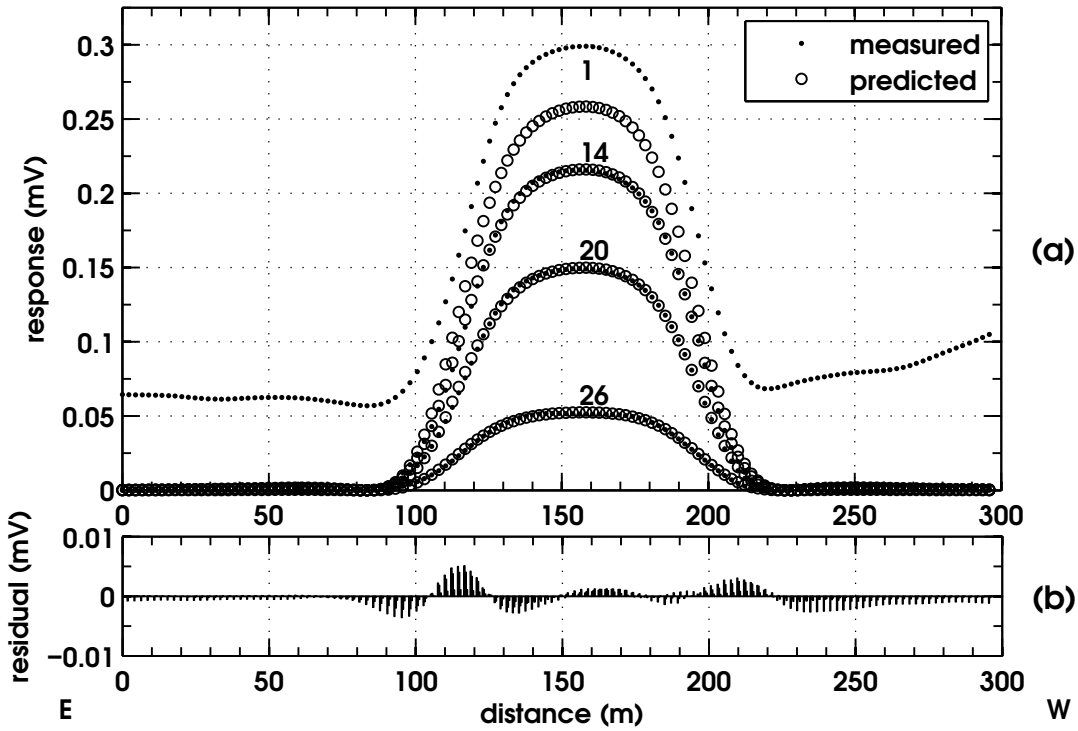

Figure 5.31: *(a) Measured (solid dots) and predicted (open circles) VTEM response for channels 1, 14, 20 and 26 of line 94 after changes of $\Delta h = -50.1$ m, $\Delta d = -7.04$ m and $A = 1.25$ were made to the predicted responses. All late time channels are fit very well by the decay, while measured channel 1 is substantially larger than the predicted values. (b) Differences between fitted and measured values for each fiducial of channels 14, 20 and 26. Channel 1 is not shown due to the obvious misfit shown in (a).*

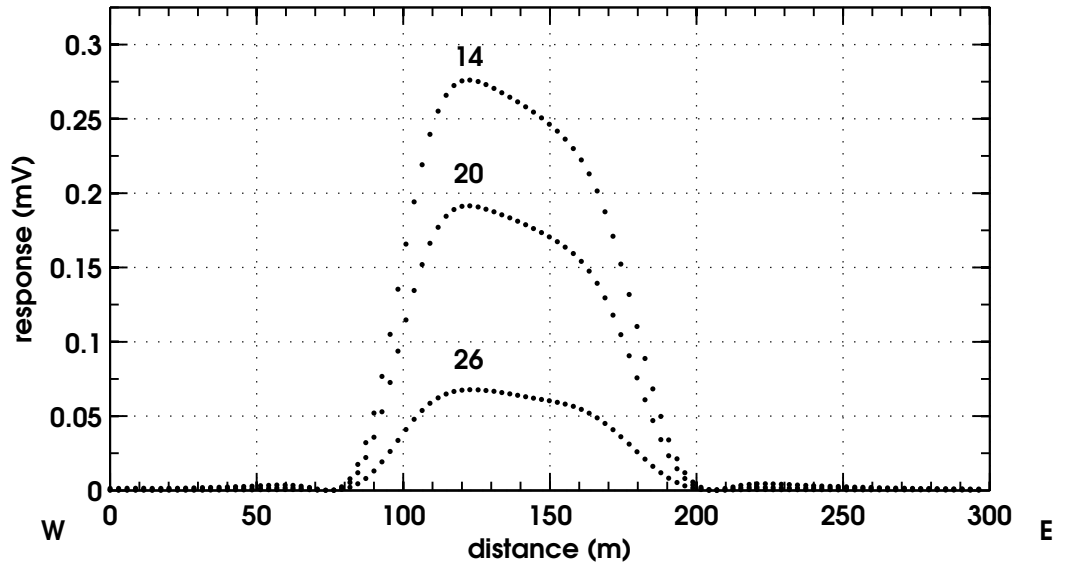

Figure 5.32: *Measured (solid dots) VTEM response for channels 14, 20 and 26 of line 93. Lopsided shape of peak of response suggests transmitter and receiver pitch.*

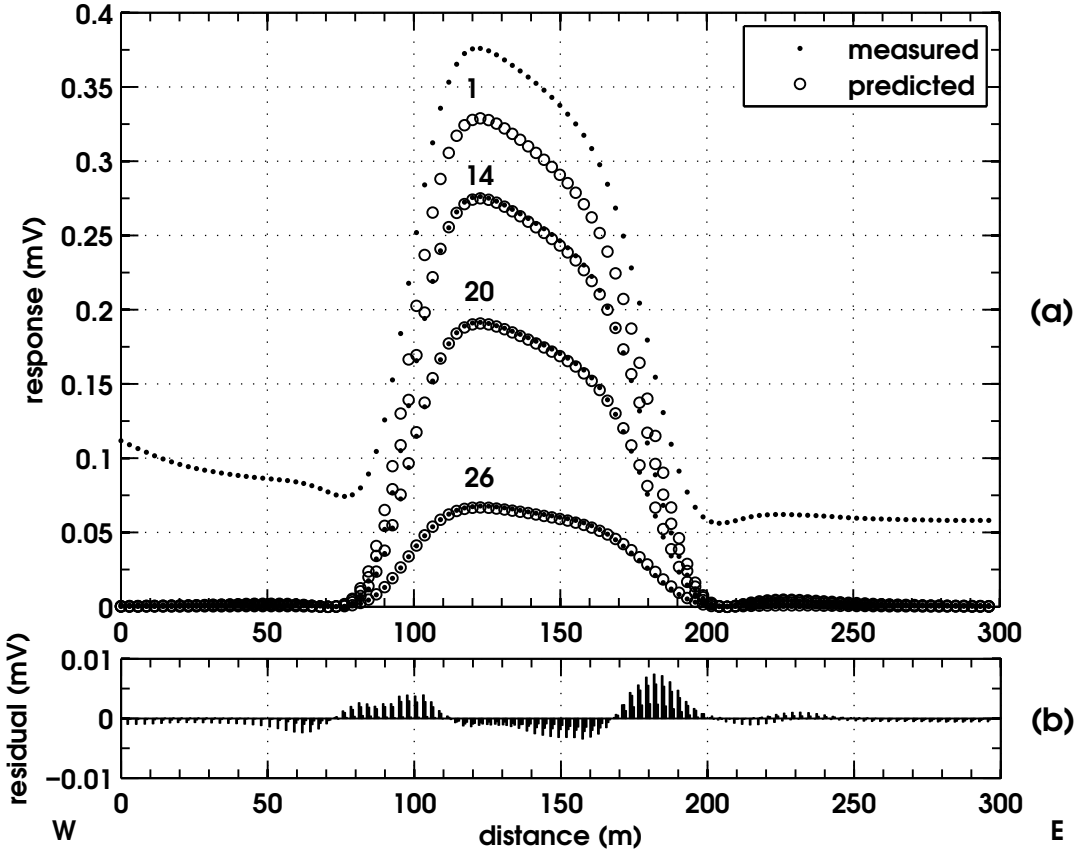

Figure 5.33: *(a) Measured (solid dots) and predicted (open circles) VTEM response for channels 14, 20 and 26 of line 93 with fitting parameters $\Delta d = 5.5$ m, $\Delta h = -52.0$ m and $\theta_b = -9.33°$. The addition of bird pitch corrects the shape of the prediction: it closely matches the measured curve. (b) Differences between measured and fitted curves for channels 14, 20 and 26.*

$\Delta d = 5.5$ m, $\Delta h = -52.0$ m and $\theta_b = -9.33°$. The predicted response curves for delay channels 1, 14, 20 and 26 are shown in panel (a) of Figure 5.33, while the difference between fitted and measured responses for channels 14, 20 and 26 are shown in panel (b).

It is clear from Figure 5.33 that the addition of pitch to the fitting parameter alters the shape of the predicted curve so that the difference between the measured and predicted responses is less than 0.01 mV (cf. Figure 5.31). As before with line 94, measured and predicted channel 1 disagree by a significant amount due to the conductivity of the earth beneath the loop. It is important at this point to remember that the key conclusions drawn from Chapters 3 and 4 that bird swing is a very real phenomenon that affects all towed bird AEM systems. In the case of VTEM, which had a nominal vertical helicopter-bird separation of 45 m, the period of an in-line swing would have been about 13 s. At an average ground speed of 25 m/s for these lines flown, one swing would have covered approximately 325 m. We can see from Figure 5.33 that the ground loop flyover results in signal that persists for about 100 m; this amounts to about 1/3 of a predicted swing period. Line 92 provides an excellent example of this because it was flown very slowly (mean helicopter ground speed 20 m/s) and very low to the ground (mean transmitter height 15.5 m). The measured response of channel 14 of line 92 is shown with solid dots in Figure 5.34. This figure clearly shows the effects of bird pitch and lower altitude. The peak response for channel 14 for this line is about 0.65 mV, approximately twice that of line 93 (which was flown at an average transmitter altitude of 29 m over the loop). Furthermore, the double peaks in the response are uneven: a sure sign of bird pitch for a coincident loop system. The double labels on the abscissa mark both time and distance, so the response for this line lasts for approximately half a bird swing. It is not surprising, then, that the fit predicted curve for channel 14 ($\Delta h = -51.5$ m, $\Delta d = -4.7$ m and $\theta_b = 8.3°$, open circles) does not match the measured response for the entire curve. Although the amplitude of the 40 m peak is matched by the

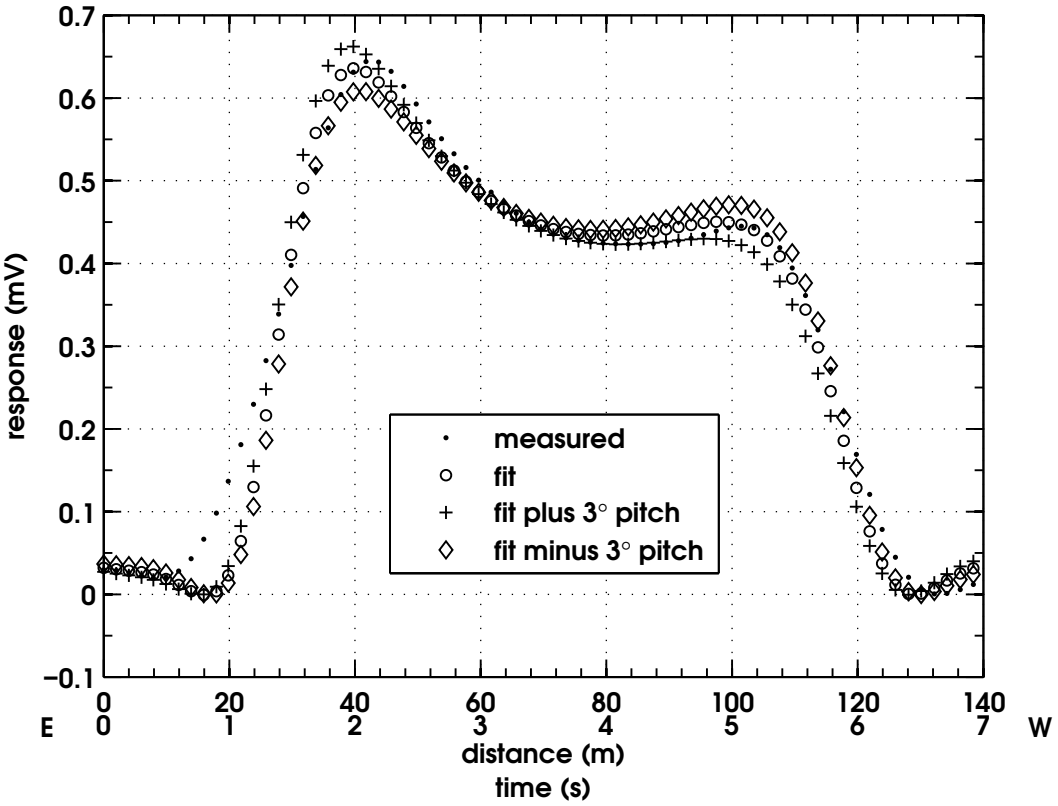

Figure 5.34: *Measured (solid dots) and fitted predicted (open circles, $\Delta h = -51.5$ m, $\Delta d = -4.7$ m and $\theta_b = 8.3°$) VTEM responses for channel 14 of line 92. Low altitude and slow flying show yield a large amplitude response that lasts for about 7 s. Also shown is the predicted fit with bird pitch $\theta_b = 11.3°$ (plus signs) and with bird pitch $\theta_b = 5.3°$ (diamonds).*

fit, the position of it is not: the predicted curve peaks too early. The second, lower, peak at 100 m is also matched in amplitude by the predicted fit, but it drops off too quickly compared to the actual response. To attempt to explain these findings, I have included 2 extra curves in Figure 5.34. The first curve, marked with + signs, uses the same fitting parameters as the open circle curve, but a bird pitch of 3° extra ($\theta = 11.3°$). The second curve has a pitch of only 5.3°.

All three fitted curves show that bird swing plays in important role in calibrating AEM systems, just as it does in interpreting data collected on survey. The plus- and minus-pitch curves are representative of the oscillations we might expect in a bird swing. In Figure 4.26, I showed that the RESOLVE towed bird could change its pitch by as much as 15° in 6 s. A movie, Figure D.5 in Appendix D.2 (see note at the

beginning of the Appendix), shows that the towed bird's horizontal inline position, in relation to the helicopter's, can change by a few metres in under a second. A shift such as this may account for the mismatch between the predicted and measured curves. In Figure 5.34, I used the measured antenna positions of the GPS mounted on the helicopter and assumed that the towed bird was a constant distance behind it. While this assumption may work for a fast-flying system at survey altitude of ∼30 m, where bird swing will be effectively masked by the larger spatial average and lower amplitudes of the system, it will fail for low, slowly flying systems that couple more strongly to the ground loop. Until the positions of the transmitter and the receiver(s) are monitored, the geometry problem of AEM systems will never be able to be rectified.

5.6.4 Changing the Ground Loop Resistance

In Section 5.5.4, I described a part of the HoistEM calibration experiment where the resistance of the ground loop was changed by approximately 12 000 Ω. A similar experiment was performed in Botswana for the VTEM system. For lines 97, 98, 183 and 184, the ground loop was left open circuit with the ends of the loop held approximately 2 m apart. The measured response for channels 1–5 of line 97, shown in Figure 5.35, shows a surprising result. Instead of getting little or no response, the receiver measures a signal that appears to ring in the decay channels! This is exactly what was seen in Figure 5.24, only here it is much more pronounced and persists for a longer time. I will explore this result in more detail in Chapter 6.

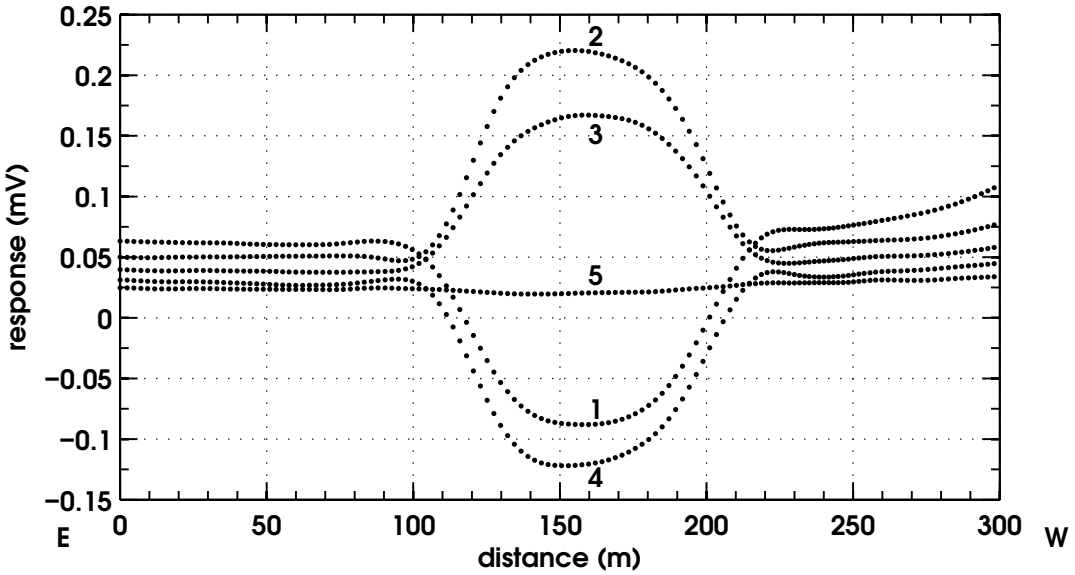

Figure 5.35: *First 5 VTEM channels measured over the open circuit ground loop laid out in Botswana (line 97). Like Figure 5.24, the response oscillates: it doesn't appear to decay away until channel 5 (100 μs after transmitter shut-off).*

5.7 Calibration of the SkyTEM System

The last system that I examine in this chapter is the helicopter-borne SkyTEM AEM system designed at Aarhus University in Denmark (Halkjær et al., 2006; Sørensen and Auken, 2004; SkyTEM ApS, 2007). The system was flown in November 2006, over conductive ground near the Bookpurnong area of South Australia.

5.7.1 Description of the System

SkyTEM is one of the newest helicopter-borne time domain AEM systems in commercial use worldwide. The transmitter is hexagonally shaped with the front and rear vertices flattened slightly to make an 8-sided loop of 1 to 4 turns. Unique among AEM systems, SkyTEM is capable of transmitting independent high-moment and low-moment waveforms during survey. Both waveforms are square-wave half-cycles with exponential on-ramps and turn-offs. For this test, the high-moment transmitter peak current was about 85 A with half-cycle on-time of 0.01 s and a 35 μs shut-off. The low-moment transmitter peak current was about 39 A with an on-time of 0.8 ms

Table 5.9: *High and low moment receiver windows and centre times (time measured from start of waveform) for the SkyTEM system.*

	High Moment		Low Moment	
Channel	Width (μs)	Centre (ms)	Width (μs)	Centre (ms)
1	10	10.047	4	0.812
2	10	10.060	4	0.818
3	10	10.073	4	0.825
4	16	10.089	4	0.831
5	21	10.112	4	0.838
6	31	10.146	10	0.847
7	33	10.183	10	0.860
8	47	10.233	10	0.873
9	57	10.293	17	0.889
10	79	10.371	21	0.912
11	98	10.464	31	0.945
12	122	10.580	33	0.983
13	158	10.728	47	1.034
14	198	10.911	57	1.092
15	250	11.145	79	1.171
16	310	11.425	98	1.264
17	390	11.785	122	1.380
18	500	12.250	158	1.528
19	630	12.815	194	1.709
20	790	13.535	246	1.943
21	1 000	14.440	-	-
22	1 260	15.570	-	-
23	1 590	17.005	-	-
24	2 000	18.800	-	-

and a 4.06 μs shut-off. The period of the high moment pulse cycle was 25 Hz, while the low moment cycle was 222 Hz.

The SkyTEM system has two dipole receivers, one mounted vertically about 12.4 m behind and 2.09 m above the centre of the transmitter loop and a horizontal one mounted in the plane of and directly behind the transmitter loop. Both receivers are constructed from 125 turns of wire in a 0.5×0.5 m square coil. The receiver windows for the high and low moment waveforms are given in Table 5.9.

Position of the SkyTEM transmitter is estimated from the recorded position of a GPS antenna mounted on the control box that is slung underneath the helicopter as

part of the payload. Altitude is monitored by two laser altimeters mounted on the front two sides of the transmitter loop. SkyTEM is also equipped with sensors that measure the pitch and roll of the transmitter. These are mounted near the front of the transmitter loop. A photograph of the SkyTEM system as it was being flown over my ground calibration loop is shown in Figure 5.36.

5.7.2 Description of the Experiment

The calibration ground loop was a 3-turn 100×100 m loop made from ordinary housing wire. Each turn consisted of 7 strands of wire of cross-sectional diameter 0.25 mm. The self inductance of the loop was calculated to be 8.23 mH. A 1 Ω resistor was used to close the loop, making the total resistance of the loop 9.6 Ω, so that the decay time τ of the loop was 0.86 ms. The GPS coordinates of the corners of the loop are displayed in Table 5.10.

The SkyTEM system was flown twice over the ground loop, with both high moment and low moment transmitters operating. I will only present the high moment data in this section. A schematic of the waveform and the receiver timing windows are shown in panel (a) of Figure 5.37. Since I do not know the time constants of the turn-on and shut off, I will assume a trapezoidal waveform of linear 35 μs ramps. The next panel of Figure 5.37 shows the first derivative of the high moment transmitter current waveform, while panel (c) shows the predicted measured response of the z-axis receiver if it were capable of measuring continuously at the same gain.

Two lines were flown over the ground loop as a part of this test. The first line, shown in Figure 5.38, was flown from the northeast to the southwest. The loop was closed with a 1 Ω resistor, across which I measured the emf generated in the loop. From the SkyTEM flight path recovery, the measured altitude, pitch and roll of the bird, and the current measured in the high moment transmission, I calculated the values of the peak current induced in the ground loop. These values, marked with

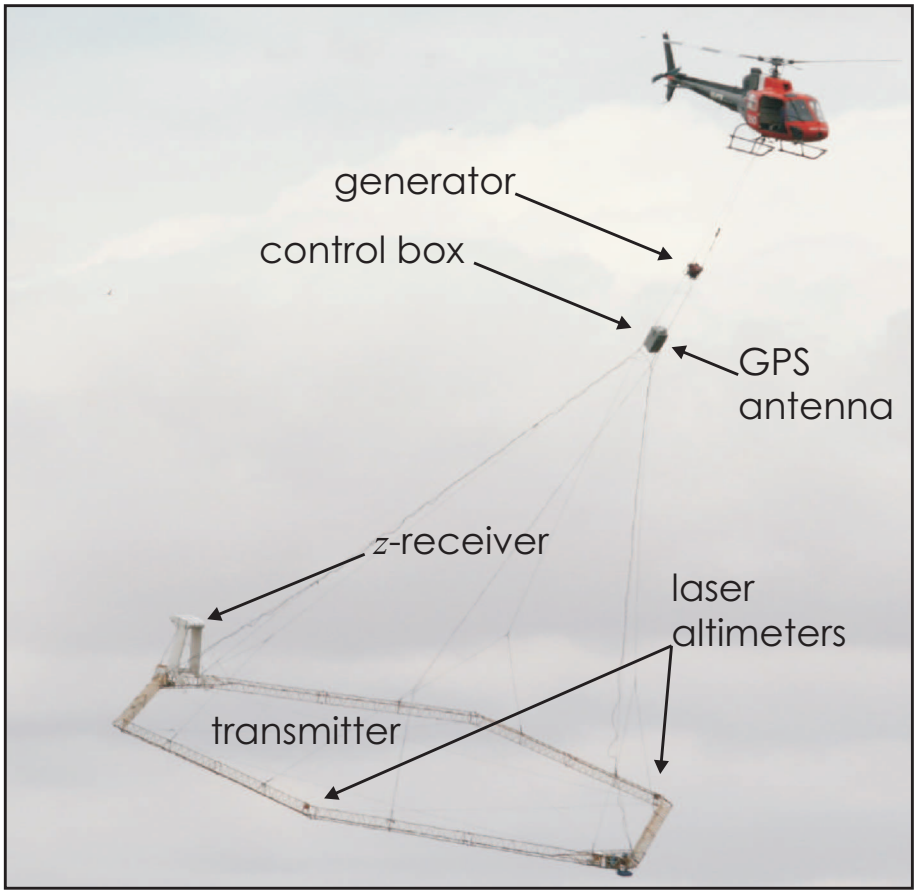

Figure 5.36: *Photograph of the SkyTEM system as it was being flown over a calibration ground loop near Berri, South Australia.*

Table 5.10: *GPS coordinates of the corners of the ground calibration loop (GDA94, UTM Zone 55) for the SkyTEM calibration test.*

Easting (m)	Northing (m)
$_{4}62_{582}$	$_{62}00_{821}$
$_{4}62_{632}$	$_{62}00_{734}$
$_{4}62_{725}$	$_{62}00_{787}$
$_{4}62_{669}$	$_{62}00_{870}$

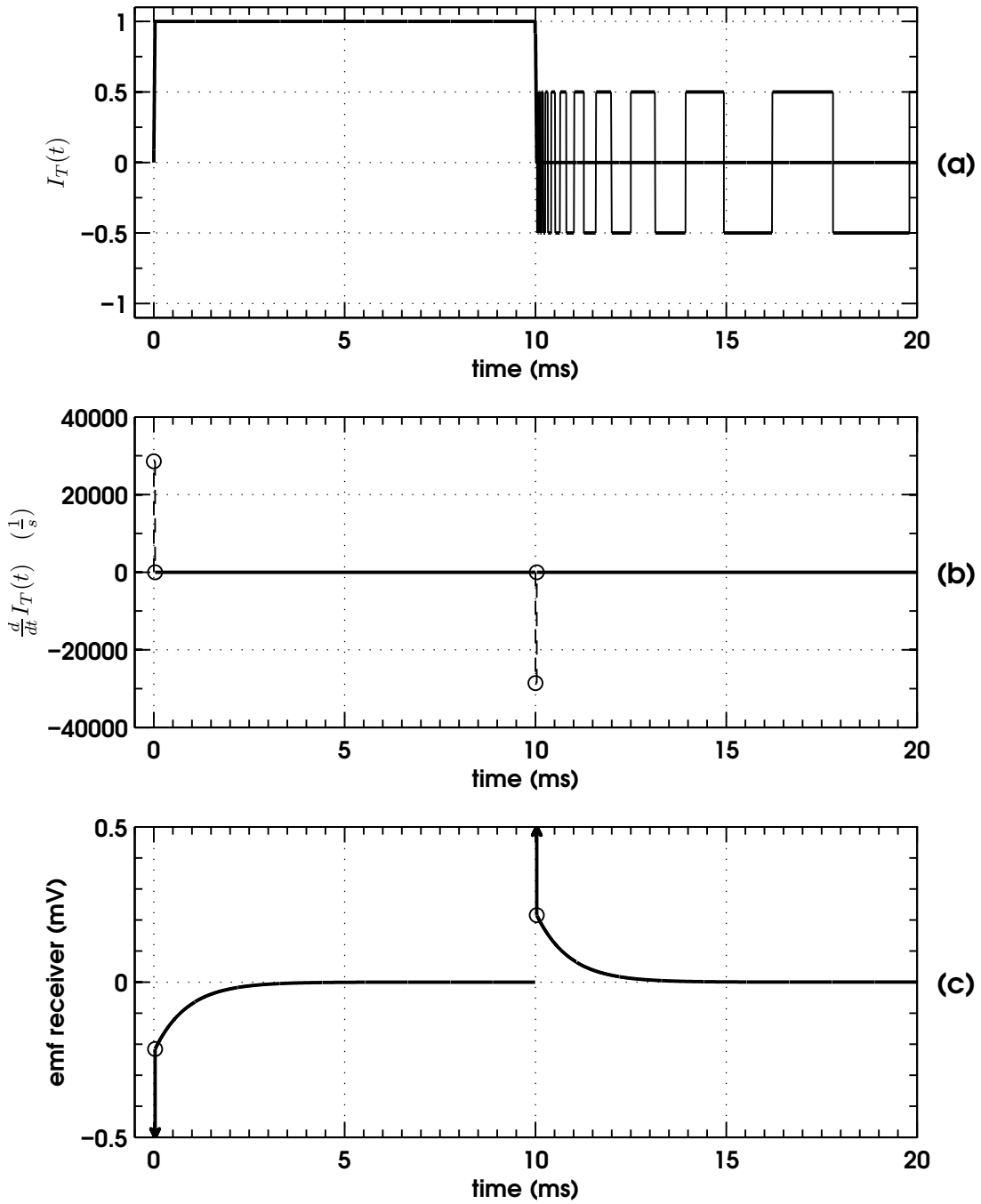

Figure 5.37: *(a) Schematic of the high moment SkyTEM waveform for the ground loop experiment. The linear ramps at the beginning and the end of the on-time are proposed by me and may not be the actual waveform. (b) First derivative of the transmitter current waveform with respect to time. (c) Predicted response of the vertical receiver if it were capable of measuring continuously at the same gain. Responses at 0 s and 0.01 s are off the vertical scale; they are shown with arrows.*

red dots in Figure 5.39, are plotted together with the measured induced ground loop current.

Figure 5.39 shows close agreement between the measured and predicted currents for most of the system flyover, and particularly over the central region from 15 s to 20 s. It is interesting to note that I didn't have to alter the laser altimeter in order to force agreement between measured and predicted values for this system. This is due to the fact that the laser altimeters of the towed bird are rigidly mounted to the bird itself and have a slant angle correction applied, thereby minimising the altitude error. Although I haven't reported them here, the pitch of the SkyTEM system was quite large for the two lines flown that day, mainly due to high airspeed used for most of the morning that the experiment was conducted. During the flyovers, Nick Ebner and Dr. Tim Munday took continuous photographs of the SkyTEM system. Nick was stationed slightly to the northwest of the ground loop, while Dr. Munday was positioned southeast of the loop, directly in line with the flight path. Using the digital photograph file headers, I have meshed the streams of photographs together into a movie. It is shown in Figure D.8 in Appendix D.4 (again, see note at beginning of Appendix D).

Now that we know that the SkyTEM system excited the ground loop as predicted, we must analyse the measured response at the receivers. Using the flight recovery, altitude, attitude and receiver position relative to the transmitter, I calculated the predicted response for the vertical and horizontal receivers. The measured and predicted values of the vertical receiver are shown in Figure 5.40a; panel (b) shows the responses for the horizontal or x-axis receiver. Both panels only show the measured and predicted responses for channels 10, 14 and 20. Earlier time channels will not fit on the scale due to the relatively high conductivity of the earth. Signal from the conductive ground saturates the ground loop response even for the very late delay channels. The horizontal receiver does not even record negative response values in channel 10 at 220 m (panel (b) of Figure 5.40). It is therefore impossible

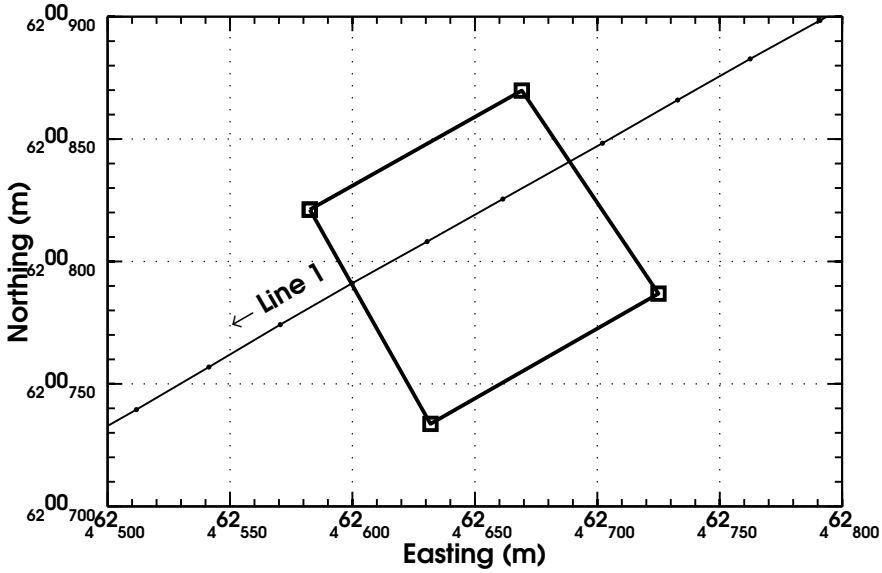

Figure 5.38: *Flight path of line 1 during the SkyTEM ground loop calibration test in November 2006. Ground loop corners are marked with open squares.*

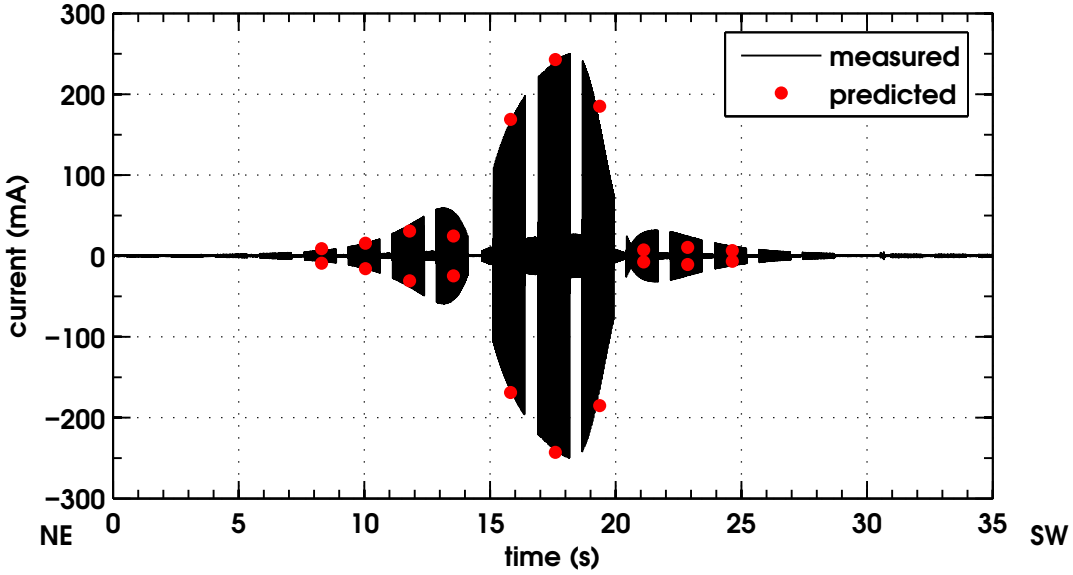

Figure 5.39: *Measured current induced in the ground loop during the flyover of line 1 (black). Peak induced current predicted from SkyTEM flight path recovery, pitch, roll, altimeter and current measurements (red dots).*

to calibrate the receivers of the SkyTEM system in this experiment over conductive ground, even though it was very easy to calculate the expected peak currents induced in the ground loop during the flyover.

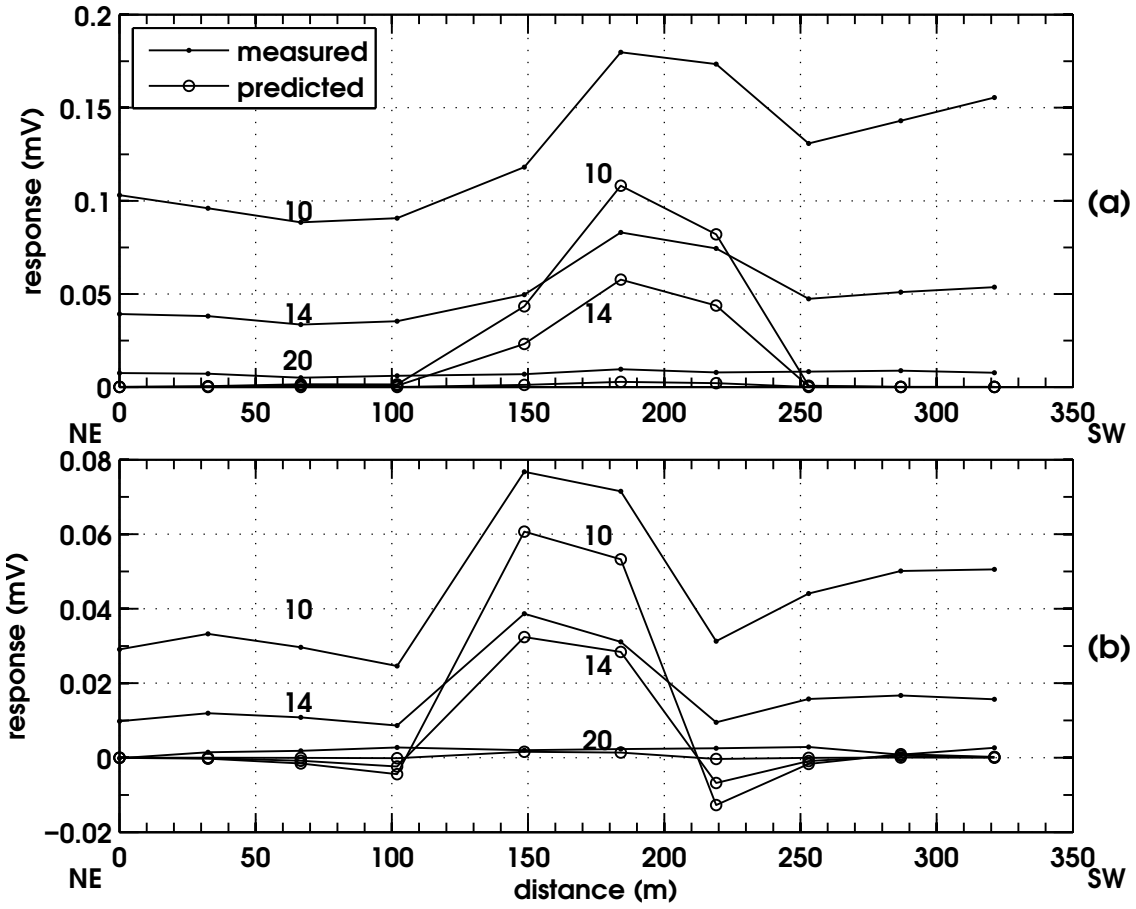

Figure 5.40: *Measured (dots) and predicted (open circles) SkyTEM responses for channels 10, 14 and 20 for (a) the vertical receiver and (b) the horizontal receiver (line 1). The conductive ground under the calibration loop overpowers the signal from the ground loop itself: calibration of the receivers was impossible in this location.*

5.8 Summary and Conclusion

In this chapter, I motivated the topic of the need for calibration of time domain AEM systems. It is inherently difficult to calibrate such systems for reasons such as geometry and saturation of the receivers during the on-time. I have proposed and developed the method of AEM system calibration using a conductive ground loop of known geometry and electrical properties.

After understanding the physical principles of mutual inductance that govern the generation of electrical current in the ground loop and the consequent time changing magnetic field that can be detected with the receiver, the mathematical development is very much simplified if we take the system input/output perspective using Laplace operators and the convolution theorem. The transmitter current waveform can be viewed as the input to the entire transmitter loop to ground loop to receiver system, and the measurable emf in the receiver is the output. A core ingredient of the process is the ground loop's induced current: another measurable quantity. Through measurement of the system geometry and knowledge of the transmitter waveform and timing scheme in the receiver, it is possible to predict the output of the total system as it evolves in time.

The calibration method was tested on 4 different AEM systems under different conditions. Each experiment that I presented illustrated a different aspect of this method. The AeroTEM system, flown in South Africa, showed that although the system could be well calibrated for a late delay channel in every line by altering the measured altitude and changing the horizontal offset between GPS antenna and transmitter, there were still large differences between the measured and predicted signals for other channels. In every case, the prediction for delay channel 4 was larger than what was actually received. The most likely cause of this was probably due to waveform and receiver timing windows. But the most significant difference between the two signals was one of envelope width. In all lines flown, the measured signal existed for longer periods of time than the predicted one. This leads me to believe that there is a certain amount of averaging done to the received data as it is processed by the contractor. Due to the fact that the lines flown over the ground loop cut diagonally across it and the towed bird was very likely slightly offset in the cross-line direction from the direction of travel, it is very difficult to ascertain just how much averaging was applied to the data. Even so, an important conclusion can be drawn from this, namely that the system should be flown over the loop at

right angles to the sides, and the ground loop should be longer than it is wide (not attempted).

Measurement of the current induced in the ground loop provides an excellent two-part calibration of the AEM system data. Just as receiver response can be predicted from system geometry and timing information, the magnitude of the peak current induced in the ground loop can be predicted from the electrical properties of the loop, the peak transmitter current and geometry alone. This eliminates the timing and receiver response from the calibration scheme and allows us to focus on the system geometry. This technique was very nicely illustrated with the HoistEM system in Western Australia. The prediction of peak induced current allowed me to alter and fix the geometry of the Hoist (altitude and GPS antenna-transmitter separation) and apply the corrections to the prediction of the receiver response. The result was excellent, showing that the measured response exhibited not only significant averaging but that there was a problem with the amplitude gains in the receiver as well. This was in contrast to (Vrbancich and Fullagar, 2004) who, in the absence of conclusive evidence, attributed the observed errors to altitude.

Attempted calibration of the VTEM system provided two other insights to the use of this method. The first one, also seen in the HoistEM example but more spectacularly seen here, was ringing in the received response when the loop was left open circuit. This capacitive antenna effect will be studied in more detail in the next chapter. The second insight—one that is extremely appropriate after a chapter on bird swing—is that I found it impossible to fit the predicted responses to the measured responses by changing altitude position and gain alone. It was necessary to add yet another parameter to the fitting process: pitch. This was particularly apparent for the VTEM system due to the 26 m diameter transmitter loop, since geometrical changes in such a large loop are easily discernable in the measured response.

The addition of pitch and roll sensors, as well as altimeters positioned on the transmitter itself and a GPS antenna closely positioned to the centre of the trans-

mitter loop, promised to yield exciting results with the SkyTEM calibration test in South Australia. With little changing of in-line offset and no changing of altimetry, peak predicted and measured current matched remarkably well when bird pitch and roll were accounted for in the prediction. Unfortunately, due to the conductive ground underneath the loop, the second part of the calibration could not be undertaken.

The ground loop calibration method in resistive terrain is successful. It is an accurate, fast and inexpensive method that can be used almost anywhere to calibrate any time domain AEM system provided certain conditions are met. The first one is that the ground must be as resistive as possible. Conductive ground will affect the measured response and interfere with the calibration procedure. The second condition is ground loop geometry and electrical properties. The loop needs to be accurately surveyed and laid out ideally on flat ground. Furthermore, the time constant of the loop should be such that some signal will persist to the mid time channels of the receiver, yet ideally have disappeared by the next half cycle. In order to ascertain the time constant of the loop, the resistance of the loop when it is laid out should be measured and the self inductance either measured or calculated. If the induced current in the ground loop is measured, the time constant may be estimated from that.

I believe that the ground loop method is a valuable and viable way to calibrate AEM systems. Good results can be achieved despite the problems with geometry, as it provides a simple input/output approach to match the transmitter current waveform to the receiver response. For this reason, I have included some recommendations for conducting the ground loop calibration test. These may be found in Appendix F. In this chapter, I only hinted at the information that can be gathered if the current in the ground loop is also monitored during flyover. Not only does it allow us to determine geometry for the flyover, it also gives us almost direct information about the transmitter waveform. In Section 5.3.1, I showed that the ground

loop current is the convolution of the loop impulse response with the derivative of the transmitter current waveform. If we know the transfer function of the measurement device used to measure the ground current, it is possible to deconvolve the signal and hence obtain the transmitter waveform. This is the subject of the next chapter, where I take a closer look at the interesting and tantalizing ground loop responses that I showed earlier in this chapter.

Chapter 6

Ground Loop Current Measurements

6.1 Introduction

In addition to providing an intermediate step to the calibration of a time domain AEM system, whereby the geometry of the transmitter is determined based on current strength and peak ground loop current, measurement of the induced ground loop can provide extra information about an AEM system. In this chapter, I discuss the advantages gained by measuring the current induced in the ground calibration loop as an AEM system is flown over it during a calibration experiment.

The first advantage that has not been properly explored in this thesis is one of synchronisation. When the ground current monitoring device is synchronised with a GPS clock, the ground current can in turn be synchronised with the airborne EM system. To my misfortune, the only trial where synchronisation was successful was with the SkyTEM calibration experiment in South Australia where the ground was so conductive that the calibration loop response was almost indistinguishable from the ground response. Theoretically, it is possible to synchronise ground loop recordings to airborne and thereby gain an idea of the spatial averaging and shifting applied to the data independently of the curve-fitting technique of the last chapter.

A more important advantage from measuring the induced current comes from the mathematical development of the calibration as a whole. In chapter 5, I focussed mainly on the emf produced in the airborne receiver and very little attention was paid to the measured current. It is possible, however to use the measured induced ground loop current to determine the waveform of the transmitter current. In this chapter, I develop this idea further and derive a method to determine the transmitter waveform through deconvolution of the ground loop current in Fourier space. I will use this technique to produce a catalogue of transmitter waveforms in a variety of different AEM systems at different times between 2003 and 2007. I will show how changing the resistance of the ground loop alters the characteristic time constant of the loop, and that a larger ground loop resistance provides a better means of determining transmitter waveform by reducing the need for accurate deconvolution.

Changing the resistance in the ground loop to too large a value can cause clipping and slew-rate problems in the ground loop current measurement instrument. While briefly touching on these topics, I will show how adding too large a resistor in the otherwise conductive ground loop leads to displacement currents and capacitance effects that cause the loop to act as an electric field antenna: an effect that can be seen both in the air and on the ground. I will develop the theory of this anomalous behaviour and briefly model it for the cases of HoistEM and VTEM mentioned in Chapter 5.

Finally, I show how the principle of ground loop calibration can be applied to frequency domain AEM systems just as easily as time domain. This will be exemplified by a ground loop test conducted on the RESOLVE system on the Chowilla Floodplain in 2005. Although the ground there is too conductive to complete a full calibration, I will show how the monitored current can be analysed for frequency composition. By fitting cosine and sine curves of the transmitter frequencies to the measured ground loop current, I show how the phase of the ground loop current switches and the transmitter coupling reverses as the RESOLVE system is flown

over it; and particular attention will be given to the difference between the mutual inductance coupling of vertical and horizontal dipoles to a ground loop.

6.2 Deconvolving the Ground Loop Current

In Section 5.3.1, I showed that the current in the ground loop $I_L(t)$, induced by the changing current in the transmitter, can be expressed by equation (5.7), repeated here for convenience:

$$I_L(t) = -\frac{I_T M_{TL}}{L}\,\mathfrak{L}^{-}\left[\frac{1}{s+\dfrac{R}{L}}\mathfrak{L}\big[i'_T(t)\big]\right], \tag{6.1}$$

where I_T is the peak current in the transmitter, M_{TL} is the mutual inductance between the transmitter and the ground loop, L and R are the total self inductance and resistance of the ground loop and $i_T(t)$ is a piecewise continuous function of time whose value is no greater than 1. The variable s is the Laplace transform variable which, on the righthand side, represents the convolution of the time rate of change of the transmitter current with the exponential decay ($\frac{L}{R}$) characterised by the electrical and geometrical properties of the ground loop. If we ignore the terms outside the brackets and concentrate only on the argument of the Laplace transform on the right, then removal of the exponential decay effect due to the loop, and integration of the remaining signal, should give us the transmitter current's waveform.

Of course, things are never as simple as they appear. The equation above assumes that the input signal and the measured ground loop current are analog functions and that the current is measured with a device that has a perfectly linear transfer function. This is not necessarily the case. Although both currents are analog and continuous, the measurement of the ground current is a digital process whereby the analog voltages across the damping resistor in the ground loop are converted

to digital signals through an A/D converter such as the Edirol UA-5 used in my experiments. Furthermore, measurement of a simply repeating square wave shows that the Edirol suffers from bandwidth limitations that cause the measured voltage to 'slump' during the periods of constant voltage. This effect is shown in Figure 6.1 for a square wave input of approximately 25 Hz. One simple interpretation of Figure 6.1 is that the slumped waveform is the output of the transfer function of the Edirol UA-5 to a step or Heaviside input. This effect will also be present in the measurement of the induced ground loop current during flyover. Practically, this means that equation (6.1) above does not give the whole story, and further modifications to the righthand side must be made.

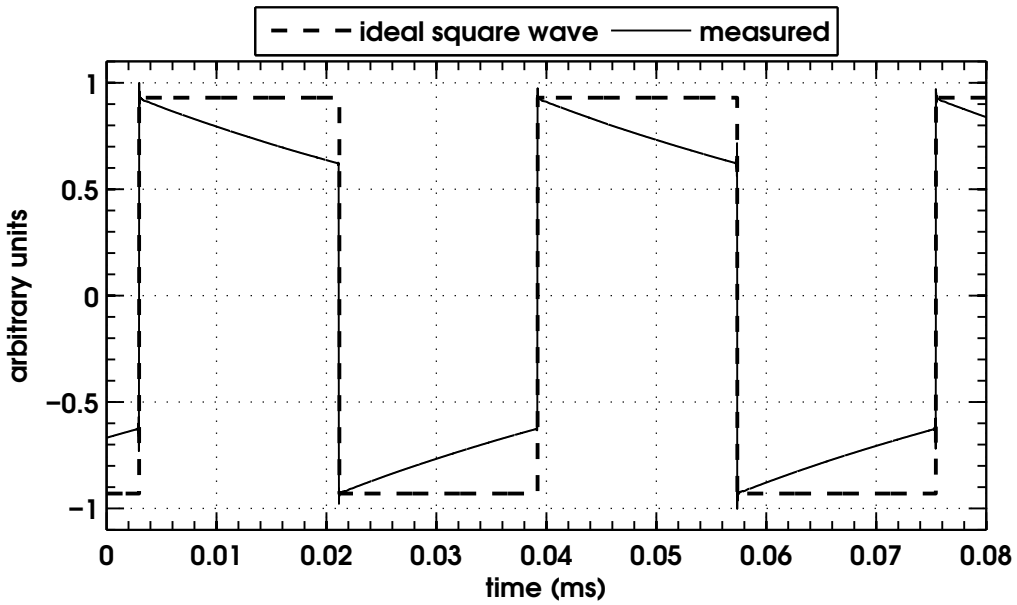

Figure 6.1: *Comparison of a 25 Hz analog input square wave (dashed line) and the output as digitised by the Edirol UA-5 (solid line). Constant voltages are seen to 'slump' due to low frequency cut at about 20 Hz.*

Recall from Chapter 5 that the Laplace transform is a useful tool when determining the response of a system to its input. I will apply that tool to the response of the Edirol UA-5 to an arbitrary input. In the present case, the input is the voltage across a 1 Ω resistor closing the ground loop during flyover, which amounts to $I_L(t)$, the current induced in the ground loop. It is modified by the *incidial* response of the system, which I have shown in Figure 6.1 for a 25 Hz square wave. The output

of the UA-5, defined as $V_{UA-5}(t)$, can therefore be calculated in the following way:

$$V_{UA-5}(t) = \mathfrak{L}^{-}\big[R_{UA-5}(s)\mathfrak{L}[I_L(t)]\big], \tag{6.2}$$

where $R_{UA-5}(s)$ is the incidial response of the UA-5, and $I_L(t)$ is the calibration loop current defined in equation (6.1). Thus, we see that the response measured by the UA-5 is actually the ground loop current convolved with the incidial response of the unit itself.

6.2.1 Convolution and the Discrete Fourier Transform

The convolution of two discrete time series $a(n)$ and $b(n)$ of length N, where n is an index starting at 0 ($n\epsilon\{0, 1, 2, \ldots, N-1\}$), creates another time series $c(n)$. The p^{th} element of $c(n)$ is expressed as

$$c_p = \sum_{k=0}^{p} a_k b_{p-k};$$

and a_k is the k^{th} element of $a(n)$ and b_{p-k} is the $p-k^{th}$ element of $b(n)$ (e.g. Lyons, 1997; Gubbins, 2004). The convolution of two series is often written in the following form that simplifies the notation:

$$c(n) = a(n) * b(n).$$

Any time series $c(n)$ can be transformed to an equivalent Fourier series $C(\omega)$, whose elements are complex numbers that represent the magnitude and phase of a sine wave of angular frequency $\omega = 2\pi n f_s$, where f_s is the sampling frequency of the time series (e.g. 96 kHZ for the Edirol UA-5). The series $C(\omega)$ is obtained through application of the discrete Fourier transform (DFT), $\mathfrak{F}$, which acts on the time series (Gubbins, 2004):

$$C(\omega) = \mathfrak{F}\big[c(n)\big].$$

The term by term expression for the Fourier transform is as follows:

$$C(\omega) = \frac{1}{N} \sum_{k=0}^{N-1} c_k e^{-2\pi i n k/N}.$$

The time series is obtained back from the Fourier series by application of the inverse discrete Fourier transform $\mathfrak{F}^-$:

$$c(n) = \mathfrak{F}^- \big[C(\omega) \big],$$

and we therefore arrive at the identity

$$c(n) = \mathfrak{F}^- \big[\mathfrak{F} \big[c(n) \big] \big]. \tag{6.3}$$

If we apply the DFT to the convolution of two time series, we arrive at the following powerful relation:

$$\mathfrak{F} \big[a(n) * b(n) \big] = \mathfrak{F} \big[a(n) \big] \, \mathfrak{F} \big[b(n) \big], \tag{6.4}$$

which states that the DFT of the convolution of two time series is equal to the term-by-term multiplication of the elements of each Fourier series. This method can be used to deconvolve two or more time series. Let $d(n)$ be a time series made from the convolution of the time series $a(n), b(n)$ and $c(n)$, i.e.

$$d(n) = a(n) * b(n) * c(n).$$

Furthermore, let's say that all time series but $a(n)$ are known, and it is this one that we wish to recover. This can be done through the use of equation (6.4). Applying the Fourier transform to both sides of the relation above we get

$$\mathfrak{F} \big[d(n) \big] = \mathfrak{F} \big[a(n) \big] \, \mathfrak{F} \big[b(n) \big] \, \mathfrak{F} \big[c(n) \big],$$

and rearranging to isolate $\mathfrak{F}\big[a(n)\big]$:

$$\mathfrak{F}\big[a(n)\big] = \frac{\mathfrak{F}\big[d(n)\big]}{\mathfrak{F}\big[b(n)\big]\,\mathfrak{F}\big[c(n)\big]}.$$

Next, we apply equation (6.3), which leaves us with the following expression for $a(n)$:

$$a(n) = \mathfrak{F}^{-}\left[\frac{\mathfrak{F}\big[d(n)\big]}{\mathfrak{F}\big[b(n)\big]\,\mathfrak{F}\big[c(n)\big]}\right]. \tag{6.5}$$

This is only one of several different ways to deconvolve a time series from a convolution of several series (e.g. Gubbins, 2004), but it is the one that I will apply in this thesis.

6.2.2 The Ground Loop Current

It is a simple matter to apply the arguments developed above to the response of the Edirol UA-5 and the measurement of the ground current. As stated in Chapter 5, the Edirol UA-5 is a device that possesses an analog to digital converter. Thus, the continuous ground loop current goes through an anti-alias filter and is then digitised and sampled at 96 kHz: the output, $V_{UA-5}(t)$ is therefore a time series, say $v_{UA-5}(n)$. In terms of the notation above, the time series output is thus a convolution of the UA-5 step response $r_{UA-5}(n)$ and the ground loop current $i_L(n)$. Equation (6.2) can be re-written as

$$v_{UA-5}(n) = r_{UA-5}(n) * i_L(n);$$

and since $i_L(n)$ is itself a convolution of $r_L(n)$ the indicial response of the ground loop and the time derivative of the transmitter current $i'_T(n)$, we may write

$$v_{UA-5}(n) = r_{UA-5}(n) * r_L(n) * i'_T(n)$$

for the description of the sampled response as measured by the UA-5. Applying the deconvolution technique of equation (6.5) and rearranging for $i'_T(n)$, we arrive at

$$i'_T(n) = \mathfrak{F}^- \left[\frac{\mathfrak{F}\big[v_{UA-5}(n)\big]}{\mathfrak{F}\big[r_{UA-5}(n)\big]\mathfrak{F}\big[r_L(n)\big]} \right]. \tag{6.6}$$

Finally, we can make use of a beautiful feature of the properties of the discrete Fourier transform: integration. As is easily found in Box 2.2 in Gubbins (2004), and many other books on signal processing, the integral of a time series can be obtained by transforming the time series to the Fourier domain, dividing every n^{th} element of the Fourier series by i times the discrete frequency ω_n, adding a constant and transforming back. Using this approach on equation (6.6), the transmitter current waveform is

$$i_T(n) = \mathfrak{F}^- \left[\frac{\mathfrak{F}\big[v_{UA-5}(n)\big]}{\mathfrak{F}\big[r_{UA-5}(n)\big]\mathfrak{F}\big[r_L(n)\big]} + c_i \right], \tag{6.7}$$

where $\omega_n \epsilon \{0, \frac{2\pi}{f_s}, \ldots, \frac{2\pi n}{f_s}, \ldots, \frac{2\pi(N-1)}{f_s}\}$, and c_i is the constant of integration (chosen as 0). In all analyses that follow, the Fourier transforms of all time series data are calculated using the `fft.m` and `ifft.m` functions supplied with the MATLAB package (The MathWorks, 2007).

6.3 Example: HoistEM

The first example of recorded ground current and recovered transmitter current waveform will be from the HoistEM calibration discussed already in Section 5.5. The recorded induced ground loop current from line 1 was shown in Figure 5.17, repeated here for convenience as Figure 6.2. Zooming in on the measured signal reveals the structure of the induced current envelope. Figure 6.3 shows the ground loop current from 5 s to 5.08 s, a time span of only 80 ms. During this time, we see

two complete repetitions of the transmitter current waveform. Note the similarity of the measured signal to the ground loop current predicted by theory in Figure 5.12.

As is common with measuring repeatable signals, several complete ground current waveforms are stacked together to increase the signal to (random) noise ratio (e.g. Gubbins, 2004). To correct for timing differences between the AEM system and the ground sampling, I interpolate or resample the waveform by a factor of 10. This process may introduce a non-existent high frequency component to the signal but, since the waveforms of interest are generally 25–30 Hz, and the Edirol UA-5 is band-limited to ∼20 000 Hz, this is not a problem. For HoistEM, I took the waveforms from 5–7 s, as marked by the vertical lines in Figure 6.2. The result, after stacking, is shown in Figure 6.4.

The Fourier series of equation (6.7) are next obtained: $\mathfrak{F}\big[v_{UA-5}(n)\big]$ is the DFT of the stacked waveform, $\mathfrak{F}\big[r_{UA-5}(n)\big]$ is the DFT of the stacked 25 Hz step response shown in Figure 6.1, and $\mathfrak{F}\big[r_L(n)\big]$ is the DFT of an exponential waveform of time constant τ =0.296 ms (cf. Section 5.5). These Fourier series are placed into equation (6.7), divided by $i\omega_n$, and the inverse Fourier transform is computed. The result, normalised to 1 is shown in Figure 6.5

Evidently, the HoistEM waveform really does have an exponential turn-on and a very sharp cutoff about 5 ms later. Looking more closely, Figure 6.6a shows the first half-cycle and the nominal waveform that I used in my calibration in Section 5.5, showing that the nominal waveform rises slightly more quickly than the deconvolved one. Looking down to panel (b), we see that although the HoistEM transmitter current shut-off is approximately 40 μs long, it begins to shut off at about 4.965 ms rather than 5 ms as shown by Boyd (2004).

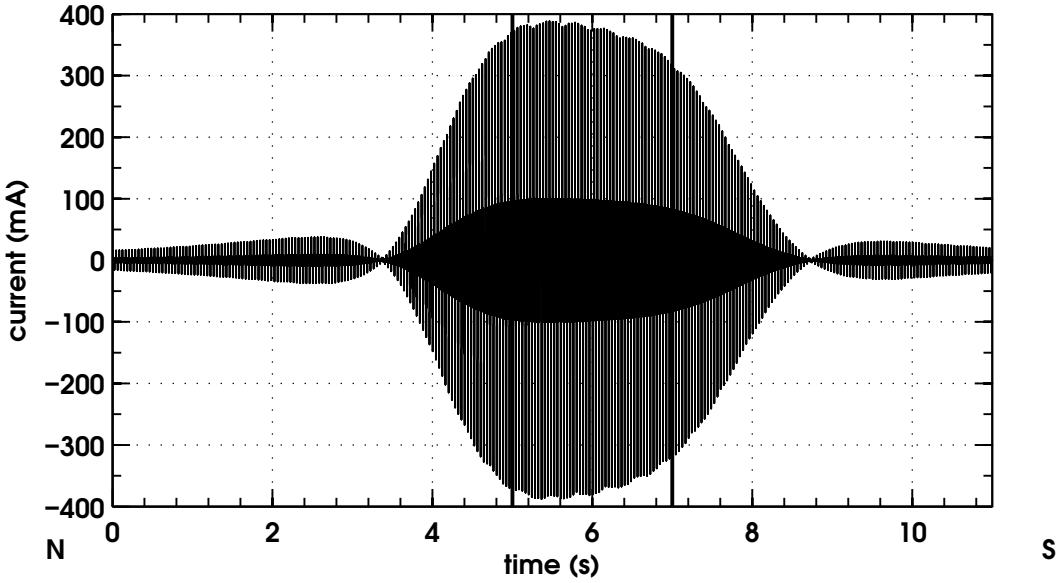

Figure 6.2: *Figure 5.17, repeated here for convenience (HoistEM).*

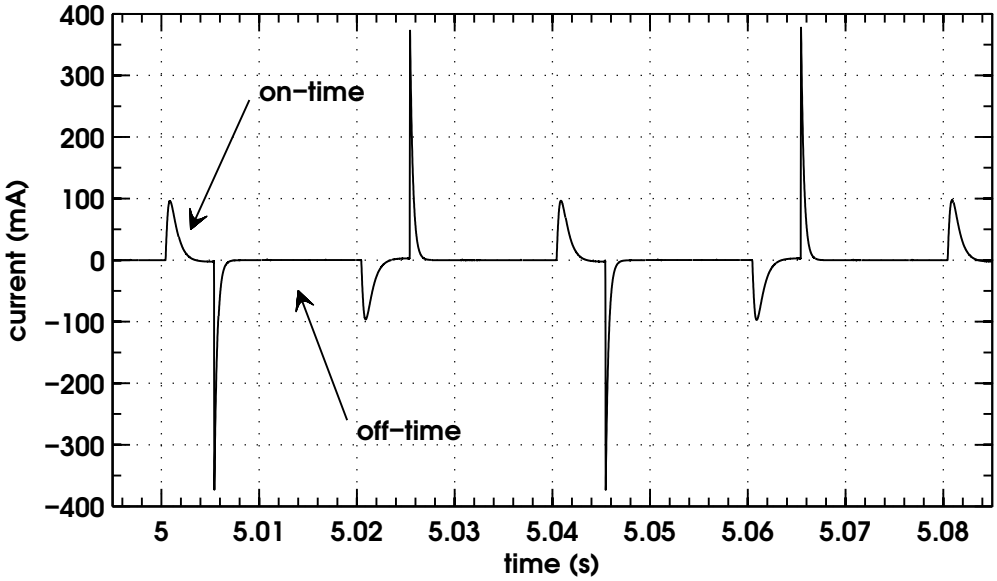

Figure 6.3: *Detail of Figure 6.2, from 5 s to 5.08 s, showing 2 complete cycles of the current induced in the ground loop.*

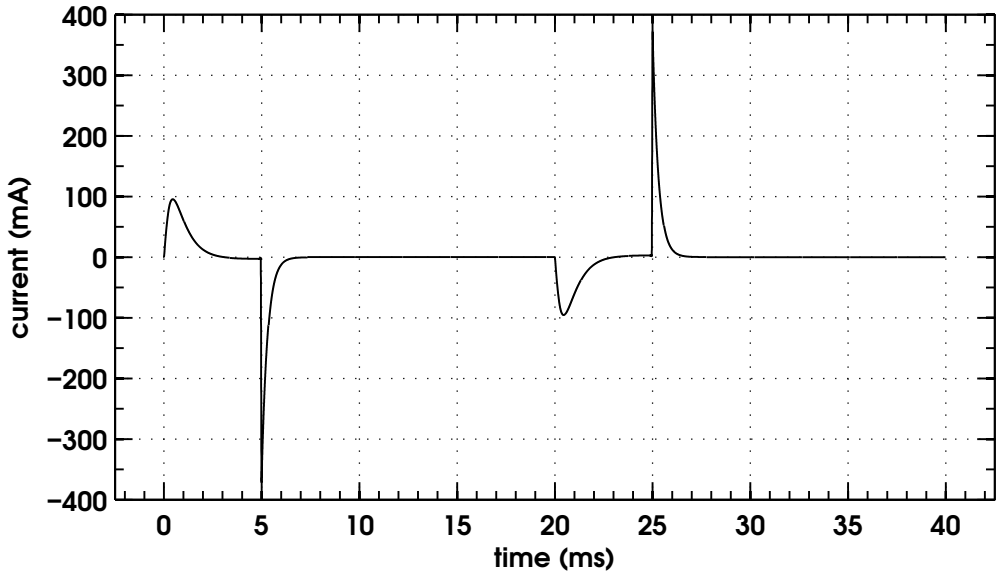

Figure 6.4: *Ground loop waveform constructed from interpolating and stacking the measured signal from 5 s to 7 s (system over the calibration loop as shown in Figure 6.2).*

6.4 Catalogue of Waveforms

Now that the process of obtaining the transmitter current waveform from the current induced in the calibration loop has been explained and exemplified, I present a catalogue of measured ground currents and deconvolved waveforms from the various systems that have taken part in the calibration experiment. The tests and experiments have taken place from 2003–2006, with various refinements and changes to the experimental set-up. Several people have been involved with the ground loop calibration tests; my thanks go to all of them.

6.4.1 VTEM

The first system to be discussed is the VTEM system flown in Sudbury, Ontario, Canada in October 2005. The ground loop had an estimated self inductance of 23.6 mH and a resistance of 15.97 Ω: the characteristic decay constant was $\tau = 1.47$ ms. The current measured in the ground loop is shown in Figure 6.7a.

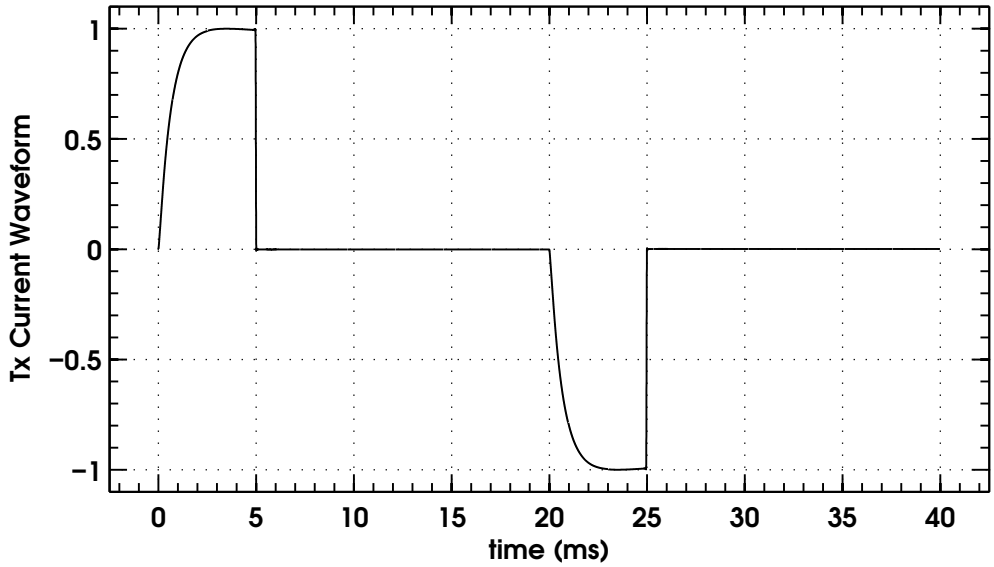

Figure 6.5: *The HoistEM transmitter current waveform, as measured in the ground loop and deconvolved from the exponential decay of the loop and the Edirol's incidial response.*

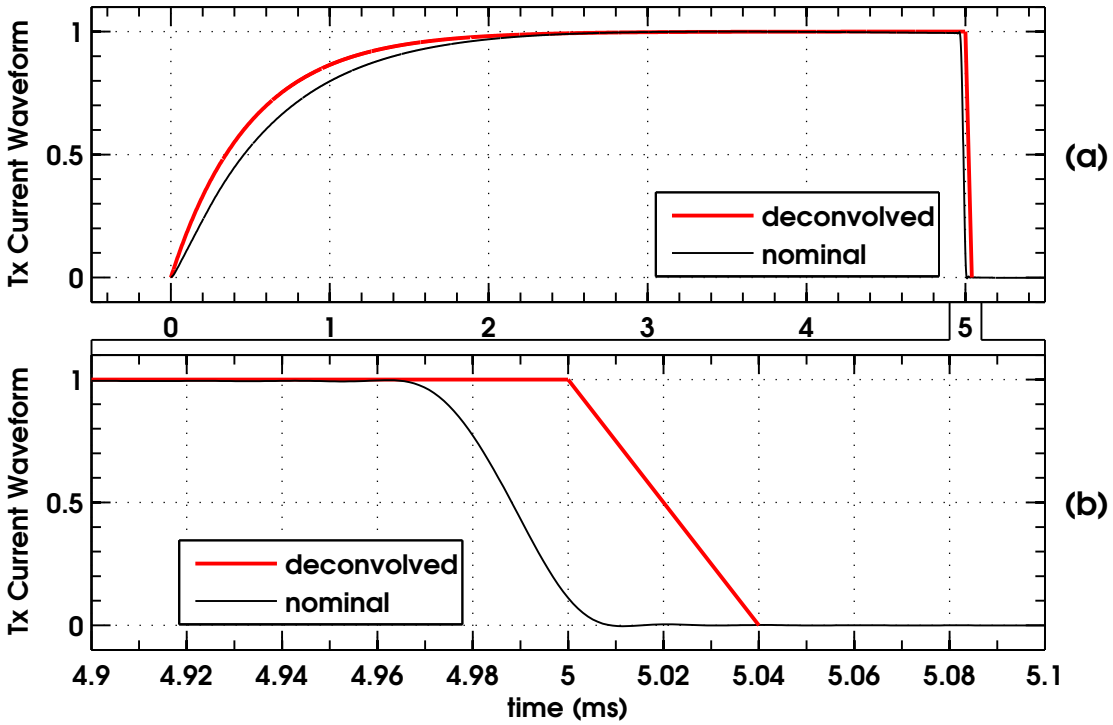

Figure 6.6: *(a) The positive half-cycle of the deconvolved HoistEM waveform shown with the nominal waveform used in Section 5.5. (b) The shut-off of both waveforms, shown at an expanded time scale.*

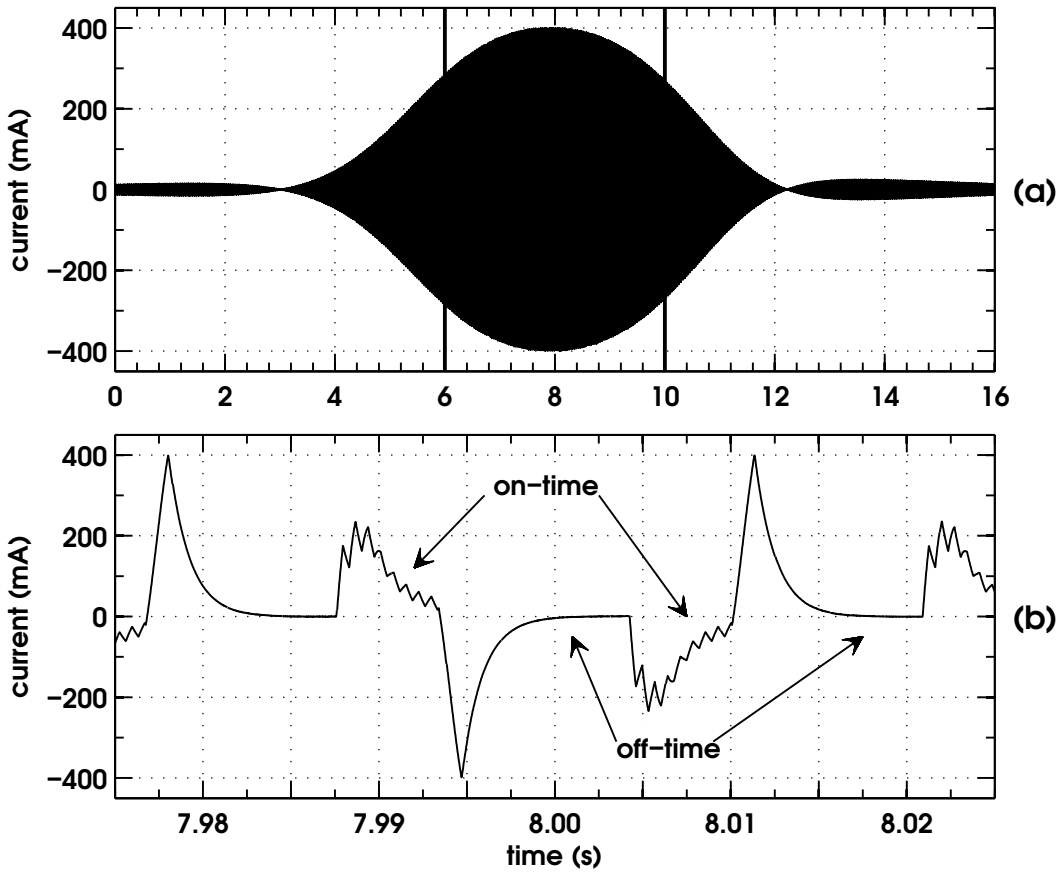

Figure 6.7: *(a) Envelope of current induced in a ground loop during a VTEM flyover in Sudbury, Ontario, Canada in October 2005. (b) 50 ms window centered at 8 s, showing 2 complete half-cycles.*

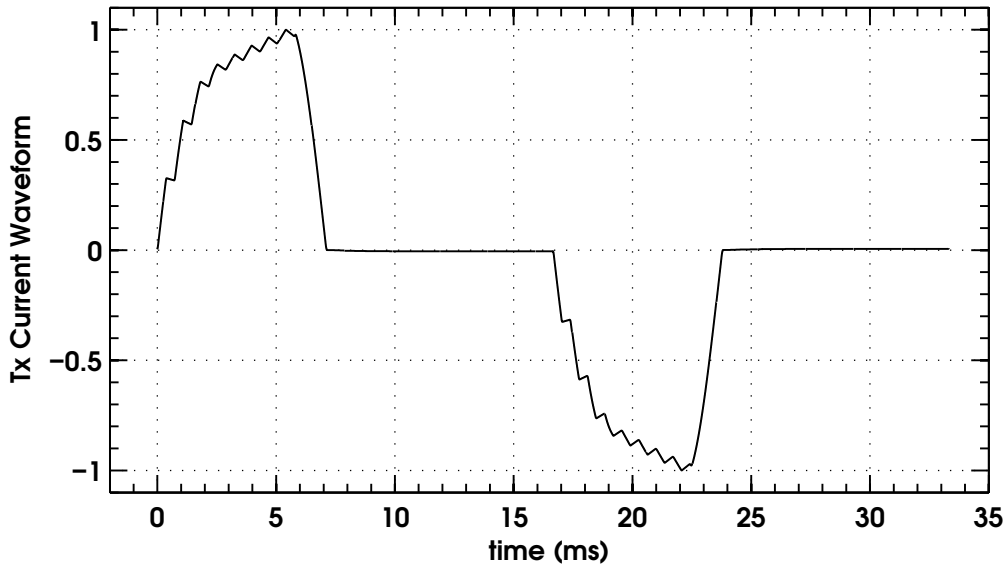

Figure 6.8: *Deconvolved waveform of the transmitter current of the VTEM system used in Sudbury in October 2005.*

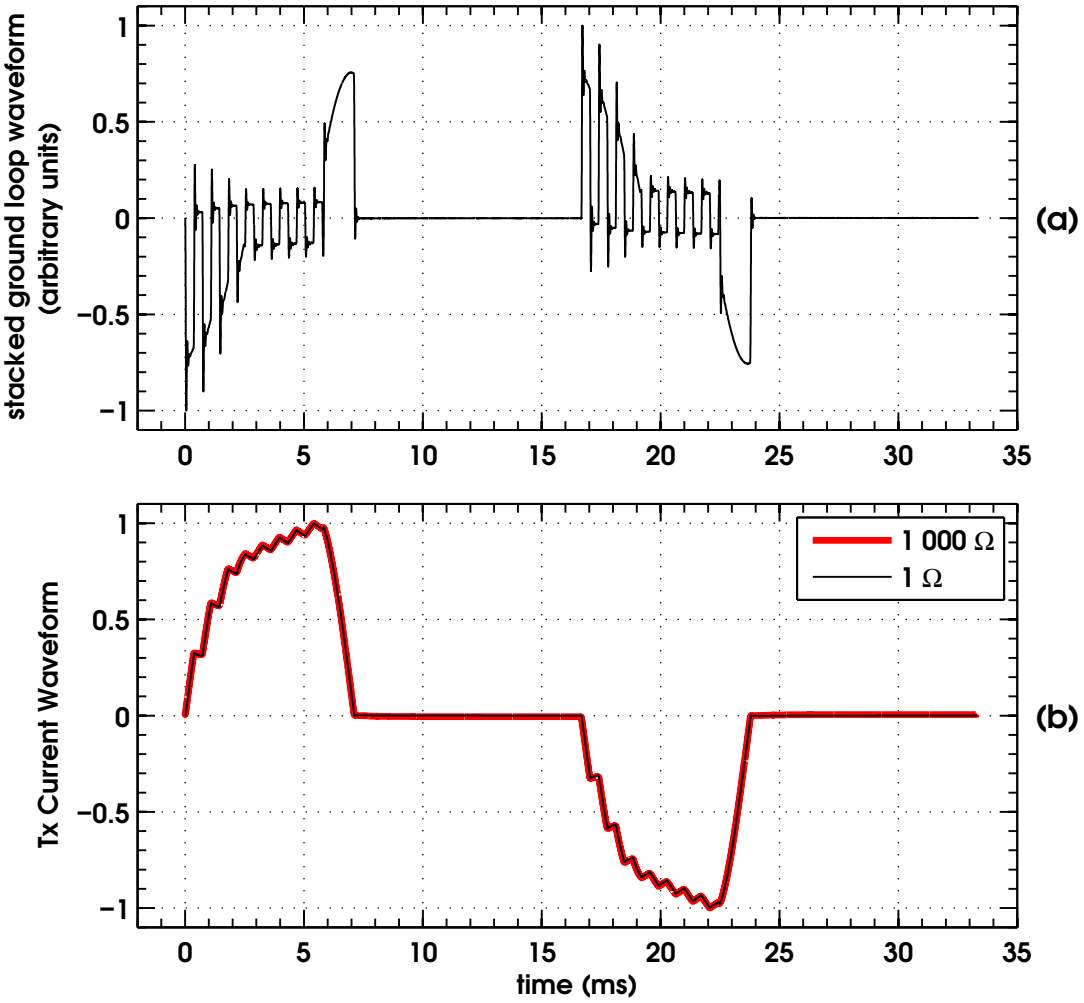

Figure 6.9: *(a) Stacked ground loop current measured by the Edirol UA-5 with a 1 000 Ω resistor closing the ground loop. (b) Deconvolved VTEM waveform of the transmitter current recovered from the high resistance loop (black) and the low resistance loop (red).*

The induced current nulls at 3 and 12 s are clear indications that the ground underneath the calibration loop is very resistive. The smooth, well-rounded envelope of the induced current shows that the VTEM transmitter loop was parallel to the ground loop for the flyover. Other than that, however, it is difficult to garner much information from the ground loop current, and we must enlarge the horizontal scale. Panel (b) shows the measured induced current for a 50 ms window centered on 8 s. Here, we can plainly see the curiously shaped on-time and off-time of both half-cycles of the transmitter waveform, as well as the exponential decay of the current in the off-times. After stacking the waveform from 6 s to 10 s (shown with vertical lines in Figure 6.7a), the deconvolved waveform of the VTEM transmitter current is displayed in Figure 6.8.

Changed Resistance in the Ground Loop

During another VTEM flyover, I changed the resistance closing the ground loop from 1 Ω to 1 000 Ω. This effectively changed the time constant τ from 1.47 ms to ∼1.47 μs, due to the much higher resistance in the ground loop. Applying the same methodology of stacking and deconvolving, the stacked waveform is displayed in Figure 6.9a, while the deconvolved waveform is shown in panel (b) of the figure. The waveform from Figure 6.8 is included (in red) for comparison. Note that they are, as expected, virtually identical.

6.4.2 SkyTEM

For the SkyTEM calibration tests done outside Berri, South Australia (cf. Section 5.7), I closed the ground loop with a 1 Ω resistor (line 1) and also with a 1 000 Ω resistor (line 2). For the first line flown, the decay constant was 0.86 ms, while for the second, the decay constant was ∼0.86 μs.

Using the methods of the last section, I stacked and deconvolved the measured ground current for the high and low moment transmitter current for both the low

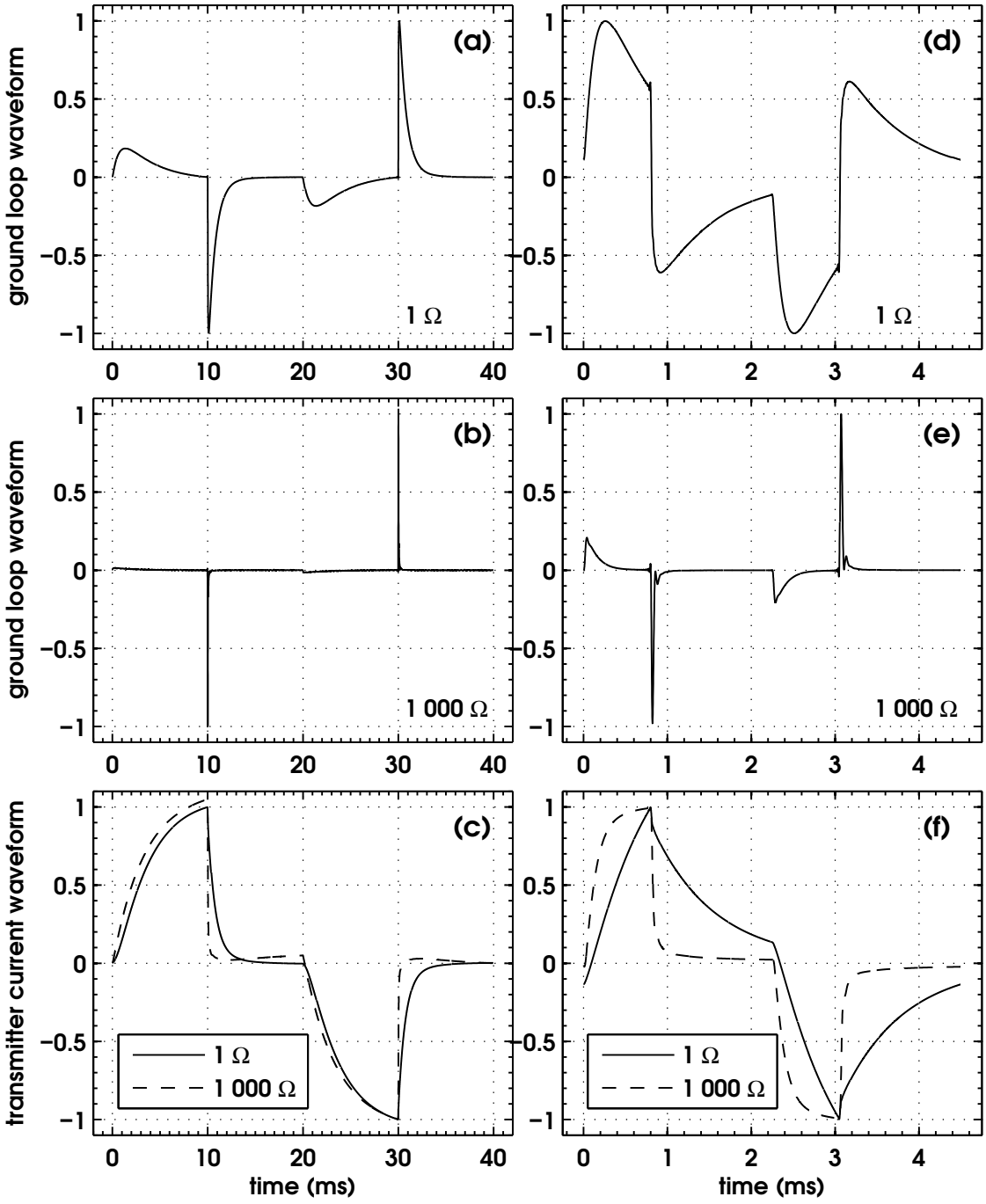

Figure 6.10: *SkyTEM system (a) stacked high moment ground loop waveform measured by the Edirol UA-5 with a 1 Ω resistor closing the ground loop. (b) Stacked high moment ground loop waveform with a 1 000 Ω resistor closing the ground loop. (c) Deconvolved high moment waveform of the transmitter current recovered from the low resistance loop (solid) and the high resistance loop (dashed). (d) Stacked low moment ground loop waveform (1 Ω). (e) Stacked low moment waveform (1 000 Ω). (f) Deconvolved low moment waveform of the transmitter current recovered from the low resistance loop (solid) and the high resistance loop (dashed).*

and the high resistance loops. The results are shown in Figure 6.10. Panel (a) shows the stacked high moment waveform recorded by the UA-5 with the low (1 Ω) resistor closing the ground loop, while the stacked high moment ground loop waveform as recorded with the large resistor is seen in panel (b). The deconvolved transmitter waveforms for both recordings are shown in panel (c). Clearly, there is a difference between the two resulting transmitter waveforms for the high moment cycle, but the differences are nothing compared to panels (d), (e) and (f) for the low moment cycles. The deconvolved transmitter waveforms for the low resistance loop (solid black lines in panels (c) and (f)) show much slower decays in the off-time than the high resistance counterparts. Due to the long decay time the ground loop current shown in panel (d), the Fourier transform method of deconvolution fails for this case. The induced current never quite decays to zero current, and it is probably better in a situation like this to use a recursion method of deconvolution (e.g. Gubbins, 2004). Of course, these panels also show that the calibration is best done on resistive ground.

6.4.3 TEMPEST

The next system presented is the fixed-wing towed-bird TEMPEST system operated by Fugro Airborne Surveys (Fugro Airborne Surveys, 2005*d*). The TEMPEST waveform is a square-wave operating with a 50% duty cycle at 25 Hz. In this experiment, conducted near Mandurah, Western Australia in 2003, the TEMPEST system was flown over a ground loop placed on fairly resistive terrain. The ground loop was closed with each of a 1 Ω and a 12 000 Ω resistor. The stacked measured ground loop signals are shown in panels (a) and (b) of Figure 6.11, while the deconvolved transmitter current waveform for each trial is shown in panel (c). This panel clearly shows that the actual TEMPEST waveform indeed approximates a square-wave oscillating at 25 Hz, with a 50% duty cycle. Data are delivered to the client as a 100% duty cycle square wave response after processing.

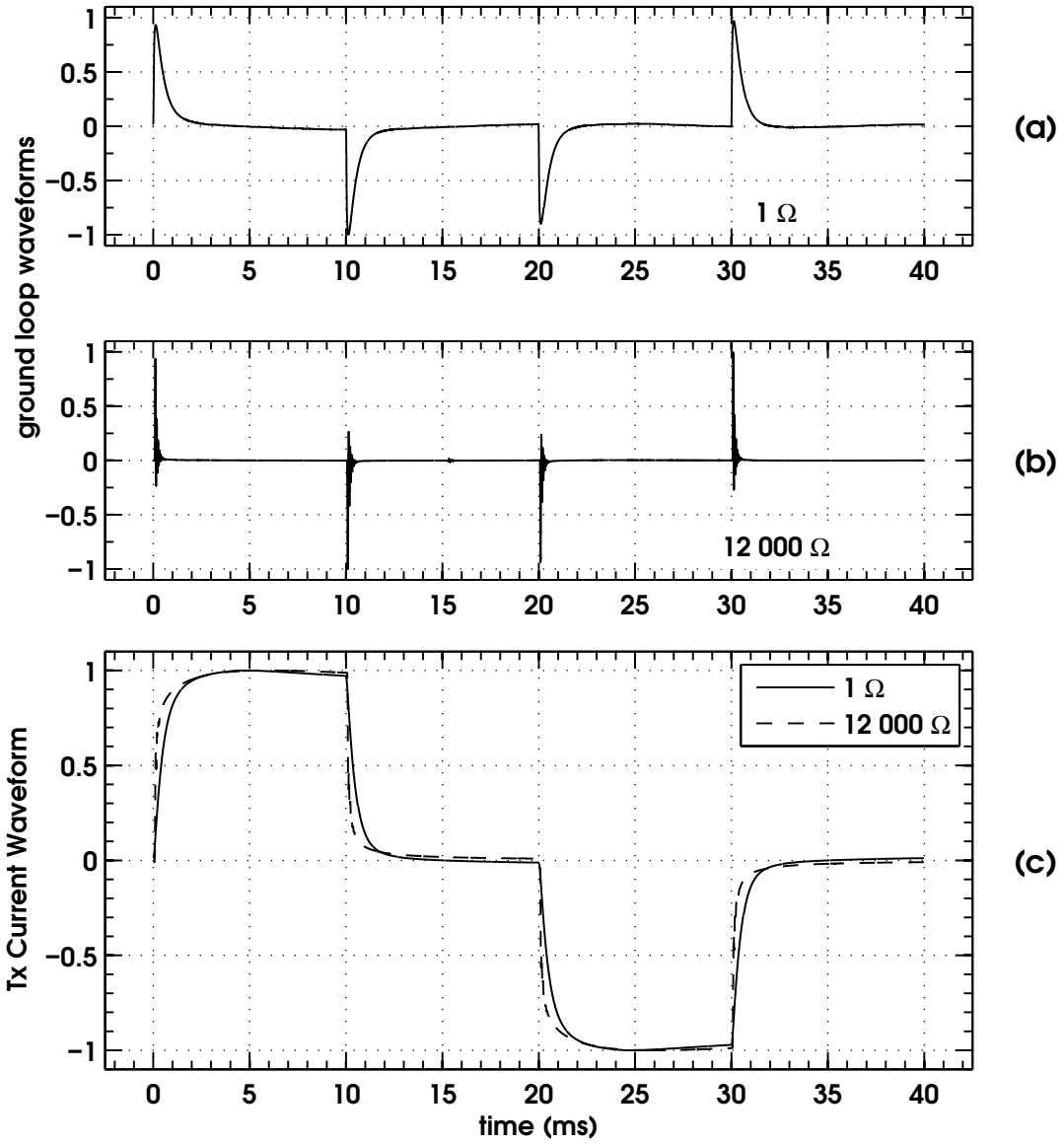

Figure 6.11: *TEMPEST system (a) stacked ground loop waveform measured by the Edirol UA-5 with a 1 Ω resistor closing the ground loop. (b) Stacked ground loop waveform with a 12 000 Ω resistor closing the ground loop. (c) Deconvolved TEMPEST waveform of the transmitter current recovered from the low resistance loop (solid) and the high resistance loop (dashed).*

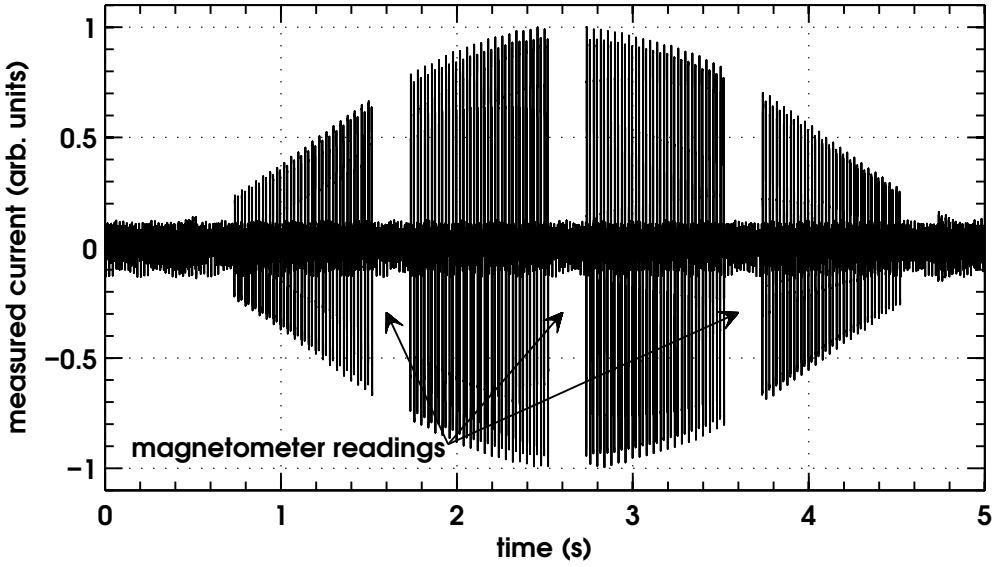

Figure 6.12: *Current measured as the GEOTEM system was flown over the ground loop in Western Australia, 2003. 'Dead' times, where the GEOTEM transmitter was shut off and magnetometer readings were taken, are marked with arrows.*

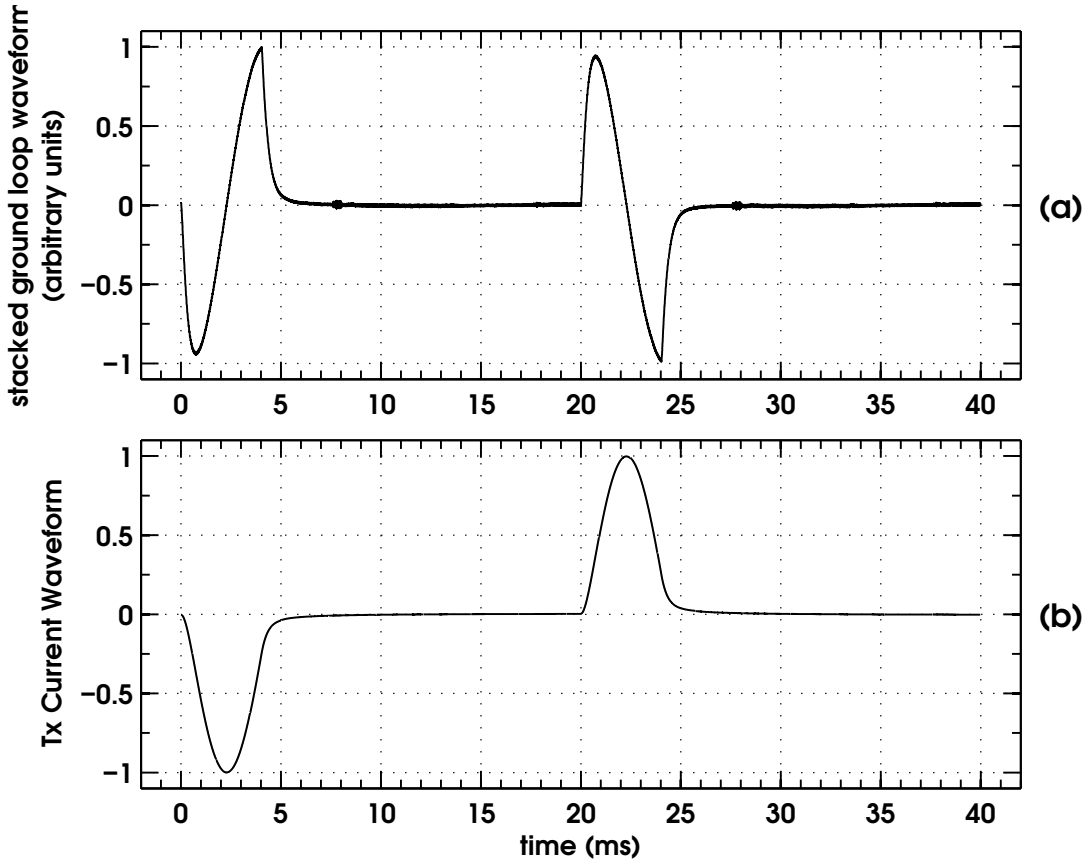

Figure 6.13: *(a) Stacked ground loop waveform of the GEOTEM system (loop closed with 1 Ω resistor). (b) GEOTEM transmitter current waveform deconvolved from the ground signal.*

6.4.4 GEOTEM

Three months before the TEMPEST tests, a GEOTEM (Fugro Airborne Surveys, 2005*a*) system was flown over a ground loop in the same area: it was closed with a 1 Ω resistor. The measured induced current envelope is interesting because, during the flyover, the transmitter cycle was interrupted every second for 20 ms in order measure magnetic field. The measured ground loop signal, in arbitrary units, is shown in Figure 6.12. The stacked ground loop waveform and the deconvolved transmitter waveform are shown in panels (a) and (b), respectively, of Figure 6.13. Panel (b) shows that the transmitter current waveform consists of half sine waves of 5 ms in duration, repeating at a frequency of 25 Hz.

6.5 Antenna Effects in the Wire Loop

In Section 5.5.4, I showed the interesting effect that increasing the resistance in the ground loop has on the airborne receiver response. As shown in Figure 5.24, repeated here in Figure 6.14, showing more delay channels and an exaggerated scale, the airborne receiver response exhibited a quickly decaying oscillation. I believe that with a large resistance, the ground loop acted less like a closed loop and more like a very lossy electric field antenna. When we look at the current measured in the high resistance ground loop during flyover, we can see a decaying, damped oscillation.

6.5.1 HoistEM: South Australia

Figure 6.15 shows the current measured in the ground loop by the Edirol UA-5 during flyover 3 (cf. Figure 5.14, p. 188). The current induced in the high resistance ground loop during this flyover is evidently much lower than in lines 1 and 2 (0.5 mA compared to ∼350 mA). The signal is unfortunately clipped during the measurement, as is evidenced by the flattened envelope from 10 s to 15 s. If we look at the side

lobes in Figure 6.15 where the signal is not clipped, the peak currents of 0.25 mA are still a factor of 100 less than the side lobe currents in Figure 6.2.

Consistent with the stacking method described above, I stacked the 25 Hz signal of line 3 from 10 s to 15 s, marked by thick vertical lines in Figure 6.15. The resulting waveform is shown in panel (a) of Figure 6.16. Due to the high resistance in the ground loop, the induced current decays very quickly in this figure compared to Figure 6.4. Panel (b) shows a section of the first half-cycle at an exaggerated horizontal scale. This portion is during the shut-off of the transmitter current, but shows that the current in the ground loop oscillates and decays exponentially. Using the functional form of

$$F(t) = e^{-\frac{t}{\tau}} \sin(\omega t + \phi_f), \tag{6.8}$$

where τ is a time constant, ω is an angular frequency and ϕ_f is a phase shift, I found that the decay constant was $\tau = 58.5$ μs, and the frequency of the oscillation was $\omega = 116\,516$ rad/s, making a period of oscillation of 53.9 μs. The exponential decay

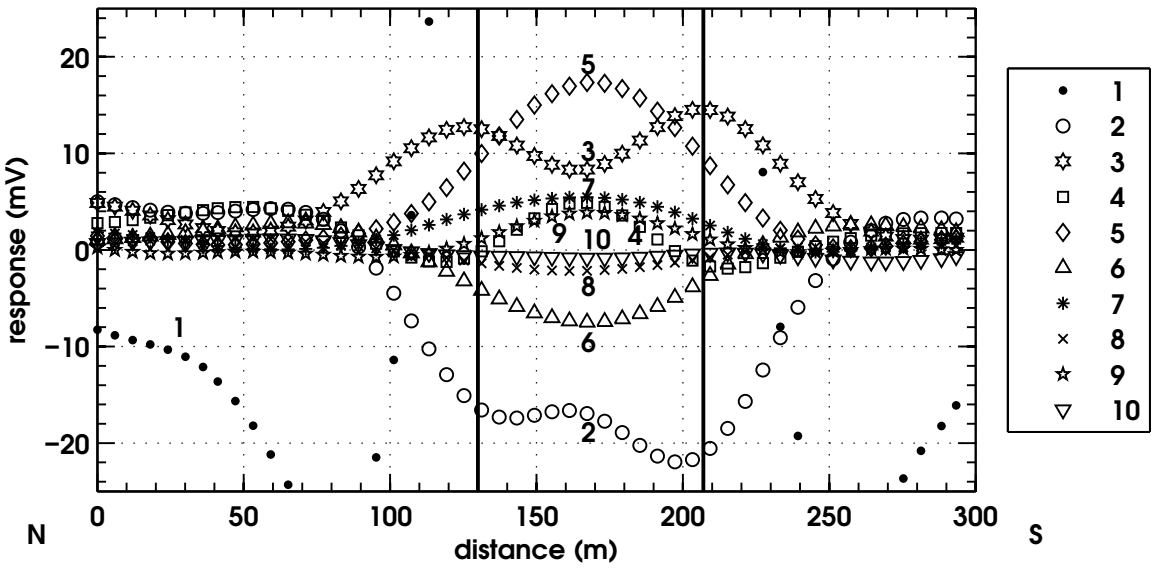

Figure 6.14: *Figure 5.24, the HoistEM response during line 3 flyover (loop closed with a 12 000 Ω resistor), repeated here with more delay channels (1–10) and an exaggerated vertical scale. Vertical lines at 130 m and 207 m show the limits of a spatial average applied to the data to model an oscillatory decay.*

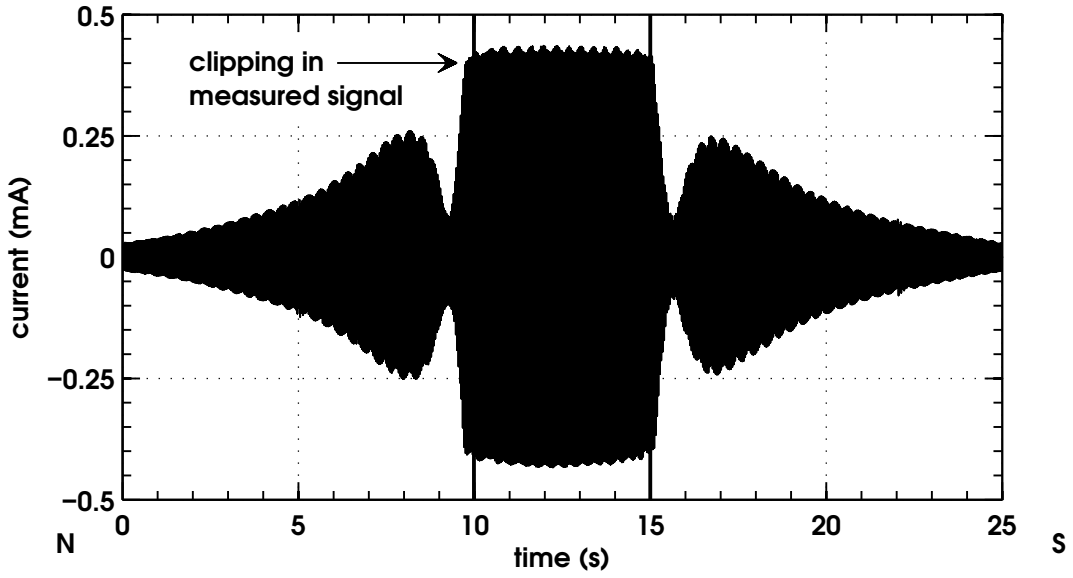

Figure 6.15: *Current measured in the ground loop during line 3 of the HoistEM calibration experiments. Resistance closing the ground loop was 12 000 Ω. The measured signal was clipped between 10–15 s and most probably limited by the slew rate of the Edirol UA-5.*

curves are shown as dashed lines in panel (b) of Figure 6.16, while the actual fitted curve is shown as solid dots. An almost perfect fit was observed after 5.05 ms.

An LRC Circuit

Equation (6.8) represents an exponentially decaying curve of characteristic time τ and oscillation frequency ω. When analysed with reference to a series circuit containing an inductor L, a resistor R and a capacitor C, equation (6.8) is a solution to the homogeneous differential equation that describes the current flowing in the series circuit in response to a motivating voltage:

$$0 = L\frac{d^2}{dt^2}i(t) + R\frac{d}{dt}i(t) + \frac{1}{C}i(t).$$

This relation is well known. Calvert and McCausland (1978), for example, shows that the characteristic decay τ and the angular frequency ω can be expressed in

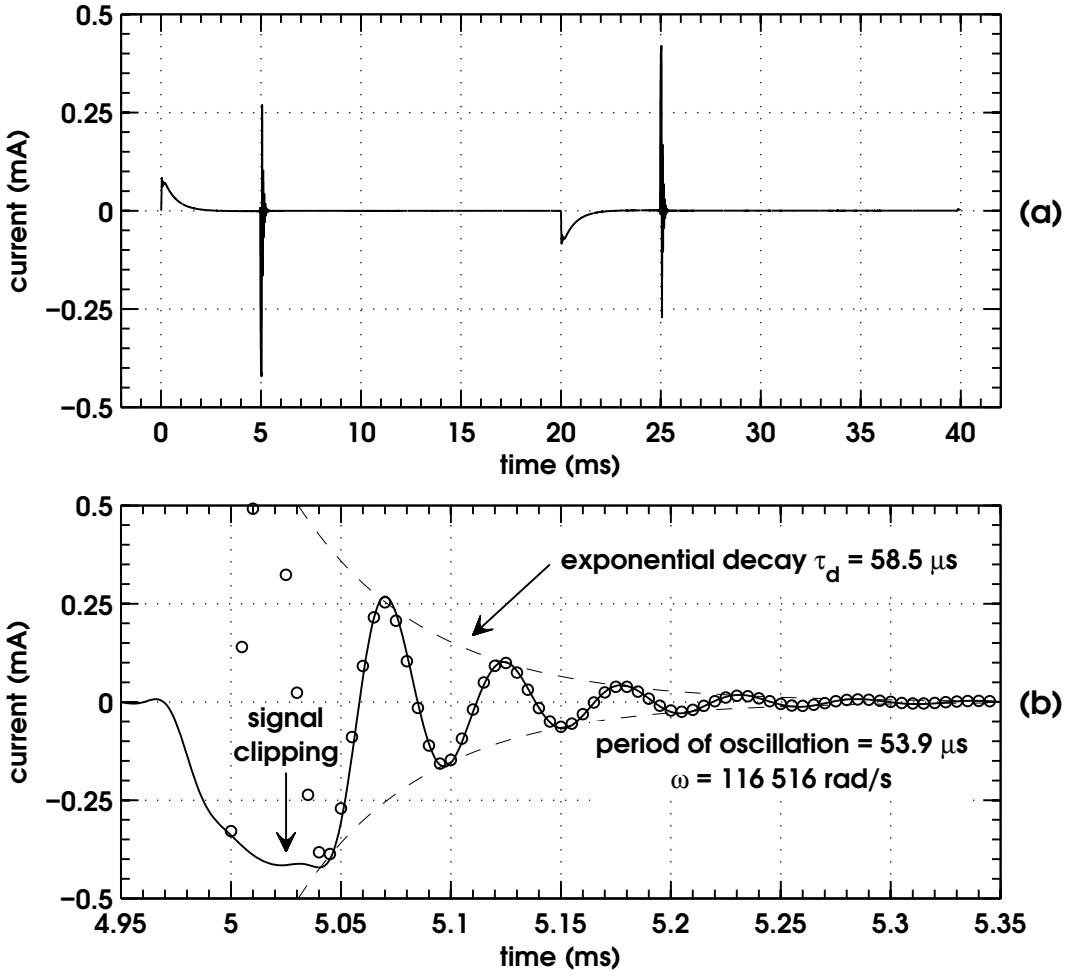

Figure 6.16: *(a) Stacked complete cycle of the measured ground loop current during line 3 of the HoistEM calibration experiment. Loop is closed with a 12 000 Ω resistor. (b) Zoom on the shut-off of the first half cycle showing clipping in the measured waveform as well as a characteristic decaying ringing in the observed ground loop current (solid line). Exponential decay curves of $\tau = 53.9$ μs are marked with dashed lines, while a fitted damped oscillation is marked with open circles.*

terms of L, R and C in the following way:

$$\begin{cases} \tau = \dfrac{2L}{R}, \\ \omega = \sqrt{\dfrac{1}{LC} - \dfrac{1}{\tau^2}}. \end{cases} \tag{6.9}$$

In the case of line 3 of the HoistEM test, using $L = 7.91$ mH and $R = 12\,000\ \Omega$ I predict that the simple closed loop decay constant τ is 1.32 μs: this is contrary to the evidence of Figure 6.16b. Instead, assuming that the self-inductance L of the

loop has not changed, we can allow the effective resistance R to be determined by the newly measured τ and L. In my opinion, it is reasonable to assume that the magnetic inductance does not change while the resistance does, since the mutual inductance of the parallel wires and turns of the loop does not change for a comparatively low frequency oscillation of only 116 516 rad/s (∼18 500 Hz). Changes in mutual inductance due to skin depth do not become meaningful until much higher frequencies are reached (Jackson, 1999). It is reasonable to assume that the wires in the loop are acting like transmission lines, which are fully described in many texts (Ramo et al., 1984), and possess distributed resistance, inductance, capacitance and shunt resistance. These distributed values can be replaced by a lumped inductance, resistance and capacitance in an LRC circuit; of which the latter two are solved for by assuming that we know the inductance. Following this assumption, the effective R is calculated to be 271 Ω and, using the lower expression in equation (6.9), $C = 9.11$ nF. These numbers are the generalised effective values of a resistance and capacitance representing the interaction of the wire loop with free space, itself and, possibly, the ground beneath. The capacitance is reasonably a combination of a capacitive coupling of the loop to the ground and the distributed self-capacitance of the wire loop (Massarani and Kazimierczuk, 1997). The resistance must represent the effective resistance of the loop as an electric field antenna that accounts for displacement currents that exist in the loop circuit. It is very interesting to note that the effective resistance is of the same order of magnitude as the impedance of free space, which is 377 Ω (Smith, 1993).

The oscillations of parallel wires in a circuit have also been seen by Mutoh et al. (1997) when they analysed the noise patterns generated in parallel lengths of housing wire after the sudden disconnection of a DC current flowing in the lengths. The application sought there is to use housing wire as the transmission cable for Internet broadband (See et al., 2005). It is not my intention to explain the antenna effect of a high resistance ground loop, only to attempt to numerically model the physical

phenomena associated with it. Evidently, very little induced ground loop current went through the 12 000 Ω resistor closing it during the flyover. Yet, the measured response in the first delay channel of the HoistEM receiver was greater for this line than for lines 1 and 2, even though the bird altitude was about 9 m greater for line 3.

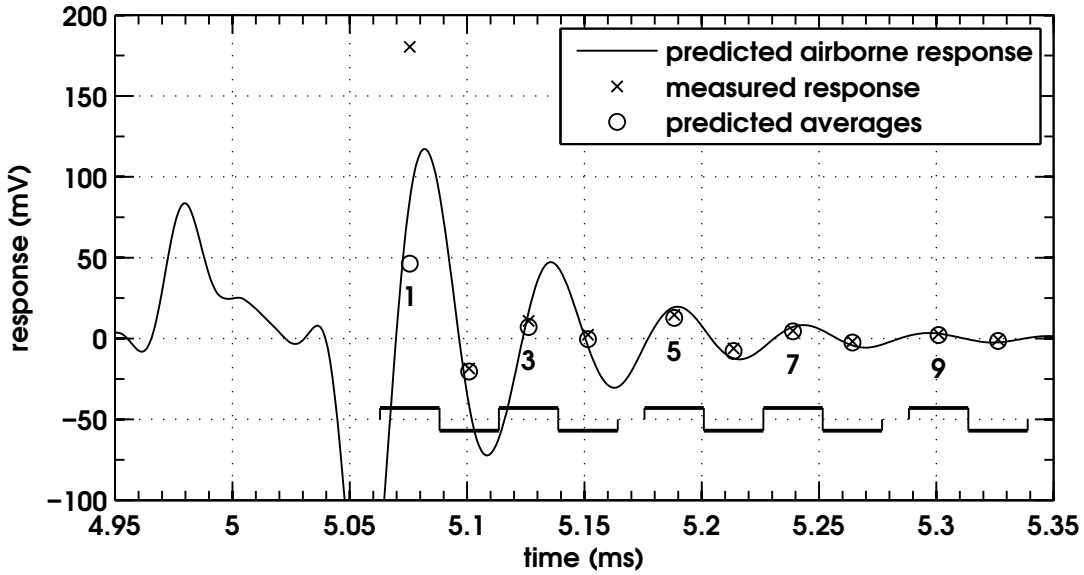

Figure 6.17: *Predicted HoistEM responses for channels 1–10 based on the numerical time derivative of the measured ground current (solid) averaged over the window widths given in Table 5.4. Crosses mark the spatially averaged airborne receiver response, while open circles are the predicted responses. Channel timing windows are marked at the bottom of the figure.*

In order to analyse the airborne receiver response to the ground loop, I took a spatial average for each channel of the airborne response from 130 m to 207 m (marked with vertical lines in Figure 5.24). In Chapter 5, I proved that the airborne receiver response at any time is proportional to the time derivative of the ground current (equation (5.3), page 163). Taking the time derivative of the stacked ground loop current in Figure 6.15 produces a waveform that is proportional to the receiver signal. Using the window widths of the HoistEM airborne receiver for each channel (given in Table 5.4), I calculated windowed averages of the numerical time derivative of the ground loop current and scaled the amplitude of the resulting series according

to the following relation:

$$A = \frac{\sum_{i=2}^{10} F_i R_i}{\sum_{i=2}^{10} F_i F_i},$$

where F_i is the numerical windowed average of the derivative of the ground loop signal for each delay channel, R_i is the airborne response and i goes from 2 to 10. The amplitude A is then applied to all channels. The numerical derivative of the ground current multiplied by A is plotted in Figure 6.17. Also plotted is the averaged airborne receiver response for the first 10 channels as well as the windowed averages calculated numerically from the ground data. The agreement between the measurements and the predictions for channels 2–10 is excellent. Channel 1 is not predicted as well, but this may be due to the clipping and slew rate problems mentioned earlier in Figure 6.15. Clearly, the airborne response for channel 1 is much greater than was modelled with a simple LRC-type decay.

6.5.2 VTEM: Botswana

Interestingly, the antenna effect was also seen for several lines of the VTEM test conducted in Botswana (cf. Section 5.6.4), even when the ground loop was left open circuit. In these cases, the current completing the ground loop circuit can only have been a displacement current. The decaying oscillatory response for line 97 was shown in Figure 5.35, repeated here as Figure 6.18 with slight modifications.

Figure 6.18 shows the VTEM response for the first 10 channels of the airborne response, although only the first 5 are marked. The background earth response for each channel is marked in red. In order to model an LRC-type curve to the data, I stripped the background response from the loop response for each channel and computed a spatial average of 10 channels of the response from 140 m to 180 m.

Using equation (6.8) as the base function, the windowed average for each delay channel is the integral of $F(t)$ from t_o to t_f divided by $t_f - t_o$, where t_o and t_f are

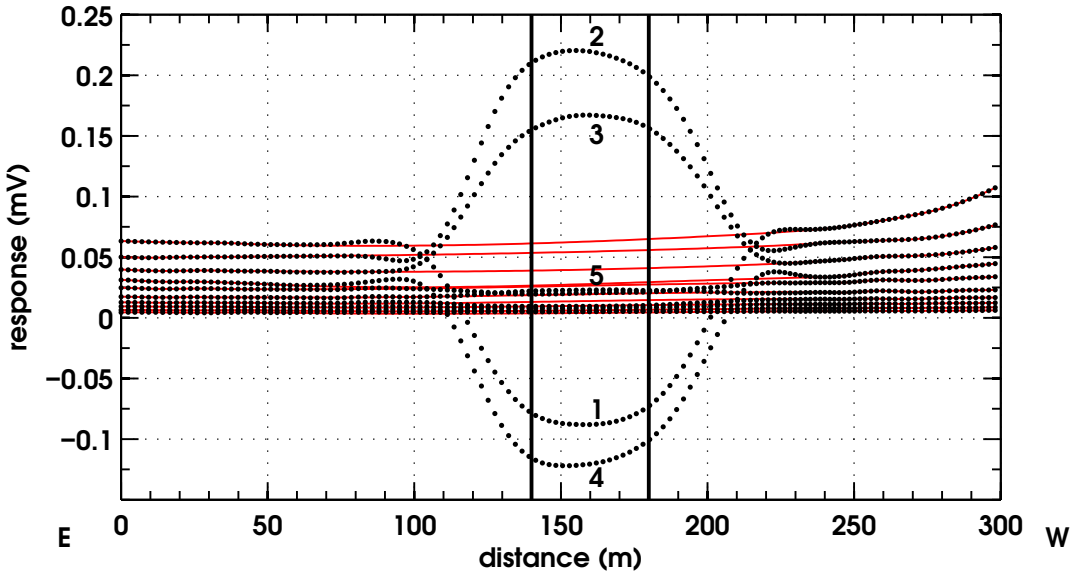

Figure 6.18: *Figure 5.35, the VTEM response (dots) over an open loop, repeated here with more delay channels (1–10). Red lines are a background fit that strips the earth response from the loop response. Black vertical lines show the limits of a spatial average used to model the loop response.*

the start and finish times for the time window. The windowed response for the i^{th} channel can be written as

$$W_i = \frac{A}{t_f - t_o} \int_{t_o}^{t_f} F(t)\, dt,$$

which becomes

$$W_i = \frac{A}{t_f - t_o} \frac{\tau}{1+\omega^2\tau^2} \Big(e^{-\frac{t_o}{\tau}} \big(\sin(\omega t_o + \phi_f) + \omega\tau \cos(\omega t_o + \phi_f) \big) - e^{-\frac{t_f}{\tau}} \big(\sin(\omega t_f + \phi_f) + \omega\tau \cos(\omega t_f + \phi_f) \big) \Big).$$

The decay of the airborne response can be modelled by a least squares fit between the measured and predicted data according to the following model: we strive to minimise the measure of misfit E between the measured response for each of the 10 delay channels R_i and the predicted response $W_i(A, \omega, \tau, \phi_f)$. The equation for the

error is

$$E = \sum_{i=1}^{10} \big(W_i(A, \omega, \tau, \phi_f) - R_i\big)^2,$$

where we minimise E by changing the fitting parameters A, ω, τ and ϕ_f. For line 97, the misfit between measured and predicted channels was minimised with $A = 0.284$, $\tau = 172$ μs, $\omega = 78\,191$ rad/s and $\phi_f = -1.44$ rad. Using the definitions in equation (6.9) for τ and ω and the self inductance of $L = 13.4$ mH, the effective resistance of the ground loop is $R = 161$ Ω and the capacitance is $C = 11.7$ nF. The spatially averaged airborne response, fitted windowed average and the decay curve are shown in Figure 6.19. For completeness, I repeated the fitting process for lines 98, 183 and 184; the fitted values of τ and ω, and the calculated values of R and C, are shown in Table 6.1, showing excellent agreement for each line and values of R and C similar in magnitude to the HoistEM example.

6.6 RESOLVE in Chowilla

In the last two chapters, I have concentrated exclusively on the ground loop calibration process with respect to time domain AEM systems. However, there is no reason that the process cannot be applied to a frequency domain system. In fact, the mathematical development has already been done in Chapters 2 and 5. For a system such as RESOLVE, we can calculate the mutual inductances between the transmitters and the loop by using the derived equation for mutual inductance between a dipole and a wire segment (Section 2.7.4). When the RESOLVE survey was conducted over the Chowilla Floodplain in South Australia, I had the opportunity to lay a ground loop out along the repeat calibration line. Unfortunately, the ground in the area was too conductive in order to do a full transmitter/loop/receiver calibration, but I was able to measure the current induced in the ground loop as the RESOLVE system was flown over it. Additionally, I used the second input channel of the Edirol to synchronise the device to a GPS clock, thus providing extremely

Table 6.1: *Fitted values τ and ω, and calculated values of R and C for Botswana VTEM lines 97, 98, 183 and 184.*

Line #	τ (μs)	ω ($\frac{\text{rad}}{\text{s}}$)	R (Ω)	C (nF)
97	172	78 245	161	11.7
98	170	78 201	163	11.7
183	176	78 685	157	11.6
184	167	78 376	165	11.7
average	171±3	78 377±200	162±3	11.7±0.1

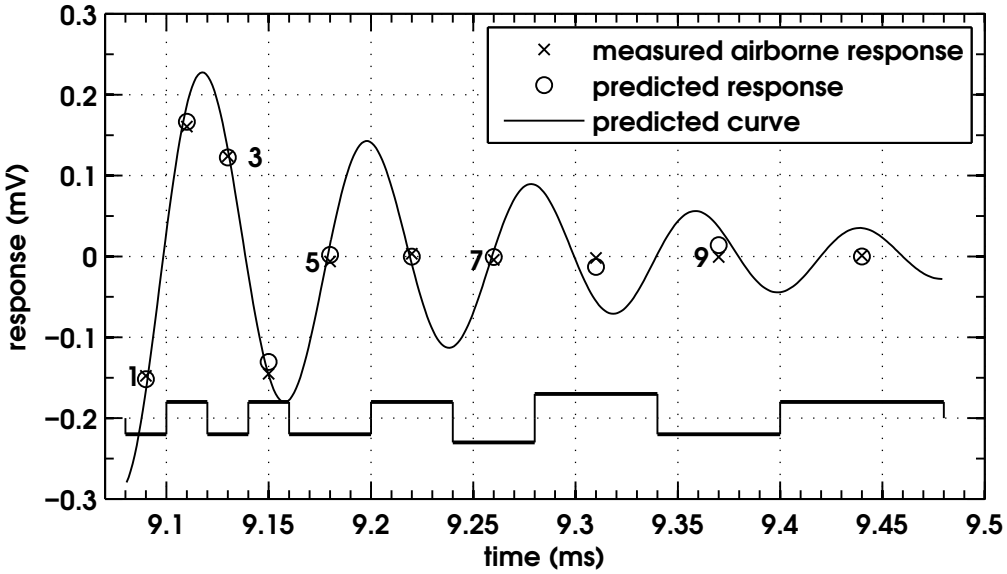

Figure 6.19: *Stripped and averaged VTEM response for line 97 with an open circuit ground loop (crosses). Fitted response with A=0.284, $\tau = 0.172$ ms, ω=78 191 rad/s and $\phi_f = -1.44$ rad (open circles). Solid line shows the airborne response curve that produces the windowed average. Averaging windows are also marked on the figure.*

accurate signal timing. The current in the ground loop for line 9003, as measured with the Edirol UA-5 recorder, is shown in Figure 6.20. Conductive ground effects are clearly shown in the lack of induced current nulls at the cross-over points at 4 s and 7 s.

As stated earlier, the RESOLVE system has 6 transmitters, each operating at different frequencies. The nominal operation frequencies are displayed in Table C.1 in Appendix C. By taking the Fourier transform of the measured ground signal, we can get an excellent measure of the strength of each RESOLVE transmitter. Furthermore, with such a long time series to analyse, we gain a very high resolution of the frequency components. The single-sided amplitude spectrum of the digital Fourier transform of the line 9003 time series is shown in Figure 6.21. The contribution of the first five frequencies are easily seen and are clearly marked in the figure. Because the sampling frequency of the Edirol UA-5 is limited to 96 kHz and the device is band-limited to 20–40 000 Hz, the contribution of the 140 000 Hz transmitter is not detected in this frequency spectrum.

Figures 6.20 and 6.21 are interesting because they show that the ground loop method provides an extremely easy way to measure the exact frequencies of a frequency domain AEM system. Synchronising the Edirol UA-5 with GPS clocks further improved the accuracy of the method. Furthermore, if the ground is resistive, the ground loop calibration for amplitude and phase change can be employed. During this experiment, I left the ground loop out overnight and asked the RESOLVE crew to fly the system over the ground loop at the end of the next day's flying. The frequency of the first 5 transmitters recorded for line 9003 and 9005 are shown in Table 6.2.

In addition to determining the frequency components of the ground signal, I divided the ground signal into sections of 9 600 samples each and calculated the sine and cosine contributions of each frequency in each section. By taking the arctangent of the ratio of the sine to the cosine contribution, the phase of each frequency was

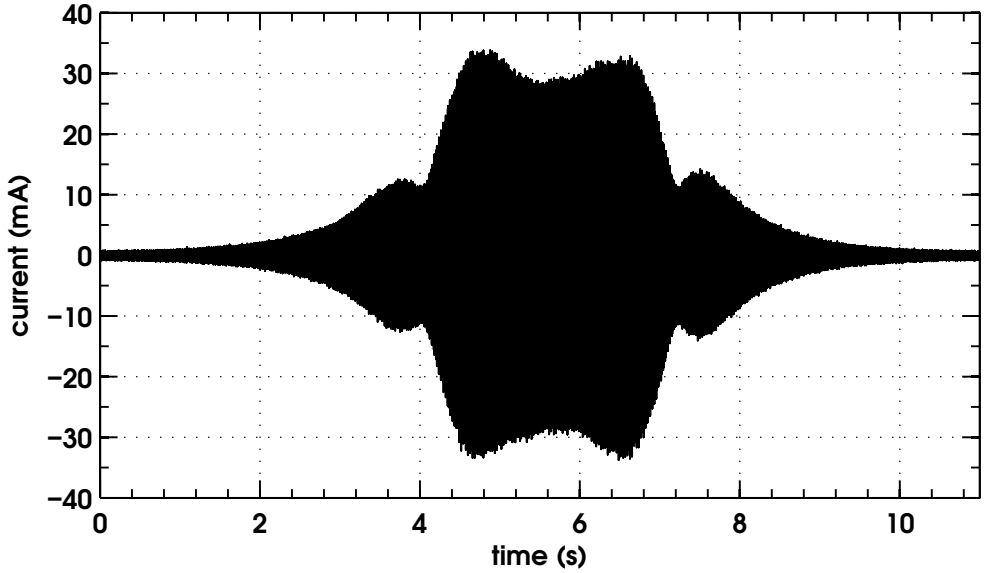

Figure 6.20: *Induced current measured in the ground loop during a calibration experiment for the RESOLVE frequency domain AEM system in Renmark, South Australia (line 9003).*

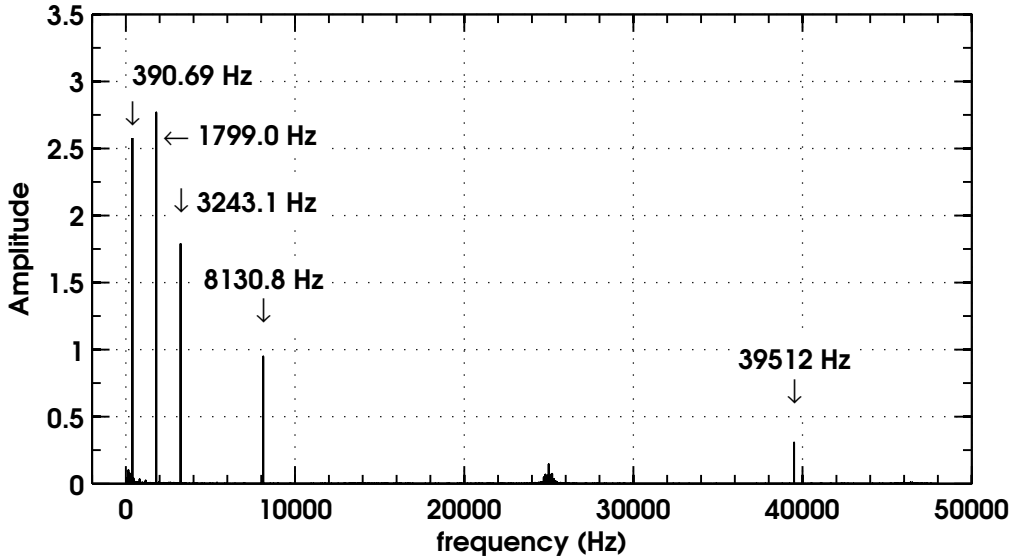

Figure 6.21: *Single-sided amplitude spectrum of the digital Fourier transform of the line 9003 time series (shown in Figure 6.20). The frequencies of the first five transmitters are marked on the figure above their respective signals.*

also determined. The phase of the ground loop current as a function of time for the 400 Hz HCP and 3 300 Hz VCA components are shown in Figure 6.22.

The choice of phase is an arbitrary one. For the 400 Hz component, I chose zero phase when the vertical dipole transmitter was to the left of the ground loop. As the vertical dipole was flown over the centre of the loop, the current induced in the ground loop changed direction due to the change in mutual inductance coupling. This is seen as a phase change of π radians at 4 s. As the dipole left the loop, the induced current once again changed direction. This is shown at 7 s, where the phase goes back to 0 radians.

The horizontal dipole shows a different story, and the coupling between it and the ground loop is a little more complicated. On the left-hand side, the coupling is chosen to be zero, while on the right-hand side, the coupling must be opposite. We see this in Figure 6.22 with the dashed line, where on the left-hand side I have chosen the phase to be zero. On the right-hand side, the phase is π. The mutual inductance between the horizontal dipole and the ground loop is at a maximum as the dipole crosses over the edge of the loop. These maxima occur at 4 s and 7 s in the figure and are opposite in sign. In the middle of the loop the mutual inductance changes sign. At some point, there is zero coupling between the ground loop and the dipole, and the phase is undefined.

To make these phenomena more clear, Figure 6.23 shows $M_{\perp}$ the calculated mutual inductance between a vertical dipole at an altitude of 20 m and a 100×100 m ground loop. On the left-hand side, $M_{\perp}$ starts as a negative value and changes sign as it crosses the left edge of the ground loop. It reaches a positive maximum over the centre of the ground loop and then changes sign again as it leaves the loop. Thus, the phase in the induced current must change by π radians at -50 m and again at 50 m. Also shown in Figure 6.23 is $M_{\vdash}$, the mutual inductance between a horizontal dipole at 20 m and the ground loop. Like $M_{\perp}$, $M_{\vdash}$ starts negative at -200 m, but it reaches a negative maximum by -50 m and changes sign at 0 m. At this point,

Table 6.2: *Nominal and measured frequencies of the RESOLVE AEM system for line 9003 (on 6 July) and line 9005 (7 July 2005) near Renmark, South Australia. GPS timing lock was obtained by monitoring the pulse-per-second of a GPS receiver on the spare channel.*

Nominal Frequency (Hz)	Line 9003 6 July 2005 (Hz)	Line 9005 7 July 2005 (Hz)
400	390.7	390.9
1 800	1 799.0	1 800.2
3 300	3 243.1	3 244.5
8 200	8 130.8	8 136.6
40 000	39 512	39 527

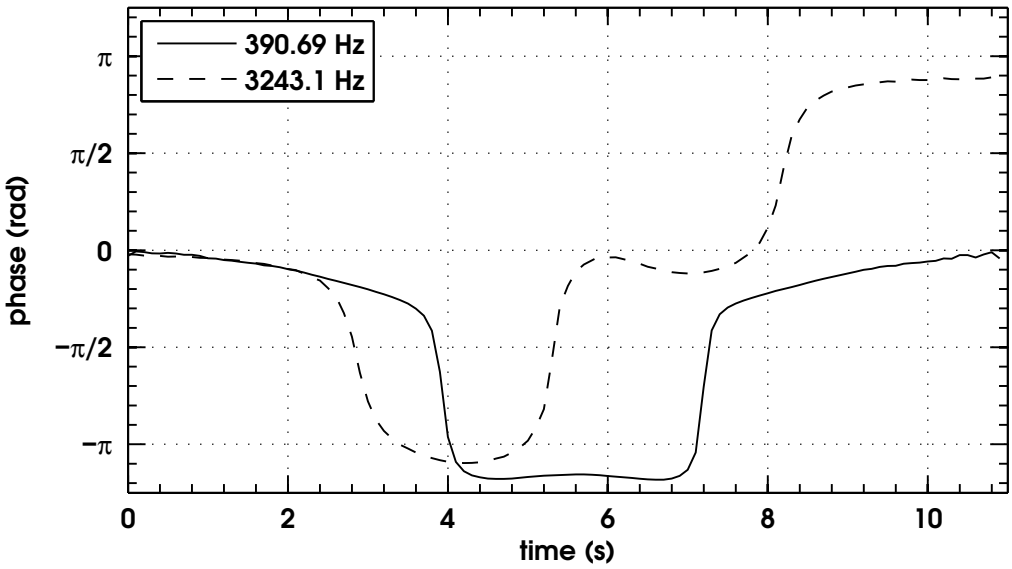

Figure 6.22: *Phase of the ground loop current for the 400 Hz HCP and 3 300 Hz VCA current components. Phase of 0 rad is an arbitrary choice.*

the current induced in the ground loop by the horizontal dipole becomes zero due to the minimum in mutual inductance coupling. Phase of the ground current at this point is meaningless. After crossing the minimum at 0 m, $M_{\vdash}$ increases to a positive maximum at 50 m and stays positive for the rest of the traverse. Thus, at 200 m the phase of the current induced in the ground loop must be π radians different from the induced current when the transmitter was at -200 m. These changes are seen in Figure 6.22, but are complicated by the effects of the conductive ground under the loop.

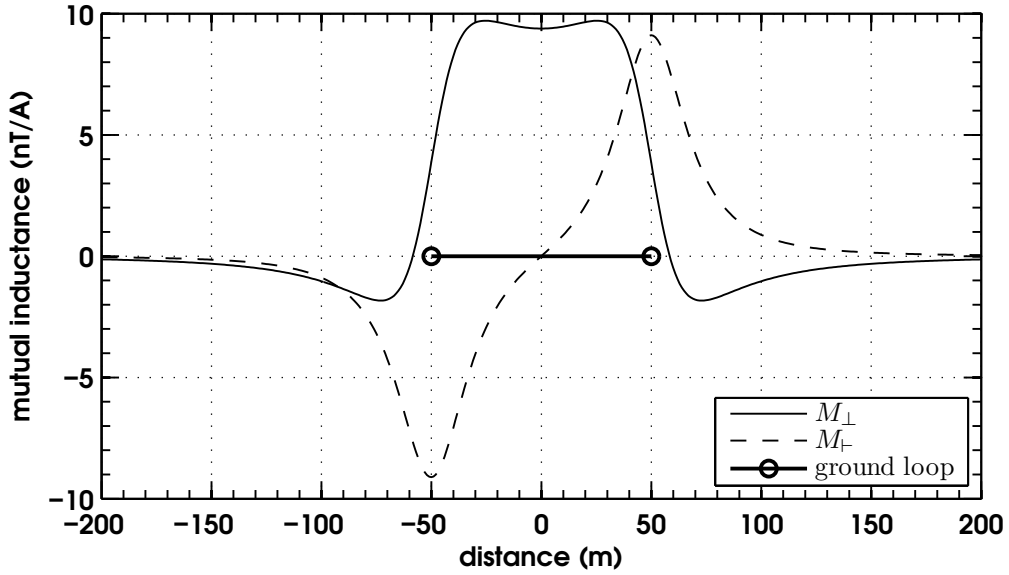

Figure 6.23: *Calculated mutual inductance $M_{\perp}$ between a vertical dipole and a 100×100 m ground loop (solid), and a horizontal transmitter and the ground loop ($M_{\vdash}$, dashed). Both dipoles are at an altitude 20 m above the ground loop.*

6.7 Summary and Conclusion

Chapter 5 showed that the ground loop method offers a practical and effective way to calibrate time domain AEM systems by comparing measured signals to predicted ones. There, I also showed that if we are capable of measuring the current induced in the ground loop during flyover, we can effectively estimate the geometry of the AEM system. In this chapter, I showed that the current induced in the ground loop

can offer us much more than a geometry check. It can show us interesting features like the transmitter shut-off to allow for magnetometer readings (GEOTEM), and also the switching between high and low moment transmitter waveforms (SkyTEM). Most importantly, though, the measured ground loop current also offers us a method of determining the shape or waveform of the current in the airborne transmitter.

By using the theory already developed in Chapter 5, I showed that the current induced in the ground loop is composed of the incidial ground loop response convolved with the time derivative of the transmitter current waveform. In this chapter, I showed that through the use of the Fourier transform, we can obtain the transmitter current waveform from the measured signal. In essence, we can deconvolve the transmitter current waveform from the ground signal. This was shown with an example from the HoistEM calibration experiment, where the deconvolved waveform very closely matches the one given in the literature.

I then showed the deconvolved waveforms of the transmitters from VTEM, SkyTEM, TEMPEST and GEOTEM. The VTEM waveform is undoubtedly the most curious of them all; and showed an interesting sawtooth pattern. It is important to note that the waveforms recovered are the transmitter waveforms for particular to each system at a particular time, and that waveforms are often changed to match a particular application.

In the VTEM and SkyTEM examples, I showed how increasing the ground loop resistance reduces the time constant of the loop and, in my opinion, offers an easier waveform to deconvolve. Deconvolution of a waveform is a tricky business, and noise plays an evil role. For the VTEM system, changing the loop resistance changed the resulting predicted waveform very little: this is due to the highly resistive ground beneath the loop. SkyTEM, on the other hand, showed how conductive ground can lead to problems, with the high and low resistance deconvolved waveforms looking quite different from one another.

Changing the resistor closing the ground loop can create another problem. Once the resistor closing the ground loop exceeds a limit, capacitive coupling and displacement currents become dominant considerations. The ground then loop acts like an antenna, and the induced current oscillates in addition to decaying. When the closing resistance was increased to $\sim$12 000 Ω in the HoistEM tests, the oscillating ground loop current was recorded by the Edirol showed an oscillating envelope decay with time constant of 58.5 μs and period of oscillation of 53.9 μs. This is consistent with an effective resistance $R = 271\ \Omega$ and an effective capacitance $C = 9.11$ nF acting in series with an inductor $L = 7.91$ mH. Using the HoistEM receiver time windows, the numerical average of the time derivative of the ground loop current closely matched the measured response in most of the early time channels. The HoistEM result was corroborated by the ringing seen in the response in the VTEM Botswana example when the ground loop was left open circuit. The results are perhaps not so surprising when we remember that AEM systems are sensitive to cultural devices such as wire fences, but to fit the decaying response with an LRC circuit and allow for the presence of a displacement current is a fascinating departure from the usual quasi-static approximation.

Finally, this chapter was instrumental in showing that the ground loop calibration method can be applied to frequency domain systems as well as time domain. In the specific example shown, the ground was much too conductive to offer an opportunity for complete calibration; but it showed that this method is an effective way to measure the exact frequency of the transmitters. In this test, I showed that the transmitter frequencies are quite stable but do suffer some day-to-day drift. The measured ground loop current not only shows the frequency content, but also can exhibit the changes in phase in the current induced by each frequency which reflect the effects of secondary currents induced in the earth.

The transmitter waveforms of Airborne EM systems change according to the application of the instrument, the needs of the client and research. The VTEM

waveform, for example has gone through at least one metamorphosis from a trapezoidal wave with sharp turn-on and turn-off to the saw-toothed square-wave in this chapter. After survey, it may be difficult for a client to know the shape of the transmitter waveform if any post-processing is to be done to the recorded data. I therefore recommend that, if a ground loop calibration is undertaken, the current induced in the ground loop should be monitored. Not only does the measured current provide a geometry check on the airborne data, it provides an excellent method to directly recover the waveform of the transmitter current. For a time domain AEM systems like HoistEM which cannot record during the transmitter on-time, this is a particularly useful step. With a fast sampling system that has a well known transfer function, the transmitter waveform is easily recoverable from the ground loop current. If the resistance is high enough and the ringing current is recorded, the resulting decay could potentially be used to calibrate the windows of the airborne receiver. With GPS timing synchronising the ground loop current to the airborne system, this is a very possible method of independently determining receiver window widths. Finally, if a frequency domain system is used, the ground loop calibration method offers a practical and viable way to measure the frequency composition of the transmitters, in addition to the calibration procedure outlined earlier in this thesis.

Chapter 7

Summary, Discussion & Conclusions

This thesis began with a discussion of the phenomenon of electromagnetic induction, but I quickly moved to its application in the field of geophysics. More and more often, the electromagnetic induction method is being applied to land use issues. Although exploration geophysics is the core motivator of the electromagnetic method, its popularity for dealing with environmental problems is growing year by year, and the applicability and cost-effectiveness of AEM is extremely inviting. However, environmental applications of geophysics are generally constrained to the top 5–20 m of the surface of the earth, which brings us to the central theme of my thesis: the quantitative improvement of airborne electromagnetic systems for survey applications.

Starting with the Maxwell equations, I reviewed the theory of electromagnetism in Chapter 2, paying particular attention to Faraday's Law, the production of magnetic fields from wire loops, and the concept of how magnetic induction stores magnetic energy between two arbitrary systems. I explained how magnetic induction is fundamental to the understanding of an airborne electromagnetic system and gave examples of the mutual and self inductance calculations of wires, loops and dipoles.

A simplified example of the mutual inductance of three loops was introduced; an idea that was of pivotal importance for the remainder of the thesis. It is this model that supports the framework of the inductive limit calculation; it is fundamental to the concept of the $\phi\beta$ domain and is the essential component behind the ideas of using a ground loop for the calibration of AEM systems.

The pendulum-like motion of towed birds was the subject of the next two chapters. All birds towed behind an aircraft will experience harmonic motion when on survey, the effect of which is to add specious information to the recorded data. This was clearly shown in two independent surveys with the introduction of the concept of the dimensionless β domain developed by Ley-Cooper et al. (2006), which is calculated by taking the ratio of an inductive limit extrapolated from data to the geometric inductive limit G. The DIGHEM survey, completed over conductive water in the Sydney Harbour should have given constant but different values of β for each frequency for the entire survey. Instead we saw periodic oscillations of 9–10 s in period in the magnitude of β for each line. Further analysis showed that every frequency showed the same behaviour, indicating that the oscillations were affecting the entire system.

Spurred by this realisation, I used video recordings of the RESOLVE system on survey in South Australia to prove that towed bird oscillations recorded on video camera could be predicted from the horizontal offsets of the GPS antennas mounted on the nose of the RESOLVE bird and the tail of the helicopter towing it. A statistical analysis of the entire Chowilla Floodplain dataset showed that the RESOLVE towed bird was experiencing oscillations that could be conveniently broken down into cross-line and in-line directions, and that the mean period of oscillation for both of these motions was different. Again using β, I showed that in-line swings of the towed bird corresponded to periodic changes in amplitude, and that forward swings increased beta while backward swings reduced it. This offered incontrovertible proof that bird swing had an effect on recorded EM data.

Once the existence of a relation between bird swing and EM data was established, I generalised the geometric factor G to include arbitrary bird pitch and roll in addition to altitude changes. This allowed me to model bird swing as the combination of two effects: altitude changes due to the swinging of the tow cable and bird ('altitude effect') and mutual inductance coupling changes due to bird pitch and roll ('geometric effect'). When using an altimeter mounted on the aircraft (rather than the bird), altitude changes of the bird are not detected by the instrument: hence, bird swing is readily detected in β through the altitude effect. When a bird-mounted altimeter is used to measure altitude, altitude effects in the EM data are reduced since the measured altitude more closely approximates the actual altitude of the bird. However, with altimeters such as laser range finding devices, the altitude measurement is subjected to slant range errors that arise due to bird pitch and roll. Compounded is the geometric effect of bird pitch and roll which changes the coupling of the transmitting and receiving coils to the ground. By modelling these effects separately, I have shown that the contributions of bird swing effects are different for each configuration. When using aircraft mounted altimetry, altitude effects far outweigh the effects caused by bird pitch and roll. When using bird-mounted altimetry, cable swing and altitude effects are minimised, but bird pitch and roll effects are enhanced due to the slant range effect.

Regardless of whether the periodic changes in β are caused by altitude or geometric coupling changes, I have successfully designed and implemented a filter that removes the effects of bird swing from the data provided the main frequency of the swing is known. The filter is applied to data in the β domain, which is then transformed back to in-phase and quadrature values for normal processing. The bird swing filter operates on β by removing both the fundamental frequency effect and the first harmonic effects of bird swing. The first harmonic effect has a magnitude term that must be altered based on the method of altimetry used. For aircraft-mounted altimeters, the magnitude term must be added to β, while for bird-mounted altime-

ters, it must be subtracted. The effect of filtering β for bird swing was nicely shown in Figures 4.11 and 4.12 (pp. 113–114), and a definite improvement in the recorded AEM data can be seen.

By generating a stop-action movie from sequential photographs, I determined the fundamental frequency of oscillation of the in-line cable swing and bird pitch of the towed bird in the Sunraysia RESOLVE survey. The observation of these frequencies is supported by the bird pitch measurements performed by the contractor. Additionally, I developed an algorithm that predicts the instantaneous roll of the bird resulting from cross-line cable swings from the simultaneous position solutions of the helicopter-mounted and bird mounted GPS antennas. This may eliminate the contractor's present need for 3 GPS antennas mounted on the bird—for bird roll and pitch motions—down to 2 (just pitch), although I suggest further testing of the concept. Bird pitch predictions from GPS antenna positions do not match the measured bird pitch angles because the GPS antenna method only predicts bird pitch from a rigid cable model (whereby the bird is not allowed to pitch independently of the cable's swing), which is unrealistic. The Sunraysia video I produced shows that while bird pitch is related to cable swing, its prediction is unreliable.

Finally, in Chapter 4, I presented my findings on the relation between bird and cable swing based on the observations of a scale model. This model, essentially a simplification of the classical chaotic double pendulum experiment, allowed me to demonstrate that while the cable swing period increases with cable length, bird pitch period decreases with increased attachment length. Using a Lagrangian and Hamiltonian formalism, I developed a simple model that reproduces the basic two-period behaviour of a towed RESOLVE or DIGHEM bird from the first-order differential equations.

Revisiting the concepts of mutual- and self inductance, I developed the mathematical framework for the generation of a secondary emf in a airborne receiver from the Faraday inductions coupling a transmitter of arbitrary current waveform inter-

acting to an accurately surveyed ground loop whose electrical properties are well known. Using Laplace transforms, I developed an input/output system approach to calibrating AEM systems based on the flyover of a calibration ground loop. Two issues of time domain calibration were identified: the 'waveform' problem and the 'geometry' problem.

The waveform problem was the subject of Chapter 6. In it, I developed and implemented the mathematical theory of deconvolution of two or more time series. Using the input/output approach of the Laplace transform, I showed how an AEM transmitter's current waveform could be recovered from the measurement of the current induced in a ground loop during a system flyover. Using Fourier transforms, the deconvolution process becomes a simple matter of division. I found that increasing the resistance in the ground loop increased the loop's decay rate, thereby limiting the convolution of the exponential decay with the transmitter current waveform. Consequently, a cleaner representation of the transmitter current waveform was able to be recovered. Too much resistance in the ground loop, however, changed its physical behaviour. Increasing resistance in the loop causes it to act like a poor antenna: the oscillating induced current quickly decays to zero with a greatly increased time constant, nevertheless causing a response in the airborne receiver.

The geometry problem is much more difficult to solve. In Chapter 5, I showed how the secondary response in the airborne receiver can be predicted from knowledge of the transmitter waveform, system geometry and accurate timing. Again using Laplace transforms, the entire transmitter/ground-loop/receiver system can be viewed as an input/output flow where the transmitter current waveform is the input and the windowed induced emf in the receiver is the output. Using survey experiments from AeroTEM, HoistEM, VTEM and SkyTEM, I showed that the method is successful over resistive ground. For example, with the AeroTEM system flown in South Africa, I showed that although the predicted curve could be matched to the measured curve for a late time channel, the corrections could not be applied

to the predictions for the earlier delay channels. While this could be due to conductivity of the ground, I believe that waveform and receiver windowing issues are the cause for the discrepancy. The lack of agreement between measured and predicted experiments of the HoistEM lines flown in Western Australia showed that there was a problem associated with the amplitude gains in the HoistEM receiver for that system in 2003: this was corroborated by Vrbancich and Fullagar (2004). Other conclusions were drawn from the comparisons between measured and predicted response curves. It is obvious from comparisons between measured and predicted data that spatial or temporal averaging is used in the post-processing of most of the AEM systems studied. Although data quality can be improved by calibrating the transmitter waveform, receiver timing windows and gains, it is impossible to calibrate the geometry of a towed bird AEM system for an entire survey based on a single or even several ground loop experiments: the effects of bird swing are just too great. As was shown in Chapters 3 and 4, the position of the towed bird relative to the aircraft changes constantly and, in my opinion, there is little reason to believe a 'nominal geometry'. This has been demonstrated time and again in Chapter 5, where the altitude, in-line position and transmitter pitch needed to be altered independently for each line in each case studied. Most unfortunately, SkyTEM—the only AEM system that recorded pitch and roll measurements as a routine part of operation—was tested over conductive ground and the bird attitude could not be included in checking the receiver response.

Bird swing and the pendulum-like motions of towed transmitters and receivers will continue to be the greatest contributing error to the quantitative analysis of airborne electromagnetic data. The concept of nominal system geometry is only a first approximation. It is my firm belief that pitch and roll sensors need to be attached to the towed bird, as well as an accurate means of measuring its position, preferably in synchronicity with the position of the aircraft. Until this is done, there will always be an uncertainty in measured data: there will always be a 'geometry error'.

In order to do a complete calibration of the AEM system, the waveform, peak current, rigid system geometry and timing scheme must also be known. This information must be garnered from the literature or from the manufacturer, and can be difficult to get. However, even supposing all of these conditions have been met, absolute calibration of the AEM system will be impossible until the enormous problem of system geometry is remedied. Bird swing, resulting in pitch, roll positional and altitudinal errors must be attended to if any advancement is to be made in system calibration. Geometry is the key to accurate measurement of AEM signals, and we are now in the position with high speed, accurately timed and controlled transmitters and receivers to detect geometry errors. I recommend the practice of placing GPS antennas on the towed system, as is done with the RESOLVE system. Using helicopter-mounted GPS antennas to estimate bird position is not sufficient, and does not provide accurate enough position information. Roll and pitch sensors, such as are used on the SkyTEM system, are an important step forward. I strongly recommend that they be used as well, even though I am aware that they can generate noise in the receiver response. Range-finding laser altimeters mounted on the bird provide better altitude information than radar or laser altimeters mounted to the aircraft. However, unless the roll and pitch of the bird is also measured, the laser altimeter will contribute a different, rotation- and altitude-dependent slant-range error.

It is my opinion that more attention must be given to EM system altimetry. As others have done before, I have shown that laser and radar altimeters do not necessarily yield the same altitude for the bird. Radar altimetry is prone to error due to the fundamental assumption that the bird remains at a constant 30 m separation from the helicopter during the entire length of the survey. I have categorically shown that this is not true. Furthermore, the 30 m separation assumption can lead to constant differences between laser and radar altimetry that can be on the order of metres. The Sunraysia dataset proved that this is not uncommon. Exclusively using

the laser altimeter to measure bird-earth separation also leads to errors in altimetry due to bird swing. All of these errors can cause problems during interpretation and inversion. My recommendation is that if laser altimeters are going to be used to measure bird-earth separation, a scanning laser altimeter rather than a range-finding laser altimeter is used. A range-finding laser altimeter finds the distance to the first object that intercepts its beam. Scanning laser altimeters calculate the bird-earth separation distance by taking averages of distances based on the interception of a fan or beam of light spread out over the surface of the earth. If this type of laser altimeter is mounted underneath the rotation point of the towed bird, I predict that the measured altitudes would be far more reliable than they are at present.